Design and characterisation of a novel translucent solar concentrator

Nazmi Sellami

Submitted for the degree of Doctor of Philosophy

Institute of Mechanical, Process and Energy Engineering

School of Engineering and Physical Sciences

Heriot-Watt University

Edinburgh, United Kingdom

June 2013

Abstract

This thesis begins with an investigation into the optical performances of the Crossed Compound Parabolic Concentrator (CCPC) for photovoltaic application and introduces the novel concept of a Translucent Integrated Concentrated Photovoltaic (TICPV). The use of solar concentrators in BIPV enables a reduction in the cost of generating photovoltaic electricity lending to yet another field of research known as Building Integrated Concentrated Photovoltaics (BICPV). The potential of BICPV as the most promising technologies for future electricity supply is examined by the design, optimisation and testing of the main component of the TICPV, a novel static nonimaging transparent 3-D concentrator coined the Square Elliptical Hyperboloid (SEH), for the use in building fenestrations.

The SEH concentrator was designed and optimised via ray-tracing technique. A preliminary investigation into the optical efficiencies of 160 SEH concentrators of varying geometries was conducted and from this 20 concentrators were chosen and studied in more detail using the developed optical model with the aim of obtaining an optimised SEH concentrator out of these 20. The optimisation process proved to be far from straightforward, however, after careful consideration, five SEH concentrators with the best optical performances, each with different heights, were chosen. These concentrators were fabricated and used to assemble five separate TICPV modules. Subsequent to carrying out the simulation, the five optimised TICPV modules were examined in different environments (indoor and outdoor). The results of the indoor test, where the TICPV modules are exposed to direct radiation from a solar simulator, provided clear validation of the optical model; the results of the outdoor test added further to the validation and confirmed the power output of the TICPV modules when exposed to both direct and diffuse radiations.

The TICPV modules are developed in a way such that they collect sunlight during most of the hours throughout the day, allowing the generation of electrical power whilst maintaining the level of transparency of the fenestration. It was found that the TICPV modules are capable of saving more than 60% of the solar cells used in conventional flat PV systems. The designed TICPV modules simultaneously provide solar energy generation and optimised day lighting. The TICPV module designed in this thesis provides a viable solution to coping with the increasing energy demands and will create a new age of energy efficient buildings reducing the carbon footprint of both existing buildings and buildings of the future.

Dedication

This dissertation is dedicated to my late father and to my mother who had always had confidence in me and offered me encouragement and support in all my endeavours.

It is also dedicated to my darling wife for her care, love, understanding, and patience. Her unwavering encouragement has meant to me so much during the pursuit of my degree and the writing of the thesis.

Acknowledgements

Alhamdulillah (Praise be to Allah) for the good and the bad times - I have learned a lot and hope to continue learning.

Thanks go to my supervisor Professor T.K. Mallick for his advice, guidance and encouragement over the last four years. I am fortunate to have him as my advisor. I would like to thank Dr Nabin Sarmah for his continuous help and collaboration setting up the Solar Energy testing site. I am thankful to the Engineering and Physical Sciences Research Council (EPSRC) and to the School of Engineering and Physical Sciences, Heriot-Watt University for providing the financial support and research facilities during my PhD.

I would like to thank all of the technicians in the mechanical engineering workshop for their help in making my experimental hardware and for their assistance, providing support and help as and when needed setting up the solar energy testing site.

Finally, I would like to express my gratitude to my mother for her support over the long years of study – she instilled in me the desire to seek knowledge and learn. A special gratitude, thanks, and appreciation go to my wife for putting up with me throughout the whole process and for her understanding and love. She was always there for me, keeping me focussed and maintaining my perspective on life when things got tough. Most importantly she strengthened my faith reminding me that without patience, constant perseverance and Allah's help, I would not succeed in life. Her support and encouragement was in the end what made this dissertation possible. Thanks to my adorable three children for their patience during the busy times of my PhD; I thank Allah for these precious gifts. Thanks also to all my family and friends in Edinburgh, particularly to my parents-in-law for their continual care, help and support and to all my family and friends in Tunisia and Qatar, particularly my brothers and their wives for their continuous encouragement and humour. It has been an amazing journey and I am sincerely grateful to Allah for providing me with such a positive environment and network of support from my friends and family. Thank you all.

Table of Contents

List of figures

List of tables

Nomenclature

a	CCPC entry aperture half width
A	Side of the square exit aperture
a'	CCPC exit aperture half width
A_a	Entry Aperture area
A_{abs}	Exit aperture or absorber area
a_T	Truncated CCPC entry aperture half width
C_g	Geometrical concentration ratio
C_{opt}	Optical concentration ratio
$Eff_{Optical}$	Optical Efficiency
F	Focal distance of the parabola
$FPSC$	Flat-plate static concentrator
H	Height of the concentrator
H_T	Truncated height of the concentrator
$\mathbf{I}$	Unit vector of incident ray
I_0	The reverse saturation current
I_{01}	The reverse saturation current (Diode1)
I_{02}	The reverse saturation current (Diode2)
I_{ph}	The photocurrent current
k	The Boltzmann constant (1.3806503×10^{-23} J/K)
n	Number of concentrated rays
$\mathbf{N}$	Unit vector along the normal
n_1	The ideality factor (Diode 1)
n_2	The ideality factor (Diode 2)
NR_i	Number of reflections of the concentrated ray i
q	The electron charge (1.60217646×10^{-19}C)
R	Distance between the sun and the concentrator
r	Sun radius
$\mathbf{R}$	Unit vector of reflected ray
R_s	The series resistance
R_{sh}	The shunt resistance or the parallel resistance.
T	The temperature of the p-n junction in Kelvin
V	The voltage across the PV cell
$V_{oc}(T_{ref})$	The open circuit voltage at reference temperature.

β	Open circuit voltage temperature coefficient (V/^{o}C)
θ	Incident angle
θ_c	Half acceptance angle
θ_i	Angle of incidence
θ_r	Angle of reflection
θ_{sun}	Semi-angle subtended by the sun
ρ	Reflectivity of the side reflectors of the CCPC (ρ =0.94).
$\varphi_{entry\ aperture}$	Flux at the entry aperture
$\varphi_{exit\ aperture}$	Flux at the exit aperture

Abbreviations

2-D	Two dimensional
3-D	Three dimensiona
ACPC	Asymmetric Compound Parabolic Concentrator
ACPPVC	Asymmetric Compound Parabolic Photovoltaic Concentrator
AM	Air Mass
BICPV	Building Integrated Concentrated Photovoltaics
BIPV	Building Integrated Photovoltaics
CCPC	Crossed Compound Parabolic Concentrator
CPC	Compound Parabolic Concentrator
CPV	Concentrated Photovoltaics
DiACPC	Dielectric Asymmetric Compound Parabolic Concentrator
EAR	Elliptical Aspect Ratio
$Eff_{Exp,optical}$	Experimental optical efficiency
$Eff_{Optical}$	Optical efficiency
E-W	East-North
HAR	Height Aspect Ratio
LGBC	Laser Grooved Buried Contact
LSC	Luminescent Solar Concentrators
MaReCo	Maximum Reflector Collector
PMMA	Polymethyle Methacrylate
PV	Photovoltaic
SEH	Square Elliptical Concentrator
S-N	South-North
TICPV	Translucent Integrated Concentrated Photovoltaic
TIR	Total internal reflection
UV	Ultra-violet
CNC	Computer numerical control

List of publications (to date)

Patent:

- Mallick T K., **Sellami N**., 2012. "*Solar Concentrator Design for Double Glazing Window Units*". PCT/GB2012/053221.

Journal:

- **Sellami, N**. and T.K. Mallick, "*Optical efficiency study of PV Crossed Compound Parabolic Concentrator*". Applied Energy, 2013. 102(0): p. 868-876.

- Mammo E D., **Sellami, N**., Mallick T K**.**, 2012, "*Performance Analysis of a Reflective 3D Crossed Compound Parabolic Concentrating Photovoltaic System for Building Façade Integration*". Progress in Photovoltaics. (available online)

- **Sellami, N.**, T.K. Mallick, and D.A. McNeil, "*Optical characterisation of 3-D static solar concentrator*". Energy Conversion and Management, 2012. 64(0): p. 579-586.

- **Sellami, N**. and T.K. Mallick, "Optical design of a Static Window Integrated Concentrating Photovoltaic System. WICPV". Solar Energy, 2013. 91: p. 273-282.

Conferences:

- **Sellami, N**. and T.K. Mallick. "Design of a Non-Imaging Static Solar Concentrator for Window Integrated Photovoltaic", in 8th International Conference on Concentrating Photovoltaic Systems (CPV8). 2012. Toledo, Spain: AIP.

- **Sellami, N**., Mammo E. D, G. Aritra and T.K. Mallick, "Comparative experimental characterisation of reflective and refractive type 3-d static low concentrating photovoltaic system", in 7th Photovoltaic Science Applications and Technology (PVSAT7). 2011: Edinburgh. p. 245–248.

- **Sellami, N**., T.K. Mallick, and D.A. McNeil, "Opticla characterisation of 3-D static soalr concentrator", in The International Renewable Energy Congress (IREC). 2011: Hammamet, Tunisia.

- **Sellami, N**., T.K. Mallick, and D.A. McNeil, "Optical performance modelling of a typical 3D crossed compound parabolic photovoltaic concentrator using ray trace technique", in 6th Photovoltaic Science Applications and Technology (PVSAT6). 2010: Southampton, UK. p. 153-157.

Chapter 1: Introduction

The world today is facing two major problems for the continuity of life on planet earth: the limitation of energy resources and the emission of greenhouse gases due to excessive energy generation. Both problems are related to satisfying the needs of the energy demands of society. The solution can be found in renewable and clean energies; one such solution is the use of solar energy. Harnessing the light and heat from the sun relates back to ancient times; despite the development of ever-evolving technologies, however, the conversion of solar energy to electrical energy is not yet cost effective to replace conventional sources of power generation due to the high cost of the solar cell. This renewable energy can be more cost effective when using solar concentrators; the expensive solar cells are replaced with inexpensive concentrator materials.

This chapter presents the history of the solar concentrators used for photovoltaic applications. The properties of different types of solar concentrators designed are summarised and introduced. Pointing out the benefits of the use of the static solar concentrators in building integrated photovoltaics BIPV, a literature review of the different nonimaging solar concentrators is presented starting with the fundamental concepts of non imaging optics arriving to the semitransparent PV module which is the point of interest of the current research. Looking at these types of PV modules, it was found that only a few research and industrial projects have studied the performance of the integration of the 2-D solar concentrator in a semitransparent PV module to be used in building integrated concentrated photovoltaic systems (BICPV). No studies, however, have looked at the use of a 3-D solar concentrator in semitransparent BICPV modules; this will be the main objective of the work carried out in this thesis.

1.1 Background

Human life nowadays is totally reliant on the availability of electric power; everything we do from working to relaxing, and from travelling to communicating are associated with the availability of electric power. The importance and necessity of electricity for the benefit of human life go without saying, however, there are two major issues that we are faced with due to the excessive generation of it, and there is a desperate need for a quick and instant solution.

The main problem is that fossil fuels are limited and their supplies and prices are becoming more and more intermittent due to the fact that we have been relying on them

for such a long time. A large percentage (68%) [1] of the electricity nowadays is generated using fossil fuels in steam cycles. This kind of energy production has created serious problems. The second main problem is environmental; the burning of fossil fuels in power plants is the principal source of CO_2 and other harmful gases emissions. Most of the scientists and scientific organisations agree that the excessive greenhouses gases in the atmosphere are the main reason behind global warming [2]. Global warming describes the rise of the average temperature of the earth's surface and oceans. Since the last century, the surface temperature of the earth has increased by 0.75°C and will rise further, between 1.1 to 6.4°C, during the twenty-first century [3].
In this respect, humanity is facing two major challenges to meet their needs, for the continuity of their existence and the preservation of planet earth:

- Provide reliable and affordable sources of energy
- The energy systems have to have low-carbon emission and be environmentally friendly.

The solution to these challenges can be found only in alternative energy sources that can reduce CO_2 emissions compared to that of fossil fuel. The alternative can only be found in clean renewable energy sources, which will enhance the quality of life on planet earth by creating a better living environment, preserving nature and reducing health problems. Moreover clean renewable energies are sustainable thus will secure the need in energy for the current population on earth as well as for the coming generations.

One of the leading solutions to reduce CO_2 emissions is the generation of electricity from sunlight using solar photovoltaic (PV) systems. Solar energy represents a big potential; the total amount of solar energy received by the earth is $1.5\ 10^{18}$ kWh/year [4].

The simplest and most direct method of generating electricity from solar radiation is the PV module. There is a barrier, however, in competing with the more conventional source of energy using fossil fuel; this is due to the high initial investment cost associated with PV systems. Despite advances in the development of solar cells material and the improvement of their efficiency, the commercialisation of PV panels is still limited. This limitation is due mainly to the high cost of the solar cells material and the failure to target the mass market.

The most expensive component of the PV module is the silicon material. The cost of the solar cells represents 72% of the full cost of fabrication of the PV module [5, 6]; in addition there is a shortage of silicon feedstock. One approach of reducing the cost of the PV module is replacing the silicon material with a thin film solar cell module [7]; their disadvantage, however, is that they less efficient compared to other PV modules.

In the search for a solution to reduce the cost of the PV module, two modern axes of research in the use of solar cells for electricity generation were born. The first approach is to replace part of the solar cells material with solar concentrator material to make Concentrated PV (CPV) systems. The main reason behind the use of the solar concentrator is to reduce the cost of the PV module and therefore reduce the cost of the solar energy produced. The existence and promotion of the CPV technology rely essentially on the design and fabrication of the concentrator part. The idea of photovoltaic power generation using concentrated sunlight is about as old as the first activities in terrestrial photovoltaics. The concentration is achieved via an optical device with the objective of reducing the area of the expensive solar cells in addition to the advantage of increasing their efficiency. The silicon solar cells cost 150 €/m^2 compared to the lenses costing only 30 €/m^2 and the mirrors costing only 15 €/m^2 [8].

One of the disadvantages and main barriers of the CPV is the necessity of a tracking system to track the sun movement especially for high and medium concentrations. Tracking systems are costly, bulky, consume electric energy and require continuous maintenance. They are not well suited to the existing PV market that serves small remote loads and, more recently, building integrated applications.

The main disadvantages of tracking system are:

- They are expensive; their cost may be higher than the cost of the photovoltaic cells for what the CPV was employed.
- Their complexity makes them difficult to install.
- Installation of tracking systems is awkward in applications such as residential roof tops or façades.
- The mechanical parts decrease the lifetime of the CPV system, adding to the cost of the periodical maintenance needed.
- Trackers consume electric energy, therefore the total efficiency of the CPV will be reduced.

An advantage of low concentration CPV systems is the exclusion of the tracking system. In addition, the solar cells used by low concentrations are usually silicon cells with a typical efficiency of 15% costing only 150€/m^2 compared to the triple-junction III-V solar cells required for the high concentration CPV systems costing between 35,000 –50,000 €/m^2 for an efficiency of 40% [8]. This makes low concentration PV systems more appealing for use, especially for small remote loads and building integrated systems.

The second approach followed by researchers to reduce the cost of the PV module is to incorporate the PV system into existing buildings thus reducing the need for separate costly structures. This line of research is known as Building Integrated Photovoltaics (BIPV) based on the existing potential of space readily available that can be used for PV installation; this space is the surfaces of the façades and roofs in buildings.
The 23 billion square metres of building surfaces in 14 countries selected with good yearly solar radiation can exceed 1000 GWp taking into consideration only 5% photovoltaic efficiency [9]. This amount of power generated is the power of 1000 nuclear plants. In addition to providing a large public market for the solar cells, BIPV systems have more advantages compared to the usual PV panels as outlined by Oliver and Jakson [10]:

- Avoiding the cost of the areas and land needed for installation, in addition to the cost of the structures needed for the PV panels.
- The electricity generated by the BIPV systems is used for the building on site, resulting in a reduction of the losses that occur during the transmission and distribution of the electricity in regular PV systems. This advantage is highly relevant for commercial buildings when the peak power demand corresponds with the peak power supply.
- The PV panels in BIPV can replace some of the important components of the roofs or façades reducing the need for extra structures which can be very costly. In addition, the building will be more energy efficient as they will become producers of energy.

Building integrated photovoltaic systems (BIPV) have a role in generating and fulfilling the electricity demands for domestic uses. The current BIPV market is largely dominated by conventional or flat plate PV modules, which are manufactured by

covering large areas of the module with silicon solar cells. Despite its mature manufacturing technologies, abundance, and simple Si-cell formation process, silicon solar cells are still expensive. As previously mentioned, in a typical PV module, the silicon wafer covers an immense fraction of the total cost of the module. To facilitate wide application of BIPV systems, the cost per generated power should come to a value lower than other sources of electricity. The cost of conventional solar photovoltaic (PV) systems for integration to buildings can be reduced by increasing the output per unit solar cell and this could be done by replacing expensive solar cells with a low cost optical material (concentrator). As mentioned previously, the use of concentrating optics can reduce the cost by minimising the area that is covered with the silicon to obtain the required power output [11, 12]. In general, the price of concentrating photovoltaic (CPV) systems is lower than flat plate systems and as a result many projects have been carried out to identify ways for lowering the manufacturing costs using various types of solar concentrators to develop CPV systems [13-18]. Furthermore, the CPV can be even more efficient when used in hybrid photovoltaic/thermal system applications which produce electricity and hot water simultaneously [19, 20]. This recent line of research, using CPV systems in BIPV, is referred to as Building integrated concentrating photovoltaics (BICPV) and will be discussed in more detail later on in Chapter 1 in section 1.5.2.

Currently there is a huge amount of interest in concentrating solar energy to generate electricity. With the growing fuel problem, has come the fast growing line of research into PV systems and the likes. It transpires here that within each area of PV arise various problems needing attention and from these problems stem advances in research.

Using CPV systems in buildings is the topic of research that will be the focus of this thesis. The aim of the current work is to design a new solar concentrator suitable for BIPV application and more precisely suitable for integration in transparent surfaces and façades of buildings.

1.2 Solar cell technologies

A solar cell converts the energy of the incident photons into electrical energy by the photovoltaic effect which involves the generation of free electron-hole pairs which are separated by the electric field at the p-n junction which is primarily an electrode diode, resulting in a photovoltage across its two terminals. When a p-n junction is formed, typically in a c-Si material with a homojunction, the majority carriers move across the junction under effect of diffusion, where electrons and holes recombine leaving aside immobilised carriers (positive donor and negative acceptor atoms) resulting in an electric field at the junction. When light is incident on the solar cells, photons are absorbed in the semiconducting material of band gap Eg, when hυ≥ Eg. This will lead to creation of free electron –hole pairs which will be separated by the existing electric field at the junction, resulting in a photovoltage [21].

When the solar cell is connected to an electrical load, the circuit is referred to as closed. The connection is established due to the metal contacts as shown in Figure 1.1

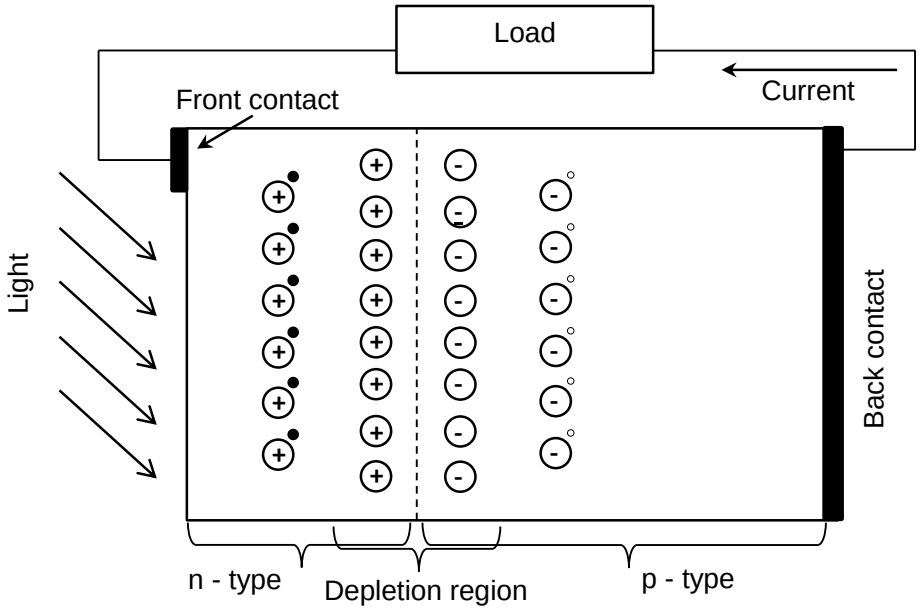

Figure 1.1: A schematic drawing of a simple conventional solar cell: creation of electron-hole pairs [22]

1.2.1 Brief history of photovoltaics

PV technology started 160 years ago when a French scientist Alexandre Edmond was the first to observe light-electricity conversion using metal electrodes and electrolytes [23]. The history of PV is summarised in the table below.

Table 1.1: Brief history of photovoltaics

Year	Action/News
1839	Alexandre Edmond Becquerel discovers the light-electricity conversion when he was experimenting with metal electrodes and electrolytes.
1883	It is only 50 years later, that Charles Fritts, an American inventor, presents the first solar cells made from selenium wafers. The efficiency was only 1% at the time.
1922	Einstein wins the Nobel prize for a photoelectric effect paper published in 1904.
1954	Bell Laboratories are the first to commercialise solar PV. They discover that silicon has the photoelectric properties and quickly produce Si solar cells, achieving 6% efficiency.
1950's	The commercialisation of solar cells begins to face difficulties due to the high price of kWh generated from them. However the adoption of solar cells as the power source for satellites saves the technology and keeps it running until now: All space applications would have been impossible if not for solar cells. All the leisure in telecommunication we have now from satellite navigators to TV channels are due to the solar powered satellites.
1963	Japan installs a 242-watt PV array on a lighthouse, the world's largest array at the time using a photovoltaic module of a silicon solar cell produced by Sharp corporation.
1970s	The cost of PV's are driven down 80% following the advance of research in the field. This development spread the application of solar PV in many applications such as offshore navigation warning lights and horns, lighthouses, railroad crossings, and remote use where utility-grid connections were too costly.
1989	Concentrator solar cell achieves an efficiency of 37% due to the increased

	intensity of the collected energy.
1990	The subsidisation for solar PV starts in Germany and Japan to push even further the improvement and development of the technology.
2007	An efficiency of **40.7%** is measured and independently confirmed for a metamorphic three-junction GaInP/GaInAs/Ge cell under the standard spectrum for terrestrial concentrator solar cells at 240 suns _24.0 W/cm2, AM1.5D, low aerosol optical depth, 25 °C.[24]
2012	The National Renewable Energy Laboratory (NREL), and their industry partner Solar Junction achieved another world record of 44% efficiency for multi-junction PV cells. (at 947 suns) [25]

1.2.2 Solar cell types:

Different solar cell technologies are available on the market. Different manufacturing processes and materials are used to make the silicon solar cells. Below a brief description of the main types of solar cells is given.

1.2.2.1 Crystalline silicon solar cells

There are two main silicon solar cell types based on their manufacturing process, the crystal size and the structure of the silicon wafer. The monocrystalline solar cells, better known as the single crystal silicon solar cells are the most expensive but have the highest efficiencies. The maximum efficiency of the monocrystalline solar cell reported recently is 25% [26]. The monocrystalline solar cells are known by their uniform dark black colour, and the corners of the cells are usually missing as a result of the production process and the physical nature of monocrystalline silicon, as shown in Figure 1.2(a) [27].

Polycrystalline solar cells (Figure 1.2(b)) are less expensive to produce but are less efficient than the monocrystalline cells. The efficiency of the polycrystalline solar cell is limited because of the minority carrier recombination. The recombination takes place due to the intragrain defect (impurities and precipitates) and dislocations. The polycrystalline solar cell can be identified by its non-uniform variation of light and dark blue colour: some patches are lighter than others, as shown in Figure 1.2(b) [27]. The differences in appearance come about as a result of the manufacturing process.

(a) (b)

Figure 1.2: The two main silicon solar cell types: (a) monocrystalline silicon (a) and polycrystalline silicon (b)

1.2.2.2 Thin film solar cells

Thin film solar cells may also be referred to as second generation solar cells due to better material utilisation as the thickness of the device ranges in a few microns as opposed to c-Si wafers which could be as thick as 200 microns. Some of the frontline technologies are, a-Si (amorphous silicon), CdS/Cu_2S (Cadmium sulfide/Copper(I) sulfide), CdTe (Cadmium telluride) and CIGS (Copper indium gallium (di) selenide) solar cells. CdTe and CIGS thin film solar cells are currently under intense research with already established commercial production world-wide ranging in a few GW per year. Of these, CIGS-based solar cells are currently best with a record efficiency of 20.4% [28] (EMPA, Switzerland) and 15.7% [29] (TSMC, Taiwan)for small scale laboratory and modules respectively [30], whereas CdTe-based solar cells have achieved a laboratory and module efficiency of 19.1% and 16.1 %, by First Solar [31]. Some of the advantages of these technologies include lower material requirements, a variety of processing methods and lightweight modules. A thickness of ~2-4 µm of thin film solar cells is enough for light absorption, whereas c-Si (crystalline silicon) needs to be ~180-300 µm thick to absorb all incident radiation efficiently. Due to the thinner layer produced, this leads to the faster processing steps and yield reducing the capital cost.

1.2.2.3 Multi-junction solar cells

The absorption of light can be increased efficiently by using multi-layered materials of different band gap for better utilisation of the solar spectrum, which are referred to as third generation solar cells. III-V material such as Gallium Arsenide (GaAs), indium phosphide (InP) and gallium antimonide (GaSb) are found to have excellent opto-electronic properties to manufacture high efficiency solar cells [32]. It is reported that a theoretical conversion efficiency of 86.6% [33] can be achieved of the concentrated sunlight. The National Renewable Energy Laboratory (NREL), and their industry

partner Solar Junction achieved a world record of 44% efficiency for multi-junction solar cells (at 947 suns) [25].

1.2.3 Solar cell I-V characterisation

The I-V curve characterising a typical solar cell has the shape illustrated in Figure 1.3 (red line). The voltage across the load is swept from zero to V_{oc}. Many important parameters of the solar cell can be determined from this curve. These parameters are V_{oc}, I_{sc}, I_m, V_m, P_m, FF which are described in detail in the section below:

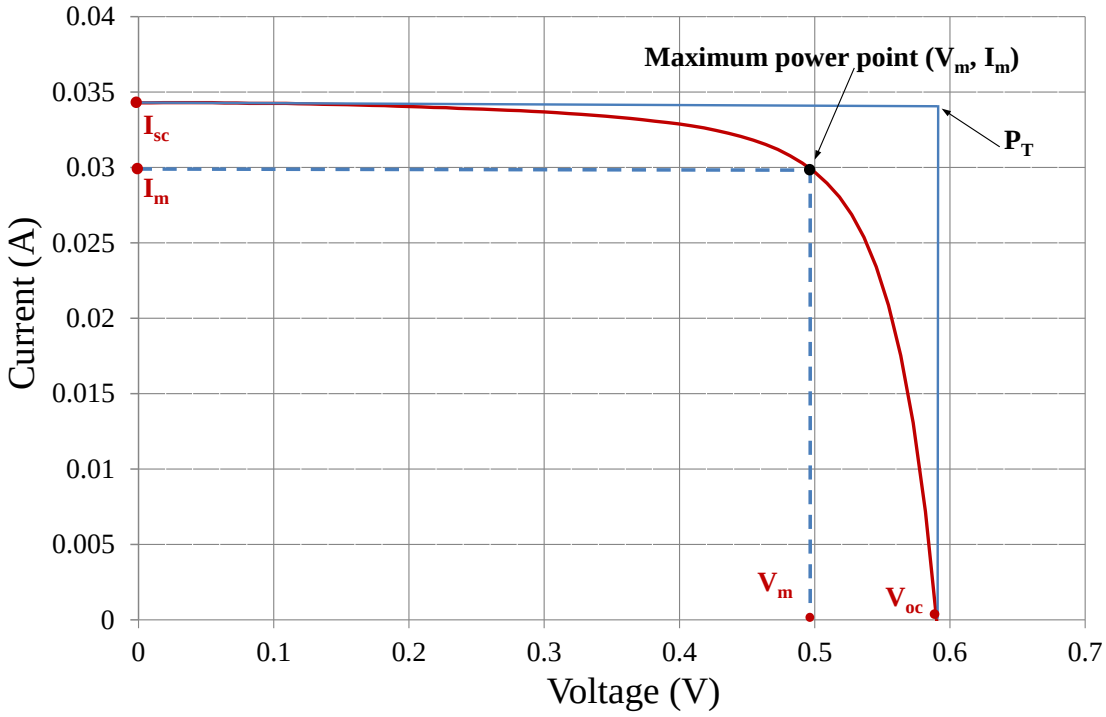

Figure 1.3: Typical Current-Voltage (I-V) characteristics of the silicon solar cell connected to variable resistive load

1.2.3.1 Short Circuit Current (I_{sc})

The short circuit current I_{sc} corresponds to the short circuit condition when the impedance is low and is calculated when the voltage is equal to zero. It is the maximum amperage generated by a solar cell exposed to sunlight with the output terminals shorted. I (at V=0) = I_{sc}

1.2.3.2 Open Circuit Voltage (V_{oc})

The open-circuit voltage V_{oc} is the maximum voltage generated by a solar cell exposed to sunlight with no load connected. It occurs when there is no current passing through the cell. V (at I=0) = V_{oc}

1.2.3.3 Maximum Power (P_m), Current at P_m (I_m), Voltage at P_m (V_m)

The maximum power P_m is the power produced by the solar cell in Watts. It can be easily calculated along the I-V sweep by the equation:

$$P_m = I_m \times V_m \tag{1.1}$$

The PV solar cells must be operated at their maximum power point (MPP) in order to achieve the maximum efficiency from the system. However, the MPP is directly affected by the illumination and temperature of the solar cell, as well as the radiation [34] and thus the dynamic control of P_m is very vital in optimising the maximum output from the PV system.

1.2.3.4 Fill Factor (FF)

The fill factor, *FF*, is essentially a measure of the quality of the solar cell which primarily depends on the parasitic resistances of the device such as series and shunt resistances. It is the ratio of the actual rated maximum power P_m to the theoretical (not actually obtainable) maximum power P_T as shown in Figure 1.3:

$$P_T = V_{oc} \times I_{sc} \tag{1.2}$$

The *FF* can be calculated from the following equation (1.3).

$$FF = \frac{I_m \times V_m}{I_{sc} \times V_{oc}} \tag{1.3}$$

The *FF* is a key parameter in evaluating the performance of solar panels. Typical commercial solar panels have a fill factor > 0.70, while grade B solar panels have a fill factor ranging from 0.4 to 0.7.

1.2.3.5 Efficiency (η)

Efficiency is the ratio of the electrical power output P_{out}, compared to the solar power input, P_{in}, into the PV cell. P_{out} can be taken to be P_m. P_{in} can be calculated by the product of the irradiance of the incident light measured in W/m^2 with the surface area of the solar cell in m^2.

The efficiency of the solar cell and P_m are directly affected by the temperature variation of the solar cell and the intensity and spectrum of the incident light. For this reason, it is recommended to test and compare PV cells using similar lighting and temperature conditions, called standard test conditions (STC).

1.2.4 Equivalent circuit model for a photovoltaic cell

In this section, descriptions of the different equivalent circuit models for photovoltaic cells (solar cells) are presented.

1.2.4.1 Ideal model

The simplest solar cell model consists of a diode (diode represents the p-n junction of a solar cell) and a light generated current source (I_{ph}), (directly proportional to the solar radiation), connected in parallel, it is called the ideal solar cell model and is illustrated in Figure 1.4.

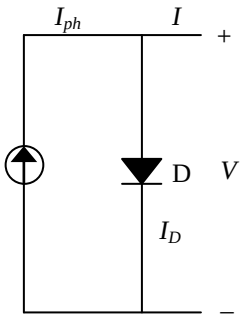

Figure 1.4: An equivalent circuit representation of an ideal solar cell

The photocurrents I_{ph} can be written as:

$$I = I_{ph} - I_D \tag{1.4}$$

or

$$I = I_{Ph} - I_0 \quad e^{\frac{q \times V}{n \times K \times T}} - 1 \tag{1.5}$$

Where:

I_{ph}: the photocurrent

I_0: the reverse saturation current

q: the electron charge ($1.60217646 \times 10^{-19}$C)

k: the Boltzmann constant ($1.3806503 \times 10^{-23}$ J/K)

T: the temperature of the p-n junction in Kelvin

V: the voltage across the PV cell

n: the diode ideality factor

1.2.4.2 One single diode model

The single diode model takes account of material resistivity and the ohmic losses due to levels of contact and the shunt resistance effects in the device. These losses are represented by a series resistance R_s and the shunt resistance R_{sh} in the equivalent circuit as illustrated in Figure 1.5

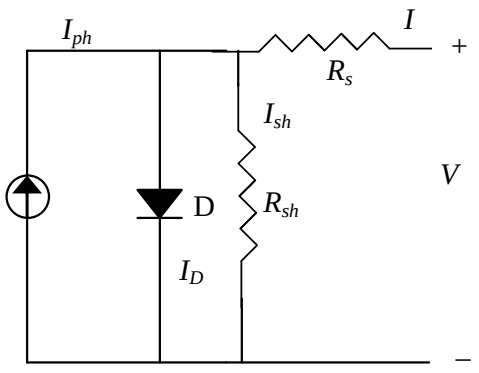

Figure 1.5: Single diode model with R_s and R_{sh}

The output current of the solar cell for the single diode model with R_s and R_{sh} can be written as follows:

$$I = I_{ph} - I_D - I_{sh} \tag{1.6}$$

The current through the parallel resistance can be written as:

$$I_{sh} = \frac{V + I \times R_s}{R_{sh}} \tag{1.7}$$

The output current when developing the terms I_D and I_{sh} can be written as:

$$I = I_{Ph} - I_0 \left[e^{\frac{q\ V+I\times R_s}{n\times K\times T}} - 1 \right] - \frac{V + I \times R_s}{R_{sh}} \tag{1.8}$$

Where:

R_s: series resistance

R_{sh} is the shunt resistance or the parallel resistance.

1.2.4.3 Two-diode model

The two-diode model represents an improvement to the one-diode model to extract parameters from outdoor or indoor I-V data of polycrystalline-Si PV modules. Zainal et al. introduced an improved model to reduce the computational time by reducing the input parameters to four [35].

The solar cell is represented as a current source in parallel with two diodes and shunt resistance R_{sh} representing the shunt leakage through the p–n junction and a series resistance R_s in series with them representing all ohmic losses as shown in Figure 1.6.

The first diode D1 models the recombination in the neutral region of the cell with an ideality factor n_1, and the second diode D2 compensates the recombination loss in the depletion region with an ideality factor n_2.

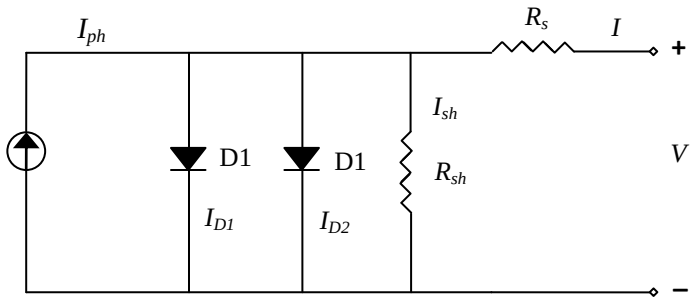

Figure 1.6: Two-diode electrical equivalent circuit of a non-ideal solar cell

The output current of the solar cell is divided in four terms as shown in equation (1.9): the photocurrent (I_{ph}), the current through the shunt resistance (I_{sh}), the diffusion-diode current (I_{s1}), and the recombination-diode current (I_{s2}).

$$I = I_{ph} - I_{D1} - I_{D2} - I_{sh} \tag{1.9}$$

Equation (1.9) can be written as:

$$I = I_{Ph} - I_{01}\ \left(e^{\frac{q\ V+I\times R_S}{n_1\times K\times T}} - 1\right) - I_{02}\ \left(e^{\frac{q\ V+I\times R_S}{n_2\times K\times T}} - 1\right) - I_{sh}\ \text{[36]} \tag{1.10}$$

where

$I_{sh} = \frac{V+I\times R_S}{R_{sh}}$ as detailed in equation (1.8)

The two diode model incorporates the temperature and the concentration ratio effects. There are seven unknown parameters in the model:

I_{ph}: the photocurrent current

R_s: the series resistance

R_{sh}: the shunt resistance

I_{01}: the reverse saturation current (diode1)

I_{02}: the reverse saturation current (diode2)

n_1: the ideality factor (diode1)

n_2: the ideality factor (diode2).

n_1 and n_2 are the diode ideal factors which are generally in the range of 1 and 2.

The photocurrent as a function of the temperature and the concentration ratio can be written as:

$$I_{Ph}\ T\ =\ I_{sc\ ref}\ + \alpha \times\ T - T_{ref}\ \times \frac{G}{G_{ref}}\ \text{[37]} \tag{1.11}$$

where:

$I_{sc(ref)}$: the light generated current at the reference temperature and a surface irradiance of 1000W/m^2.

T_{ref}: reference temperature of the solar cell.

G: irradiance on the solar cell

G_{ref}: reference irradiance 1000W/m^2

α: short circuit current temperature coefficient (A/ºC)

The reverse saturation current I_{01} and I_{02} at a given temperature can be written as [36]:

$$I_{01} = I_{s1} \times e^{\frac{q \times E_g}{n_1 \times K} \times \frac{1}{T_{ref}} - \frac{1}{T}} \times \frac{T}{T_{ref}}^{\frac{3}{n_1}} \quad (1.12)$$

$$I_{02} = I_{s2} \times e^{\frac{q \times E_g}{n_2 \times K} \times \frac{1}{T_{ref}} - \frac{1}{T}} \times \frac{T}{T_{ref}}^{\frac{3}{n_2}} \quad (1.13)$$

I_{s1} and I_{s2} are the saturation dark current associated with each diode in the model at reference temperature. They can be written as [38, 39]:

$$I_{s1} = \frac{\frac{1}{2} I_{sc\ ref}}{e^{\frac{q \times V_{oc}}{n1 \times K \times T_{ref}}} - 1} \quad (1.14)$$

$$I_{s2} = \frac{\frac{1}{2} I_{sc\ ref}}{e^{\frac{q \times V_{oc}}{n2 \times K \times T_{ref}}} - 1} \quad (1.15)$$

where:

V_{oc}: the open circuit voltage.

The open circuit voltage at a given temperature can be written as:

$$V_{oc}\ T\ = V_{oc}\ T_{ref}\ \times\ 1 + \beta \times\ T - T_{ref} \quad (1.16)$$

where

β: open circuit voltage temperature coefficient (V/ºC)

$V_{oc}(T_{ref})$: the open circuit voltage at reference temperature.

1.3 Concentrating solar energy

1.3.1 History of solar concentrators

The actual concept of solar concentration may date even further back to ancient Greece where legends relate that the famous Greek scientist Archimedes used to concentrate sunlight to generate fire on invading Roman ships. In 2005, a group of students attempted to burn a small ship using concentrating solar radiation and confirmed the feasibility of the legend's account of Archimedes [40].

While solar concentration may have first been used by Archimedes, it wasn't until the late 19th century that the first parabolic solar concentrator system was invented and designed by a French mathematics teacher, Augustin Bernard Mouchot in 1866. Mouchot began in 1860 by experimenting with solar cooking whereby he produced steam to provide motive power for a small steam engine. From there, he increased the scale of his solar experiments as his interest grew in finding new alternative energy sources. He managed to obtain funding from the government to carry out research into concentrating solar power with a specific aim to improve his solar driven steam engine. The dream of the ambitious inventor, however, came to an abrupt halt, when the French government decided that solar energy was uneconomical following the improvement in efficiency in internal transportation for coal delivery and ended his funding in 1880.

Mouchot had then predicted the actual problem of a lack of fossil fuel resources when he said, after demonstrating an early industrial application of solar thermal energy in 1880: "Eventually industry will no longer find in Europe the resources to satisfy its prodigious expansion... Coal will undoubtedly be used up. What will industry do then?" [41]. Had his funding continued then perhaps today the development of concentrating solar power would be further advanced and the problems surrounding fossil fuel less severe. The world was not yet aware of the gravity of the impending problem in the same way as he was and as such the doors to his research were closed.

Nearly a century passed before research into solar concentrators resumed. The first concentrating PV (CPV) system was designed by Sandia National Laboratories[1] in the late 1970's. The CPV was composed of a Fresnel lens to concentrate sunlight on silicon

[1] Sandia is a US national security laboratory involved in a variety of research and development programs to help secure a peaceful and free world through technology.

solar cells having two axes tracking structures. This first prototype needed a water cooling system to cool down the solar cells at the time.

Subsequently, just after the Sandia CPV prototype, Ramón Areces[2] developed a similar CPV system using Fresnel lenses but with a passive heat sink instead of the water cooling system to cool down the solar cells. The concentration ratio was in the range of 40× and rated power about 1 kWp.

These designs were all in the early stages of development and it was not until 1978 that the leading kick off for CPV eventually came about when the US department of energy (DOE) contracted Sandia Laboratories to start seventeen experiments on CPV. These experiments concerned:

- The concentration type: Fresnel lenses and reflective mirrors in different geometries
- Solar cells materials
- Cooling systems
- Tracking systems: one axis or two axes.

In the 1980's, CPV did not find any commercial success apart from a few experimental installations; they could not be cost effective with only a peak efficiency of 10%. The research, however, on silicon devices showed amelioration in solar cells in some laboratory experiments. Stanford University reported 28% at 140× with high resistivity point contact cells and the University of New South Wales reported 25% at 110× with low resistivity cells.

At the beginning of the 1990's, again the DOE backed-up the CPV research by creating the Photovoltaic Concentrator Initiative program (PVCI). This initiative comprised collaboration between four cell manufacturers (ASEC, Spectrolab, Sunpower and Solarex) and four module manufacturers (Entech, Solar Kinetics, Alpha Solarco and the SEA Corporation). The result was very promising by achieving a peak efficiency of 25% with point and line focus lens concentrator

[2] The Ramon Areces Foundation is a non-profit organisation created in 1976 to broadly encourage scientific and technical research in Spain, as well as education and culture in general, values that the institution consider to be the main driving forces for progress and modernity in society.

design [42]. But again there was a problem with the funding: the DOE brought an end to the PVCI program when they decided to cut the funds in 1993.

Across the Atlantic in Europe, another program called JOULE gave hope again to CPV research by subsidising the EUCLIDES Project (European Concentration Light Intensity Development of Energy Sources). Results emerged in 1995 in Madrid where a prototype using a reflective parabolic trough was installed with an efficiency of 14% [43].

The 1990's ended with an innovative concept of the 'two stages concentration' using a parabolic trough in the first stage and a Compound Parabolic Concentrator (CPC) in the second stage to change the focus shape. The concept was developed by The Fraunhofer-Institut for Solar Energy Systems (FISE) with a total concentration ratio of 300×.

Now, at the beginning of the 21st century, many new ideas and technologies are under investigation; there still lacks a clear idea and definitive answer, however, as to which CPV will be the best and the most cost effective. The most prominent project aiming to develop the CPV in this century is called IDEOCONTE which is subsidised by the European Community. The objective of the project is to develop the most efficient and cost effective CPV system based on silicon cells with a concentration level going from 2× to over 200× [44].

Concurrently, in Australia, Solar Systems are building the biggest PV heliostat solar concentrator power station in Mildura, Victoria. The project with a power of 154 MW will generate 270,000 MWh per year, enough for more than 45,000 homes. This will be partially operational in 2010 and in full commissioning in 2013 [45].

Depending on the use of the CPV, many research directions emerge. Some researchers are looking for high concentration systems for bulk generation of electricity to compete with fossil fuel and other renewable energy resources, whilst others are looking for the low concentration CPV systems which are more suitable for use with small devices or building integration. In this project, it is the latter line

of research that will be followed. In particular the aim is to investigate a new geometry for CPV with a low concentration ratio.

1.3.2 Types of solar concentrators

The concept of light concentration is to reflect or refract the maximum amount of light, as efficiently as possible, onto a smaller area on the exit aperture of the concentrator which is most commonly referred to as the absorber or receiver. This concentrated light has to be received by the absorber area as uniformly as possible, especially for PV applications. Solar concentrators are always characterised by their ability to concentrate light rays to which the term geometric concentration ratio (C_g) refers. This is defined as the ratio between the area of the entry aperture (A_a) and the area of the exit aperture (A_{abs}) in equation (1.17):

$$C_g = \frac{A_a}{A_{abs}} \tag{1.17}$$

There is a limit of C_g that any concentrator can achieve based on the second law of thermodynamics stating that there is no heat transferred between two bodies with the same temperature.

Rabl has elaborated an equation (1.18) for the maximum C_g based on the distance between planet earth and the source, the sun (S) [46]:

$$C_g = \frac{R^2}{r^2} E_{abs \to S} = \frac{E_{abs \to S}}{\sin^2 \theta_{sun}} \tag{1.18}$$

where $E_{abs \to S}$ represents an exchange factor that cannot be greater than the unity and R is the distance between the centre of the sun and the entry aperture of the concentrator and r is the radius of the sun as illustrated in Figure 1.7.

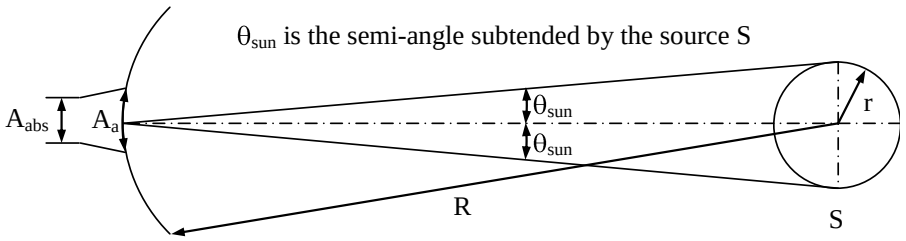

Figure 1.7: Solar radiation transfer through aperture A_a to absorber A_{abs}

Basic geometry shows that $\frac{r}{R} = sin\,\theta_{sun}$, therefore, for a 2-D concentrator (mainly referred to as linear concentrators)

the maximum C_g can be written as:

$$C_{g\_2-D} = \frac{1}{\sin \theta_{sun}} \tag{1.19}$$

And for 3-D concentrators (mainly referred to as circular concentrators) the maximum C_g can be written as:

$$C_{g\_3-D} = \frac{1}{\sin^2 \theta_{sun}} \tag{1.20}$$

Taking into consideration that θ_{sun}=0.262º [47], therefore the maximum $C_{g\_2\text{-}D}$=218.53 and the maximum $C_{g\_3\text{-}D}$=47756.32 referring to equations (1.19) and (1.20).

If the receiver is immersed in a dielectric medium of index of refraction *n*, then the equations (1.19) and (1.20) become:

$$C_{g\_2-D} = \frac{n}{\sin \theta_{sun}} \tag{1.21}$$

$$C_{g\_3-D} = \frac{n^2}{\sin^2 \theta_{sun}} \tag{1.22}$$

There are different types and classes of solar concentrators; they can be divided into different classes depending on, the type of optical element used to concentrate the sunlight, the C_g, and the number of axes that characterise the tracking system. These different types are discussed below and summarised in Figure 1.8.

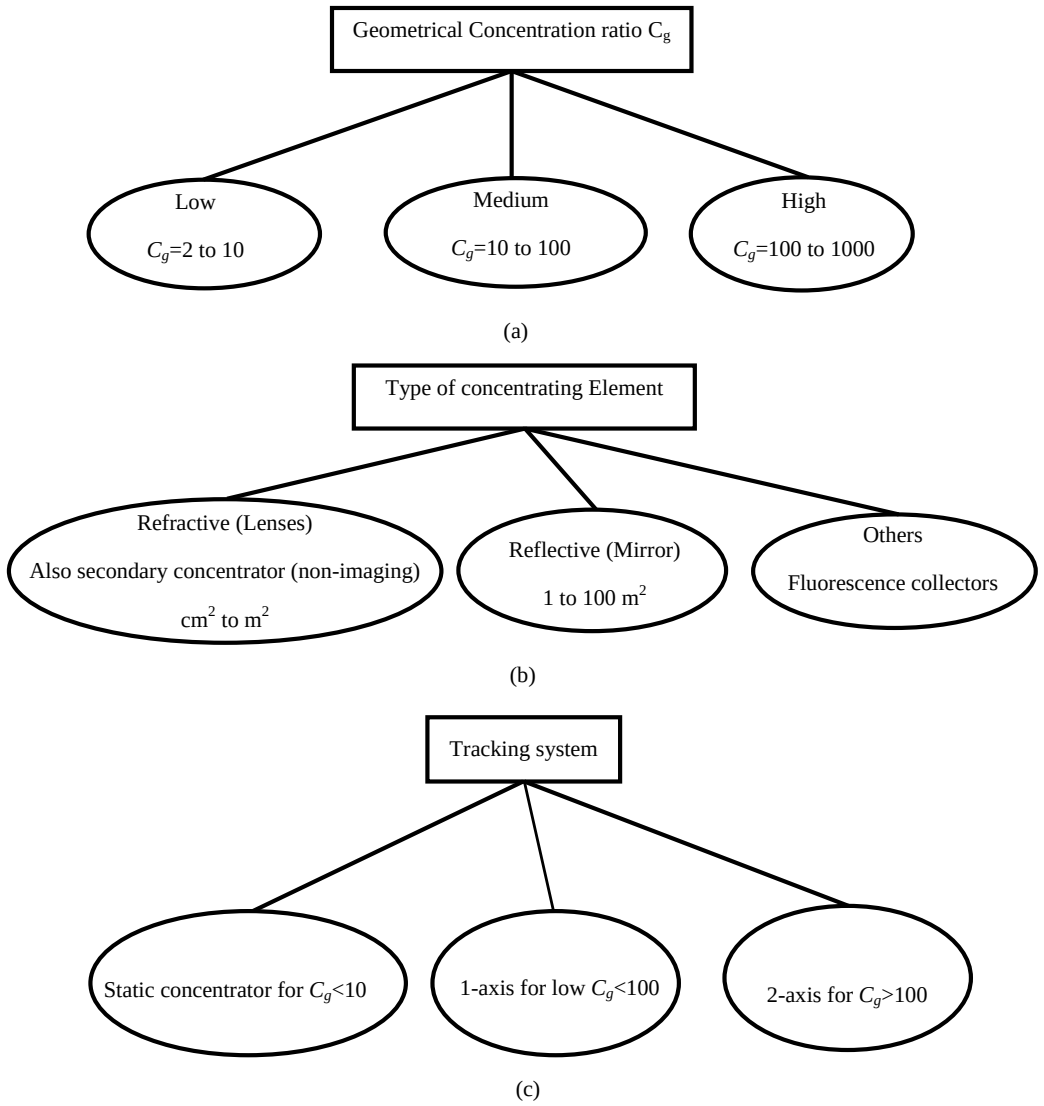

Figure 1.8: Classification of different solar concentrators based on (a) the geometrical concentration ratio, (b) the type of concentrating element and (c) the tracking system.

1.3.2.1 Geometric concentration ratio

Geometric concentration ratio is the most common name used to define the area of the entry aperture of the optical element of the concentrator divided by the active area of the solar cell. Apart from the C_g, there are other terms to measure the concentration, as the intensity of concentration, or "suns" and most of the time is represented with "×". The word "sun" is defined as the ratio of the average light intensity on the solar cell (W/m^2) divided by 1000W/m^2, which refers to the standard peak radiation. The solar concentrator can never achieve the theoretical concentration of C_g, as there are always losses of the sunlight energy when they pass through the optical device.

The solar concentrators can be divided into three classes referring to the C_g. These three classes are as represented in Figure 1.8(a):

- Low concentration, C_g = 2 to 10. Due to this low concentration ratio, low concentrating systems can be stationary. The best approved geometry until now for the low concentration is the CPC mentioned above. The earliest successful prototype of it was constructed by Roland Winston in 1969, and disclosed in U.S. Pat. No. 3,923,381. They have been studied and ameliorated since then [48].
- Medium concentration, C_g = 10 to 100. Such systems need a one-axis solar tracking system and, in very rare cases, a two-axes solar tracking system. They generally take the shape of parabolic reflectors [49, 50] or Fresnel lenses [51].
- High concentration, C_g = 100 to 1000. Such systems employ concentrating optics consisting of reflectors, Fresnel lenses or parabolic dishes [52]. These types of concentrators essentially require a two-axes solar tracking system to achieve the high concentration of the solar irradiation.

1.3.2.2 Type of concentrating elements

Generally, concentrators use both; reflective surfaces such as dishes and troughs or refractive optical elements such as lenses or mirrors. These two different types of concentrating elements are presented in detail below:

1.3.2.2.1 Reflective optical element

The reflective elements are mirrors or a combination of mirrors; they can be flat or concave. They are made from coated metal foil or coated glass. These kinds of solar concentrator systems are good for a high concentration ratio and for a large power generation scale. The best known geometry of the reflective concentrator is the parabola that will focus the sunrays that are parallel to the parabola's axis on a point located in the parabola's focus. The parabolic concentrators can be point focus or line focus as illustrated in Figure 1.9 (a) and (b) respectively.

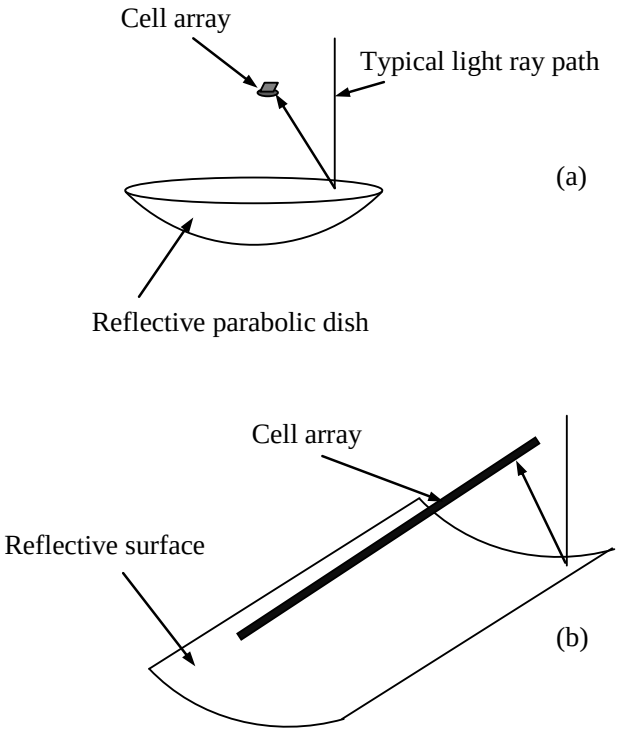

Figure 1.9: Reflective concentrator. (a) reflective point-focus paraboloid, (b) linear focus parabolic trough

For 3-D parabolic dish concentrators, the concentration ratio *C* is equal to [53]:

$$C = \cos^2 \theta_{\max,r} \left(\frac{\sin \theta_{\max,r}}{\sin \theta_{\max,in}} \right)^2 \tag{1.23}$$

where:

- $\theta_{max,in}$ is the maximum acceptance angle of the incident rays of the parabolic concentrator.
- $\theta_{max,r}$ is the maximum angle of reflection of the incident rays.

These angles are represented in Figure 1.10.

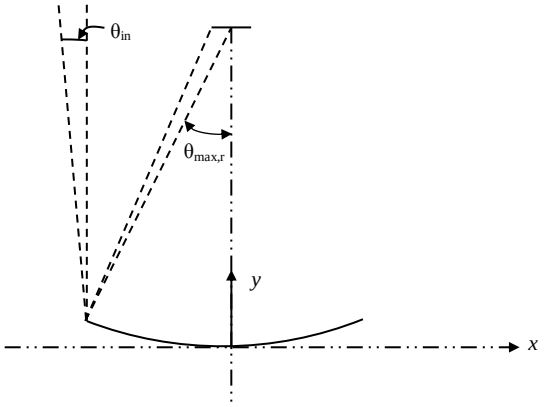

Figure 1.10: Cross section of a parabolic reflective concentrator.

The concentration ratio for a 3-D parabola is obtained when $\theta_{max,r}$ is equal to 45º and then it will be equal to [53]:

$$C = \frac{1}{4}\left(\frac{1}{\sin\theta_{\max,in}}\right)^2 \tag{1.24}$$

This represents only one quarter of the maximum theoretical value of the concentration ratio for a 3-D concentrator. In general parabolic concentrators are used for thermal applications where a high temperature is desired and the uniformity of the flux does not represent a big issue. There are some projects, however, where parabolic dish concentrators are used for PV application and they are considerably expensive compared to other designs [54].

In the case of reflection, the incoming light (or the incident ray), and the direction of the outgoing light reflected (or the reflected ray) make the same angle with respect to the surface normal as illustrated in Figure 1.11 (a), thus the angle of incidence θ_i equals the angle of reflection θ_r; this is commonly stated as $\theta_i = \theta_r$.

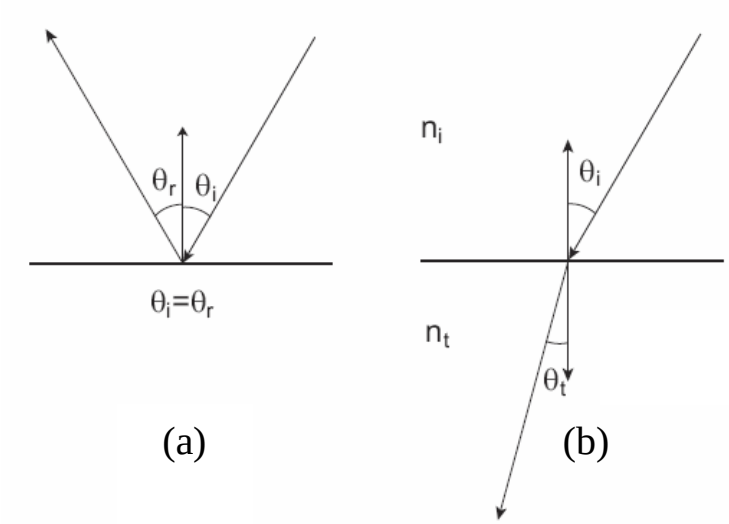

Figure 1.11: Representation of the laws of reflection (a) and refraction (b)

1.3.2.2.2 Refractive optical element

The Fresnel lenses are either point focus in the case where they have circular symmetry about their axis (they focus the sunlight on one solar cell behind it), as illustrated in Figure 1.12 (a); or linear focus in the case where they have constant cross section along a transverse axis (they focus sunlight on a linear array of solar cell), as illustrated in Figure 1.12 (b). The linear focus Fresnel lenses have been modified to the domed Fresnel lenses as illustrated in Figure 1.12 (c), to increase the rigidity of the lens. In all cases they do not give uniform concentrated sunlight, which affects the efficiency of the solar PV cell. Generally, therefore, it needs to incorporate a secondary optical element (SOE) to make the distribution of the radiation more uniform. They are generally used for a high concentration ratio system and as such require a two-axes tracking system and are relatively cheap to make and assemble with the solar cell. They are made from acrylic (polymethyl methacrylate or PMMA) which melds well.

The refraction always happens between two different mediums, the angle of the incoming light or incident ray with the normal in the first medium and the angle of the refracted ray with the normal in the second medium. This is related by the following relationship and is illustrated in Figure 1.11(b):

$$n_i \sin\ \theta_i\ = n_t \sin\ \theta_t \tag{1.25}$$

where:

- n_i and n_t are the two different refractive indices.
- θ_i and θ_t are respectively the angle of incidence and refraction of light or the ray with respect to the surface of the surface normal.

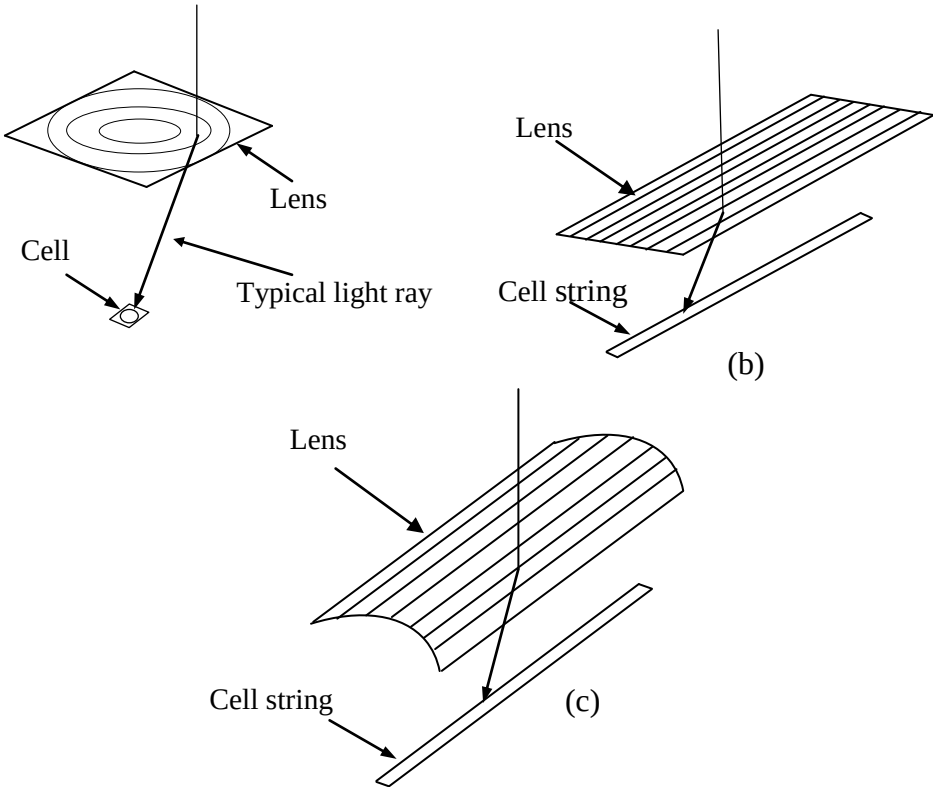

Figure 1.12: Fresnel lenses: (a) point focus, (b) linear focus, (c) domed linear focus

1.3.2.3 Tracking systems:

Concentrating the sunrays of the moving sun on the solar cells requires a mechanical tracking system. The accuracy of the tracking system needs to be higher the larger the C_g is. In most of the cases when the accuracy required is less than 0.1º, a secondary concentrator is added to the tracking system in order to relax the demand.

There are two different types of tracking system that allow the solar concentrators to track the direct radiation of the sun. The point-focus solar concentrator usually requires a two-axes tracking system in order to focus the sunlight on the solar cell. Alternatively,

the line-focus solar concentrator requires only a one axis tracking system. This represents a limitation as the one axis tracking system cannot exceed C_g=100. These are the two types of tracking system that can be used with concentrating systems; they can be different based on the mechanical engineering designs.

The requirement of a tracking system is considered as a disadvantage because of the high cost for the accurate mechanical system that needs continuous maintenance, in addition to the energy needed for its functioning. There are cases where a mechanical tracking system is not used with solar concentrators; these are referred to as static concentrators. The static concentrator, which relies on non-imaging optics, is discussed below in section 1.4.2.

1.4 Nonimaging optics and static solar concentrators

1.4.1 Fundamental concepts of nonimaging optics

One of the most important requirements for solar concentration is to have a concentrator with the ability to accept light from as large an angular region as possible. This minimises the need for the accuracy of the tracking system, but more importantly, the concentrator will collect sunrays without the need of a mechanical tracking system. These requirements have given birth to a whole new discipline called nonimaging optics. This branch of optics was founded by Professor Roland Winston and his group at the University of Chicago [55]. The research into nonimaging optics has resulted in the consideration of static solar concentrators. The existence of these kind of concentrators is directly related to and dependent on the development of nonimaging optics. In other words, a static solar concentrator can only be a nonimaging concentrator.

Nonimaging solar concentrators focus the light source on a receiver producing a different prescribed illuminance pattern. The field of nonimaging optics has seen the light because of the successful first design of the 2-D concentrator that could focus light rays with a large acceptance angle without the need for a tracking system. This system is known as the Compound Parabolic Concentrator (CPC). The first description of the CPC was introduced by Hinterberger and Winston [56]. The CPC in 2-D geometry was specified by Winston [57]. Additional descriptions were published later by Winston and Hinterberger [58] and Rabl and Winston [59].

The CPC is characterised by the acceptance that varies depending on the incident angles. The acceptance is represented by the ratio between the number of concentrated

rays and the number of rays entering the CPC. Figure 1.13 shows the acceptance of an ideal CPC having a half acceptance angle θ_c [60].

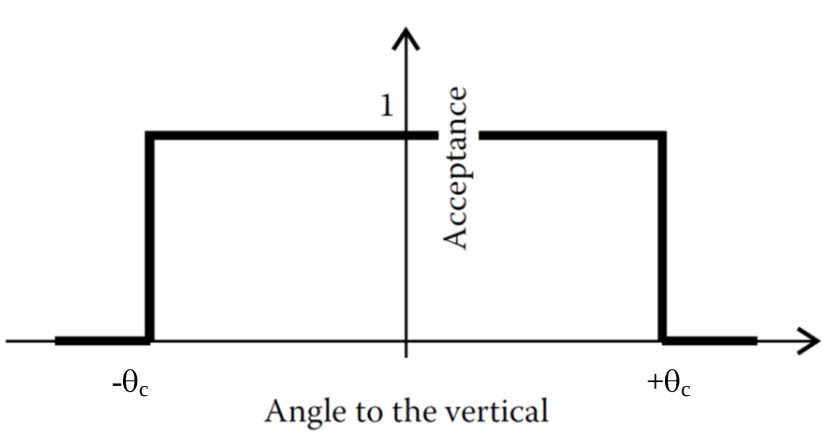

Figure 1.13: Acceptance of a CPC with an acceptance angle θ_c.

One of the characteristics of the CPC is that it focuses all of the light rays within the range of an angle known as the acceptance angle $2\theta_c$. Figure 1.14 illustrates the trajectories of light rays incident of the CPC in three different situations – the schematic diagram represents the CPC walls with the receiver placed at the bottom (horizontal line at exit aperture). All of the rays entering the CPC at an angle $\theta_1 < \theta_c$ are focused on the receiver (exit aperture) of the CPC as illustrated in Figure 1.14(a). A specific case where the light rays incident on the CPC have the same angle $\theta=\theta_c$ is illustrated in Figure 1.14(b); they will be focused on the edge of the receiver of the CPC. The last case is where the incident light rays on the CPC have an angle θ_2 with the vertical higher than θ_c; they will be reflected back to the entry aperture of the CPC, in this case the concentration of the incident rays does not happen, as illustrated in Figure 1.14(c).

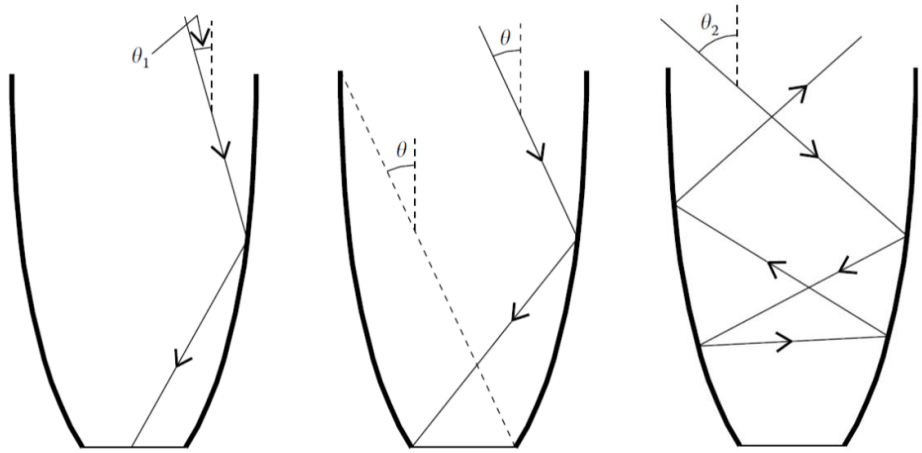

Figure 1.14: Path of three different types of rays inside the CPC: (a) a ray entering the CPC at an angle to the vertical smaller than θ_c, (b) a ray entering the CPC at an angle to the vertical equal to half-acceptance angle θ_c, (c) a ray entering the CPC at an angle larger than θ_c is rejected [61].

The exit aperture or the absorber area of the CPC can have different geometries as shown in Figure 1.15 [59]. In Figure 1.15(a) the absorber of the CPC is illustrated, it is horizontal and flat. Figure 1.15(b) illustrates a CPC with a fin absorber [62], Figure 1.15(c) illustrates a CPC with an "inverted-vee" absorber shape [63] and finally Figure 1.15(d) illustrates a CPC with a tubular absorber mainly used for thermal applications [64, 65].

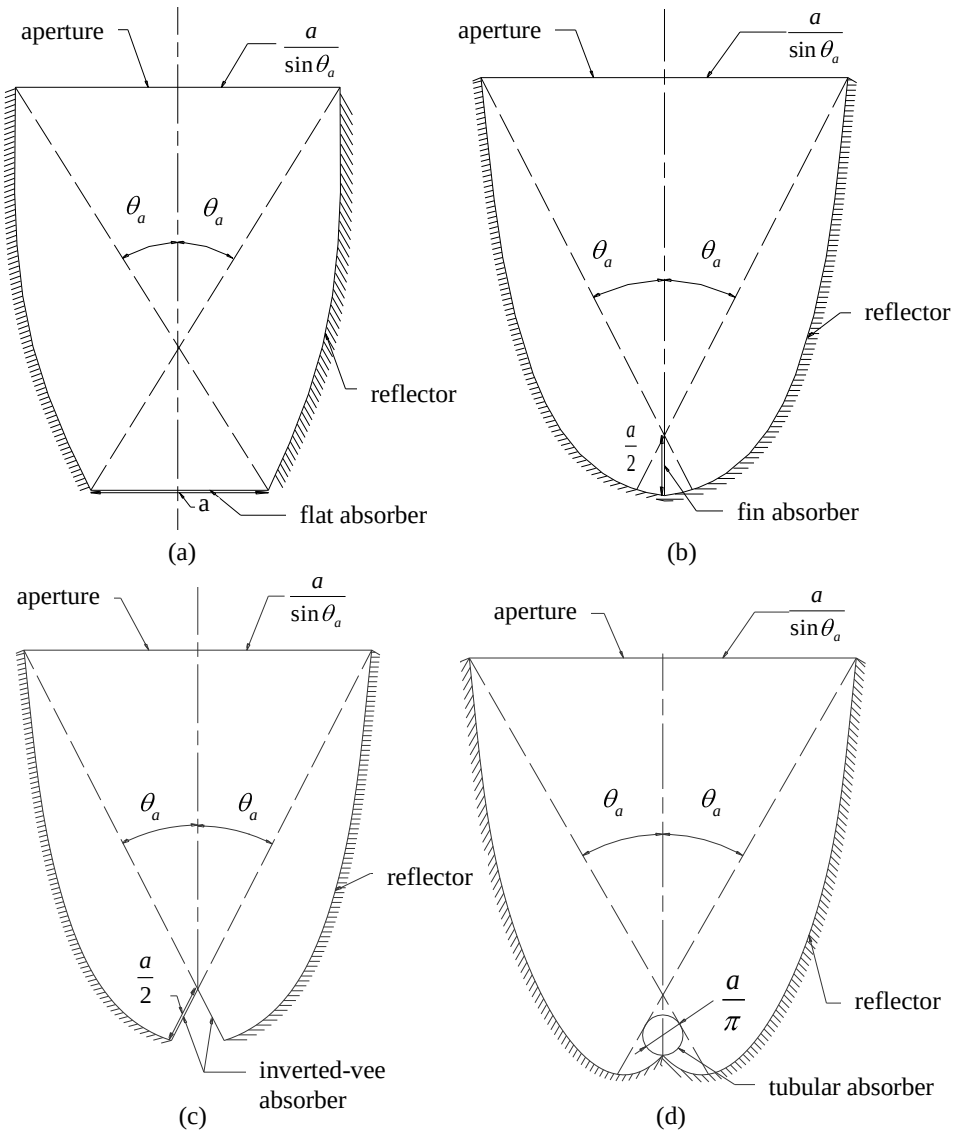

Figure 1.15: Different CPC configurations: (a) CPC with flat absorber, (b) CPC with fin, (c) CPC with "inverted vee" absorber, (d) CPC with tubular absorber [66]

These CPCs are example that have been used as static concentrators or second stage concentrators for various different PV applications.

1.4.2 Static (stationary) solar concentrator

Since the introduction of the CPC, many other concentrators have been introduced as static concentrators working without the need of a tracking system. In this section a review of the major static concentrator designs representing an enhancement of the CPC shape and other more recent designs will be outlined, focussing only on the static concentrated photovoltaics (CPV).

Edmonds et al. studied the optical performance of a 3× liquid filled lens-V trough concentrator fabricated as a thin walled plastic shell with total internal reflecting sides [67]. It was found that the liquid filled lens-V trough concentrator, Figure 1.16, is simpler to fabricate compared to the truncated CPC. The lower height to aperture ratio of the liquid filled lens-V trough concentrator allows saving dielectric material resulting in reducing of cost, absorption and weight.

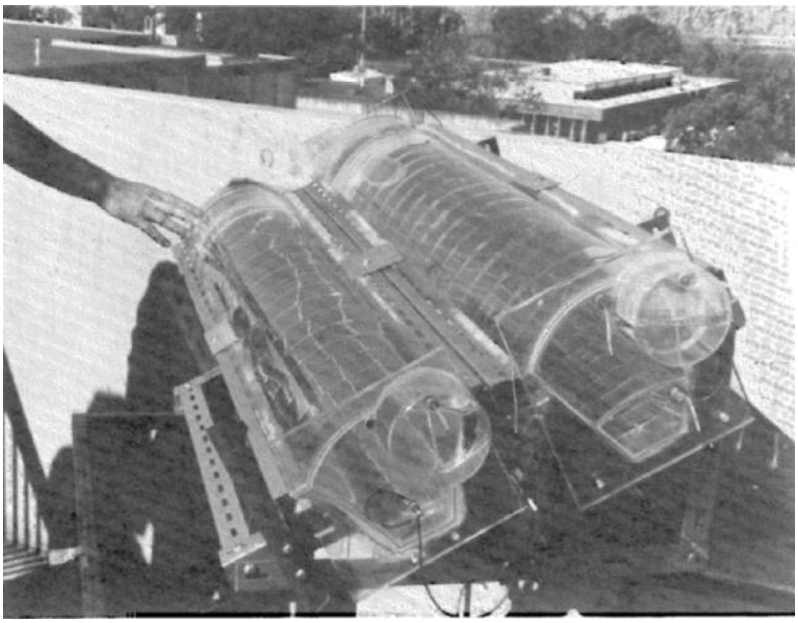

Figure 1.16: 3× concentrators mounted in East-West (E-W) orientation [67]

One of the concepts of the trough collector module is illustrated below in Figure 1.17 using bifacial cells combined with semicircular trough shaped mirrors. The collector assures full illumination of both sides without any restriction of acceptance angle [68]. This static concentrator has a complete hemispherical acceptance characteristic.

A module made of the static concentrators described can have the configuration shown in Figure 1.17. The rectangular bifacial cells are arranged in strips with free spaces of equal width in between. The cells are attached by the top cover made of glass sheet. The semicircular trough shaped mirrors are covered with a highly reflective foil. The linear region along the cups of the mirrors in the middle of the lower sides of the cells which is not illuminated can best be used for bus bars. This concept started as an idea; no further work, however, has been carried out on it.

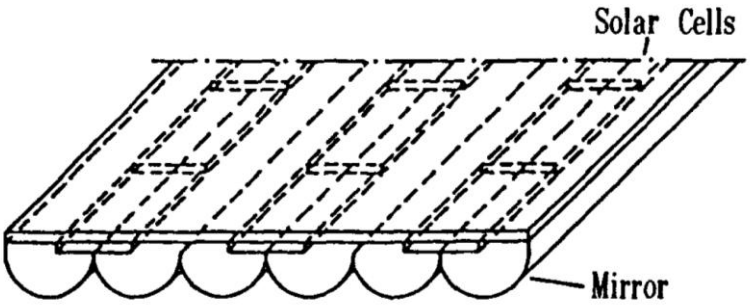

Figure 1.17: The semicircular trough shaped mirrors module saving half of solar cell area [68]

Bowden et al. [69] have developed a photovoltaic roof tie that uses a static solar concentrator using ray trace technique. The tilted grooves on the rear surface of the concentrator, as represented in Figure 1.18 (b), can achieve almost three times the concentration of sunlight in an ideal case. A prototype was built and tested giving the results of the short circuit current; there was no mention, however, of the optical efficiency of the CPV module which is the vital factor and has the most importance for the characterisation of the system. A question can be posed about the cost of the proposed system as it uses two types of concentration material: reflective mirror and dielectric material in addition to the use of the bifacial solar cells.

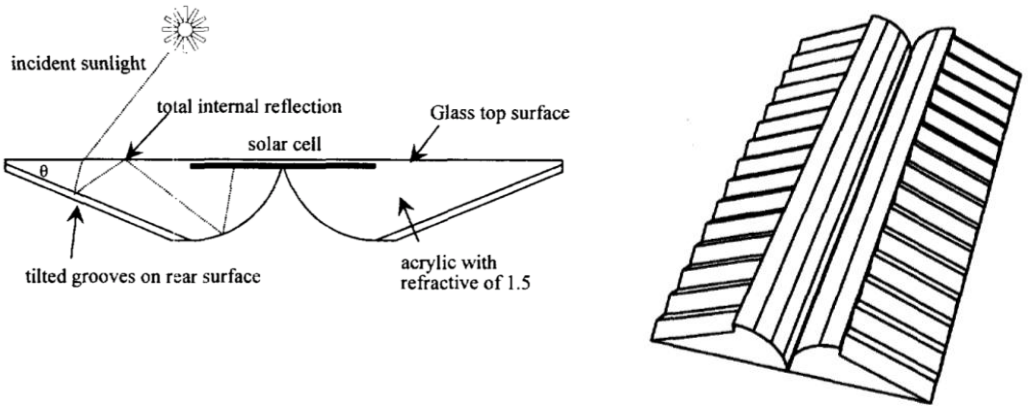

Figure 1.18: Photovoltaic roof tile with static concentrator: (a) cross section (b) rear of module showing the tilted groove structure [70]

Yoshioka et al. have devloped and introduced many static solar concentrators, starting with a 2-D nonimaging lens [71, 72]. The optical concentration ratio obtained from the 2-D lens reached 1.75. Later, they enhanced the optical conentration ratio of the 2-D

lens by investigating the 3-D lens. For the first time, the 3-D fabricated lens achieved an optical concentration ratio of 2.1 [73]. Based on the previous works of the 2-D and 3-D lenses, Yoshioka et al. introduced an enhanced 3-D lens for static solar concnetrators. The idea of the improvement was to trim the four corners of the 3-D lens into a rectangular shape, Figure 1.19. A higher optical concentration ratio of 2.3 was achieved for an incident angle up to 60º. However, the optical efficiency (ratio between the flux collected at the receiver and the flux at the entry aperutre) at different incident angles in different cross section planes of the 3-D lens has not been discussed and the original geometric concentration and the condition of the measurments were not mentioned [74, 75].

(a) (b)

Figure 1.19: Design concept of a new three-dimensional (3-D) lens for a static concentrator: (a) previous 3-D lens; (b) new 3-D lens [74]

A flat-plate static concentrator (FPSC) was developed by Uematsu et al. [76]. The FPSC focuses the light rays via the submillimetre V-grooves made from reflector sheets. The reflected rays are then reflected back on the top glass cover via total internal reflection. Finally the ray reaches monofacial or bifacial solar cells as presented in Figure 1.20. The FPSC module has been characterised based on annual irradiation in Tokyo – the authors state that it can collect 90% of the annual irradiation in Tokyo. The FPSC module however, produced only 2% more than a conventional PV module which is very low considering it has a concentration ratio between 1.5 and 2.0. For an increase of only 2%, this design does not appear to be a cost effective investment.

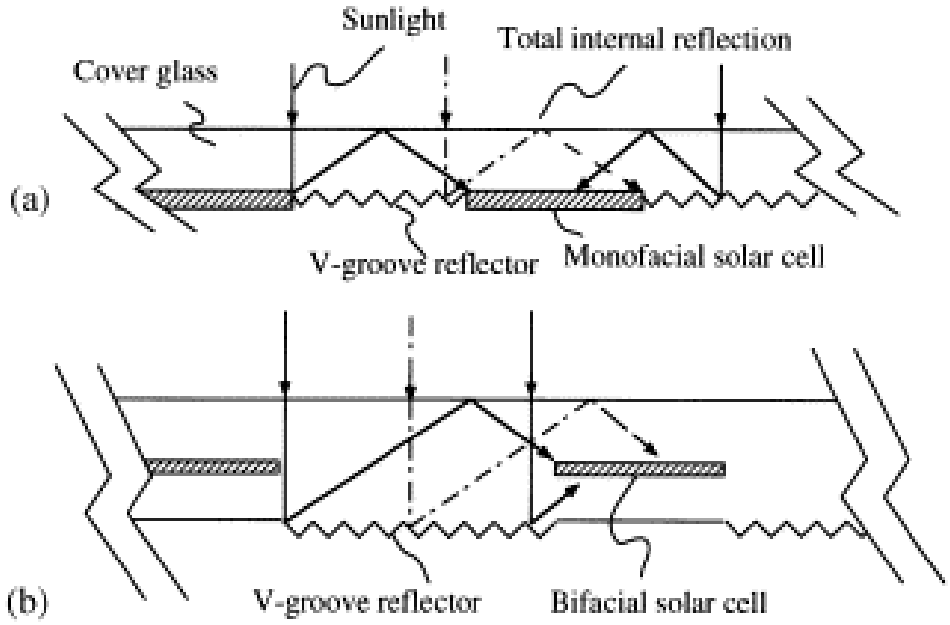

Figure 1.20: Cross-section of FPSC modules with (a) monofacial solar cells and (b) bifacial solar cells [76]

The PEC-44D is an asymmetric static concentrator which has the characteristics of having two different acceptance angles. It is a 2-D linear concentrator designed for use with bifacial solar cells as illustrated in Figure 1.21.

The so-called PEC-44D proposed by Minano and Parada in 1991 [77] has the specification of variable geometrical concentration ratios during the year. Zanesco and Lorenzo [78] optimised the PEC-44D for a ten year period with a constant daily demand. It was found that the optimised concentrator operating in Madrid can be 38% cheaper than the flat PV module based on a cost-performance study. The optimisation, however, is based on one location (Madrid) rather than on general propreties of the concentrator regarding the acceptance angle and the optical effeciency. This limits the use of the PEC-44D in different countries and at different positions.

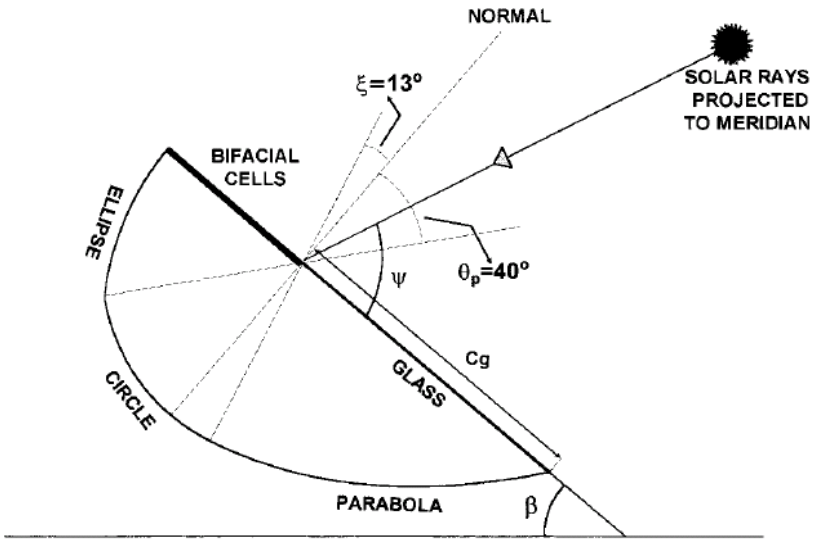

Figure 1.21: Cross-section of the PEC-44D module [78]

Alonso et al. [79] proposed a new design of static solar concentrator using bifacial solar cells for BIPV application within the JOULE III program. The concentrator is made from dielectric material coated with electroless silver. The procedure of fabrication remains complicated and costly as it includes two expensive processes of glass extrusion and silver coating. The cross-section of the studied concentrator is illustrated in Figure 1.22. The proposed concentrator has a half acceptance angle of 30º. The prototype made gives a low optical concentration ratio of 1.6, compared to the geometrical concentration ratio of 4.3, combined with a theoretical optical efficiency of 83%.

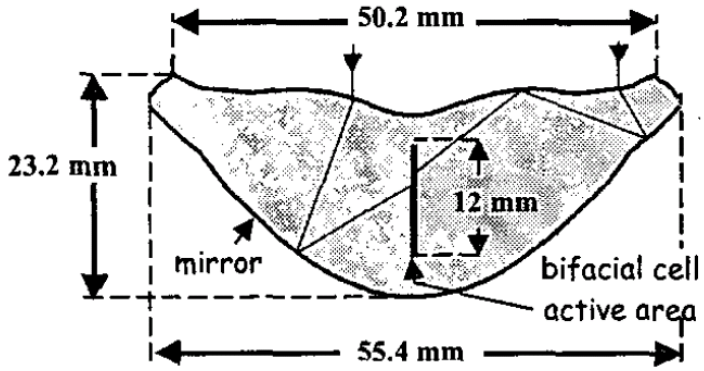

Figure 1.22: Cross section of the static concentrator proposed by Alonso et al [79].

A different type of solar concentrator was proposed by Morimoto and Maruyama for building integration [80]. The design of the concentrator is unique as the solar cells are placed vertically forming a wall frame around a white/transparent switchable plate. This plate works as a diffuse reflector in the case where the solar cells are generating electricity and they work as a transparent surface transmitting light when the solar cells do not produce any electricity. The optimisation and analysis of the concentrator are carried out via Multiple Total Internal Reflection (MTIR) model using ray tracing technique. The experimental results showed that the largest efficiency was recorded when the area of the solar cells is double the area of the bottom plate. There are two main issues that were not discussed in this publication despite their importance; the geometric concentration ratio of the concentrator and the fact that the bottom plate needs extra power to switch from reflector state to transmitter state.

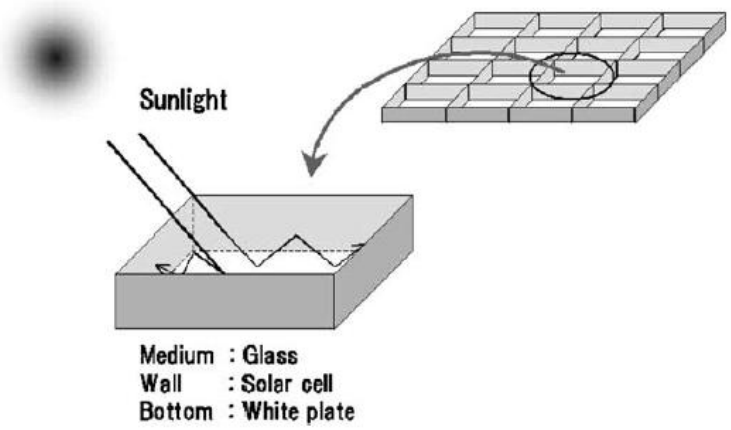

Figure 1.23: Schematic illustration of concentrator for vertical plate solar cell [81]

Nilsson et al. [82] modified the static asymmetric CPC called Maximum Reflector Collector MaReCo by introducing three different structured reflectors that create a more uniform illumination, as illustrated in Figure 1.24. The asymmetric concentrator is composed of two parabolic sides with their respective optical axes tilted in 20º and 65º from the horizontal. The proposed modified concentrator was evaluated via Monte Carlo ray tracing using the commercial ray tracing package ZEMAX[3]. The results of the optical simulation showed that all three structures reduced the peak irradiation creating a more uniform distribution; in addition the efficiency was almost constant for a large interval of 70º. The gain in uniformity, however, of the illumination on the solar cell

[3] Zemax is a widely-used optical design program sold by Radiant Zemax, LLC of Redmond, Washington (formerly ZEMAX Development Corp. and Focus Software). http://www.radiantzemax.com/en/zemax/

was replaced with a drop of 10% of the amount of radiation received by the solar cells compared to the flat surface MaReCo. Another issue consisted of the fact that the proposed concentrator is bulky and uses large reflective surfaces. It is more complicated to manufacture, thus increasing its cost compared to the flat surface MaReCo. The question that remains is whether or not the losses in the amount of radiation received and the increase in cost is worth it, only to make the illumination more uniform on the solar cells [83].

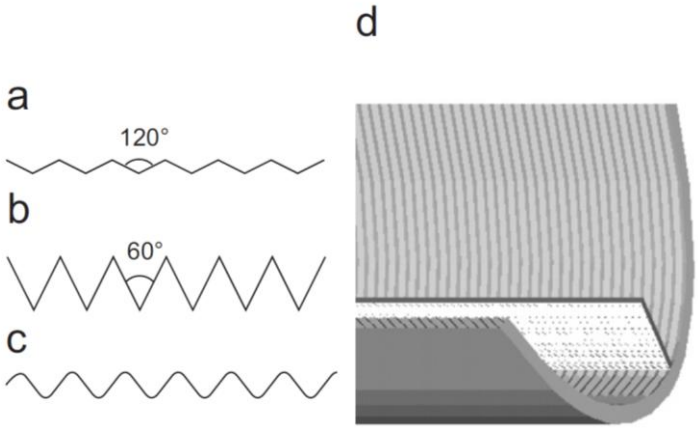

Figure 1.24: Different micro-structures of the MaReCo (a) with an opening angle of 120º, (b) with an angle of 60º, (c) with a sinusoidal shape to obtain complete randomisation; (d) the MaReCo with structured reflectors [82]

Yuehong et al. introduced a static solar concentrator represented in a modified CPC called lens-walled CPC [84, 85]. PHOTOPIA[4], a commercial optical analysis software, was used to investigate the performance of the lens-walled CPC compared to the common CPC using ray trace techniques. The lens-walled CPC was designed by rotating the parabolic curves of the CPC around the axis formed by the top and bottom ends of the curve to form the geometry of a lens to be filled with dielectric material, as illustrated in Figure 1.25. The experimental measurements carried out on the lens-walled CPC validated the results of the optical simulation obtained using PHOTOPIA. The lens-walled CPC showed an enhancement of the acceptance angle compared to the common mirror CPC having the same geometric concentration ratio 4. It has a half acceptance angle of 25º compared to the 14.5º half acceptance angle for the CPC. There

[4] Photopia is a fast and accurate photometric analysis program that produces comprehensive performance evaluations for non-imaging optical designs. http://www.ltioptics.com/Photopia/overview.html

is a considerable drop, however, of the optical efficiency from 93% for the mirror CPC to 63% for the lens-walled CPC. The drop is mainly due to the loss of energy of the light rays when they are refracted through the two newly formed lenses on the wall of the common CPC. A cost effective study would be beneficial as this would verify the extra cost due to the use of extra material of the lenses in order to gain in acceptance angle against the losses of the optical efficiency. This may have a significant decrease of the amount of electricity produced by the solar cells that are placed at the exit aperture of the solar concentrator.

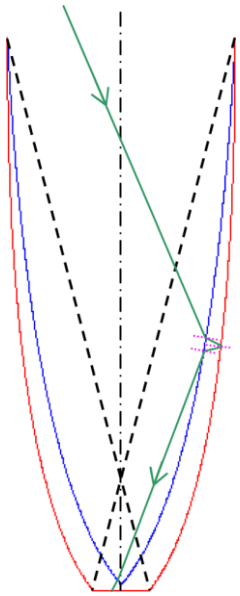

Figure 1.25: Lens-walled CPC [85]

Mallick et al. [86-88] have proposed and characterised the performance of a new static solar concentrator referred to as second generation PRIDE made of low-cost dielectric material. The concentrator is a truncated asymmetric compound parabolic concentrator (ACPC), as illustrated in Figure 1.26. The studied static concentrator is unique as it has a high geometric concentration ratio for a 2-D concentrator of 2.45 with two acceptance angles of 0º and 66º. It was found that the 2nd generation PRIDE generates a power ratio of 2.1 compared to a similar non-concentrating panel and the optical efficiency of the PRIDE system is 83%. The CPV module achieved solar to electrical conversion efficiency of 10.5%. The results obtained were used to predict a reduction of 40% of the cost compared to a similar non-concentrating system.

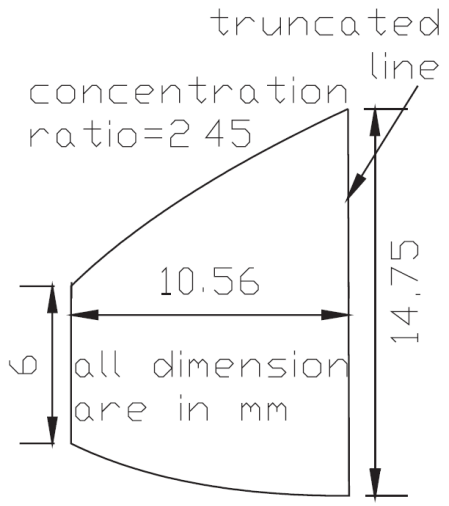

Figure 1.26: Truncated ACPC consisting of two different parabolas [86].

Further work to enhance the above ACPC was carried out by Sarmah et al. [89]. This time, the ACPC was made from refractive material (di-electric) creating the stationary Dielectric Asymmetric Compound Parabolic Concentrator (DiACPC). The optical performance of the DiACPC using ray-tracing methods was studied finding a maximum experimental optical efficiency of 80.5%. The energy flux distribution at the receiver with diffuse radiation was found to be homogeneous, with an average intensity of 520W/m².

A considerable amount of research has been carried out on CPV, with researchers investigating various different geometries and materials. The different static solar concentrators described in this section are summarised in Table 1.2 below.

Table 1.2: Characteristics of static solar concentrators

Name	Material	Cg	Solar cells	Ref
Lens-V trough concentrator	Plastic shell Water or oil	3	c-Si solar cell	[67]
Semi-circular trough shaped mirrors	Plastic Reflective foil	2	Bifacial solar cells	[68]
Photovoltaic roof tile	Acrylic Refractive foil	3	Bifacial solar cells	[69]
3-D Lens	Acrylic resin	2.69	c-Si solar cell	[73]
Flat-plate static concentrator (FPSC)	Plastic Silver coating	2	Bifacial solar cells	[76]
PEC-44D	Polymethacrylate Refractive foil	3.5	Bifacial solar cells	[77, 78]
Monolithic static concentrator	Glass Silver coating	4.3	Bifacial solar cells	[79]
Maximum Reflector Collector MaReCo	Aluminium laminated steel	3.5	c-Si solar cell	[83]
Lens-walled CPC	Acrylic Refractive foil	4	c-Si solar cell	[84, 85]
Asymmetric Compound Parabolic Concentrator (ACPC)	Polyurethane	2.45	c-Si solar cell	[86-88]

In this section, the literature presented focussed on the range of static solar concentrators developed; the following section continues with static solar concentrators with a more specific focus on their main use – in building integration.

1.5 Integration of PV modules in buildings

1.5.1 Building integrated photovoltaics (BIPV)

In the latest market research report published by GlobalData [90], the annual installations of BIPV modules is to reach 2.5 GW by 2015. The BIPV market has witnessed a boost of 121% between the years 2006 and 2010, reaching an annual installation of 682 MW in 2010 from a mere 29 MW in 2006.

Building integrated photovoltaics (BIPV) consists of integrating PV modules into buildings to play the same role as the building components: wall, window or roof.
It has the advantages of saving building material whilst reducing electricity costs, in addition to the reduction of the use of fossil fuels and the emission of ozone depleting gases. The electricity generated by the BIPV modules can be used in the building and the excess can be exported to the utility companies via grid interconnection. Compared to the non-integrated systems, the BIPV modules are cheaper because they do not need allocations for land or additional costs for infrastructure.
There are different types of BIPV systems where the photovoltaic module can be integrated into building structure:

Façade System:

BIPV façade systems represent part of the outer envelope of the building. They can be opaque or semi-transparent modules.

- Canopies: these are high PV cover structures overarching an open space that provide shade or other shelter. One of the ideas of using solar canopies was the photovoltaic charging station for electric vehicles [91]. It consisted of a cantilevered steel canopy supporting a 2.1 kW amorphous silicon solar array. The BIPV installation generated 3840 kWh saving 150000 kg of CO_2 emissions when compared to other fossil fuels that would be used for the vehicles.
- Curtain walls: these are the outer cover of a building. As the curtain wall is non-structural it can be made of a lightweight material such as the PV modules. PV curtain walls are generally semi-transparent using glass material and in some designs opaque, built with different materials such as aluminium plate or composite panels. In one study, Ishikawa et al. examined different installation structures for PV glass curtain walls using coloured solar cells [92]. Using computer graphics, they found that grey and gold coloured solar cells are well incorporated with outer walls.
- Shading systems: these are used as a passive way to limit the effect of the excessive solar gains rather than using air conditioning. Glass-glass laminated PV or any typical PV module can be easily integrated as shading systems, and can be either adjustable or fixed [93]. One study showed that south-facing PV shading systems produce electricity efficiently for lighting [94]. The study

discussed the fact that the PV shading systems have two advantages; they reduce the cooling loads and produce sufficient electricity whilst controlling daylight.

- Rainscreen systems: these are composed of two structural leafs, the inner that can be built of any material like concrete or brickwork and the outer one that can be a PV module to provide a major barrier to rain penetration and serve as a cosmetic element to the building envelope [95]. Pearsall and Wilshaw presented the 39.5 kWp PV system integrated into a rain screen installed on the south façade of one of the buildings at the University of Northumbria [96]. They found that the performance of the BIPV modules installed was affected by shading due to the urban location of the building; the shading was estimated to have resulted in 25% losses of the possible output.
- Double-skin façade: these refer to "building in building". The façade is composed of an inner skin and an outer skin separated by a large air space. PV cells are integrated in the outer façades gaining from the effective ventilation at the back [97]. Lau et al. studied the natural convection in a PV-integrated double-skin façade using computer simulation [98]. They discovered that turbulence was created behind the outer skin which was able to reduce the photovoltaic modules temperature and therefore increase the efficiency of the BIPV modules.

Roofing system:

The BIPV roofing systems replaces conventional roofing materials. There are solutions for both flat and slope roofs depending on the architectural design.

- Skylight: PV modules can replace the glass tiles in a skylight. They have the added benefits of solar shading and natural day lighting, plus the electrical power generation. Danny et al. carried out field measurements including solar irradiance, daylight illuminance and electricity generated on a semi-transparent PV skylight [99]. It was found that the daily mean electrical conversion efficiency was 10.83%. This results in an annual saving of 40,300 kg of CO_2 emissions.
- Tiles: PV tiles cover the roof, replacing the regular clay tiles. They are installed like roof tiles, with modular covering capacity and the same waterproofing qualities [100]. Murata et al. presented a new type of PV highly fire resistant tile

[101]. The PV tile introduced has attractive features with many advantages, such as a lower cost, simpler construction, better design, and greater fire resistance than previous modules.

- Shingles: flexible thin-film amorphous silicon BIPV shingles can replace asphalt shingles. In BIPV they are referred to as solar shingles or PV shingles [102]. Yagiura et al. developed a new PV shingle called "exchangeable photovoltaic (PV) shingle" [103]. The new design of PV shingles has a lower total cost, and improved fire resistance, compared with previous PV modules. The reliability tests that were conducted were based on Japanese Industrial Standards (JIS).

From the literature so far, it transpires that there is a lot of research underway investigating many different types of BIPV systems, and that work needs to be carried out to further develop the systems. Several analysts foresee potential ahead for this niche technology, however, there are some challenges and barriers that may hinder or complicate the pathway to its development and success. These challenges can be classified into five categories: price, performance, design requirements, codes and standards, and market limitations.

- **Price:** Due to the lack of BIPV market data available, it is difficult to provide exact pricing figures, however, BIPV systems generally carry a larger price tag than do flat panel systems due to the fact that they tend to be custom-made as opposed to mass-marketed. BIPV modules include additional materials compared to flat PV modules (e.g., adhesives and framing and flashing materials) [104], and additional labour costs deriving from specialised architectural design, engineering design (custom-made), and installation [105]. However their prices remain competitive compared to the large PV power plant (mass-marketed). BIPV systems may offer an offset value in the construction process through, among other things, the replacement of traditional building materials and the dispensation of rack-mounting hardware. In addition BIPV modules use free spaces already existing on building.
- **Performance:** Unlike rack-mounted PV panels, BIPV modules may experience higher operating temperatures because they are flush with the building surface and do not permit airflow between the module and the host structure. Higher temperatures may degrade the semi-conducting material of the module, which could decrease the conversion efficiency more quickly and result in premature failure. This is only applicable to certain PV materials– for example amorphous silicon, which has a

flexible form factor and hence a potentially greater integration potential – making some materials more susceptible to thermally accelerated degradation than others. PV materials with greater integration potential, such as thin films and flexible PV technologies, generally have lower efficiencies to begin with, and this may contribute to higher energy costs. In addition, a BIPV system will likely produce less electricity than a flat-panel system of the same size, because BIPV modules typically contain less semiconducting material than traditional PV modules. This disadvantage can be overcome by the use of solar concentrators in BIPV modules, which will be addressed later in section 1.4.2.

- **Design requirements:** The design of a BIPV system tends to be a more complex process than the conventional 'tack-on' PV systems; there are many important factors to consider when designing BIPV modules [106]. With BIPV, there needs to be a balance between the power produced, the cost of the system and the aesthetics –the focus should neither be on electricity only or aesthetics only. There needs to be improved building quality and energy performance, as well as addressing the aesthetics. As such BIPV in buildings facades incorporates: building process, building physics, energetic design, aesthetical concept and economical concept. A few of these factors are mentioned below:
    - Where to integrate? In vision and/or non-vision? If transparent, what is required?
    - What materials/system to use? PV technologies available?
    - Orientation? Tilted facade? Good idea to increase yield, whilst paying attention to overheating.
    - Colour window scheme requirement.
    - Determine zones not allocable to PV – near doors, trees, details, terraces.
    - Shadows often exist; therefore a shadow analysis is necessary for correct yield calculation and to avoid the hotspots on cells, etc.
    - Construction detailing – perfect air and water tightness and building connections is extremely important in any BIPV facade solution. Wiring the PV array and investigating the components in the skin need careful consideration (weather protection, thermal insulation, noise protection and modulation of daylight), as well as key safety considerations such as fire safety.

It is evident that the planning, design and implementation of BIPV systems requires the cooperation of several different trades such as electrical installation and facade construction specialists which traditionally have very little overlap during the detailed design stage. It is vital, therefore, that the services provided by the different trades are precisely defined and demarcated.

- **Codes and standards:** It is important to point out that because BIPV modules serve dual functions (providing electricity and serving as part of the structural component of the building), they must conform to the codes and standards of two separate industries (PV and construction). In other words as well as being subject to the qualification and design standards of PV modules, they need to comply with the criteria set for buildings such as performance on stability, wind resistance, durability and fire safety [107] in addition to the legality of the ownership of the roofs. This in itself can act as a market handicap. A clear set of guidelines needs to be established between these two industries in order to allow for a smooth growth platform for the BIPV industry.
- **Market limitations:** BIPV products vary hugely, not only by facade type (e.g. roof shingles, windows, and curtain walls) but also by design (differing geometries and materials). This results in the BIPV market being segmented into custom-designs unlike the flat-PV panel where modules do not vary greatly from one another, reducing the scalability of BIPV. In addition, BIPV is limited to residential and commercial building applications and as such cannot compete with the large scale PV plants. A solution to this would be the adoption of feed-in tariffs for solar PV generated power. This is currently the main driver for the BIPV market in Europe in countries like Germany, Spain and Italy and more recently, France, Switzerland and Portugal [108].

It is clear that researchers in a variety of fields need to come together to realise the kinds of cost reductions that could facilitate the adoption of BIPV and allow for the growth of the BIPV market. It is thought that increasing the aesthetic, functional and environmental value of a building at a much lower cost than in the recent past, new PV technologies will soon originate a market growth as intense as the growth of traditional PV market has been in the last 5 years [109] .

Despite the challenges facing the BIPV industry, there are many advantages making it attractive to both customer and investors over the last decade. The market is also due to

grow, the BIPV reached an annual installation of 682 MW in 2010 from a mere 29 MW in 2006. These advantages can be divided into economic advantages and environmental advantages:

Economic

- Replaces the building material used in façades and roofs
- Reduces the cost of installation and integration of separate PV panels
- Decreases the energy consumption of the building
- Energy produced is used on site; eliminates energy transportation costs and infrastructure

Environment

- Reduces CO_2 emissions significantly; energy generated within building
- Makes efficient use of land, i.e. structures needed for PV are part of the already existing building thus saving use of additional land
- Reduces environmental impact of energy transportation

The advantages of BIPV are clear, and once prices fall, due to rapid evolution of thin-film technologies, the market for BIPV systems will rapidly grow. High cost remains the major challenge with BIPV. As briefly mentioned earlier, the costs can be reduced even further by the adoption of solar concentrators to minimise the amount of solar cells used in BIPV modules; this is the topic of the following section. There are many architectural and engineering challenges to be solved, as outlined above, before that solution can be adopted and fully commercialised; researchers are currently working on this.

1.5.2 Building Integrated Concentrated Photovoltaics (BICPV)

The combination of the two areas of application of PV discussed so far (CPV and BIPV) gave birth to a new direction of application and use of the PV module. The new field is referred to as Building Integrated Concentrating Photovoltaic (BICPV). BICPV systems have the same specifications as BIPV systems; they can be installed either on the building façades or the roof replacing the existing structural elements in buildings. The only difference is the use of solar concentrators in order to reduce the amount of solar cells used. Few particular ideas have been proposed using BICPV systems with

tracking systems, however in most cases this is not possible due to the size of the tracking system and their need to be in motion, which prevents them from replacing the roof or façade material [110]. One solution has been suggested by Chemisana and Rosell [111]. It has the device concentrate radiation toward a static receiver by means of an array of reflectors which rotate together (Figure 1.27). This is an enhancement of the two-axes Fresnel reflective system developed at the University of Lleida [112]. The use of this CPV system is restricted to shading fins only. There is also a problem related to the tracking system if it breaks; the sunlight will not be focused on a desirable area of the façade of the building which will create hazards.

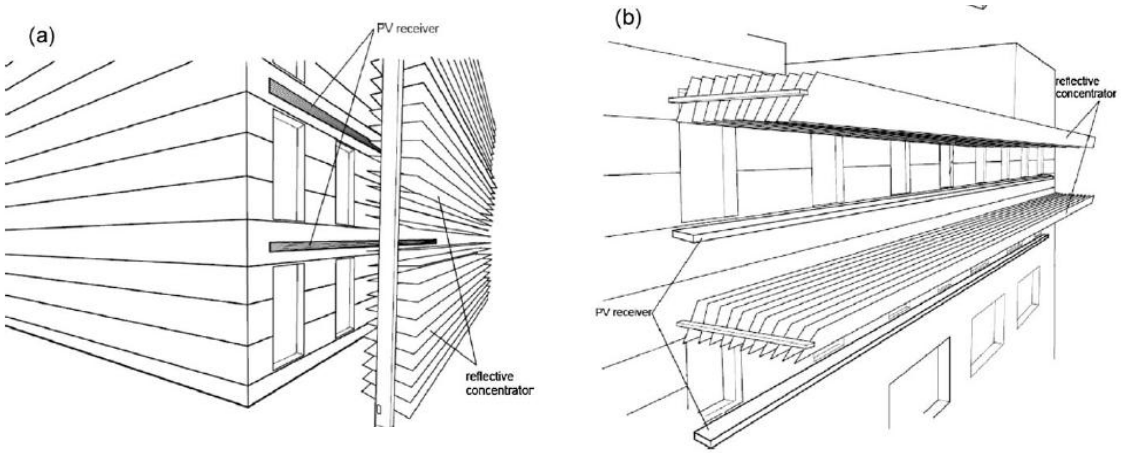

Figure 1.27: Building integrated system presented by Chemisana and Rosell: (a) curtain wall architectural design and (b) parasol architectural design [112]

Tracking systems for CPV systems create many obstacles for the development of BICPV:

- The volume that the tracking systems need for their functioning; this volume needs to be added to the volume occupied by the building.
- The mechanical parts and motor of the tracking system that require continuous maintenance and consume electrical energy, in addition to their noise and vibration.
- They cannot replace the roof or façade materials because of their continuous movement.

Seen in this light, the use of tracking systems in BICPV should be limited.

1.5.3 Semi-transparent CPV

Buildings are composed of opaque and transparent or semi-transparent façades. Many solutions have been proposed for integrating PV modules into transparent façades [99, 113-118]. Transparent photovoltaics also known as "translucent photovoltaics" is a branch of BIPV that has combined advantages compared to the standard PV module. They replace conventional window glass to transform incident solar radiation to electricity and transfer part of it into the building. Recently, a comprehensive review of solar façades focusing on transparent and translucent solar façades was published [119]. Different types of transparent and translucent façades were presented in this review; the interesting fact was that none of the research to date of the publication (2013) had investigated the use of solar concentrators as translucent PV. The research carried out in this thesis aims to bridge the gap in this area.

CPV systems usually use solar concentrators that are opaque to visible light; they cannot be used, however, in BICPV on areas where the natural light is supposed to penetrate to the interior of the building. To date, no CPV products have been developed which are sufficiently transparent to replace vision glass; a few applications for semi-transparent CPV are detailed below.

One of the solutions for the use of CPV on transparent façades can be found in the static solar concentrators called luminescent solar concentrators (LSC) [120-134]. They focus the light rays using a large surface of luminescent material by redirecting them on to smaller areas which are generally the edges of these large surfaces where the solar cells are placed. The luminescent materials are generally glass or plastic containing or topped with a thin layer of fluorescent material. These concentrators are compact; the main disadvantages, however, of these static concentrators are the losses of the light rays that escape from the bottom and top of the luminescent surfaces. Much research has been carried out on the LSC. One study showed that 40-50% of all absorbed energy is lost through the surfaces of the LSCs concentrators [135]. Researchers continue to work on enhancing the efficiency of these concentrators [120, 136].

Another solution for the use of CPV concentrators in transparent façades can be found in holographic solar concentrators that were first introduced in the early 1980s [137-142]. Muller demonstrates light-directing holograms for both day lighting and PV power generation [143]. The acceptance angle, however, of these kinds of concentrators remains very low due to the rapid fall of diffraction efficiency of thick phase transmission holographic concentrators when the angle of incident ray changes [144].

Building upon the research of the 2-D concentrator, the use of 2-D nonimaging static solar concentrators in translucent PV application has been successful for some of the projects described below.

Muhammad-Sukki et al. designed and optimised a 2-D static dielectric totally internally reflecting concentrator (DTIRC) used in a Solar Photonic Optoelectronic Transformer (SPOT) [145] as illustrated in Figure 1.28. SPOT was proposed by SolarEmpower Ltd.; it is a BIPV system able to convert solar radiation to electricity, hot water, space heating, illumination, ventilation and shade for a building. The DTIRC which was first introduced by Ning et al. [146], was optimised based on the maximum concentration method. It was found that the geometric concentration of the DTIRC had improved but with a larger size compared to the initial DTIRC developed.

(a) (b)

Figure 1.28: (a) Solar concentrator in the SPOT system, (b) SolarBrane mounted on the wall of a house [145]

In another published study investigating the use of 2-D solar concentrators in semi-transparent PV systems, the performance of a see-through photovoltaics module that uses a low-concentration prism concentrator was examined for a specific location in Japan [147]. The module generates 15% more electricity than a conventional module while operating with 63% less solar cell area. The module, however, is see-through only when looked at from certain angles of view.

Considering the appeal of BICPV, especially in terms of costs and savings, the research has extended to industry. Some start-up companies are in the process of commercialising BICPV modules as translucent PV using 2-D static solar concentrators.

The first example of these modules is the BeeHive PV from SolarOr Ltd [148]; its concentrators were designed based on the nature geometry, it has the shape of a honeycomb. The Beehive PV module is illustrated in Figure 1.29 and is part of the website of the start-up company [148]. The specifications given on the website have not been confirmed by any laboratory test; no scientific paper has been found detailing the design of the static concentrator used. The second example of a commercialised product is the BICPV window from Pythagoras Solar [149] illustrated in Figure 1.30. Similarly, the details of the design of the 2-D dielectric concentrator used by Pythagoras Solar have not been published in any scientific journal; however, the design is very similar to the see-through prism concentrator presented in [147].

(a) (b)

Figure 1.29: BeeHive PV, view from: (a) inside the building and (b) outside the building [148]

Figure 1.30: Pythagoras Solar BICPV window [149]

The main disadvantage of the three examples cited above is that the transparency of the BICPV module has not been suitably achieved as it is difficult to see the outside landscape from inside the building; in addition the solar concentrators used were 2-D, which represent a limitation of saving of silicon solar cell material. The BICPV modules for transparent façades are summarised in Table 1.3 below.

Table 1.3: BICPV modules for transparent façades

Name	**Geometry**	**Shape**	**Company**	**Ref**
Dielectric totally internally reflecting concentrator (DTIRC)	2-D	Convexly curved receiving surface Concavely curved side surface	SolarEmpower Ltd	[145]
BeeHive PV	2-D	Honeycomb	SolarOr	[148]
BICPV window	2-D	Prism	Pythagoras	[149]

From the table, it can be seen that a variety of different shapes have been examined for the BICPV module. The problem, however, is that these are all industrial designs and not much information has been given with regards to the efficiency.

In addition only 2-D geometries have been used in BICPV modules for transparent façades.

1.6 Research motivation, aim and objectives:

BIPV is a multifunctional technology that combines the photovoltaic module with the outer surface of a building providing the building with new functions while producing a portion or total building electricity usage. The successful introduction of PV into the building industry requires the merging of functional and aesthetic issues as well as addressing financial constraints. In terms of reducing the costs of BIPV systems, the combination of two areas of PV application (CPV and BIPV), has given rise to a relatively new field of research known as BICPV as described in section 1.5.2. Having reviewed the BICPV research it becomes evident that much work is needed to develop systems which are both economically and aesthetically viable, especially within the field of semi-transparent CPV. The solutions offered so far, for the use of CPV on transparent facades, include research carried out into static luminescent solar concentrators (LSC) and holographic solar concentrators as described in section 1.5.3. Both of these solutions, however, have limited efficiency and research continues to enhance their efficiency. Other solutions proposed in translucent PV applications, examine the use of the 2-D non-imaging static concentrator, as described in section 1.5.3. The major disadvantages associated with these designs, however, is the low level of transparency of the BICPV modules and the fact that the designs use 2-D solar concentrators, as opposed to 3-D concentrators which use less concentrator material and have increased saving of solar cell material. It becomes clear from the literature that there is a need to develop an alternative solution to the current BICPV modules for use in translucent facades. To date, no 3-D solar concentrator has been designed to be used in translucent BICPV.

Written in this evolving context therefore, **the aim of this research work is focused on designing and characterising a novel 3-D static solar concentrator to be used in translucent façades or roofs of buildings.** The preference of developing a 3-D static solar concentrator stems from a combination of factors. In practical terms, the research has shown that the use of tracking systems in BICPV should be limited therefore, a static concentrator was chosen. In financial terms, the use of a 3-D concentrator instead of a 2-D concentrator will result in more savings and hence provide a more economically viable solution long term. In terms of the available products on the

market, the novel 3-D design intends to overcome the transparency issues observed in the 2-D designs discussed above. Seen in this light, the novel 3-D design is a symbiosis of functional and financial issues. The introduction of this novel 3-D design in the field of semi-transparent BICPV will not only add another dimension to the current research but hopefully pave the way for future designs and will, in turn, address some of the current challenges facing BIPV.

The main research objectives are:

- To design the geometry of the novel 3-D static solar concentrator to be used. It has to collect maximum sunrays with the best efficiency, in addition to allowing the penetration of daylight into the building.
- To choose and develop the methods to be used for the design and characterisation of the novel 3-D static solar concentrator.
- To develop the 3-D parametric equation of the novel 3-D static solar concentrator in order to simplify the optimisation of its geometric characterisations.
- To find the optimum geometry of the novel 3-D static solar concentrator in order to provide the flexibility required for BICPV.
- To develop a computational model in order to predict the power output of the designed BICPV module working in different weather conditions.
- To test the performance of the developed translucent BICPV module in indoor and outdoor conditions to be compared with the simulation results.
- To understand the real time behaviour of the developed translucent BICPV module.

1.7 Outline

The aim of the current work is to contribute to the growing research of PV and in particular to the field known as BICPV. The CPC is the most studied solar concentrator. From the literature so far, it appears to be the case that many concentrators have been designed based on the CPC shape. The fact that the CPC is a known geometry prompted an in depth investigation where it was decided, for the purpose of this thesis, to investigate further the Crossed Compound Parabolic Concentrator (CCPC), derived from the original CPC.

Chapter 2 provides a complete characterisation of the CCPC, which has not been documented before. The study includes the use of ray tracing techniques via a written code as well as commercial software; ray tracing techniques are the groundwork of the design of any optical device such as solar concentrators. Various different techniques and instruments are used to fabricate the CCPC and to test its performance. Furthermore the optical performances of the CCPC (reflective and refractive) are examined in detail; two journal articles outlining the study in this chapter have been reviewed and published in well-known scientific journals in the field [38, 150] providing new scientific data on the CCPC and showing their advantages compared to the circular cross-section CPC.

Following on from here, the geometrical specifications of the novel 3-D static solar concentrator to be designed are presented and demonstrated in Chapter 3. The developed geometry has never been studied before, neither in the industrial or research domain. The new 3-D geometry is not obtained from the revolution or the composition of an original 2-D geometry; it is a completely new way of obtaining and designing a 3-D solar concentrator. This is a novel investigation; it is fundamental, therefore, to find a method of how to draw the 3-D geometry of the novel concentrator in order to be able to reproduce the geometry in the CAD software. A complex 3-D parametric equation of the new geometry of the 3-D static solar concentrator is systematically developed from scratch and then validated using a self-elaborated MATLAB code; it is the key starting point to drawing the novel concentrator using the CAD software in order to be able to use the integrated commercial optical software (OptisWorks/SolidWorks) for the ray tracing simulations; the boundary of the outside surfaces depends only on the 3-D parametric equation. This chapter represents the theoretical core of the thesis.

Chapter 4 contains the optical model developed and used to optimise the geometry of the novel 3-D solar concentrator based on different geometrical parameters. Numerous ray tracing simulations are performed for the optimisation using commercial optical software. Results of the optical performance of the novel 3-D solar concentrator are presented and the dimensions and profiles of the optimised concentrators are summarised; these results have been published [151, 152]. This chapter is fundamental to this research work, as the remainder of the work is based on the optimisation results obtained in this chapter.

In Chapter 5, the different steps of fabrication of the 3-D solar concentrator are discussed, starting from the design of the casting mould to the fabrication of the casted optimised concentrators and finishing with the assembly of the translucent BICPV modules. The test of the optimised concentrators in indoor conditions is also described; the results of the indoor experiment are used to validate the optical model used in the optimisation stage.

The following chapter presents the different BICPV modules fabricated and assembled to be tested in outdoor conditions. The experimental set up and the test site in Edinburgh are presented with details of the instruments used to measure the power output of the BICPV modules, the different solar radiations and the weather conditions. In addition, the method used for the modelling of the power output of the BICPV modules in outdoor conditions is described. This involves the development of an electrical model based on the two-diode equivalent circuit model, in corporation with the optical model which examines how the incident angles of the sunrays affect the performance of the BICPV modules fabricated when they are exposed to the sun radiation during the day. The integrated power output model developed involves the integration of the optical and electrical models, in addition to the calculation of the sun angles to be used as one of the inputs. The results of the integrated model are the simulated power output of the BICPV modules as if it were in outdoor conditions. The chapter concludes with the results obtained from the outdoor experiment and presents a comparison with the simulated results obtained by the developed model. Furthermore, the results provide validation for the integrated optical/electrical model. The results give an idea of the behaviour of the designed BICPV modules in different weather conditions.

The final chapter, Chapter 7, gives a general conclusion to the thesis and work carried out throughout the research study. Preliminary work investigating the prediction of the yearly power output is presented. In the second part of the chapter, recommendations for future work that can be carried out to enhance and complete the research are outlined; this covers many branches of research ranging from theoretical work on the prediction of the solar cell temperature and the effects of the non-uniformity of the optical flux on the solar cell efficiency to a more commercial proposal of the large scale fabrication of the concentrators and BICPV module.

Chapter 2: Optical modelling of solar concentrator using a ray tracing technique

This chapter presents a comprehensive optical characterisation of the Crossed Compound Parabolic Concentrator (CCPC). This is the first published detailed study of its kind on this atypical 3-D concentrator geometry. The optical study involves both the use of ray tracing technique via a written code and commercial software and examines the optical efficiency as a function of the incident angle of the incoming rays. In addition, the optical flux distribution at the exit aperture of the CCPC is also investigated. Following on from the simulation study, the CCPC is fabricated and an indoor experimental study is carried out in order to validate the optical model developed. The various different techniques and tools used to fabricate the CCPC are presented in detail thus forming the manufacturing groundwork for the remainder of the thesis. The optical simulation results are compared to the experimental results.

2.1 Introduction

Prior to the design of the novel 3-D concentrator, it is important to gain an understanding of the various techniques needed for this purpose. From the literature so far, it appears to be the case that many concentrators have been designed based on the Compound Parabolic Concentrator (CPC) shape. In this chapter, the optical performance of an atypical 3-D Compound Parabolic Concentrator (CPC) is investigated theoretically and experimentally using ray tracing techniques. This concentrator was chosen as it is a known geometry with confirmed properties.

The chapter begins with a description of an atypical 3-D CPC, including its geometry and construction. An optical modelling study of the atypical 3-D CPC built with reflective material is then presented. Validation of the optical model developed is carried out followed by an indoor experimental study of the optical efficiency for the reflective concentrator. Finally, the concentrator built with a refractive material is investigated both theoretically and experimentally. The reason behind building separate concentrators, one reflective and one refractive, was so that the results obtained from both concentrators could be compared and used to determine which material would be better for the development of the novel concentrator forming the basis of the research carried out in the remainder of the thesis.

2.2 Review of the Crossed Compound Parabolic Concentrator (CCPC)

Many ideas of designing specific geometries for concentrating PV systems have been proposed since the birth of non-imaging optics in the 1970s [68]. Examples of these include the use of the converging lenses (Fresnel) as a refracting element [153], and the design of an asymmetric compound parabolic photovoltaic concentrator which enables the capture of a large part of the diffuse solar radiation in addition to the direct component [48].

One of the most studied solar concentrators is the 2-D CPC. This is the most efficient solar concentrator because of its characteristics of collecting and concentrating all the rays within a specified acceptance angle [154]. Building integration PV systems require a static concentrator which will allow for maximum radiation; the 2-D CPC represents a solution but with limitations in concentration and in solar radiation collection.

Another way to obtain a 2-D CPC is the Annular Compound Parabolic Concentrator, A-CPC (Figure 2.1). This is obtained by rotating the section of the 2-D CPC around an axis parallel to the 2-D CPC axis. The advantage is evident in its ability to provide uniform irradiation to an annular absorber, however its geometrical concentration ratio, which is equal to the 2-D CPC is still very low compared to the 3-D CPC geometrical concentration ratio [155]. In addition, the annular shape of the entry aperture limits the use of the A-CPC to very specific cases such as a second stage concentrator.

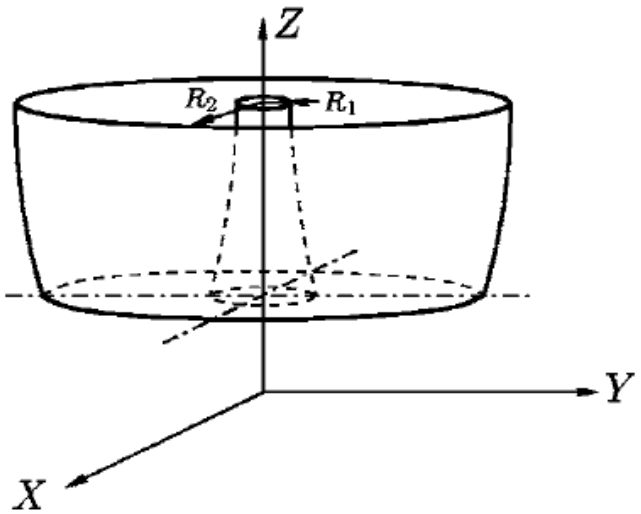

Figure 2.1: Annular compound parabolic concentrator (A-CPC) [155]

The circular-sectional 3-D CPC (Figure 2.2) is obtained by revolving the 2-D CPC around its axis. It is generally used in solar concentration as a second stage concentrator in order to increase the concentration ratio of the two-stages concentrator [156]. The circular-sectional 3-D CPC represents an improvement on the 2-D CPC; the geometrical concentration ratio is increased and the size of the solar cells used is reduced. The losses in the 3-D CPC have been studied, however, only as a second stage concentrator. This relies on rays coming from the first stage concentrator in limited and specific directions and is not a direct study of the rays coming directly from the sun [157].

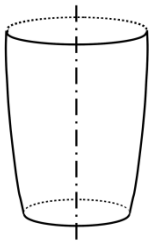

Figure 2.2: Circular-sectional 3-D CPC

The concentration of the circular-sectional 3-D CPC is the square power of the concentration ratio of the 2-D CPC; this represents a huge gain in concentration. Despite the gain in concentration compared to the 2-D CPC when only one concentrator is used as a second stage concentrator, the limits of the 3-D CPC lie in the circular shape of the entry and exit apertures which represent losses respectively in the area used for solar radiation collection and in the solar cell used. The packing efficiency decreases since the geometry of the entry aperture area is circular, and this reduces the use of the incident solar radiation on the used space. The factor of packing efficiency of using the radiated area will be equal only to $\frac{\pi}{4}$ as we can see in Figure 2.3 below.

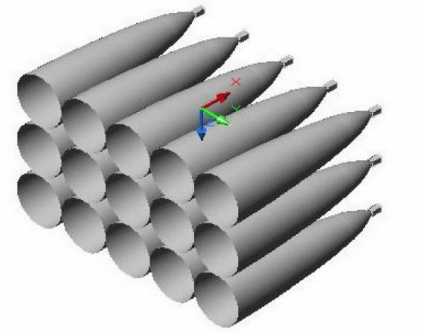

Figure 2.3: Assembling of CPCs with circular input aperture (fill factor $=\frac{\pi}{4}$)

For this reason, a circular-sectional 3-D CPC was modified by cutting the entry aperture to a hexagonal shape and studied for a thermal system (Figure 2.4) [158]. The system was analysed to be static and it resolved the dead-space problem that occurred in the conventional 3-D CPC. The disadvantages of this system, however, are the decrease in the geometrical concentration ratio in order to shift from the circular shape of entry aperture to the hexagonal shape and the fact that the circular shape remains at the exit aperture.

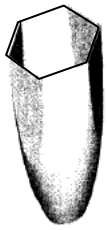

Figure 2.4: Modified hexagonal 3-D CPC [158]

The atypical 3-D CPC studied in this chapter is the Crossed Compound Parabolic Concentrator (CCPC). it is called crossed because contrary to the circular-sectional 3-D CPC which is obtained by revolving a 2-D CPC around its axis, the CCPC is obtained by intersecting two 2-D CPC's. The advantage is presented in the square shape of the entry and exit aperture of the CCPC compared to the circular geometry of the entry and exit aperture of the typical 3-D CPC. PV power technology uses semiconductor cells (wafers), generally several square centimetres in size. Seen in this light therefore, it would be more beneficial to have a square exit aperture area for the geometry of the solar concentrator; the geometry of the CCPC represents the solution.

The first CCPC was introduced as early as 1978 by Welford and Winston [68] and further examined by Molledo and Luque [159] by adding a half-cylinder stage, which works by reflection. It is used to illuminate both faces of the bifacial cell, placed vertically at this stage. The geometry of the CCPC examined was optimised for Madrid where the yearly averaged solar source presents two radiance maxima near the solstices. These conditions led the authors to design the CCPC with two acceptance angles with two seasonal positions (winter and summer).

The optical performance and characteristics of the CCPC, however, as a static solar concentrator have not been studied and investigated, hence the aim of this chapter.

2.3 CCPC geometry

The following section presents how the CCPC is designed and illustrates the changes in the concentration ratio depending on the height of the CCPC.

2.3.1 Design of the CCPC

The coordinates of the parabolic shape of the sides of the CCPC need to be calculated and drawn. In order to do this the coordinates are defined in a system in which the y' axis represents the axis of the right parabolic curve and the origin lies on that curve (dotted line in Figure 2.5). Coordinates y' in terms of coordinates x' are expressed, and x' varied incrementally as an independent parameter until the whole parabolic branch is obtained. The resulting set of x', y' coordinates are rotated and translated to provide the final x, y coordinates in the desired coordinate system [160].

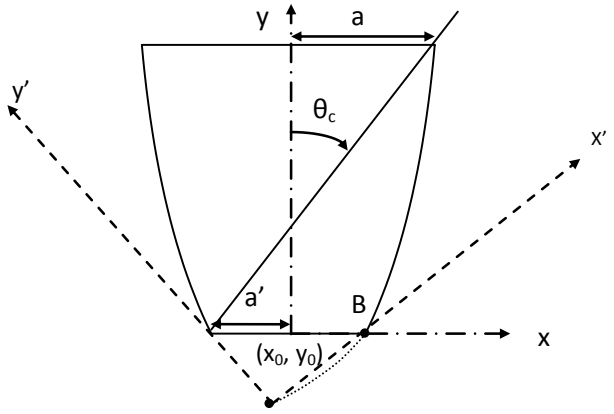

Figure 2.5: Section of the CCPC (2-D CPC)

The origin x_0, y_0, of the desired coordinate system x, y was defined to be the centre of the exit aperture area, and the y axis to be the axis of the CCPC as shown in Figure 2.5. These were calculated using the following equations [60].

$$x_0 = -a' + F \sin\ \theta_c\ = -a'\ 1 - \sin\ \theta_c\ -\ \sin\ \theta_c\ ^2 \tag{2.1}$$

$$y_0 = -F \cos\ \theta_c\ = -a'\ 1 + \sin\ \theta_c\ \times\ \cos\ \theta_c \tag{2.2}$$

$$F = a^{'} \times\ 1 + \sin\theta_c \tag{2.3}$$

where:

F: the focal distance of the parabola

a': half side of the square exit aperture

a: half side of the square entry aperture

θ_c: Half acceptance angle

To generate the set of coordinates for the right branch, the beginning is at point B (x'_1, y'_1) as shown in Figure 2.5 where:

$$x'_1 = 2a'\ cos\ \theta_c \tag{2.4}$$

and

$$y'_1 = a'\ 1 - \sin\ \theta_c \tag{2.5}$$

then x' is used as an incrementally variable independent parameter such that

$$x'_{n+1} = x'_n + \delta x' \tag{2.6}$$

and

$$y'_{n+1} = \frac{x_{n+1}\ ^2}{4F} \tag{2.7}$$

with $\delta x'$ being some suitable small increment, such as $\frac{a}{N}$ where N=500 (resolution). The right parabolic branch of the CCPC sidewall profile in the desired coordinate system (x, y) is then translated and determined from the previous equations with

$$x_n = x'_n\ \cos\ \theta_c\ \ - y'_n\ \sin\ \theta_c\ \ + x_0 \tag{2.8}$$

And

$$y_n\ x_n\ = x'_n\ \sin\ \theta_c\ \ + y'_n\ \cos\ \theta_c\ \ + y_0 \tag{2.9}$$

Now for the left parabolic curve, the coordinates are:

$$y_n\ -x_n\ = y_n\ +x_n \tag{2.10}$$

The presented equations are used to build the 2-D CPC. The CCPC is formed by the intersection of two 2-D CPC's (CPC1 and CPC2) as shown below in Figure 2.6.

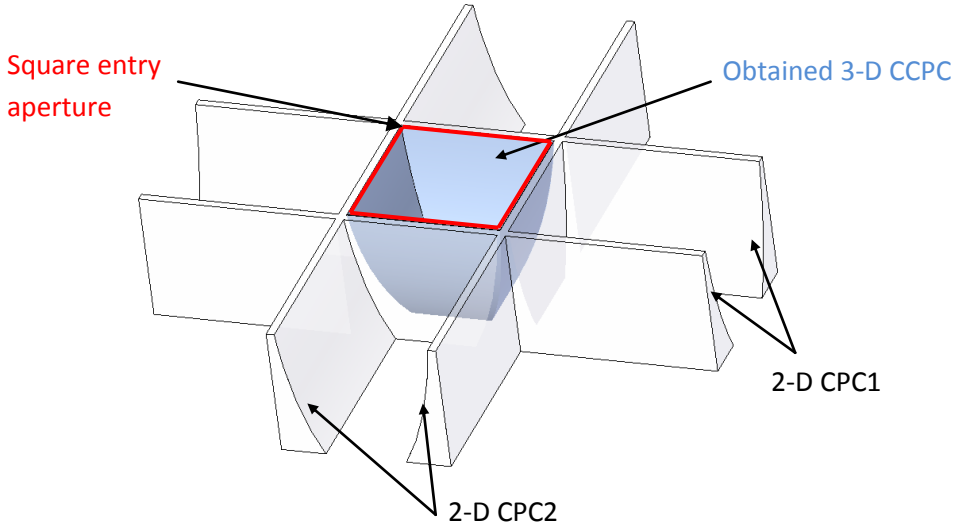

Figure 2.6: Formation of the CCPC

It is evident from Figure 2.7 below that for the same entry aperture area, the CCPC uses fewer solar cells than the 2-D CPC because its concentration ratio is higher. In other words, for the same area used to install a solar concentrator, with the same height and pretty much the same shape, fewer solar cells will be used representing a considerable reduction in cost of the most expensive part in the CPV.

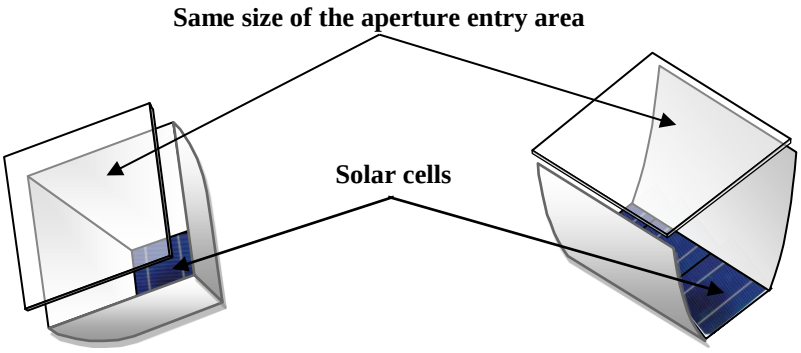

Figure 2.7: Comparison between 3-D CCPC and 2-D CPC

2.3.2 Dimensions of the CCPC

One of the disadvantages of the CCPC compared to other parabolic concentrator systems is that the height *H* is very tall compared to the width or the diameter of the collecting area. For economic reasons, and especially for large scale applications, it is important to minimise the area of the mirror, the reflectors or the dielectric material in order to reduce the costs. In addition many BIPV applications require the concentrators to be as compact as possible. This can be referred to as truncation. Truncation of the CCPC means removing part of the entrance aperture end. This is advantageous in two respects: not only will the reflector areas be reduced but the reduction in concentration that results from the truncation will be negligible. In other words, truncation results in a considerable reduction in the height of the CCPC with very little reduction in concentration. In the following equations, the letters with subscript *T* are for a truncated CPC (Figure 2.8).

The equation for the full height of a CPC is:

$$H = \frac{2 \times a' \times \ 1 + \frac{1}{\sin \theta_c}}{2 \times \tan \theta_c} \tag{2.11}$$

Where:

- θ_c: half acceptance angle
- a': half side of the square exit aperture

The equation for the truncated height of a CPC is:

$$H_T = \frac{F \times \cos \ \Phi_T - \theta_c}{\sin^2 \frac{\Phi_T}{2}} \tag{2.12}$$

Where:

- Φ_T: Truncated acceptance angle

The half entry aperture width for a truncated CPC is:

$$a_T = \frac{F \times \sin\ \Phi_T - \theta_c}{\sin^2 \frac{\Phi_T}{2}} - a' \tag{2.13}$$

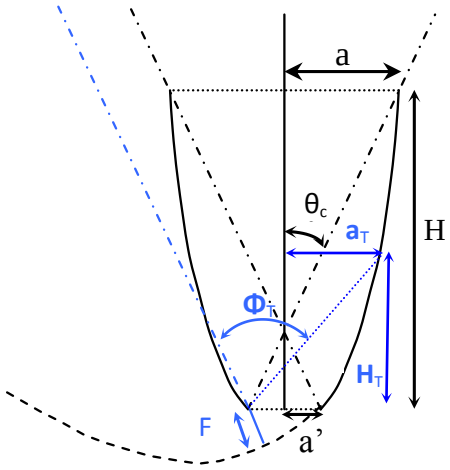

Figure 2.8: Full and truncated 2-D CPC dimensions.

Rabl [154] has drawn different plots where he explored the effect of truncation on the concentration ratio for a 2-D CPC [161]. The current study examines the effect of truncation on the concentration ratio of a 3-D CCPC; therefore, equations (2.12) and (2.13) are used to calculate the values of the truncated height and the corresponding concentration ratio.

For a full height CCPC, Φ_T will be equal to $2\theta_c$ and for a truncated CCPC we have $2\theta_c < \Phi_T < \frac{\pi}{2} + \theta_c$. The truncated angle Φ_T was varied from $(2\theta_c + 1)$ to $(\frac{\pi}{2} + \theta_c)$ incrementing it each time by one degree. Using equations (2.12) and (2.13), the corresponding truncated height H_T, and the corresponding width of the truncated aperture area (a_T) are calculated. The concentration ratio is calculated by dividing the

square power of a_T by the square power of a' to obtain $C_{T\,3\text{-}D}=\frac{a_T^{\,2}}{a'^2}$. The percentage of the truncated concentration ratio (% $C_{T\ 3\text{-}D}$) is also calculated referring to the concentration ratio of the non-truncated CCPC ($C_{3\text{-}D}$).

As an arbitrary choice, the initial geometrical concentration ratio of the studied CCPC is equal to 4, giving a half acceptance angle of θ_c=30º referring to the equation (1.20) (Chapter 1). The calculations of the truncated dimensions for the case of a half acceptance angle of θ_c=30° and a=1cm using Microsoft Excel are presented below in Table 2.1.

Table 2.1: The values of the truncated width, height and concentration ratio of the truncated CCPC.

Φ_T	a_T (cm)	H_T (cm)	$C_{T\ 3\text{-}D}$	% $C_{T\ 3\text{-}D}$
60	**1**	**2.598**	**4**	**100**
60	1.00	2.60	4	100
61	1.00	2.50	3.996453	99.91
62	1.00	2.40	3.99	99.66
63	1.00	2.30	3.97	99.25
64	0.99	2.21	3.95	98.70
65	0.99	2.13	3.92	98.03
66	0.99	2.05	3.89	97.25
67	0.98	1.97	3.85	96.36
68	0.98	1.89	3.82	95.39
⋮	⋮	⋮	⋮	⋮
115	0.5504	0.09	1.21	30.29
116	0.5403	0.07	1.17	29.19
117	0.5302	0.05	1.12	28.11
118	0.5202	0.04	1.08	27.06
119	0.5101	0.02	1.04	26.02
120	0.5	0	1	25

For the current calculations, for an acceptance angle θ_c = 0°, a'= 0.5cm and F = 0.75cm the full height of the CCPC is H = 2.59 cm giving a 3-D concentration ratio equal to $C_{3\text{-}D}$=4. For the purpose of the current study, truncation that will result in a reduction of 10% from the full CCPC concentration ratio will be considered acceptable. In order to truncate the CCPC, a reduction of 10% of the 3-D concentration ratio corresponds to a reduction of 38% of the height of the CCPC. This is a negligible reduction in the concentration ratio compared to the advantages gained by truncating the CCPC, such as a considerable reduction in the price of the reflective material [162] and the flexibility of its use in many BIPV applications.

A graph of the variation of the truncated height H_T as a function of the concentration ratio for a half acceptance angle θ_c=30° is presented below in Figure 2.9. It can be seen that for a geometrical concentration ratio less than 3.6, the truncation of the height of the CCPC has a considerable effect on the geometrical concentration ratio. In other words, if we look at the slope prior to a concentration ratio of 3.6, the slope is a gentle curve so for each decrease in height due to truncation there is a relatively large decrease in concentration. It is only at the 3.6 mark where the graph begins to take on an exponential form resulting in a lower decrease in concentration due to any truncation. At this point, after truncation, the height becomes H_T= 1.61 cm giving a 3-D concentration ratio equal to $C_{T\ 3\text{-}D}$= 3.62. So from a full height of 2.59cm to a truncated height of 1.61cm the concentration ratio only decreases by 10% from 4× to 3.6× compared to a larger decrease in concentration for the same amount of truncation (0.98cm) for any height/concentration variations below 3.6×; e.g. from a truncated height of 1.61cm to 0.63cm the concentration ratio decreases by 36% from 3.6× to 2.32×.

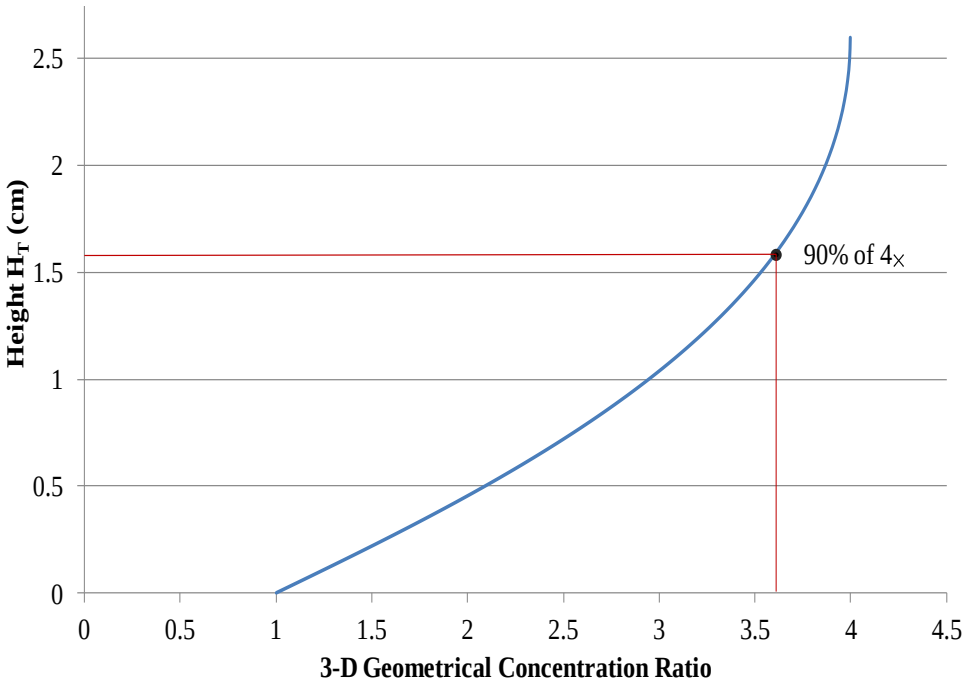

Figure 2.9: Variation of the concentration ratio as a function of the truncated height of the 4× CCPC

As previously explained, the 3-D CCPC (Figure 2.6) is constructed using two 2-D CPCs. In Table 2.2 below, the dimensions of the 2-D CPC used to construct the 3-D CCPC are summarised. These dimensions are calculated based on a fixed value of 1cm^2 for the exit aperture area.

Figure 2.10 gives the final dimensions of the truncated 3-D CCPC.

Table 2.2: Final dimensions for the 2-D CPC optimised for the city of Edinburgh.

Half acceptance angle	θ_c	30°
Focal length	F	0.75 cm
Full concentrator height	H	2.59 cm
Truncated concentrator height	H_T	1.61 cm
Exit aperture area half width	a’	0.5cm
Entry area half width	a	1 cm
Truncated CPC entry area width	a_T	0.95 cm
Truncated CPC opening angle	Φ_T	72 º
3-D concentration ratio	$C_{3\text{-}D}$	4
Truncated 3-D concentration ratio	$C_{T\,3\text{-}D}$	3.62

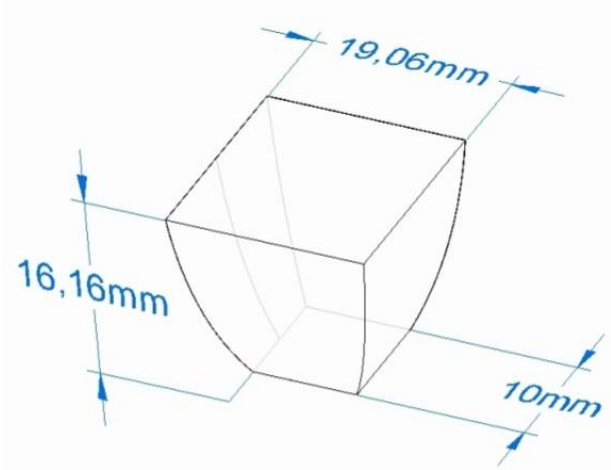

Figure 2.10: Dimensions of the truncated CCPC experimental model

2.4 Optical modelling of reflective CCPC

2.4.1 Ray tracing

In order to study the trajectory of a ray of sunlight when it is passing through an optical system, it is important to use the ray tracing technique to analyse its optical performance. When the ray hits the surface of the solar concentrator, it will be reflected or refracted. It is assumed that the side walls of the CCPC are entirely specular with reflectivity equal to 0.94, as most reflective surfaces of solar concentrators have a value

of reflectivity in the region of 0.94; this means that the light ray will lose 6% of its power after each reflection. Following this assumption, the directions of the incident ray and the reflected ray make the same angle with respect to the surface normal as illustrated in Figure 2.11.

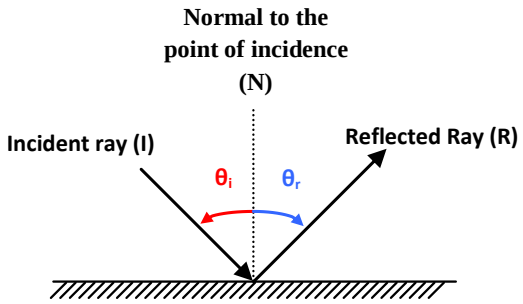

Figure 2.11: Schematic depiction of the law of reflection

The generalisation of the ray trace for all cases of reflection is possible by transforming the reflection law into vector form. The law of reflection is expressed by the vector equation (2.14) [156]:

$$\boldsymbol{R} = \boldsymbol{I} - 2 \times \boldsymbol{N}.\boldsymbol{I} \times \boldsymbol{N} \tag{2.14}$$

Figure 2.11 presents the two unit vectors $\boldsymbol{I}$ and $\boldsymbol{R}$ (Incident and Reflected) and the unit vector $\boldsymbol{N}$ along the Normal pointing into the reflecting surface. For solar concentrators with tracking systems, it is easier and enough to have a 2-D ray tracing analysis because the incident angle does not vary during the day at all or it varies only in one plane. But in static solar concentrators, the incident angle will be the angle of incidence of the solar rays, which vary in different planes during the day. Also the 2-D ray tracing does not give enough information for the illumination distribution on the exit aperture; it is suitable only for a 2-D concentrator rather than for a 3-D concentrator as has been indicated in a previous study [89].

In this study a 3-D ray tracing is carried out on the CCPC. The incident rays are considered as beam radiation, in other words all the rays entering the CCPC are parallel with the same energy and are spaced evenly. Correspondingly, all the rays have been dealt with as vectors to follow their 3-D directional path, and this is where the complexity of the 3-D ray trace appears.

In the current study, the 3-D ray trace code using MATLAB has been developed specifically for the case of the CCPC. The code has been written in the way that the

incident rays entering the CCPC face two situations; they either hit the exit aperture without reflection or hit one of the side walls to be reflected. After the first reflection, the incident ray will face one of three situations: exit the CCPC from the entry aperture and disappear, hit another or the same side wall to be reflected yet again or reach the exit aperture. The ray is followed until it either reaches the exit aperture where the photovoltaic cells are placed or exits the CCPC from the entry aperture and vanishes into space (Figure 2.12).

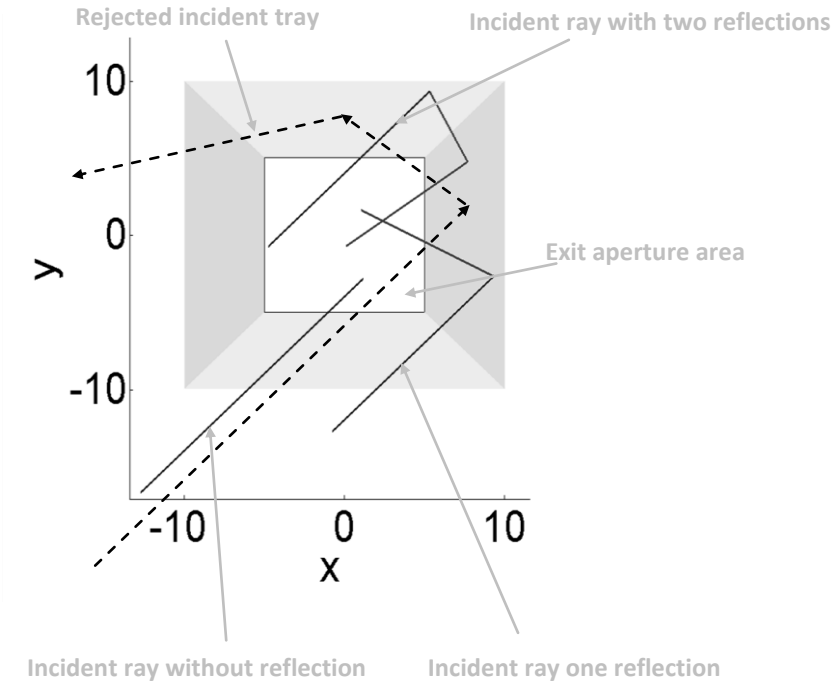

Figure 2.12: Behaviour of the incident ray on the CCPC walls.

For the purpose of ray tracing, the entire surface of the CCPC is made up of nodes or points. The distance between the two points making the CCPC or the incident ray is equal to 0.002mm. Therefore a high precision in the calculations is obtained and a low error of ± 0.001 mm in the reflection position is gained. The point of reflection is determined by calculating the nearest distance between the points of the matrix vector (forming the incident ray) and the different points of the matrix (forming the sides of the CCPC). At this point, the direction of the vector normal is calculated using the tangent vector. The vector normal is used in equation (2.14) to calculate the direction of the reflected ray.

At the beginning of each simulation, the number of incident rays is determined and the direction of the incident ray is specified by two angles, the first one in the S-N (south-north) plane called $\theta_{S\text{-}N}$ and the second angle in the E-W (east-west) plane called $\theta_{E\text{-}W}$. These two angles represent the projection of the incident angle θ on the S-N and E-W planes (Figure 2.13).

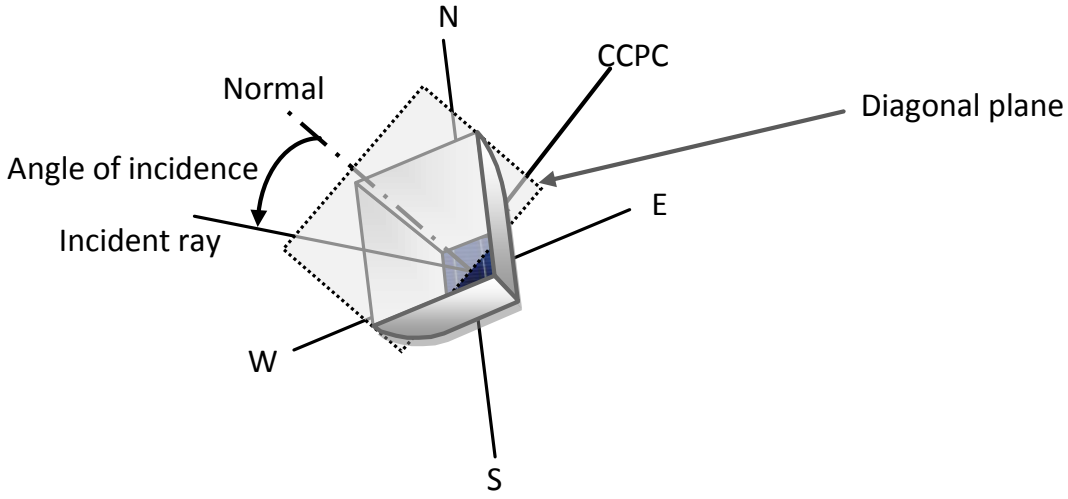

Figure 2.13: Alignment of the CCPC

Taking all possible directions of the incident ray, it will move in a number of planes between the S-N (or E-W) plane and the diagonal plane, which is later referred to as 'all directions' (Figure 2.16). The main point to note here is that the incident ray, regardless of which plane it is in, is always measured to the normal. In order to differentiate between the incident ray that is at a consistent angle but a different projection (e.g. incident ray of 10° but in the diagonal plane or between the diagonal and E-W plane), the incident angle in the simulation is referred to by the two angles representing its projection on the S-N and the E-W planes. This enables the incident ray to be tracked in all planes giving a detailed analysis of all of the incident rays in all possible planes. The incident angle is either within the acceptance angle ($-30<\theta<30$) or outside the acceptance angle ($|\theta| > 30$).

The results of the simulation show:

- The number of rays exiting the CCPC from the exit aperture (number of concentrated rays: n)
- Their (x, y) coordinates
- The number of reflections for each ray concentrated (NR_i)

- A drawing of the path of all incident and reflected rays. An example of the ray trace is illustrated in Figure 2.14.

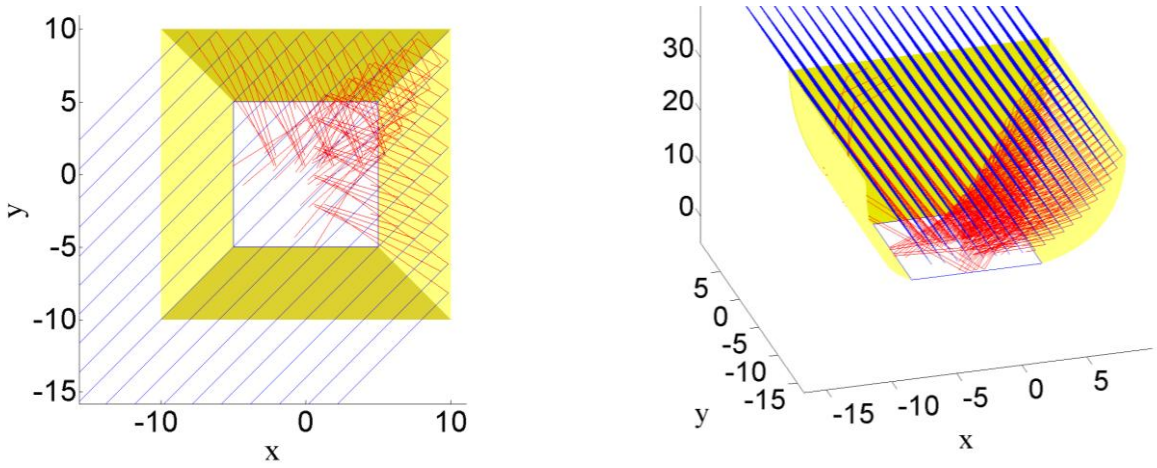

Figure 2.14: Different views of the 3-D ray trace on the CCPC, θ_{S_N}=15, θ_{E_W}=15, θ= 20.7

2.4.2 In-house development of MATLAB code

The flow chart of the MATLAB code written for the ray trace illustrated in Figure 2.15 indicates clearly the method followed for the simulation of the concentrated incident rays by the CCPC. The CCPC is considered as a composition of four sides or reflective surfaces making one envelope in order to make the calculation easier and less complicated. The MATLAB code is launched each time for different incident angles of the incoming rays. The code was written in such a way that it is flexible; it can be run for any CCPC with any geometrical concentration ratio or dimension. For the purpose of the current study and in this chapter, only the 4× CCPC truncated to 3.61× will be investigated and optically studied. The MATLAB code represents a strong and reliable method as it deals with the entire incident rays separately.

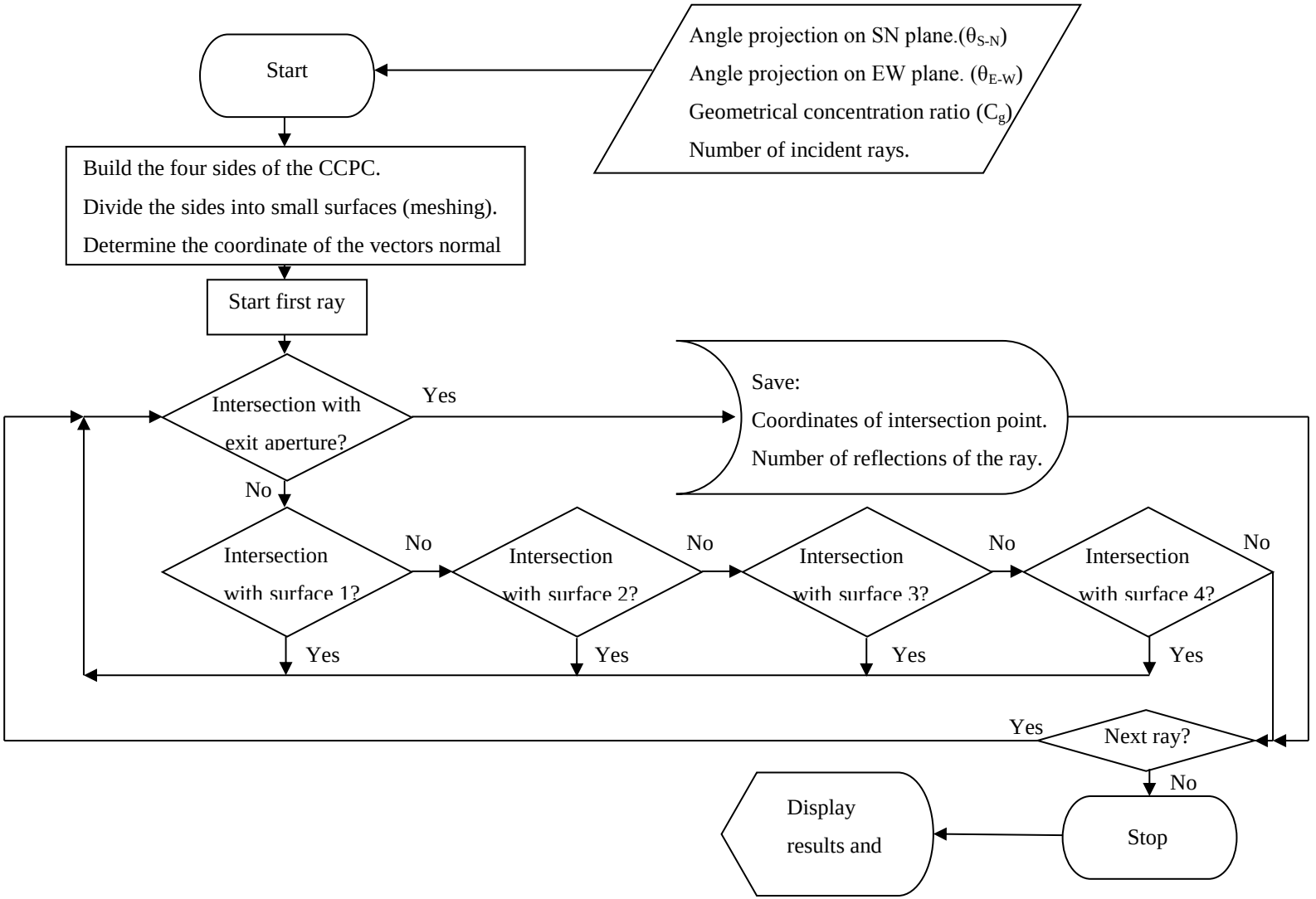

Figure 2.15: Flow chart of 3-D ray trace steps code for CCPC

2.4.3 Results of the optical efficiency of the CCPC

The acceptance angle of the CCPC is determined from the results of the variation of the optical efficiency as a function of the incident angle of the input light rays. For an ideal concentrator, 100% of the rays within the acceptance angle range are collected. The results of the ray trace give the number of rays collected using the CCPC (n) for different incident angles θ and the number of reflections (NR_i) of each ray before reaching the exit aperture. The optical efficiency is defined in equation (2.15) as:

$$Eff_{optical} = \frac{\sum_{i=1}^{i=n} \rho^{NR_i}}{Number\ of\ incident\ rays\ at\ the\ entry\ aperture} \tag{2.15}$$

where ρ = reflectivity of the side reflectors of the CCPC = 0.94.

Figure 2.16 illustrates the variation of the optical efficiency as a function of the incident angle. The dashed line represents the optical efficiency as a function of the variation of the incident angle in the S-N or the E-W (essentially the same because of the symmetry of the CCPC). The dotted line represents the optical efficiency as a function of the incident angle in the diagonal plane. The diagonal plane represents the normal plane having 45° from the S-N or E-W planes. The green circles represent the optical efficiency for incident rays in all possible planes (all directions). It can be observed from the graph that the CCPC is behaving as an ideal concentrator; it transmits most of the incident rays within the half acceptance angle equal to 30° (half acceptance angle of the original 2-D CPC). As the incident angle approaches 30°, there is a sharp drop in the optical efficiency decreasing significantly from 95% to 50%.

The optical efficiency for all possible incident angles of the light rays (represented by the small circles on Figure 2.16) is found to be within the following two limits:

- The first limit is represented by the curve of the optical efficiency of the incident angles when they vary in the S-N or E-W planes. This limit is the upper limit for incident rays <27° and is the lower limit for incident rays >27°.
- The second limit is represented by the curve of the optical efficiency of the incident angles when they vary in the diagonal plane. This limit is the upper limit for incident rays >27° and is the lower limit for incident rays <27°.

As observed in Figure 2.16, there is a critical point at an incident angle equal to 27° and optical efficiency equal to 80% that for any incident angle less than 27°, the incident rays produce a higher optical efficiency when in the S-N plane. But for incident angles higher than 27°, the incident rays produce a higher optical efficiency when in the diagonal plane.

From the results obtained, it can be seen that the CCPC is as ideal as the circular-sectional 3-D CPC; it concentrates more than 90% of the incident rays inferior to the acceptance angle and in the S-N or E-W plane. The dotted line on

Figure 2.17 represents the optical efficiency for a circular-sectional 3-D CPC [163]. The CCPC shows the same optical performance as the circular-sectional 3-D CPC. Furthermore, the CCPC has the added advantage of having the square shape of the entry and exit aperture. This is noteworthy as it increases the area of the collected solar irradiation when a group of CCPCs are aligned beside each other, in addition it will optimise the use of the solar cells when they are cut to a square shape compared to a circular shape.

The optical efficiencies of the 2-D CPC and the 3-D CCPC of the same area of entry aperture and the same heights are compared. The optical efficiencies of the two concentrators are the same when the incident rays are in the E-W plane, however the optical efficiency of the 2-D CPC drops significantly compared to the optical efficiency of the CCPC when the incident rays are in the diagonal and the S-N plane as illustrated in Figure 2.18. Consequently, it transpires that there are two major advantages of using the CCPC instead of the 2-D CPC:

- The symmetry of the CCPC geometry conserves the same optical efficiency in the S-N and E-W planes.
- For the same entry aperture areas and heights, the CCPC has a higher geometrical concentration (3.6) than the 2-D CPC (1.9). This allows the CCPC to save 47% of solar cell material compared to the 2-D CPC.

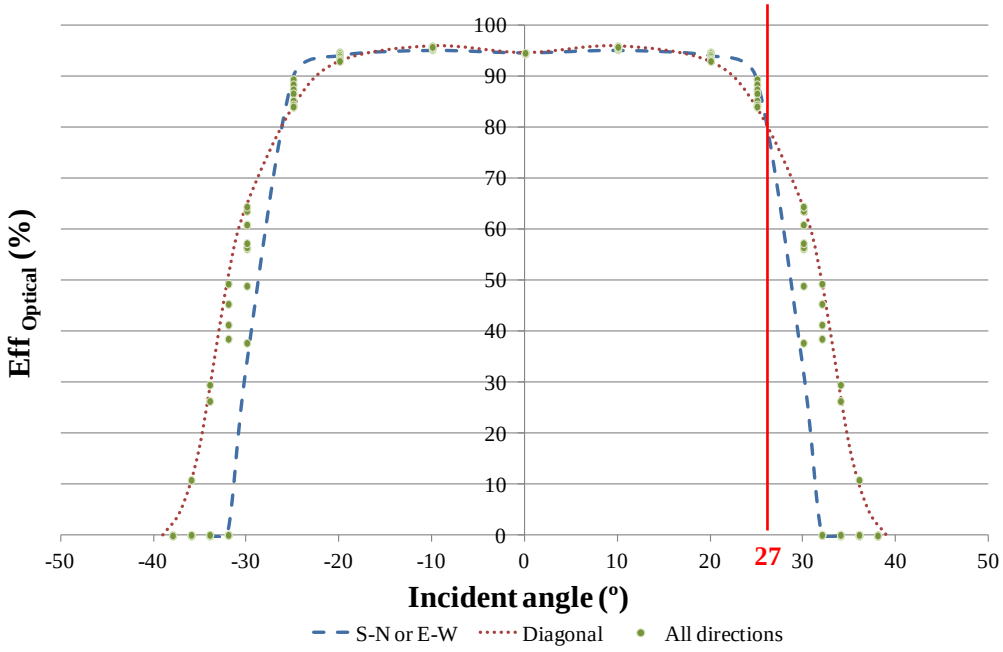

Figure 2.16: Variation of the optical efficiency as a function of the incident angle of the incoming rays.

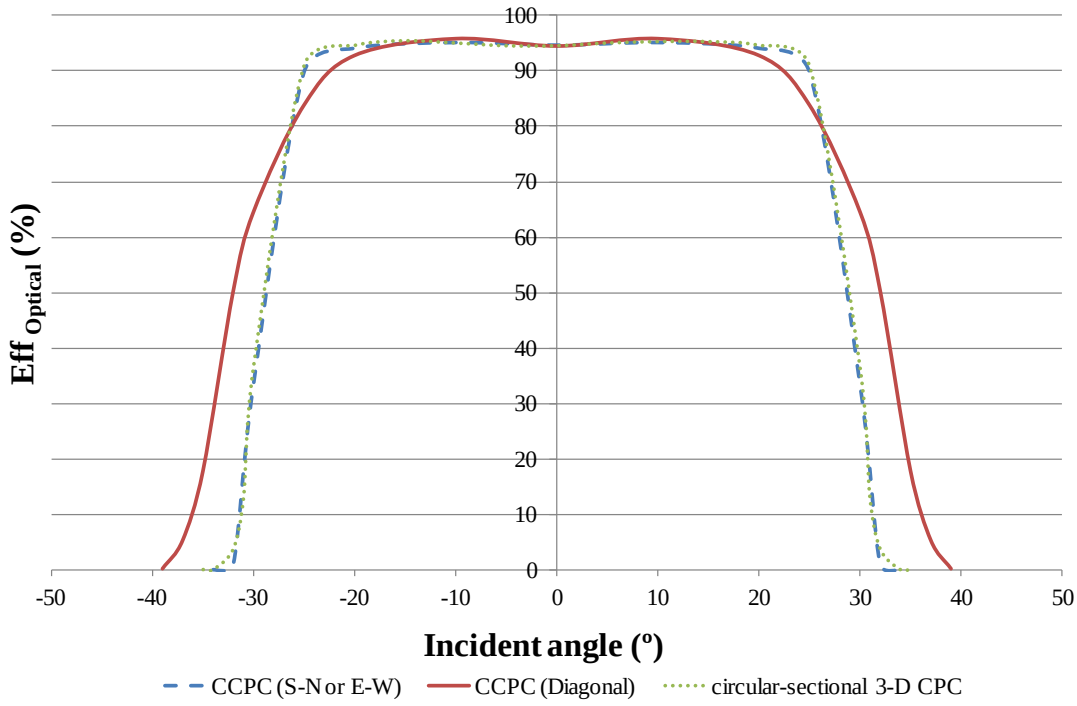

Figure 2.17: Comparison of the optical efficiency of the CCPC with the 3-D circular-sectional CPC

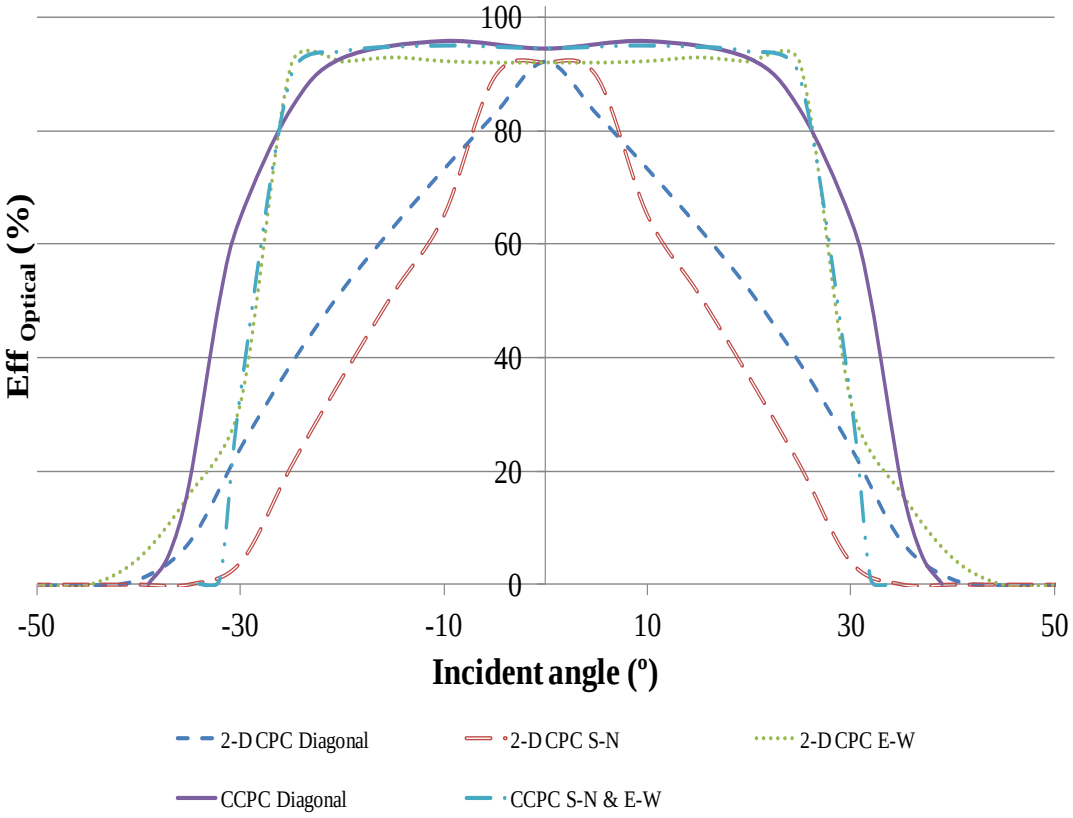

Figure 2.18: Comparison of the optical efficiency of the CCPC with the 2-D CPC

2.4.4 Optical flux distribution

With regard to the optical flux distribution, the concentrated rays on the exit aperture have a different distribution to those at the entry aperture of the CCPC. For each case of the different incident angles there will be a different distribution of the concentrated rays, resulting in a different distribution of the illumination.

At the end of the simulation using the MATLAB code, x, y coordinates of the collected rays are recorded. A few assumptions are made in order to achieve the results on the graphs below.

Assumptions:

- The side walls of the CCPC are 94% reflective.
- The ray is considered as beam radiation having an area depending on the distribution of the incident rays at the entry aperture, Figure 2.19(a).

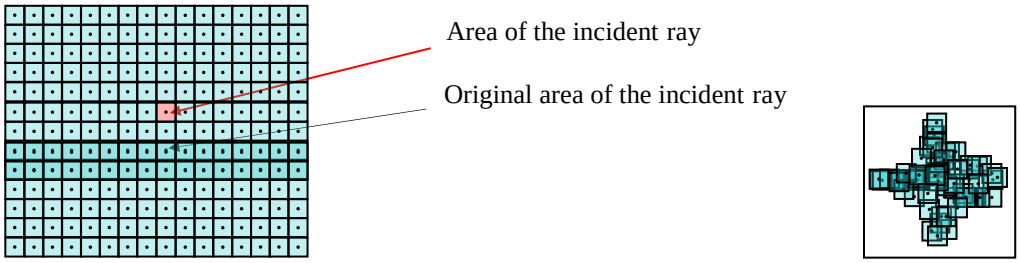

(a) (b)

Figure 2.19 : Assumption of the area of the incident and collected rays (a) entry aperture, (b) exit aperture.

As we can see in Figure 2.19 (a) the ray enters as a point; but it will be considered as a square area for ease of calculation. When the ray reaches the exit aperture, it will also be considered as a square of the same size. The superposition of the squares on the exit aperture will be used to obtain the data for the optical flux distribution.

The optical flux represents the number of rays concentrated in the same area of the exit aperture of the CCPC; it is obtained as follows. Each ray is considered as an area of a square; the size of the square depends on the number of rays at the entry aperture area. The superposition of the different squares at the exit aperture area gives the optical flux distribution. The non dimensional numbers of the optical flux distribution represent the number of rays hitting the same area; in other words it is equivalent to the local concentration ratio. All of the incident rays have a non dimensional value equal to 1. The optical flux distribution shows how the concentration is distributed on the exit aperture. Figure 2.20 illustrates some of the distributions obtained.

After reflection, the energy values of the concentrated rays falling in the same area are summed to give the optical flux value. If the energy of the incident rays at the entry aperture was equal to 1000W/m^2, the local energy at a specific area of the exit aperture of the CCPC would be equal to 1000W/m^2 multiplied by the optical flux on that specific area. This is a general method to determine the energy of the radiation at the exit aperture of the CCPC for any energy of the radiation of the incident rays.

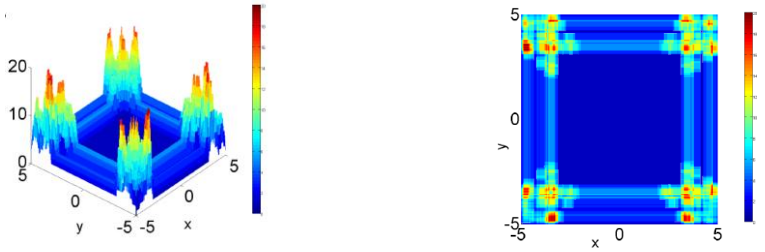

(a) **Angle of incidence θ=0, $\theta_{S\text{-}N}$ = 0, $\theta_{E\text{-}W}$ =0**

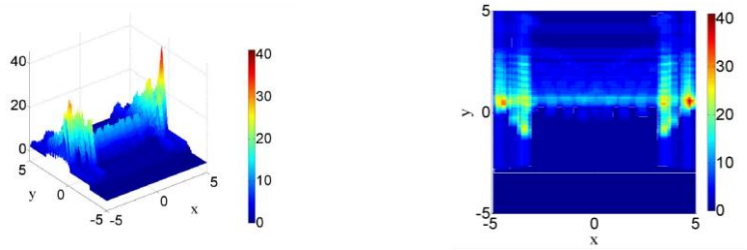

(b) **Angle of incidence θ=15, $\theta_{S\text{-}N}$=0, $\theta_{E\text{-}W}$ =15**

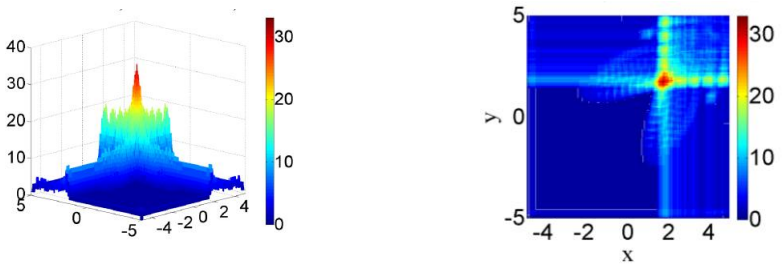

(c) **Angle of incidence θ=14, $\theta_{S\text{-}N}$=10, $\theta_{E\text{-}W}$ =10**

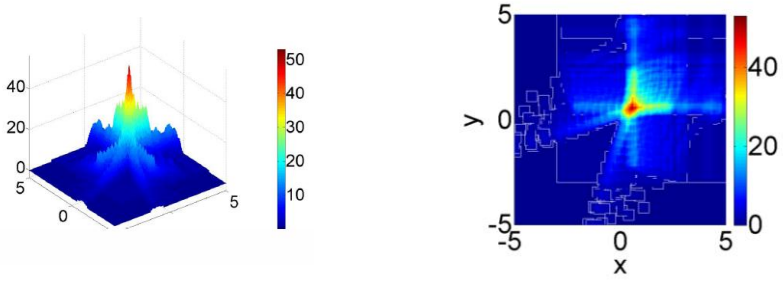

(d) **Angle of incidence θ=20.7, $\theta_{S\text{-}N}$=15, $\theta_{E\text{-}W}$ =1**

(i) (ii)

Figure 2.20 : Optical flux distribution as a function of the incident angle and its projection on the S-N and E-W planes ((i): 3-D illustration, (ii): 2-D illustration)

The results of the optical flux distribution show that the energy on some areas of the exit aperture can reach up to 50 times the energy of the incident rays. These are defined as the hotspots which are located in different positions, depending on the incident angle. At normal incident rays to the entry aperture they are located in the corners (Figure 2.20a); at an incident angle of 20° in the diagonal plane, most of the rays are concentrated in one hot spot in the middle, at a concentration level of 50 (Figure 2.20d). Generally when coming to design a solar cell and simulate its performance, one assumption is considered, which is having uniform optical flux distribution and uniform temperature on the surface of the cell. It is noticeable from the graphs in Figure 2.20, however, that the distribution is uneven and this will have an effect on the solar cell efficiency [164, 165]. The focused illumination has to be uniform to a level that the total efficiency of the CPV system does not decrease. Franklin and Coventry [166], as well as Luque and Andreev [167], mentioned the drop of efficiency in CPV systems resulting from the non-uniform optical flux. The increase in solar irradiance increases the solar cells efficiency, but at the same time the peak intensity and the increase of the temperature generate resistive losses in the cell. Therefore, there will be a stage where the increase in resistive losses is equal to or surpasses the efficiency increase due to the radiation concentration. The solution could reside in a cooling system or in decreasing the distance between the conducting fingers in the solar cells. This is obtained in concentrator cells by decreasing the spacing between the conducting fingers, using a low resistance substrate for the cell and introducing a back surface field (highly doped back substrate). This allows lowering the bulk and contacting resistance. Using techniques like these, make it possible to manufacture cells optimised for several hundred suns [168].

From the results together, it can be concluded that a CCPC formed by two 2-D CPC troughs is an ideal concentrator for a half acceptance angle equal to θ_c=30°.

2.5 Validation of the optical model

Following on from here, an experimental study is carried out in order to validate the optical model developed. The following sections describe the experiment from fabrication of the CCPC model to the results obtained.

2.6 Fabrication of reflective CCPC

An experimental model of nine CCPCs was made using stereolithography manufacturing technology. The use of stereolithography is very beneficial as the shapes fabricated can have a very complicated and precise geometry profile. The experimental CCPC model has a square exit aperture of 1cm×1cm and a height of 1.6cm. The inner surfaces of the CCPCs are covered with commercial reflective film having a reflectivity of 94% (Figure 2.21), identical to the reflectivity value entered in the simulation.

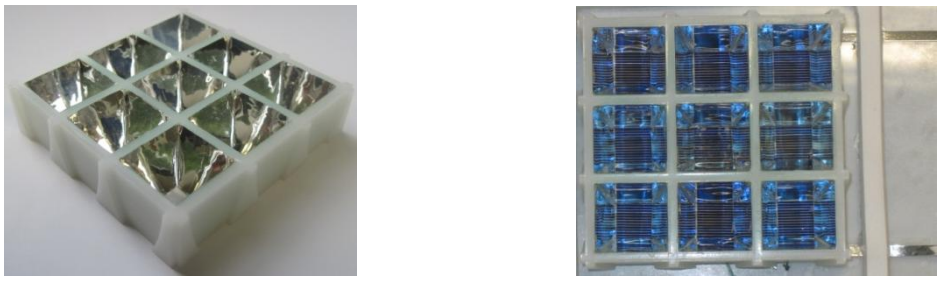

(a) (b)

Figure 2.21: (a) Experimental model of CCPC covered with reflective film; (b) concentrating cells (designed to operate at <10 suns) assembly with CCPCs

2.6.1.1 The solar cell to be used in the CPV modules

The LGBC solar cell presented in this section will be used to build all of the CPV modules in this thesis; the choice is based as these cells are designed to perform under up to 10× geometric concentration ratio. The solar cells used are provided by NaREC (National Renewable Energy Centre). They are silicon solar cells with Laser Grooved Buried Contact (LGBC) designed to generate electricity for a concentration ratio <10x [169].

The number of fingers, their thickness and their distribution on the solar cell are illustrated in Figure 2.22.

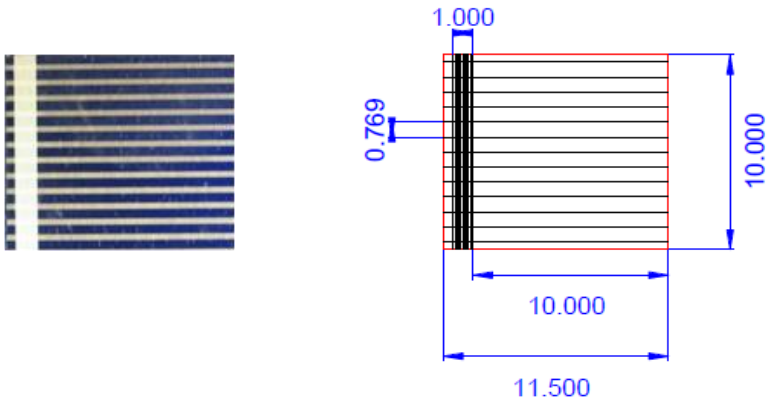

(a) (b)

Figure 2.22: 1cm^2 silicon solar cell optimised to work at less than 10× concentrations (a) image of solar cell, (b) solar cell dimensions (in mm).

The 1cm^2 silicon solar cell is cut from an original silicon wafer (green frame below). It is patterned and laser-grooved to create the bus bars and the fingers in the way presented in Figure 2.23. The bus bars are designed to be outside the active area of the solar cell of 1cm^2.

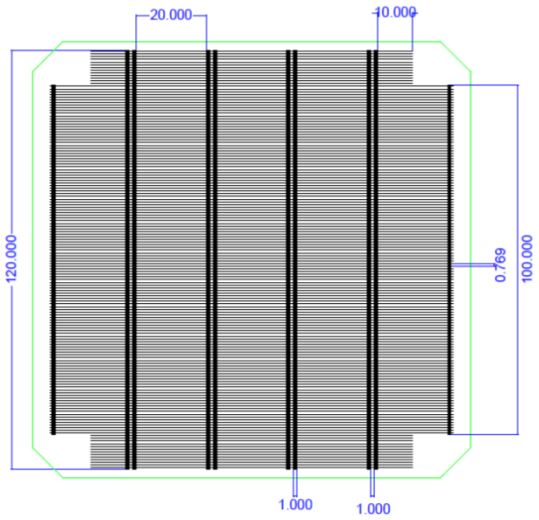

Figure 2.23: Original LGBC silicon wafer

2.6.1.2 Soldering of solar cells

Nine LGBC concentrating silicon solar cells designed for a concentration ratio <10x are connected and sandwiched between a glass plate (underside of the solar cell) and encapsulation material (top side of the solar cell). The solar cells are soldered using lead free PV ribbon with 0.1mm thickness and 1mm width; the bus bars of the solar cells have a 1mm width (Figure 2.22(b)). Lead free PV ribbons with 3mm width are used

later to connect the PV modules (with and without the CCPCs) with the measuring instruments.

The electrical connection of the solar cells is carried out following the subsequent procedure:

- The lead free PV ribbon is cleaned and cut to the required length (i.e. the distance between each solar cell). It is important that the surfaces of all of the components to be soldered should be clean and free from grease.
- The soldering iron rod is heated to 300^{o}C with a temperature controlled unit and maintained at the correct temperature.
- A small amount of liquid flux is applied to the tip of both ends of the connector piece for a more controlled and effective use of the soldering material. Flux is a key component to soldering as it removes oxidation that prevents solder from bonding to metals. Using a soldering rod, a small amount of solder is then applied to both ends of the connector piece of PV ribbon. If too much solder is used this can overflow during tabbing with the cells, causing a short-circuit. Excessive use of solder can also increase the series resistance of the module.
- One of the ends of the connector piece is then connected to the back side of the solar cell. This is carried out for all of the solar cells to be used. The PV ribbons are soldered to the back side (positive side) of the solar cells first at any convenient point. Low temperature soldering is used, as high temperature soldering can damage the cells.
- After connecting the back sides of the solar cells, the cells are placed on top of the back glass plate in their corresponding position. A small drop of super glue is used to secure the solar cells in place for the remainder of the fabrication process (this is merely a temporary effect to hold the solar cells in place for the electrical connection part of the fabrication process).
- The connector piece attached to the back of the solar cells is then connected to the front side (negative side) of the next solar cell. The same procedure is followed to connect all the solar cells in each column.
- Two strings of 3mm PV ribbon are then connected, one to the end of the negative side and one to the end of the positive side of the module. These will be used as the connectors of the PV modules.
- The last fundamental step in this procedure is to check the short-circuit connections in each string of solar cells.

2.6.1.3 Encapsulation material

After placing the soldered solar cells on top of the glass plate, the encapsulation material Sylgard-184 is cast on top, as mentioned above.

Sylgard-184 Silicone Elastomer is a two-part silicone that cures to a flexible elastomer for the protection of electrical and electronic devices in solar applications. It is also used as an adhesive/encapsulant for solar cells. It is supplied as a base and curing agent in two separate containers that need to be mixed 10 parts base to one part curing agent, by weight. During the mixing process, volatile compounds are released when mixing the curing agent and base, so all weighing, mixing and stirring are carried out wearing nitrile gloves and in a fume cupboard. The mixture needs to be stirred manually for ten minutes, thoroughly but gently so as to minimise the amount of air bubbles formed; if left to settle for a further ten minutes the majority of the air bubbles evaporate. This is known as the pre-treatment stage. Following on from here, the mixture is placed in a vacuum chamber. The purpose of this is to remove any air bubbles that may be trapped inside the mixture; all visible air bubbles are reduced after carrying out this process three to four times. The preparation of the encapsulation takes approximately 30 to 35 minutes, depending on the amount of air bubbles introduced during stirring.

Prior to pouring the encapsulation material onto the solar cell assembly, in applications requiring adhesion, priming is required. In the current case, a liquid primer (Dow-corning primer-92-023) is applied to both the solar cell and glass. Use of the primer enhances the adhesion between Sylgard and a wide variety of surfaces, such as glass and metal. It is important that the surfaces are thoroughly air-dried prior to application of the primer and the encapsulation material. The primer is applied using a brush; for best results, it should be applied in a very thin uniform coating and then wiped off after application. It is then left to dry for ten minutes; if left for longer, the primer begins to form a white pigment. It is important, therefore, that as soon the primer dries, the prepared encapsulation material is poured onto the rear glass plate.

Sylgard-184 can either be cured at room temperature (25º) or can be heat cured to speed up the curing process. The schedule given by the manufacturers is as follows: ~ 48 hours at room temperature, 45 minutes at 100°C, 20 minutes at 125°C or 10 minutes at 150°C. In the current study, the Sylgard was left to cure at room temperature for all of the modules. This was due to fact that the concentrator units need to be placed on top of the solar cells before the Sylgard cures; the Sylgard not only holds the solar cells in place but also holds the concentrators in place on top. Room temperature curing is

therefore carried out to avoid any misalignment of the concentrator receiver and the cells that could potentially occur during heat curing.

2.6.2 Experimental setup

The electrical power output of the solar cells was then measured in two different cases: coupled with and without the CCPCs using a 1 Sun abet solar simulator and MP 160 IV tracer (Figure 2.24). The lamp emits a 5800K blackbody-like spectrum with an intensity of 1000W/m^2. Furthermore, the spectral light distribution resembles the global distribution at standard reporting conditions. These same conditions have been used by Mammo et al. in his experimental measurements [170].

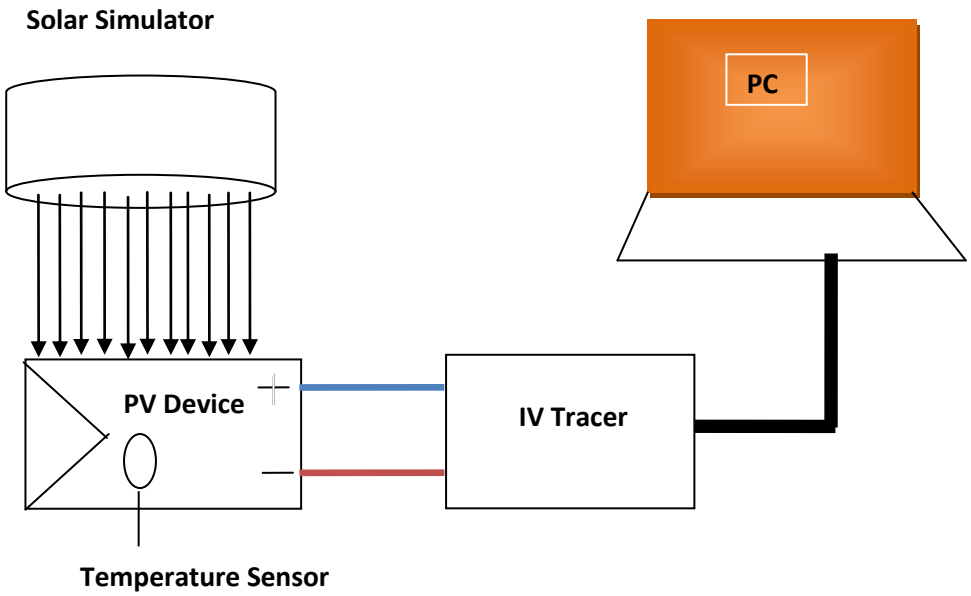

Figure 2.24. Experimental set up to characterise the PV modules.

A series of measurements were taken for different incident angles varying from normal incident angles to the exit aperture at 0º to an angle of 60º where the power output of the concentrating solar cells is ≈ 0 W; an increment of 5º was considered each time. Measurements were carried out by the I-V tracer at a maintained room temperature giving as output I-V curves of the solar cell.

Since the incident angle of the irradiation from the solar simulator cannot be changed, the different incident angles were achieved by changing the inclination of the CPV

module. Figure 2.25 shows a photograph of the set up that was devised to change the inclination angles of the modules for the indoor characterisation.

The set-up consisted of an aluminium base plate, attached to an acrylic frame by a hinge. The acrylic frame can be tilted along the axis of the hinge facilitating a change in the inclination angle of the modules. To enable the frame to be set to the correct inclination angle, a protractor was attached at the junction of the acrylic frame and the aluminium base; for very fine adjustments of the inclination angle, a digital protractor can be used. The digital protractor is accurate within ± 0.5^{o}. The frame was constructed with acrylic bars, as opposed to a continuous sheet, in order to allow natural convection from the back of the module; furthermore the design incorporates a moving bar that can fit modules up to 200mm×200mm making for a convenient adjustable set up.

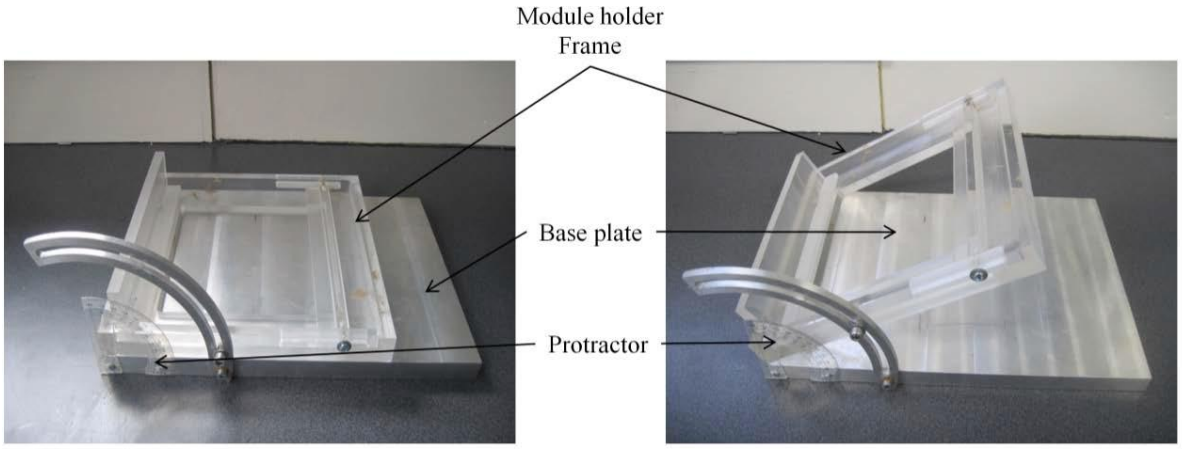

Figure 2.25: Images of the set-up for inclination of CPV modules during indoor characterisation showing (a) horizontal and (b) 30º inclination

With regard to the solar simulator, it is important to measure the flux density or light intensity from it in the working plane. In standard practice a calibrated solar cell, which has a spectral response within the range of 250-1200nm, is used to measure the light intensity of 1 sun on the working area; calibrated photodiodes can also be used for this. In this instance, to measure the light intensity from the solar simulator at Heriot-Watt University, a silicon photodiode assembly was constructed and calibrated. For the calibrated photodiode to be used as a reference to measure the light intensity from the solar simulator, it is important to maintain a constant temperature throughout the calibration procedure; changes in temperature can bring about variation in the short

circuit current and open circuit voltage of the silicon photodiode for the same light intensity.

The photodiode assembly consists of an S3477 series photodiode sensor (which has an in-built thermistor to sense the photodiode chip temperature), a heat sink, and a thermoelectric controller (to maintain the temperature). The photodiode is mounted on a customised heat sink with holes for the photodiode pins. The heat sink with the photodiode is then mounted on a box with sockets for electrical outputs of the photodiode, temperature sensor and thermoelectric controller.

A series of steps are followed to calibrate the photodiode. From the outset, a silicon solar cell calibrated by the Fraunhofer Institute for Solar Energy Systems ISE[5] is used as the reference to calibrate the photodiode.

1. The solar simulator is switched on for 2 hours to attain a stable irradiation and spectrum.
2. The reference solar cell is placed on the working plane in the middle of the illuminated area.
3. The temperature of the reference cell is monitored and the IV data collected at 25^{o}C as per the measurement standards for the reference cell.
4. The IV data is then compared to the supplied data of the reference cell for the intensity 1000W/m^{2}. By regulating the current flow to the lamp in the solar simulator, the light intensity of the solar simulator can be adjusted accordingly until the correct value is obtained.
5. Steps 3 and 4 are repeated as many times as is necessary to obtain the IV data of the reference cell to match the supplied value.
6. When the IV data of the reference solar cell corresponds to the supplied value, the reference solar cell is replaced by the photodiode. Now the IV-characteristics of the photodiode are measured at 20^{o}C.

[5] Fraunhofer ISE is the largest solar energy research institute in Europe. The work at the Institute ranges from the investigation of scientific and technological fundamentals for solar energy applications, through the development of production technology and prototypes, to the construction of demonstration systems. http://www.ise.fraunhofer.de/en

7. The calibrated value of the short circuit current of the photodiode (at 20^{o}C) is used as the standard to measure 1000W/m^2 radiation intensity from the solar simulator at Heriot-Watt University.

Having outlined the experimental setup, the experimental results are presented below.

2.6.3 Experimental results of the reflective CCPC

Short circuit current (I_{sc}) is proportional to the exposed cell area and the intensity of incident light. The experimental optical efficiency ($Eff_{Exp,Optical}$) is obtained by dividing the short circuit current produced by the solar cells coupled with the CCPCs ($I_{sc\text{-}con}$) by the short circuit current (I_{sc}) produced under 1 sun illumination multiplied by the geometrical concentration ratio C_g as shown in equation (2.16):

$$Eff_{Exp,Optical} = \frac{I_{sc-con}}{I_{sc} \times C_g} \tag{2.16}$$

$$C_{Opt} = Eff_{Optical} \times C_g \tag{2.17}$$

Experimentally, the CCPC is able to concentrate sun rays with an optical efficiency above 80% for 5 hours during the day giving a high optical concentration ratio of C_{Opt} =2.88 for a non-tracking solar concentrator. The optical concentration ratio is defined as the product of the optical efficiency and the geometrical concentration ratio as shown in equation (2.17); it gives the final concentration taking into consideration the energy losses due to reflection. The optical concentration ratio depends on the shape and the material of the concentrator. An agreement was observed between the experimental and simulated optical efficiencies of the CCPC as can be seen in Figure 2.26. The experimental characterisation of the optical efficiency was found to show a deviation of 12±2 % from the 3-D ray tracing simulation. The deviation between the experimental and simulation results can be explained by various factors such as flaws in the manufacturing of the CCPCs, placing the reflective film, and slight misplacing of the cells at the exit aperture of the CCPC.

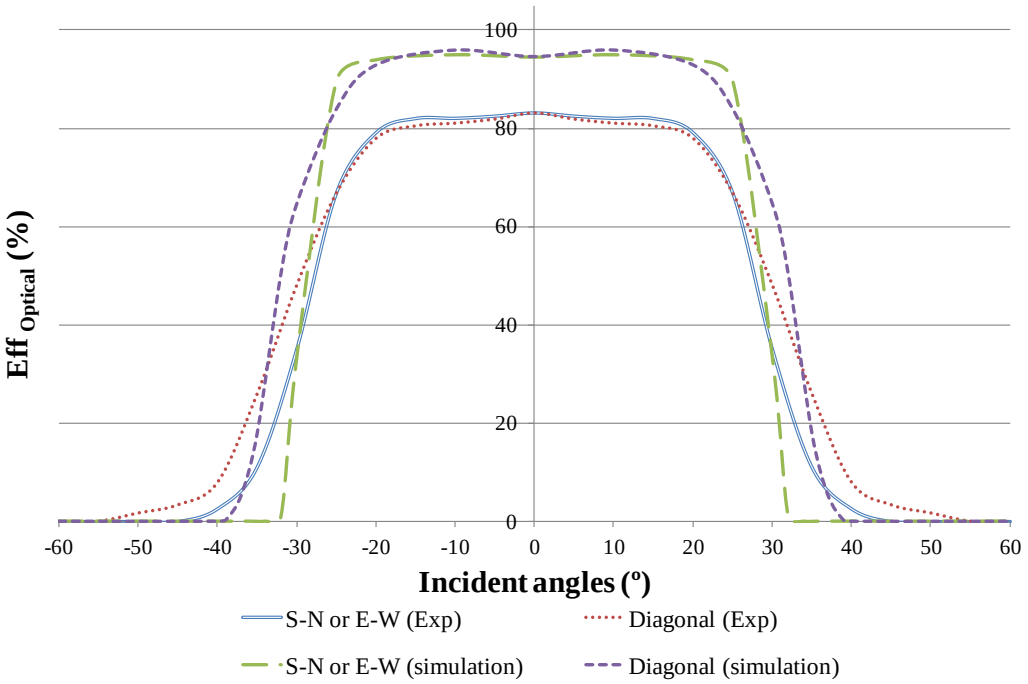

Figure 2.26: Comparison of measured and simulated optical efficiency as a function of the incident angle of the incoming rays.

From these results it can be confirmed that the developed 3-D ray trace MATLAB code is validated by the experimental results. Further likeness between the experimental and simulation results can be seen in Figure 2.26. A photo of the concentrated light distribution on the exit aperture area obtained from the experimental study (Figure 2.27(a)) corresponds to the pattern obtained at the exit aperture from the simulation study (Figure 2.27(b)). This further highlights the validity of the simulation results, and validation of the developed 3-D ray trace code.

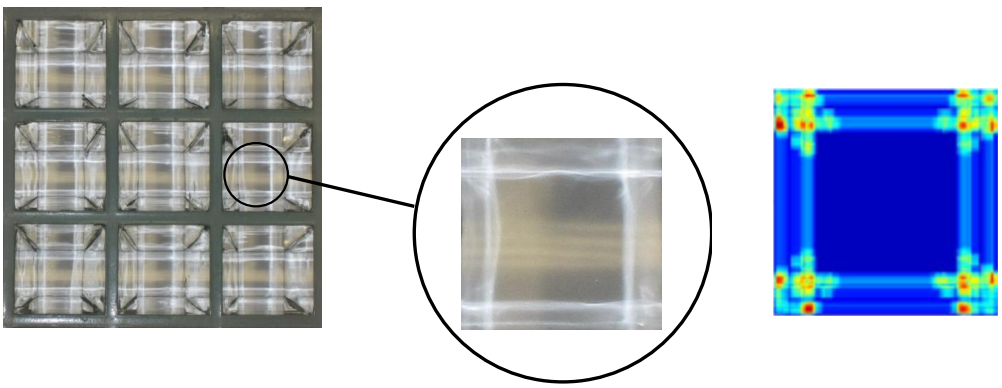

(a) (b)

Figure 2.27: a) Photo of the light distribution on the exit aperture of the CCPC under normal incident rays, b) optical flux obtained by numerical simulation under normal incident rays.

2.7 Comparison between MATLAB code and commercial software

After the validation of the optical model using MATLAB code via experimental results, it is important to mention that writing the ray tracing code has the following advantages:

- Flexibility in manipulating the different inputs.
- Full knowledge of the errors or bugs that can occur during the simulation.
- The certitude of the accuracy of the results produced.

Two obstacles remain, however; the length of time of running the simulation, in addition to the complexity of defining the geometrical boundaries for more complex solar concentrator profiles.

To maximise time, for the remaining optical simulations in the thesis and for the design of a new solar concentrator, it was decided to use a commercial software. An optical software known as OptisWorks [171] was purchased; it is a powerful industrial tool used in many optic applications. It has the significant advantage of minimising the amount of time needed to simulate the ray tracing. To validate the results thus far, however, a comparison between the MATLAB results and those obtained by OptisWorks is needed. This not only provides verification of the MATLAB 3-D ray tracing code developed, but also reinforces the remainder of the thesis with the use of OptisWorks.

2.7.1 Optical modelling of CCPC using OptisWorks

A CCPC with the dimensions given in Table 2.2 was drawn using SolidWorks CAD software. A source of light is defined in OptisWorks and applied at different incident angles on the square entry aperture of the reflective CCPC. The source is set up to generate 10 Mega rays at a chosen radiation of 1000 W/m^2. The rays are illustrated by OptisWorks in order to carry out a visual check on the reflectivity of the different sides of the CCPC as seen in Figure 2.28. Depending on the incident angle, the light ray will reflect on the different surfaces of the CCPC at different reflection angles.

An assumption is made in that all the rays are incident with the same incident angle and the spectrum of the light source is specified as blackbody-like spectrum with an intensity of 1000w/m^2. An illuminance detector is placed at the exit aperture of the CCPC; this detector measures the flux and energy of the concentrated rays by the CCPC. It is important to mention that the reflectivity of the reflective sides of the CCPC is set to 94%, the same condition that was considered in the MATLAB code.

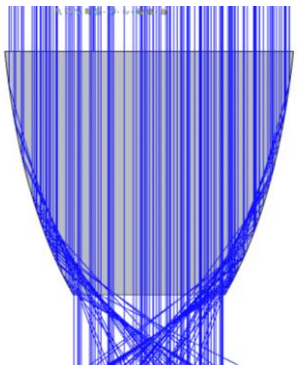

Figure 2.28: Path of concentrated incident rays obtained from the reflective CCPC illustrated by OptisWorks

The optical model built, in order to investigate the optical characteristics of the reflective CCPC, is described in the chart below in Figure 2.29.

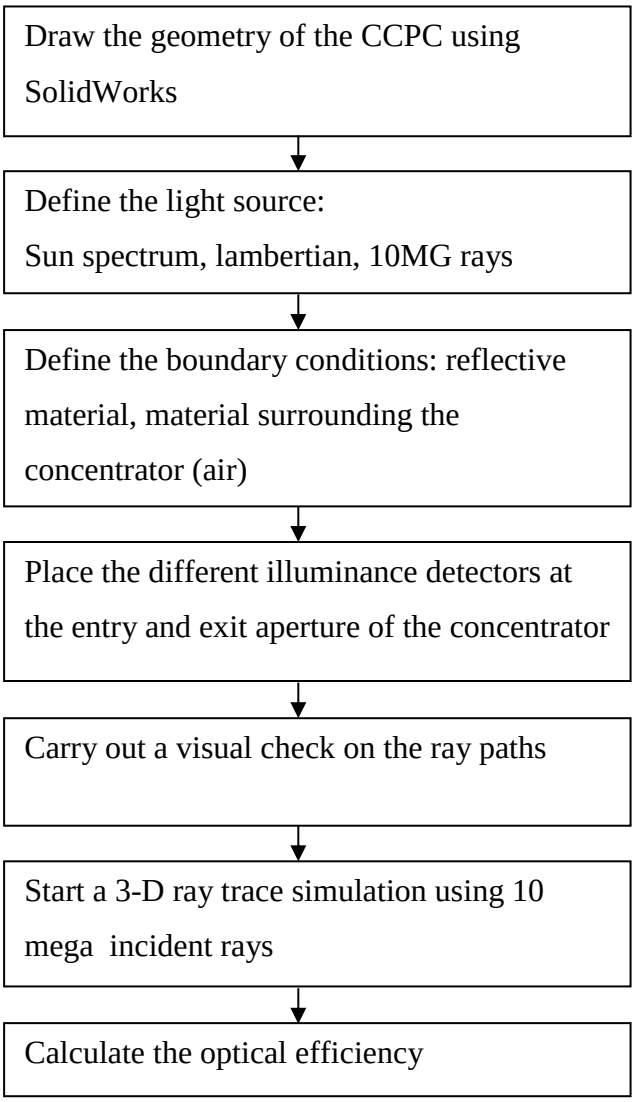

Figure 2.29: Ray trace simulation process flow chart for the CCPC.

The rays enter the CCPC at different incident angles starting from the rays perpendicular to the surface of the entry aperture (this is considered as an angle of incidence 0º) to the rays parallel to the entry aperture (this is considered as an angle of incidence 90º).

2.7.2 Results of the optical modelling using OptisWorks and MATLAB

The optical efficiency of the SEH ($Eff_{Optical}$) is calculated according to equation (2.18):

$$Eff_{optical} = \frac{\varphi_{exit\ aperture}}{\varphi_{entry\ aperture}} \tag{2.18}$$

where $\varphi_{\text{entry aperture}}$ is the flux in W detected at the entry aperture and $\varphi_{\text{exit aperture}}$ is the flux in W detected at the exit aperture.

The graphs in Figure 2.30 and Figure 2.31 present the results of the optical efficiency of the CCPC of 3.61× simulated with a self-elaborated MATLAB code (blue line) and with OptisWorks (red line). Figure 2.30 illustrates the optical efficiency of the reflective CCPC when the incident rays vary in the S-N or E-W plane. The blue and red lines on the graphs coincide perfectly with a very small variation of 1.5% between the OptisWorks and MATLAB code results.

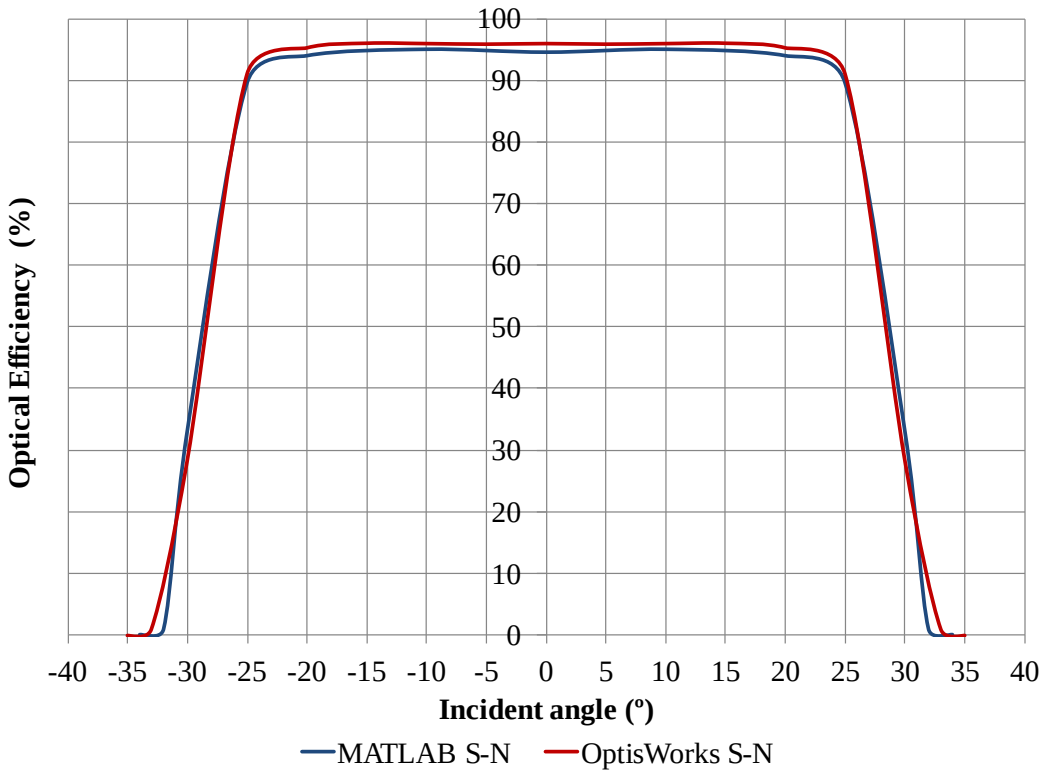

Figure 2.30. Comparison between the optical efficiency of the CCPC simulated with MATLAB and OptisWorks for angles varied in the S-N plane

Similarly, Figure 2.31 illustrates the optical efficiency of the reflective CCPC when the incidents rays vary in the diagonal plane. The two lines on the graph (red and blue) coincide with a very small variation of 1%, showing that the results obtained by MATLAB and the OptisWorks simulation are very much the same.

These results represent yet another validation of the MATLAB code after having validated the code with the experimental results obtained and discussed previously in section 2.5. At the same time the results validate the use of the OptisWorks software for the remainder of the research.

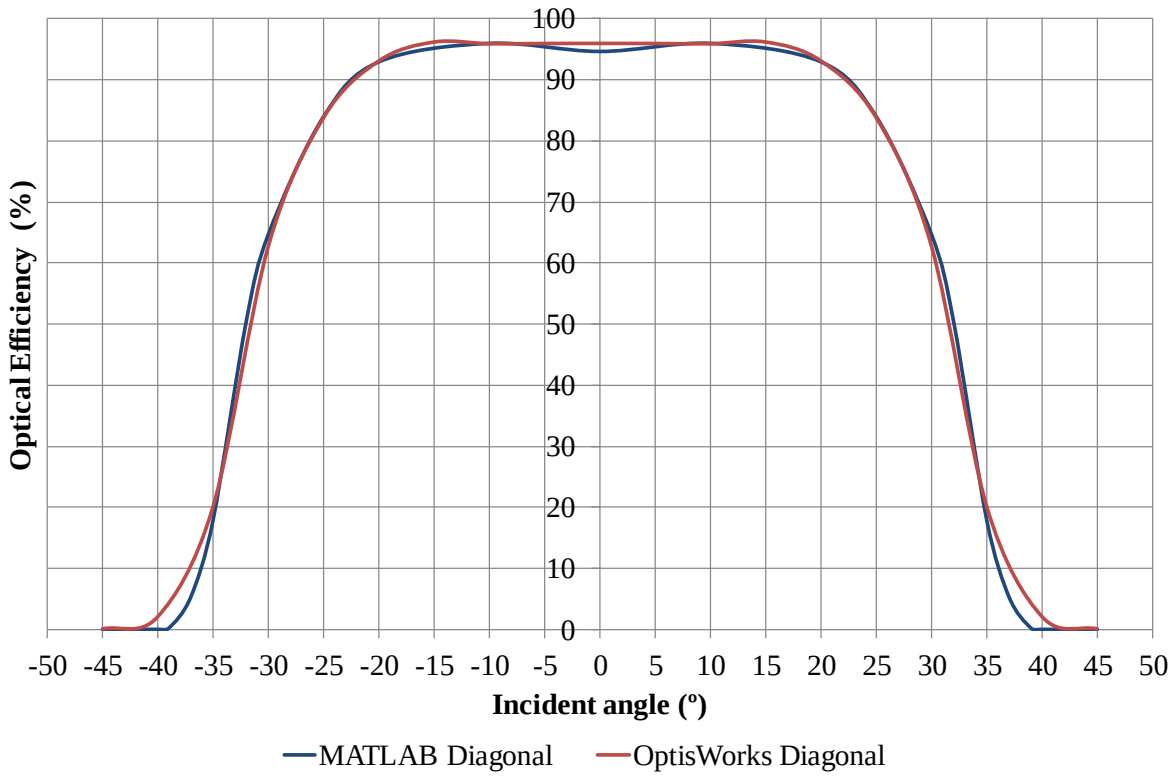

Figure 2.31. Comparison between the optical efficiency of the CCPC simulated with MATLAB and OptisWorks for angles varied in the diagonal plane.

Developing the ray tracing code via MATLAB is very beneficial to master the ray tracing technique and understand the behaviour of the incident rays concentrated by an optical device. The advantages of using the software OptisWorks, however, surpass:

- It gives the flexibility of drawing any complex geometry; OptisWorks is an Add-On that works with SolidWorks CAD software. Both represent integrated software for drawing the optical devices and for the optical simulation.
- The time of simulation is much quicker than when using the MATLAB code. For the same results, MATLAB simulation takes 1 hour to complete compared to the OptisWorks simulation which takes 10 minutes, thus saving a huge amount of time.
- The rapidity in obtaining the results in various different formats, such as the 3-D map for the optical flux distribution.
- OptisWorks can generate a larger amount of incident rays, resulting in better resolution of the optical flux distribution. This does not impact on the accuracy of the output of the results; it is merely for the aesthetical presentation where the

resolution is notably clearer. The difference in resolution can be seen in Figure 2.32.

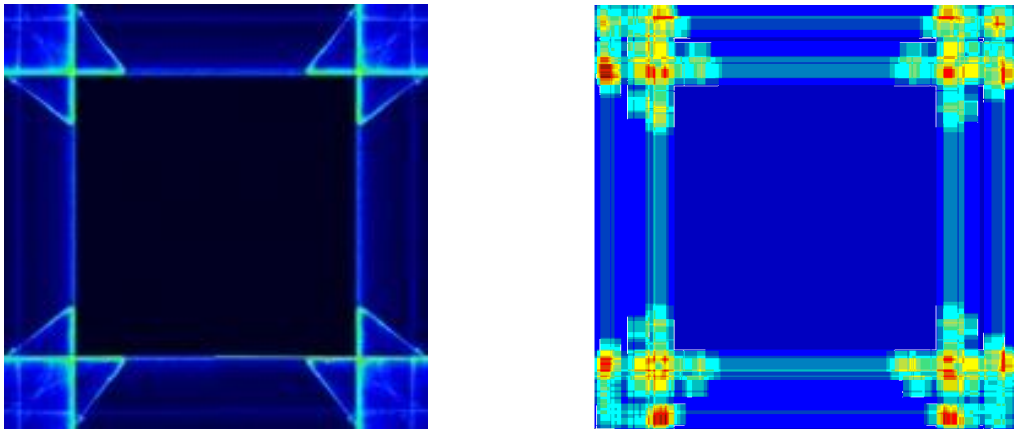

Figure 2.32: Optical flux distribution at the exit of the reflective CCPC for normal incident rays: (a) obtained by OptisWorks simulation, (b) obtained by MATLAB simulation

After having the opportunity to purchase OptisWorks, and validating the optical efficiency results comparing them to the MATLAB results, it was decided to use OptisWorks for the remainder of the thesis. From this point onward, for the remaining optical studies, OptisWorks will be used.

2.8 Optical characterisation of the refractive CCPC

The reflective CCPC studied is considered as a hollow concentrator. It is generally known that filling a hollow concentrator with a dielectric material medium (with refractive index $n>1$), the geometrical concentration ratio of a 2-D concentrator will increase by n times and for a 3-D concentrator it will increase by n^2 times based on the equations (1.21) and (1.22) respectively.

Based on this, it was decided to investigate the reflective hollow CCPC filled with a dielectric material. Furthermore, the reflective material is removed relying on the refractive CCPC to work as a concentrator following the law of total internal reflection (TIR).

2.8.1 Optical modelling of refractive CCPC

The optical model is similar to the one described in section 2.7.1 with the only difference that the refractive CCPC is drawn as a clear solid PMMA shaped in the geometry of the CCPC. The optical characteristics of PMMA are provided by OptisWorks in the material library. This choice is based on the large use of PMMA in the manufacturing of Fresnel lenses [172-174] and the availability of the optical characteristics based on the absorption coefficient and the refraction index variation. The consideration of the absorption coefficient, also known as attenuation coefficient, in ray tracing simulation of dielectric optical devices is very important; this characterises the amount of energy lost by the light rays when it penetrates a medium or a material. The longer the path of the light ray inside the dielectric material is the more energy it loses. OptisWorks takes these characteristics of the material into consideration when running the ray tracing simulation to give more precise results about the energy of the light rays on the exit area of the concentrator. The length of the path of the concentrated light ray is affected by the number of internal reflections effectuated; more reflections indicate a longer light ray path and more losses in its energy. The absorption coefficient of the PMMA material as a function of the wavelength is illustrated in Figure 2.33. It shows that the absorption coefficient of the PMMA is very low at the visible light spectrum and within the band gap of the silicon solar cell <1100nm which is due mainly to the clarity of the material.

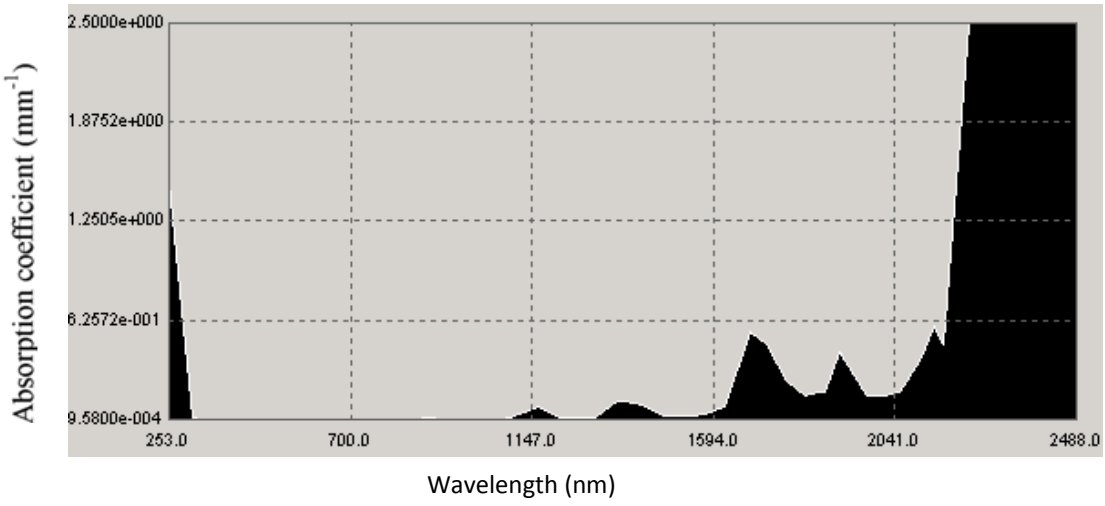

Figure 2.33: Absorption coefficient variation of PMMA

The second optical characteristic of the PMMA needed for the ray tracing simulation is the refractive index. This is a very important parameter to be considered by OptisWorks as it determines the angle of refraction of the incident rays on the entry aperture of the concentrator. The variation of the refractive index as a function of the wavelength is minimal in the order of 0.04 as shown in Figure 2.34 (from 1.48 to 1.52). This variation provides a maximum variation in the refracted angle of ±2º and also in the critical angle of TIR where the variation can make the light rays escape from the sides of the CCPC concentrator or be internally reflected depending only on the refractive index of the PMMA.

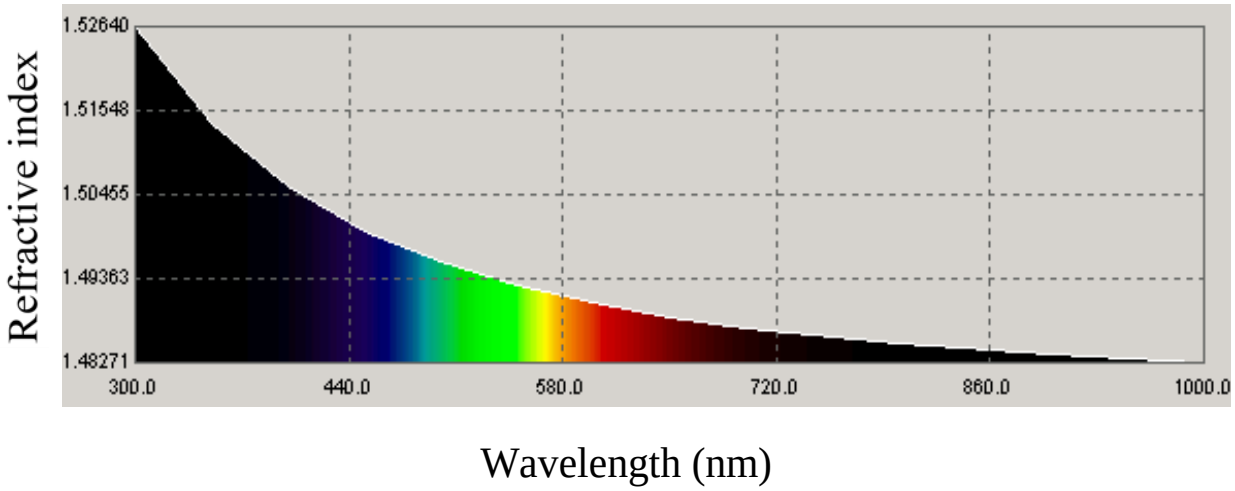

Figure 2.34: Refractive Index variation of PMMA

When the light rays reach the sides of the refractive CCPC after having entered from the entry aperture, they are about to pass from a medium with a higher refractive index (PMMA n=1.5) to one with a lower refractive index (air n=1). These rays in certain cases of large incident angles will be forced to be reflected back to the PMMA material as shown in Figure 2.35; the process is known as total internal reflection (TIR). Otherwise, following the refractive law, the sin of the angle of refraction will be greater than one.

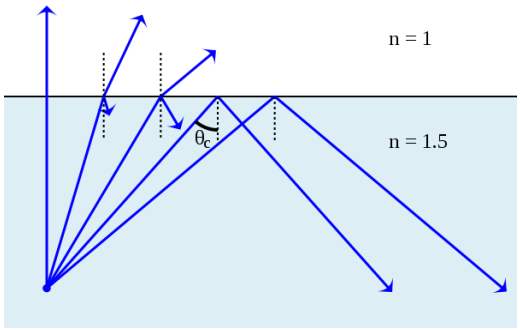

Figure 2.35: Schematic drawing of total internal reflection and critical angle

The refractive law, also known as Snell's law, describes the angles of refraction of the incident light ray passing through two different isotropic mediums with different index values. Following the law of refraction (Figure 1.11(b) and equation (1.25)), the incident rays on the entry aperture of the refractive CCPC will be refracted and then either, Figure 2.36:

- Reach the exit aperture directly.
- Be refracted out to the space from the sides of the refractive CCPC if the incident angle is less than the critical angle of TIR.
- Be reflected on the sides of the refractive CCPC once or more than one time to reach the exit aperture at the end obtaining the concentration effect.
- Be reflected on the sides of the refractive CCPC once or more than one time to escape into the space from the entry aperture.

The simulation is carried out for different incident angles in a similar way as for the reflective CCPC. The results of the optical simulation are discussed in section 2.8.3 and illustrated in Figure 2.42.

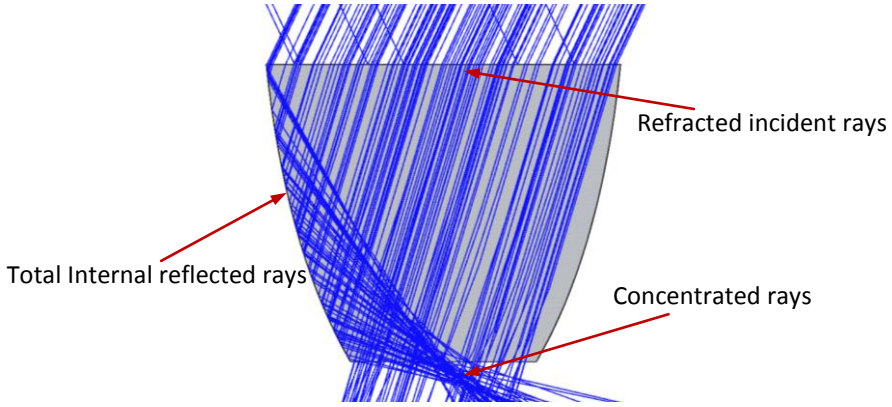

Figure 2.36: Path of concentrated incident rays by the refractive CCPC illustrated by OptisWorks

2.8.2 Fabrication of the refractive CCPC and the CPV module

A casting aluminium mould made for 81 CCPC's was designed and machined as can be seen in Figure 2.37. The sides of the mould are highly polished having a smooth finish. Polyurethane (Crystal Clear 200 Series) was chosen as the material to cast the refractive CCPC because of the following charteristics:

- Low shrinkage coefficient 0.001 in. /in.
- UV-protected, the crystal clear 200 has a special UV-additive so it will not yellow when exposed to sun light.
- Possibility to prepare it in an ambient pressure mould (non-injection mould). This leaves enough time before hardening to be mixed and poured manually in the mould.
- Assumed to have similar optical characteristics to the PMMA used for the optical modelling.
- Availability in small quantity to be purchased for prototype making.
- Low toxic risks; the polyurethane will be prepared and handled in the laboratories at Heriot-Watt University.

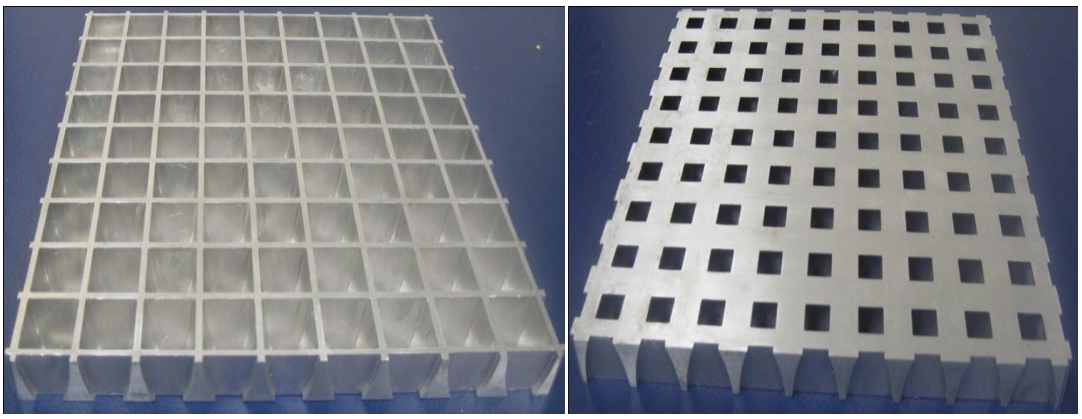

(a) (b)

Figure 2.37: Aluminium mould for refractive CCPC (a) top side and (b) underside.

The procedure of preparing the refractive CCPC is described below. The first few steps are carried out in a fume cabinet in order to minimise inhalation of any toxic fumes and to reduce the presence of dust in the mixture.

- The mould is cleaned with detergent ensuring no dust particles are settled on the side surfaces.
- The mould is sprayed with a releasing agent to facilitate the removal of the casted refractive CCPC when it is cured.
- The two parts of polyurethane are mixed with a ratio of 10 part A: 9 part B in weight (Figure 2.38). The mixing is carried out for about 5 minutes until the two parts have completely blended together.
- The previous step creates a lot of air bubbles in the polyurethane mixture. These air bubbles are removed using a powerful vacuum oven. By placing the polyurethane mixture under vacuum for about 5 minutes, the air bubbles will disappear to obtain a clear mixture.
- The mixture is poured, with care, into the aluminium mould placed on an adjusted horizontal surface.
- The mould and the polyurethane mixture are then left to cure for 6 hours in an ambient temperature followed by 6 hours at 72 ºC. Alternatively, casting can reach ultimate physical properties at room temperature in 5-7 days.
- Once the polyurethane is cured, it can be separated from the mould.

- The optically clear casted refractive CCPCs (Figure 2.39) are ready to be assembled to the PV cells.

Figure 2.38: Part A and Part B of the polyurethane material

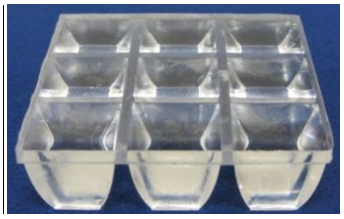

Figure 2.39: Example of casted refractive CCPC

Using LGBC concentrating silicon solar cells, two PV modules are made. The first one is coupled with the refractive CCPC and the second one is left without the concentrators. The 81 solar cells are soldered on a support heating resistant plate. The plate (Figure 2.40) has 81 grooves with the same size as the solar cells and in the exact pattern corresponding to the exit aperture area on the mould of the casted refractive CCPCs. This is done to obtain an exact (or as near to exact) superposition with the casted refractive CCPCs. The soldered solar cells are placed on a glass plate, and covered with 0.5 mm layer of encapsulation material (Sylgard), the CCPCs are then placed on top of them. The encapsulation material has a double role in this module:

- It protects the solar cells from the weather effects and holds them on the glass plate.
- It connects the solar cells to the exit apertures of the refractive CCPCs, acting as an adhesive.

The solar cells plus the encapsulation material and the refractive CCPCs together compose the CPV module that is tested indoors (Figure 2.41). It is compared with an

equivalent PV module built with 81 solar cells and encapsulation material but without being coupled to the refractive CCPCs.

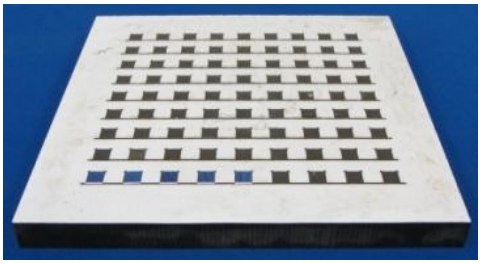

Figure 2.40: Soldering solar cells plate

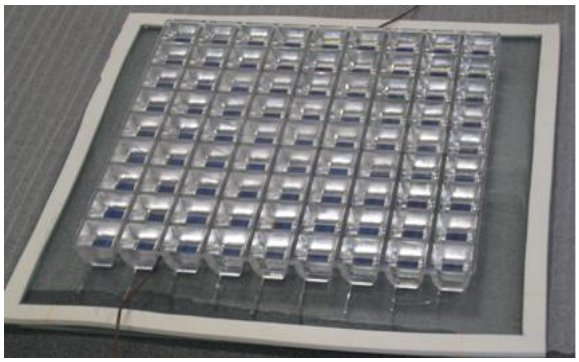

Figure 2.41: Refractive CCPC assembled with solar cells and encapsulation material

2.8.3 Optical simulation and experimental results

The two modules, PV and CPV, are tested indoors using the same equipment and conditions described in section 2.6.2, for the reflective CCPC. The optical efficiency is calculated using the same method presented in section 2.6.2 using the $I_{sc\text{-}con}$ produced by the CPV module and the I_{sc} produced by the PV module under the same measurement conditions.

The results of the optical efficiency obtained from the simulation (red line on the graph) and obtained from the experiment (blue line on the graph) are illustrated in Figure 2.42.

It can be seen that there is an agreement between both sets of results of the optical efficiencies of the refractive CCPC. There is a small variation of 9% between the two efficiencies for certain incident angles and this can be mainly attributed to the imprecision of the alignment of the CPV and PV modules during the fabrication process. It is important to note that the variation between the simulation results and the

experimental results for the refractive CCPC is less than the variation between the simulation results and the experimental results for the reflective CCPC (Figure 2.26). This can be explained by the greater level of accuracy achievable and the certitude when manufacturing the refractive CCPCs, the quality of the surface of the refractive CCPC depends only on the quality of the casting mould and the curing process. In contrast, however, the sides of the reflective CCPC are covered manually using reflective film, therefore, the potential to err is greater and due to the small size of the concentrators, it was extremely difficult to cover all of the inner corner sides of the reflective CCPC as required.

Figure 2.43 illustrates a comparison between the experimental optical efficiencies of the same sized refractive and reflective CCPCs. Although the two CCPCs (reflective and refractive) have the same geometrical characteristics, it can be noticed that the refractive CCPC has a larger acceptance angle of 80º (-40º,+40º) compared to the reflective CCPC of 50º (-25º,+25º) with only a 10 % difference in the maximum optical efficiency. The refractive CCPC collects rays at a constant level of approximately 70% (its maximum efficiency) for an incident angle <50° compared to the reflective CCPC which only collects rays at a constant level of 80% (its maximum efficiency) for an incident angle <25° before rapidly decreasing in efficiency. Furthermore, the refractive CCPC is still collecting and concentrating incident rays with an incident angle outside the range of the acceptance angle up until an incident angle in the range of -80º, +80º covering all the incident rays that may fall on the entry aperture area during the day.

Although having a slightly lower optical efficiency, it transpires that the refractive CCPC has many advantages over the reflective CCPC:

- The refractive CCPCs are easier to manufacture, one casting mould can generate a very large number of concentrators using cheap material such as polyurethane or PMMA.
- The refractive material is light; the density of the polyurethane is only 1.05 kg/litre, which will not add a large weight to the building structure.
- The refractive CCPC has a larger acceptance angle compared to the reflective CCPC; this is a very important factor to consider for a static concentrator, enabling maximum solar radiation collection during the day.

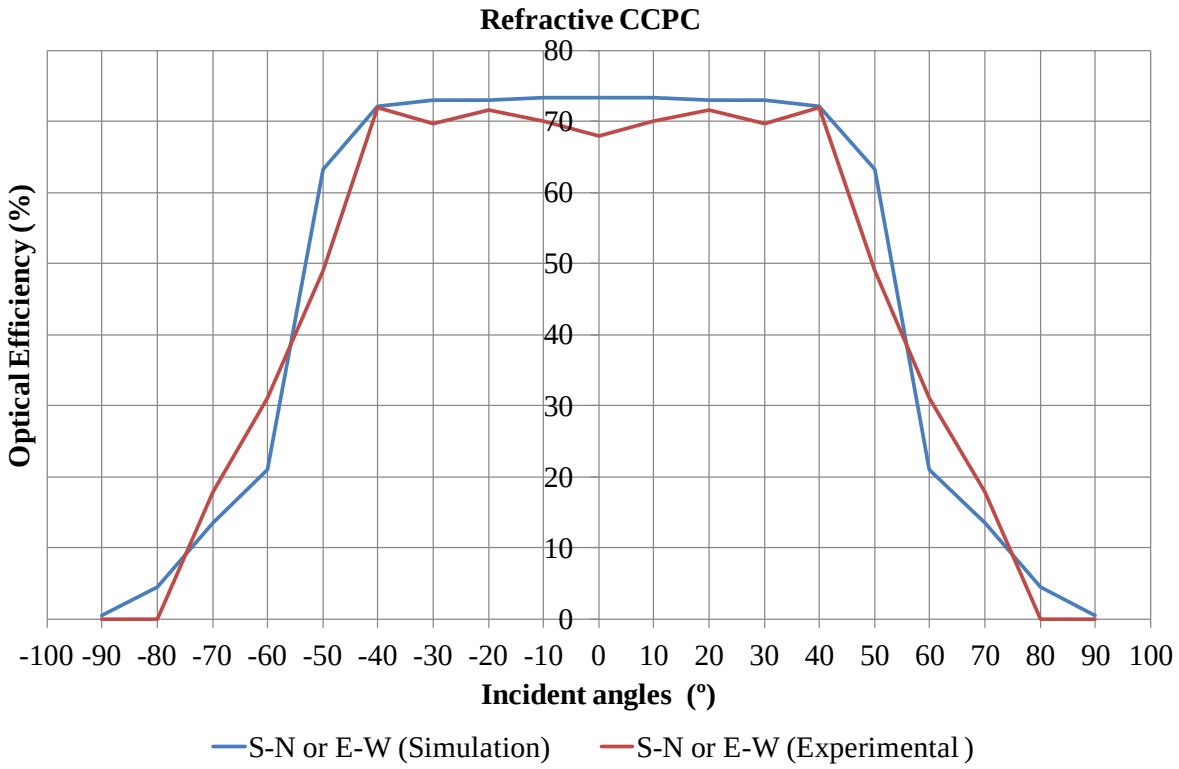

Figure 2.42: Simulation and experimental results of the optical efficiency of the refractive CCPC carried out with OptisWorks.

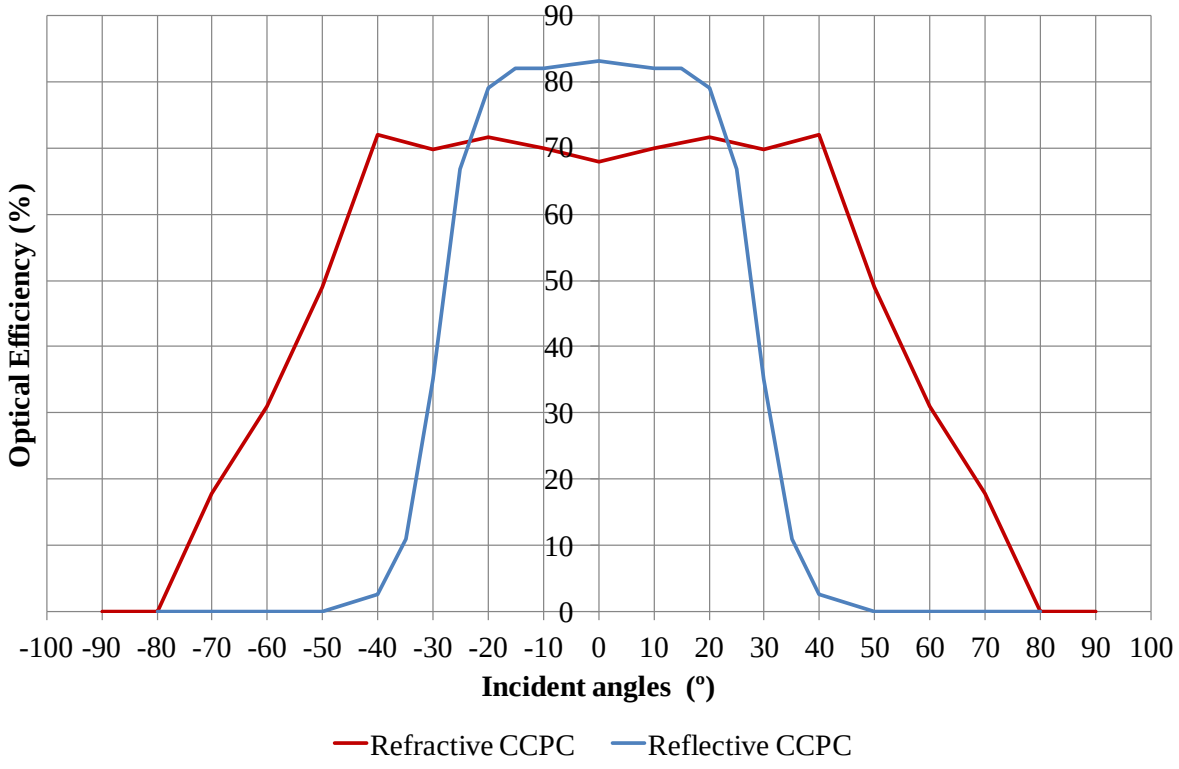

Figure 2.43: Experimental optical efficiency for the refractive and reflective CCPCs

2.9 Conclusion

The optical efficiencies of a reflective and refractive CCPC have been investigated, studied and compared. In the first instance, the CCPC showed a better optical performance compared to the 2-D CPC and the 3-D circular-sectional CPC with a specific geometrical characteristic of a square entry and exit aperture. A MATLAB code for 3-D ray trace was developed to investigate the optical efficiency and the location of hot spots of the optical flux distribution on the exit aperture of the CCPC for different incident angles of the light ray. It was found that the CCPC is an ideal concentrator for a half acceptance angle equal to 30° and a geometrical concentration ratio equal to 3.6. Secondly, it was found that the optical flux distribution is not uniform at the exit aperture and that it can reach up to 50 times the energy of the incident light rays from. This is a crucial finding as these hot spots can decrease the efficiency of the solar cells considerably.

A comparison between the simulation and experimental results showed strong agreements with a deviation of 12% for the optical efficiency for the reflective CCPC and deviation of 9% for the refractive CCPC; in addition, the light distribution patterns obtained from the optical simulation resembled the experimental results. This provides clear validation of the ray trace code developed and certifies its use to investigate different concentration ratios of the CCPC.

The study includes the use of different optical simulations, a written MATLAB code and commercial software OptisWorks. In this chapter many theoretical tools have been used in order to determine the optical charteristics of the CCPC geometry built with a different material and using experimental techniques to validate the different optical simulation models.

This chapter has a great impact on the remaining work in this thesis, as it introduces most of the theoretical and experimental techniques that are used to characterise the novel static concentrator presented in the next chapter. In addition, this chapter reveals two main important facts that form the base of the rest of the thesis:

- After having compared the ray tracing results delivered by OptisWorks software with the ones produced by the developed MATLAB code, the software can be used with confidence for the remainder of the research in the current thesis.

- The advantages of the refractive solar concentrator compared to the reflective concentrator; this will have a direct impact on the choice of material for the novel solar concentrator to be introduced in the following chapter.

The current research proposes to take this investigation further and develop a novel static 3-D concentrator. The next chapter will focus on the characterisation of the novel concentrator with particular reference to its geometry.

Chapter 3: Design and development of the Translucent Integrated Concentrated Photovoltaic (TICPV) module

The design of the novel concentrator is the focus of this chapter; it is the first study of its kind – examining the use of a 3-D solar concentrator in BICPV. Due to the nature of the novel geometry, it transpires that it is necessary to develop a 3-D parametric equation in order to progress to the optimisation stage and to be able to study its optical performance. The methodology of the development of the equation is described in this chapter concluding with its validation.

3.1 Introduction

The use of 3-D static solar concentrators has not yet been studied for the integration in transparent façades of buildings. These areas in the buildings could be skylights, double glazing, sun blinds or walk ways. The current thesis aims to identify a new geometry to achieve this application. This chapter describes the characteristics of the Translucent Integrated Concentrated Photovoltaic (TICPV) module. In addition, the design method of the novel 3-D concentrator to be used in the TICPV module is described in detail.

3.2 TICPV system description

The idea of the proposed TICPV system is to integrate the novel 3-D static solar concentrator with solar cells between two glass plates. The main functions required of the TICPV modules are to:

- Allow the penetration of the daylight into the building
- Generate maximum electrical power from the transparent surface on the building
- Maintain the structure of the transparent façades.

The 3-D static solar concentrator to be used needs to integrate easily in to any double-glazed glass surface of a building. There is therefore a limitation on the size of the concentrators and their appearance so that they may integrate into transparent façades with minimum perturbation. The gap between two glass panels in any double glazing structure will be used to integrate the CPV systems to be designed. Any standard PV or CPV modules (non-BIPV) require a back plate to hold the solar cells, a glass cover and

a frame to hold everything together. For this design purpose, however, all the costs of these components are saved as they are replaced with the already existing glazing panels and frames incorporated in most building structures. The inner glass panel holds the solar cells and the connection between them, the outer glass panel of the glazing represents the cover of the CPV system and the window or the glazing façades frame holds all the components together. The solar concentrators are coupled with solar cells using encapsulation material, as described in Chapter 2 in section 2.6.1.3, which also has the role of protecting the solar cells. Figure 3.1 illustrates the TICPV system and how the different components are arranged and integrated. In view of the fact that the idea of the structure of the TICPV system as a whole has been established, the remaining issue to be resolved is the design of the actual geometry of the 3-D concentrator to be used in the system.

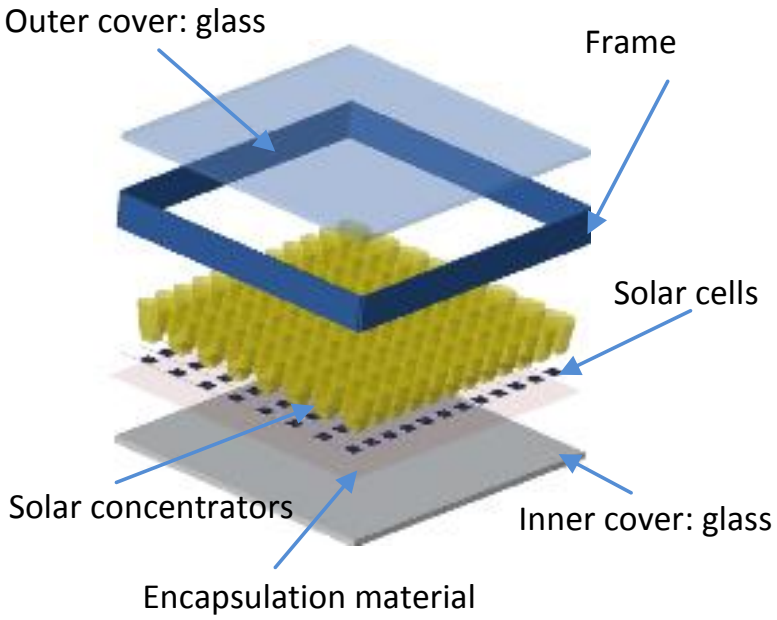

Figure 3.1: Appearance and components of the TICPV system

3.3 Analytical characterisation of the 3-D solar concentrator

In order to design and optimise a novel geometry of static solar concentrator, it is important to choose and get familiar with the different techniques needed for this purpose. The most important tool to be used for the optical design is the ray tracing technique. This will be discussed in the following sections.

3.3.1 Design of nonimaging concentrators

There are a variety of different methods that have been used in previous work in the design of nonimaging solar concentrators. The methods used to design 2-D solar concentrators can then serve to generate 3-D solar concentrators. The most well-known and simplest method followed to design nonimaging optics devices mainly used for solar concentrators is the edge-ray principle, also known as the method of strings [60]. The edge-ray principle is considered as the basis of nonimaging optics; it is based on the concentration of the incoming rays coming from the edge or boundaries of an infinite source on the edges or boundaries of the target or the receiver. The method has been explained and discussed in detail by Rabl [175], Ries and Rabl [176] and Winston et al. [55]. This method was first applied to the successful design of the 2-D CPC to be later generalised and applied to other 2-D concentrators with different sources and receiver geometries; it has been used to design different asymmetric CPCs, such as the work of Mallick et al. [48] who introduced an asymmetric CPC for building-integrated PV concentrators and Adsten et al. [177] who proposed a static asymmetric CPC profile for collection in high-latitude locations. The CPC with a tubular receiver was introduced by Baum and Gordon [65] and an asymmetric CPC with a tubular receiver was later introduced by Blanco et al. [178]. A simplified method for obtaining the sides of the 2-D concentrator using the edge-ray principle was developed and called "string method" or "gardener method" [156, 179]. The method consists of fixing the two ends of a string alternatively to the start point source and to the end point receiver; the path of a marker which is keeping the string stretched forms the sides of the 2-D concentrators designed. The use of the edge-ray principle remains limited to the design of certain concentrators and specifically to 2-D concentrators.

An enhancement of the edge-ray principal has been introduced and called "tailored edge-ray" used to tailor the reflector of the solar concentrator [180-182]. The enhanced method consists of tailoring reflecting surfaces of the concentrator to generate a desired uniform flux distribution of light. Ries and Winston [183] used the tailored edge-ray method to calculate the profile of the reflectors based on the desired acceptance angle and the illumination distribution on the concentrator receiver. In other publications, Gordon and Ries [184] and Gordon [185], a tailored edge-ray collector for secondary concentration in 2-D and 3-D parabolic primary systems or Fresnel primary systems has been designed and introduced by applying the string method. These methods rely a lot

on the assumption of perfect optics and they work well for designing 2-D concentrators but are very limited when coming to design 3-D concentrators.

Due to this limitation, researchers looked in to alternatives to edge-ray methods and its derivatives, especially since the most useful concentrator designs are obtained in 3-D. This need gave birth to another method that is used to design nonimaging concentrators; this method is called flow-line, also known as vector flux method [186]. It consists of representing the propagation of the light rays as if it were a fluid flow in six-dimensional space which is composed both of the position and momentum of elements of a fluid. The consideration of the propagation of the light rays in this way makes it possible to plot the flow lines in vector phase space from a given Lambertian source and therefore construct the reflecting geometry of the concentrator that conserves the geometric vector flux. The application of this method by Winston et al. [186], starting with a Lambertian radiator disc arriving to reflectors of a hyperboloid of revolution coincident with a set of flow lines, lead to an interesting new design of nonimaging solar concentrator considered as an ideal 3-D concentrator, illustrated in Figure 3.2.

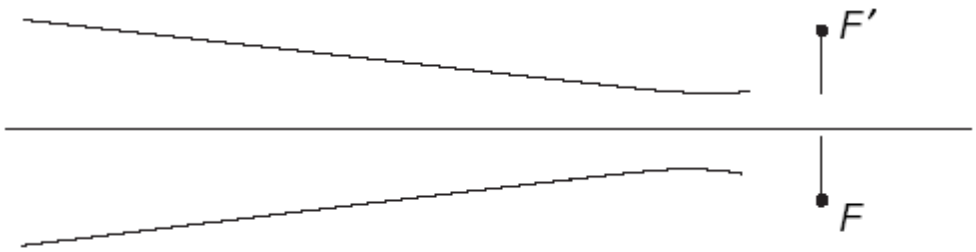

Figure 3.2: The truncated hyperboloid of evolution as a concentrator [55]

The flow-line method gave way to a new perspective of 3-D solar concentrator designs. The method, however, remains very complicated and limited only to geometries obtained by revolution, in the case of the 3-D designs. The important and interesting point to consider here is the emergence of the hyperbolic profile as providing the geometry for an ideal solar concentrator; it becomes apparent that this characteristic warrants further investigation as it has proved its ability in several research projects. Chen et al. [187] used a hyperbolic mirror as second stage concentrators to achieve a high concentration ratio of 5447× using a detector to minimise the concentrating errors. O'Gallagher and Winston [188] introduced a “trumpet” secondary concentrator with a

paraboloid dish primary concentrator; the hyperbolic shape of the trumpet was derived from the theory of the geometrical vector flux. The trumpet concentrator increased the geometric concentration ratio from 2200:1 for the primary concentrator alone to nearly 4800:1 with an efficiency of >96%. Gray [189] tested the optical performance of a hyperbolic concentrator as a second stage concentrator to find an advantage varying between 7% and 15% compared to a one stage concentrator. SolFocus[6] [190] have used the hyperbolic solar concentrator as second stage in one of their CPV systems with the aim of producing 250W peak in a single Generation 1 solar pane.

The methods presented above are the most important methods used to design the geometry of nonimaging concentrators. The design and optical performance, however, of a complex 3-D geometry (not obtained from revolution) cannot be determined analytically using these methods. An asymmetrical 3-D concentrator obtained from the intersection of two 2-D CPCs with different concentration ratios was designed by Basset et al. [191]. Detailed ray tracing simulation was needed in order to predict the optical performance due to the complexity of the 3-D geometry. The method was confirmed and used when studying the optical efficiency of the asymmetrical 3-D CPC.

3.3.2 New design of nonimaging concentrator

To date, all of the BICPV designs use 2-D concentrators. The current thesis proposes to take this investigation further and examine the use of a 3-D solar concentrator in BICPV. This is the first design of its kind as no similar designs have been used before in translucent BICPV modules. The design of the 3-D nonimaging concentrator will be based on its need to be integrated into transparent façades in buildings, forming a BICPV module. One of the novelties of this approach of designing a 3-D nonimaging concentrator is to combine different geometrical characteristics based on certain needs (translucent BICPV) or proven performance of specific geometric profiles. In this respect, regarding the use of the 3-D concentrator to be designed in translucent BICPV modules, a specific geometry of the entry aperture has to be considered in order to allow the penetration of the daylight into the building Secondly, with regard to the exit aperture, most of the 3-D CPV modules designed have a circular exit aperture as they have been obtained from the revolution of a 2-D geometry; this results in many losses of

[6] SolFocus was founded in 2005, is a leading supplier of Concentrator Photovoltaic (CPV) systems. http://www.solfocus.com/

the solar cell material when manufacturing the module. It needs to be borne in mind that solar cells are square or rectangular in shape and as such the current aim is to incorporate this factor into the new 3-D geometry design to make for a more economical design. Lastly, with regard to the geometrical profile, after having deliberated on the results of the trumpet concentrator discussed above, the adoption of the hyperbolic profile on the side of the concentrator is considered, as the optical performance is predicted to be elevated if using this profile compared to other profiles. Thus when basing the design on the needs it transpires that the 3-D aspect will not be obtained from the revolution of a 2-D profile, but instead will be built as a 3-D geometry without a revolutionary symmetry. The design of the proposed 3-D geometry, which is based on three main geometrical parameters is detailed below:

- The first parameter to consider is an elliptical entry aperture of the geometry in order to allow the control of natural light when the concentrators are arranged in a group as illustrated in Figure 3.3. The gap between the arranged elliptical entry areas of the concentrators allows for the semi-transparency of the glass façades or windows of the building. In addition, the elliptical entry is expected to maximise the acceptance angle of the geometry [192] allowing maximum collection of the light rays for different incident angles due to the length of its major axis.

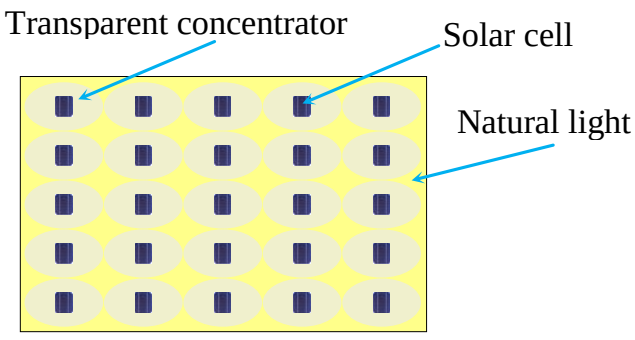

Figure 3.3: Disposition of elliptical entry aperture of solar concentrators.

- The second parameter is to have a square exit aperture, which diverges from the current conventional 3-D solar concentrators obtained from the revolution of a side branch. The circular exit aperture does not conform to the usual square and rectangular solar cell available; therefore, to reduce the wastage of solar cells and to save silicon material, the aim is to produce a geometry with a square exit

aperture. The exit aperture will be more convenient and efficient when it is square or rectangular in shape as this matches the shape of the solar cells available.

- The third and final parameter is to have a hyperbolic profile of the designed geometry – this will join the elliptical entry to the square exit. From here, the name was finalised: Square Elliptical Hyperboloid (SEH), patent pending [193]. Joining a round shape (ellipse or circle) to a shape with sharp angles (square) to create a smooth 3-D geometry is an innovative design that has never been examined before but the idea behind it shows many strengths. Previous research has shown that the hyperbolic profile in non-imaging concentrators shows an improved performance in acceptance angle and collecting the incoming rays [186-190]. It has been shown that the 3-D solar concentrator obtained from a hyperboloid of revolution has the ability of concentrating all the entering rays [194, 195]. These design features are illustrated below in Figure 3.4.

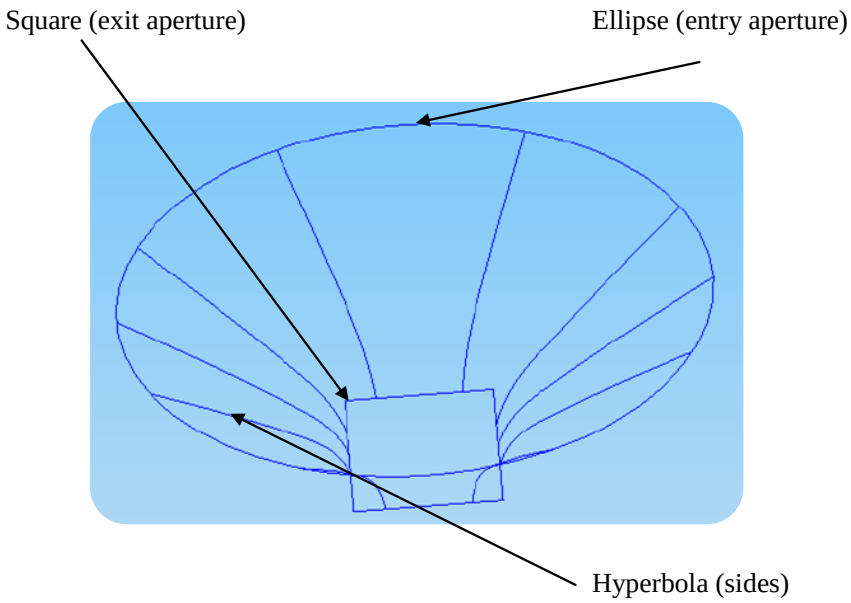

Figure 3.4: Geometrical structure of the designed 3-D concentrator

The 3-D SEH concentrator designed is built from transparent dielectric material in order to eliminate expensive manufacturing coating of reflective surfaces and to maintain the transparency of the windows where the solar concentrators will be fitted. The results from the study carried out in Chapter 2 highlighted the advantages of the refractive concentrator compared to the reflective concentrator, therefore this was taken into

consideration when developing the SEH. The light concentration will be assured by Total Internal Reflection (TIR) [196]. The use of TIR as a method to concentrate the light entering the concentrator on the exit aperture where the solar cells will be placed will provide a wide acceptance angle and a more compact concentrator compared to the reflective trough and Fresnel type concentrators. The dielectric material used to fill the hollow of the concentrator has a refractive index of >1 resulting in an increase of the theoretical concentration limit that can be increased by n^2 times for 3-D concentrators [197].

Dielectric-filled concentrators are generally heavy and expensive if they are used with large cells. However, small solar cells can be coupled with small and compact dielectric concentrators making them economical [198]. Furthermore, from the results obtained in Chapter 2, examining the optical performance of the CCPC, it was found that the acceptance angle of the refractive CCPC was wider than the acceptance angle of the reflective CCPC (Figure 2.43). A wider acceptance angle is highly desirable for static solar concentrators to enable maximum sunray collection during the day. This provides strong support for the use of the dielectric material in the new design. In addition, the transparent SEH concentrators can offer unique benefits to the internal ambience of the building by controlling the amount of light. Here becomes apparent the objective of this new geometry design, the SEH, for the use as a stationary solar concentrator in BICPV.

3.4 Development of the parametric equation

In the case of the current study, the geometry of the SEH concentrator is obtained by the construction of different hyperbolic branches connecting an elliptical and square entry and exit aperture respectively. The surfaces of the SEH concentrator are considered as parametric surfaces which are usually parameterised by two independent variables.

The surfaces of the SEH concentrator are impossible to represent by using implicit functions. Only a 3-D parametric equation is capable of representing the surfaces of the SEH concentrator as there is a link between the equations of each hyperbolic branch and the angle forming the plane where the hyperbola is placed. The development of a parametric equation is a complex task, generally reserved to mathematicians; it needs specialised knowledge and time. The acquisition of the 3-D parametric equation, however, is an essential requirement for the study of the optical performance of the SEH concentrator. Only with the 3-D parametric equation, can the geometry of the SEH concentrator be drawn using the CAD software, and only with the CAD drawing can the

optical study be carried out. A simplified method has been developed for the purpose of this thesis in order to determine the 3-D parametric equation. This method is described in detail in the following section.

3.4.1 Methodology for the development of 3-D parametric equation

The development of the 3-D parametric equation begins by determining the different parameters of the SEH geometry to be studied. The geometry of the SEH concentrator has different dimensions detailed as follows and illustrated in Figure 3.5:

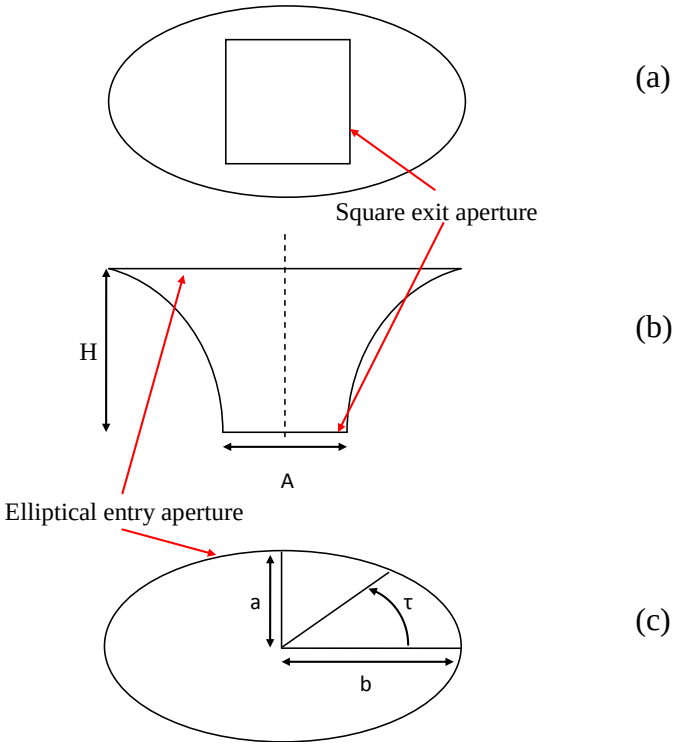

Figure 3.5: Dimensions of the SEH concentrator:
(a) underside view, (b) side view and (c) top view

a: the minor axis of the elliptical entry aperture

b: the major axis of the elliptical entry aperture

H: the height of the SEH concentrator

A: the sides of the square exit aperture

τ: the angles between different planes and the major axis b

Figure 3.6 shows that there are two symmetries in the SEH geometry. The first symmetry is on the *x*, *z* plane and the second symmetry is on the *y*, *z* plane. This results in having four identical sections of the SEH geometry. It will be enough therefore, from the point of view of simplification, to develop the 3-D parametric equation for one quadrant and reproduce the three remaining quadrants by symmetry. The 3-D parametric equation will be developed for quadrant one as illustrated in Figure 3.6. The choice is based totally on simplicity as the *x*, *y* coordinates of quadrant one of the SEH are positives; otherwise the 3-D parametric equation could be developed for any of the quadrants.

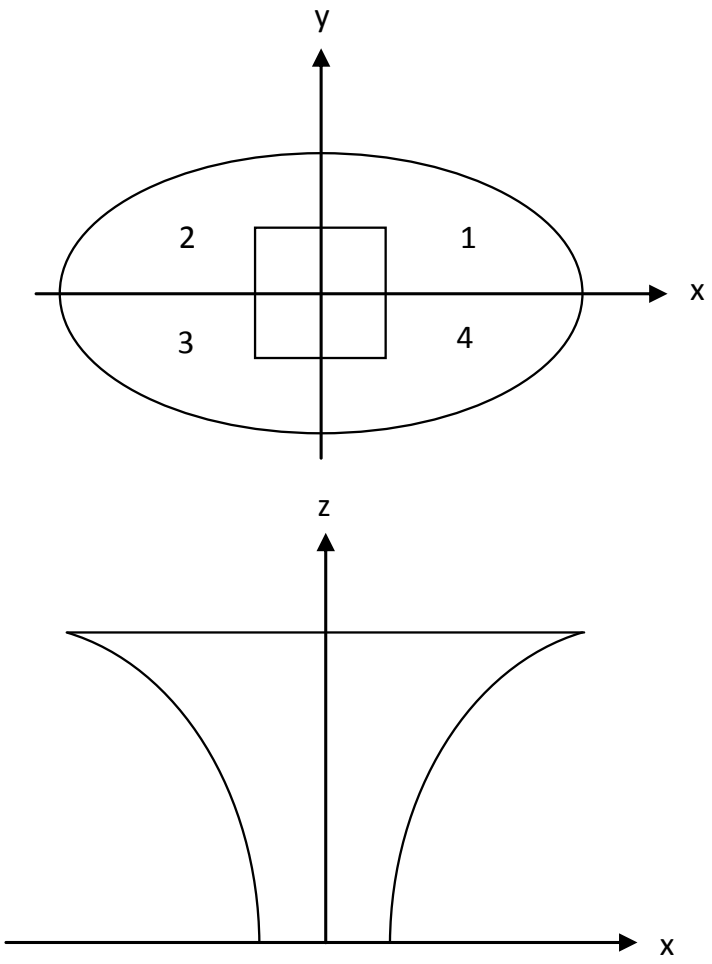

Figure 3.6: Axes and symmetry of the SEH concentrator

In quadrant one, there are two different situations to take into consideration:

- The hyperbolic branches connect the right side of the square exit aperture (blue line in Figure 3.7); they all start at $x = A/2$ for different y varying between 0 and

A/2. The hyperbolic branches are located in planes perpendicular to the *x*, *y* plane making an angle τ_1 with the *x*, *z* plane. τ_1 is varying from 0 to π/4.

- The hyperbolic branches connect the top side of the exit aperture (red line in Figure 3.7); they all start at different *x* varying between 0 and *A*/2 for *y*=*A*/2. The hyperbolic branches are located in planes perpendicular to the *x*, *y* plane making an angle τ_2 with the *x*, *z* plane. τ_2 is varying from π/4 to π/2.

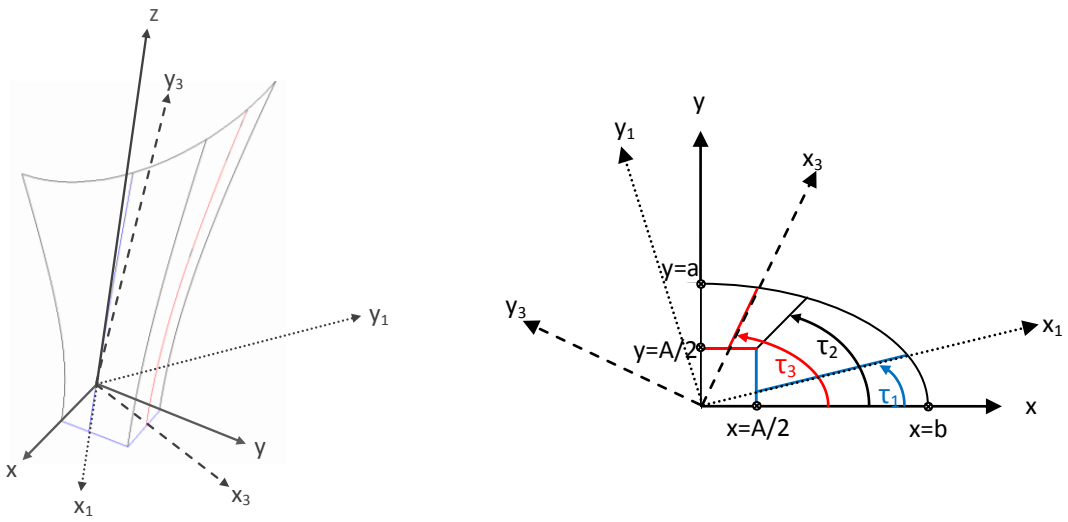

(a) (b)

Figure 3.7: Position of hyperbolic branches in section 1 of the SEH geometry: (a) isometric drawing (b) top view

The radius of the elliptical entry aperture *r* can be calculated in two different ways. The radius *r* can be written as a function of the angle τ as shown in equation (3.1):

$$r(\tau) = \frac{a \times b}{\sqrt{(b \times cos\,\tau)^2 + (a \times sin\,\tau)^2}} \tag{3.1}$$

At the same time, referring to Figure 3.7, the radius *r* can be formulated as a function of the two segments *SQ* and *HYP* as shown in equation (3.2):

$$r = SQ + HYP \tag{3.2}$$

The hyperbolic branches forming the side surfaces of the SEH geometry are expressed with the following equation:

$$\frac{{x_1}^2}{j^2} - \frac{z^2}{i^2} = 1 \tag{3.3}$$

In the coordinate system x_1, z, the hyperbolic branch *HYP* is represented with equation (3.3) where $j=SQ$ as illustrated in Figure 3.8.

At the top end of the hyperbolic branch, $x=r$ and $z=H$. Including these two conditions in equation (3.3) we find the equation of the constant i as follows:

$$i = \frac{H \times SQ}{\sqrt{r^2 + SQ^2}} \tag{3.4}$$

The segment *SQ* as a function of the angle τ and *A* can be written as follows in the equation:

$$SQ = \frac{A}{2 \times \cos\tau} \tag{3.5}$$

The coordinates of the hyperbolic branch in the plane x_1, z are summarised in the following equation after incorporating the equations (3.1), (3.4) and (3.5) in equation (3.3):

$$x_1 = \frac{A}{2\times\cos\tau_1} \times \sqrt{1 + \frac{z^2 \times \left(\left(\frac{a\times b}{\sqrt{(b\times\cos\tau_1)^2 + (a\times\sin\tau_1)^2}} \right)^2 + \frac{A^2}{(2\times\cos\tau_1)^2} \right) \times 2\times\cos\tau_1}{A\times H}} \tag{3.6}$$

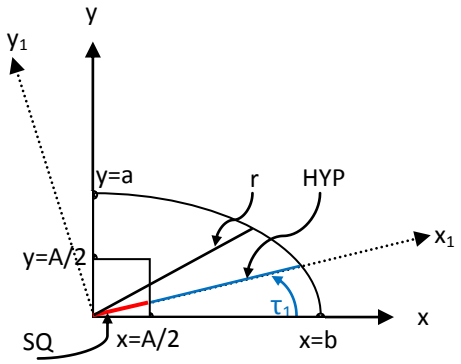

Figure 3.8: Parameters of the hyperbolic branch in different coordinates.

The coordinates of the parabolic branches are determined in the coordinates of the plane x_1, z where they are included. Now these coordinates are projected in the plane x, y using the coordinate system x, y, z. The projection of the x_1, z coordinates are projected using the angle τ_1. On the axis x the projection is achieved by the multiplication with $cos(\tau_1)$ and on the axis y the projection is achieved by the multiplication with $sin(\tau_1)$.

The same procedure used above to determine equation (3.6) and its projection in the x, y, z coordinate system for the case where the hyperbolic branches are connected with the right side of the square exit aperture is followed to determine equation (3.8) and its projection in the x, y, z coordinate system for the case where the hyperbolic branches are connected with the top side of the square exit aperture. The difference between the two cases is mainly due to the fact that the equation of the segment SQ changes to become:

$$SQ = \frac{A}{2 \times \sin \tau_2} \tag{3.7}$$

$$x_1 = \frac{A}{2 \times \sin \tau_2} \times \sqrt{1 + \frac{z^2 \times \left(\left(\frac{a \times b}{\sqrt{(b \times \cos \tau_1)^2 + (a \times \sin \tau_1)^2}} \right)^2 + \frac{A^2}{(2 \times \sin \tau_2)^2} \right) \times 2 \times \sin \tau_2}{A \times H}} \tag{3.8}$$

3.4.2 3-D parametric equation of the SEH geometry

After developing the equations of the SEH geometry in the desirable coordinate system and simplifying them, the final 3-D parametric equation obtained can be written as follows:

$$\tau \in \frac{7\pi}{4} + n\pi, \frac{\pi}{4} + n\pi \quad n = 0,1; K = \tan \tau \quad ; M = \sin \tau \; ; N = \cos \tau$$
$$t \in 0, H$$
$$\tau \in \frac{\pi}{4} + n\pi, \frac{3\pi}{4} + n\pi \quad n = 0,1; \; K = \frac{1}{\tan \tau} \; ; M = \cos \tau \; ; N = \sin \tau$$

$$\begin{cases} x = \frac{A}{2} \times \cos \tau \times \left(C + \frac{\sqrt{(H \times A)^2 + (4 \times t^2 \times D) - (A \times t)^2}}{H \times A} \right) \\ y = x \times \tan \tau \\ z = t \end{cases} \tag{3.9}$$

Where:

$$C = \sqrt{1 + k^2}\_1 \tag{3.10}$$

$$D = \left(\sqrt{\left(F + \left(E - \frac{A \times K}{2} \right)^2 \right)} + \frac{A}{2} \right)^2 \tag{3.11}$$

$$E = \frac{a \times b \times |N|}{\sqrt{(b \times \cos\tau)^2 + (a \times sin\theta)^2}} \tag{3.12}$$

$$F = \left(\frac{a \times b \times |N|}{\sqrt{(b \times \cos\tau)^2 + (a \times sin\tau)^2}} - \frac{A}{2} \right)^2 \tag{3.13}$$

K, *M* and *N* are the terms which differ in the two equations for the two different cases (variation of τ) of the hyperbolic branches detailed.

Equation (3.9) is the 3-D parametric equation of the SEH concentrator geometry. It is function of two variable parameters:

- The rotational angle *τ*, it varies from 0 to 2π. For *τ=0*, the hyperbolic branch is the widest and for *τ*=π/2, the hyperbola branch is the narrowest.
- The height *t*, it varies from *0* to *H*. For *t=0*, the transversal section is a square and for *t=H*, the transversal section of the SEH is an ellipse.

And four constant parameters:

- The major axis b
- The minor axis a
- The width of the square exit aperture A
- The height of the SEH concentrator H

The geometrical concentration ratio C_g of the SEH concentrator is defined by a, b and A:

$$C_{g\_SEH} = \frac{a \times b \times \pi}{A^2} \tag{3.14}$$

3.4.3 Validation of the parametric equation

The final step in the development of the 3-D parametric equation is the validation. A MATLAB code is written using equation (3.9) to generate the envelope surface of the SEH geometry. This step is important in order to be able to carry out a visual check of the geometrical characteristics of the designed SEH. The MATALB code is launched for different dimensions and geometrical concentrations of the SEH. As input, it is enough to enter a, b, H and A to generate the desired SEH geometry. One example of the generated geometry of the SEH concentrator is illustrated in (3.9). It can be observed that the geometry does not show any discontinuity despite the fact that the geometry of the SEH has an entry and an exit aperture shape not belonging to the same family. The drawings obtained via MATLAB, using the parametric equation, portray accurately the SEH geometry as envisaged in the conceptual stages of its design at the beginning of this chapter. Moving from a height *H* to a height zero, the transversal section of the SEH geometry transforms from a rounded shape (ellipse or circle) to a square belonging to the quadrilateral shapes group with four sides and four sharp angles hence validating the parametric equation developed.

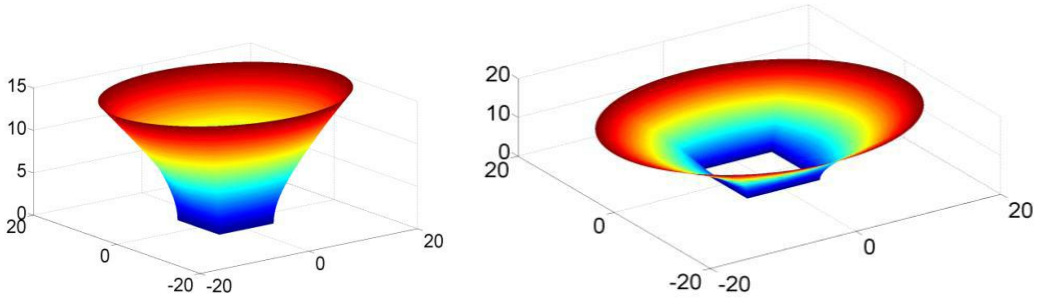

Figure 3.9: Different 3-D views of the SEH illustrated using MATLAB: H=15mm, A=10mm, b=20mm and a=15mm.

The x, y, z coordinates are calculated for different rotational angles τ varying from 0 to 2π. The generated coordinates are illustrated via MATLAB graphics using the "surface" function. The different colours in (3.9) are only for illustration purposes to clarify the geometrical appearance of the SEH; they do not have any scientific significance.

3.5 Drawing of the SEH using CAD software

The CAD software used in the upcoming optical study is SolidWorks. The main challenge in drawing the SEH geometry using CAD software is the function to be used. There are a few techniques available that are common with all of the CAD software to draw 3-D geometries which can be classified as follows:

- Extrude: this method consists of extruding a 2-D shape along one direction to create a 3-D geometry. It can also be used to extrude cut on existing 3-D geometry to create a composed geometry. It is impossible to use this method to draw the SEH geometry because it has two different shapes to start and end with: the ellipse and the square.
- Revolved: this consists of revolving a 2-D shape around an axis of revolution. The obtained 3-D geometry shape would have a circular symmetry, which is not the case for the SEH geometry. This the most common feature used to create 3-D geometry for solar concentrators such as the parabolic dish, the point focus Fresnel lenses, and the circular section CPC.
- Swept: this method is similar to the Extrude function, the difference is that the Swept is an extrusion following a curved direction and not in a straight line direction as is the case for the Extrude. Here the obtained 3-D geometry has the same section profile along the swept direction curve. This is not the case for the SEH geometry.
- Lofted: this is a very useful feature used to draw a complex 3-D geometry with a different area of the entry aperture and the exit aperture as is the case for the SEH geometry. This feature works well with the same profile of entry and exit aperture, like starting as a square shape (or ellipse) to finish with a larger square (or ellipse) shape. In addition, the lofted feature allows one to generate a complex geometry in a single feature. It does this by interpolating surfaces between various cross-sections of a model. These cross-sections can be sketches, faces, or edges. It would be possible to draw the SEH geometry using this feature but for visual purposes only; there would be two majors problems faced. The first problem is that it would be difficult to control the loft sufficiently to produce the SEH geometry with the desired precision; for the generated 3-D geometry to be perfect using this feature, an infinite number of cross-section coordinates to be connected from the entry to the exit aperture would need to be calculated and inserted. This creates the second problem of time, where-by the

creation of these cross-section coordinates by drawing them separately would be a hugely time consuming task for a geometry optimisation study requiring the creation of a large number of SEH geometries with different profiles.

After considering the usual features used in CAD software to generate a 3-D geometry, it becomes clear that they are not valid to generate the SEH geometry. A separate distinctive method is needed to achieve this task with maximum precision in order to preserve the charteristics of the SEH geometry. After several trials using the common methods to generate the 3-D SEH geometry, the idea of using the same procedure used to build complex 3-D models like creating anatomical objects (such as prosthetics) for medical purposes occurred. This complex but effective method can be achieved in SolidWorks by activating the SolidWorks premium add-in "ScanTo3D " as illustrated in Figure 3.10.

ScanTo3D is an indispensable tool for any designer who needs to capture physical concept models, existing anatomical objects and use these scanned renditions to build SolidWorks models. With ScanTo3D, you can easily convert extremely organic shapes to solid models [199]. ScanTo3D is a SolidWorks Add-in, working on a point cloud or mesh; it provides mesh processing and automatic surfacing. SolidWorks made possible to take a raw point cloud or mesh data directly from a 3-D scanner and use the data to create a SolidWorks model from it. Ye et al. have demonstrated how useful ScanTo3D is in Reverse Innovative Design (RID) which allows an engineering illustration of any innovative consumer product design [200].

From here came the idea of generating the SEH geometry using ScanTo3D from cloud points where the coordinates have to be calculated. A very fine distance between the cloud points has been chosen of 1/1000mm. The coordinates of the cloud point forming the SEH geometry are calculated using the developed equation (3.9) via MATLAB code and saved in files with an extension format ".xyz" to be read by SolidWorks. The cloud point file is opened by SolidWorks to show the SEH geometry built from very close points as illustrated in Figure 3.11. These points are first converted to mesh using "mesh preparation wizard" and then converted to surface. Once the surface forming the envelope of the SEH geometry is obtained, a 3-D solid SEH body is built from it (Figure 3.12).

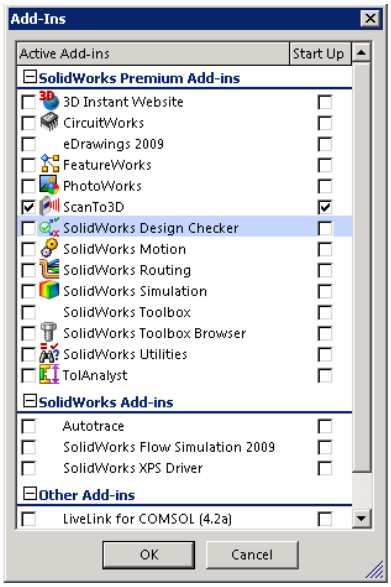

Figure 3.10: Scan To 3D Add-ins within SolidWorks.

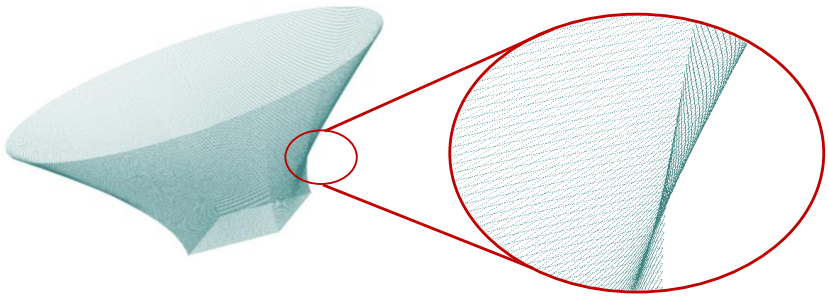

Figure 3.11: Cloud points of the SEH geometry imported by SolidWorks

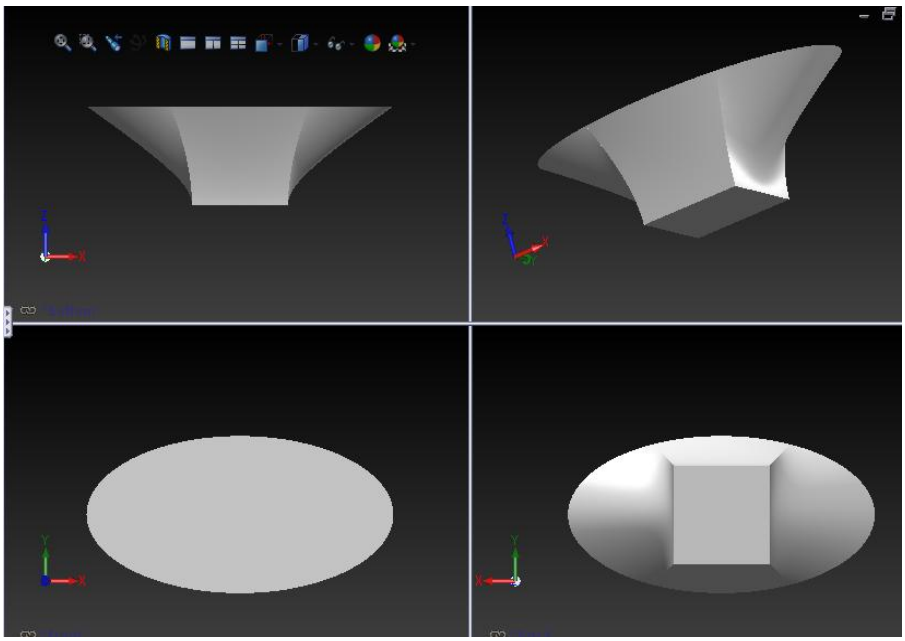

Figure 3.12: Final views of the SEH concentrator built using SolidWorks

3.6 Conclusion

The design of the nonimaging concentrator to be used in the BICPV system for transparent façades (TICPV) has been introduced. The main component of the TICPV module that allows for its translucency is the 3-D static concentrator coined the SEH. The geometry of the SEH concentrator is obtained from the combination of different geometrical characteristics in order to allow for day light penetration into the building and to achieve maximum optical performance. In a main embodiment of the geometry of the SEH concentrator the exit aperture is square and the entry aperture is elliptical. Joining a round shape (ellipse or circle) to a shape with sharp angles (square) to create a smooth 3-D geometry is an innovative configuration. In order to achieve this novel shape, it was necessary to develop a specific 3-D parametric equation. The equation has served to represent the SEH using CAD software; this is a vital step which will enable the optical performance of the different SEH profiles to be investigated. The complexity of the 3-D geometry of the SEH concentrator has required the use of special tools and options available in SolidWorks used mainly for drawing anatomical objects.

Now, after having mastered the employment of the 3-D parametric equation with SolidWorks software via MATLAB, any profile of the SEH concentrator can be created. From here, it is possible to begin the optimisation process. The following chapter is devoted to the optical characterisation of the SEH concentrator, with the objective of

selecting the geometrical profile of the SEH concentrator with the best optical performance.

Chapter 4: Optical analysis and optimisation of the SEH concentrator

This chapter is dedicated to the optical characterisation of the SEH concentrator. A comprehensive optical simulation study using ray tracing technique is carried out on various different SEH concentrators with different geometrical concentration and dimension ratios. The optimisation process consists of a series of methodical steps investigating various aspects of the SEH geometry; based on the results, the chapter concludes with a summary of the properties of the optimised SEH concentrators.

4.1 Introduction

The geometrical appearance and composition of the SEH concentrator has been discussed and determined in the previous chapter. The dimensions and geometric proportions of the SEH concentrator, however, are still unknown; they need to be ascertained in order to complete the design and geometrical characterisation of the SEH concentrator. The dimensions and geometric proportions of the SEH are specified based on the optical performance of the SEH. An optimisation method is established in this chapter in order to find the optimum dimensions of the SEH concentrator which achieves the best optical performance; the optimisation method is based on optical simulation via a ray tracing technique.

4.2 Ray tracing technique

As discussed in the previous chapter, the geometry of the SEH concentrator has been designed based on the amalgamation of different geometric designs of the entry aperture, exit aperture and the side surface. After careful consideration of both the literature and software options, it has been established that only a ray tracing technique can be used to find the optical performance of such a complex SEH geometry. The ray tracing technique is employed to generate the path of the reflected rays on the sides of the SEH concentrator and to generate the optical flux distribution on the square exit aperture of the SEH.

Ray tracing is a known technique used to design optical devices such as lenses and reflectors used in different applications such as cameras and microscopes. The use of ray tracing to perform calculations dates back to early times before the advent of the computer. The calculations were performed using hand drawings, trigonometry and

logarithmic tables. The ray tracing calculations are now performed using algorithms or commercial software. The principles of the early used algorithms are detailed by Spencer and Murty's fundamental paper [201].

The ray tracing technique was the support for designing and enhancing several solar concentrators.

In a recent study, Zheng et al. [202] employed ray tracing to study the effects of the incident angle of the light ray on the efficiency and concentration ability of a new kind of trough solar collector. It was found that the new proposed solar concentrator collected more light compared to a traditional trough paraboloid system with a half acceptance angle equal to three degrees. The ray tracing simulation was established by drawing the concentrator system using the commercial package UG[7] and exporting it to an optical software (not specified). The light beam used in the ray tracing simulation has a fixed wavelength of 550nm. This assumption can work with reflective concentrators; it cannot, however, be considered for refractive concentrators as the absorbance and refractive index of the refractive material vary as a function of the wavelength.

Colina-Marquez et al. [203] developed a mathematical model based on ray tracing in order to simulate the reflection of direct solar radiation on a CPC. One of the results of the study is the energy distribution at the absorber; it was found that it depends on the surface reflectivity – it is more uniform when the reflective surfaces of the CPC have better reflectivity. The model developed was a 2-D model to simulate the ray trace of the incident rays from the sun, but the sun rays vary in 3-D during the day and do not stay in one plane. In the current study, the consideration of a 3-D model is thought to be necessary in order to provide a more comprehensive set of results.

Groulx and Sponagle [204] presented a ray tracing analysis which was conducted on a 2-stage solar concentrator made of two parabolic mirrors. The ray tracing simulation was conducted using MATLAB code. The effects of the various distances of the concentrator system were studied, mainly the secondary mirror's focal length and the distance between the secondary mirror and the target (receiver), in addition to the effects of the misalignment of the concentrator with the sun. It was found that the solar concentrator system is very sensitive to misalignments with respect to the sun and that a

[7] NX, also known as NX Unigraphics or usually just U-G, is an advanced CAD/CAM/CAE software package developed by Siemens PLM Software.
http://www.plm.automation.siemens.com/en_gb/products/nx/

misalignment of ±0.2º would bring the concentration efficiency of the concentrator to zero. The developed ray tracing model works well for reflective solar concentrators, however it cannot be applied to refractive solar concentrators made out of dielectric material as the equations to solve are different; in addition the material properties and the length of the concentrated rays have to be taken into consideration.

Pei et al. [205] used the ray tracing technique via LightTools [206] optic software to investigate a truncated solid dielectric 2-D CPC. The analysis showed that part of the incoming rays do not undergo total internal reflection, even within the half acceptance angle of the 2-D CPC. Despite the fact that the optical performance of the 2-D CPC is well known and studied as well as its geometry, only the ray tracing analysis was able to show the losses in the dielectric 2-D CPC working with refraction. The authors proposed using mirror coating on the areas of the 2-D CPC surface where there were found to be losses; this resulted in an increase of 13.5% in the optical concentration ratio of the 2-D CPC compared to the same concentrator without the coating. The authors proved the necessity of applying a mirror coating on the side of a truncated solid dielectric 2-D CPC; this could not have been done without the employment of the ray tracing analysis.

In the current study, the software that is used is OptisWorks, a powerful commercial software widely used by architecture, lighting and car industries, to optimise, investigate and study the optical performance of the novel design of the static 3-D SEH concentrator. Since the SEH is a 3-D refractive concentrator, OptisWorks offers the solution for the optical study using the ray tracing technique taking into consideration the different physical characteristics varying from the nature of the source of light to properties of the dielectric material.

The main optical characteristic to be investigated using the ray tracing technique via OptisWorks software is the optical efficiency ($Eff_{Optical}$) of the SEH concentrator. The second most important optical characteristic to be studied and analysed is the optical flux distribution on the exit aperture of the SEH concentrator, also known as the receiver of the SEH. The term “optical flux distribution” has been referred to with several different appellations. For clarification, Chen and Hopkins [207] used the expression “flux densities distribution” when they used the ray tracing technique to study the trough funnel concentrator optics, Colina-Marquez et al. [203] used the expression “energy distribution” in their ray tracing study on the CPC. Another expression “concentrated spot distribution” was used by Wei et al. [208] when they

employed the ray tracing technique via written code for the optical characterisation of a beam-down solar concentrating system, using the optical software ZEMAX. Leviton and Leitch [209] used the term "irradiance distributions" when using ray trace analysis on throat-to-throat compound parabolic concentrators; the same term was used by Nishioka [210, 211]) when using the ray tracing technique in designing a solar concentrator using the optical software ZEMAX. Negi et al. [212] used a different expression "local concentration ratio distribution" in their study of a cylindrical parabolic trough and that of a polygonal trough. Daly [213] used the expression "flux distributions" in his study of parabolic and circular cylinder solar concentrators.

All six expressions used in these different studies using ray tracing simulation refer to the same meaning, which is the distribution of intensity of light on the receiver of the solar concentrator. In the current study another term, "optical flux distribution", will be used that is thought to be more descriptive to the results obtained on the exit aperture of the SEH concentrator [152].

4.3 Execution of the optical model

The optical simulation using the ray tracing technique via OptisWorks is carried out on different SEHs with different geometrical concentration and dimension ratios.

OptisWorks is a software integrated in the SolidWorks software from Dassault Systems[8] offering a significant advantage of drawing and analysing optical devices within the same software. In addition to the various tools and options within OptisWorks, the optical design and analysis of optical devices benefit from the powerful option and tools within SolidWorks that save time and simplify the optimisation process. From these tools it is worth mentioning "configuration" that can save a considerable amount of time in simulation as it allows the launch of ray tracing simulations for different geometric and optical conditions successively and saves the results in different folders. The optical modelling commences with the development of the 3-D model using ray tracing via OptisWorks. The different steps of the modelling process will be discussed in detail in the following sections.

4.3.1 Meshing of the SEH 3-D geometry

For any simulation of a physical phenomena using geometric models, a subdivision of these models into small pieces (surfaces for 2-D and portions for 3-D) is needed. These

[8] Dassault Systems is a world-leading company 3-D design software, 3-D Digital Mock-up and PLM (Product Lifecycle Management) solutions.

small simple shapes called elements are connected at common points called nodes; this action is referred to as meshing. Ray tracing simulation also requires a meshing of the optical device to be studied, which in this case is the SEH concentrator. The accuracy of the solution of the ray tracing simulation depends on the quality of the mesh to be applied on the SEH geometry. Generally, the finer the mesh the better is the accuracy and the longer is the simulation. OptisWorks offers two different options of meshing via the tab "Tessellation" that allows defining the geometry precision for the calculation in the ray tracing simulation. The two different options of meshing are "Deflection" and "Max facet width". They both use polygon mesh which is the most used in ray tracing simulation [214, 215] because of its mathematical simplicity.

The meshing of the first option "Deflection" is illustrated in Figure 4.1; the obtained mesh using the deflection method gives a large surface mesh. These surfaces, however, do not provide a uniform meshing due to the variation of their sizes between the flat entry and exit aperture surfaces and the hyperbolic surfaces on the side of the SEH geometry.

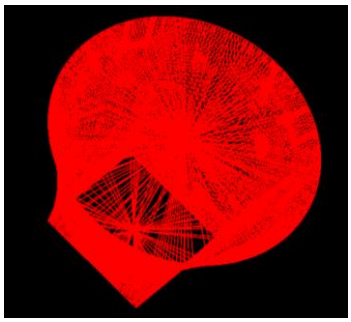

Figure 4.1: SEH mesh using deflection method

The second option is the "Max facet width method". The obtained meshes are small triangular faces with the same size for the entire surface of the SEH geometry making this method more suitable and able to mesh the precise details of the hyperbolic profile of the SEH uniformly as can be seen in Figure 4.2. It was found that for a Max facet width equal to 0.5 mm, the same results were found when carrying out preliminarily ray tracing simulations for a Max facet width less than 0.5mm. This indicates that 0.5mm is just as sufficient as 0.1mm to produce the mesh.

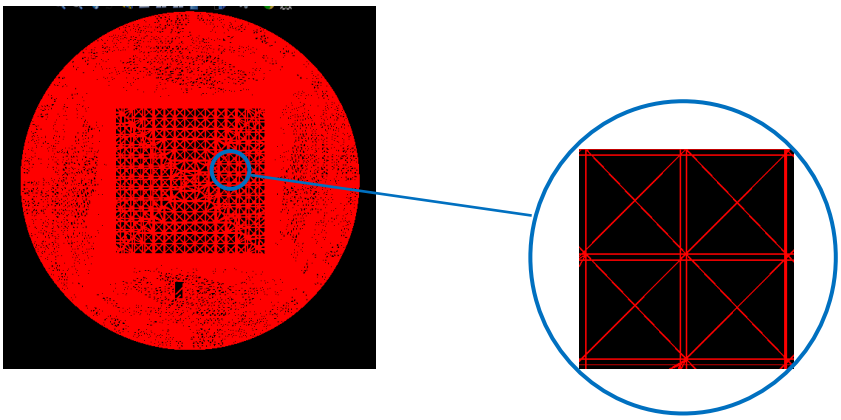

Figure 4.2: SEH mesh using the Max facet width method

The SEH geometry is tessellated using the "Max Facet width" method with a Max facet width equal to 0.5 mm in order to minimise the time of simulation (compared to 0.1mm) yet still obtain maximum precision of the ray tracing simulation solution.

4.3.2 Material of the SEH

In the simulation, the SEH concentrator is built from clear acrylic polymethylmethacrylate (PMMA) material, details of which are found in Chapter 2 section 2.8.1.

4.3.3 Light source

A source of light is applied at different incident angles on the elliptical entry aperture of the SEH. The source is set up to generate 10 Mega rays at a chosen radiation of 1000 W/m^2. This corresponds to 10 000 rays per 1mm^2 resulting in a high resolution and precision in the ray tracing simulation. The light source is the light of the xenon arc lamp fitted in the solar simulator that emits a 5800K blackbody-like spectrum [216].

The intensity of the light rays generated by the ray source is considered as Lambertian with a limited half angle equal to 0º. This means that all the rays generated by the light source are parallel and perpendicular to the surface of the light source. "A lambertian surface reflects or emits equal (isotropic) luminance in every direction" [217], by considering the half angle equal to 0º, all the rays are emitted in one direction making an angle 0º to the normal of the surface of the light source. The light source is a flat surface drawn with SolidWorks and assigned the above characteristics. The assumption made for the light source helps to investigate the optical performance and behaviour of the SEH concentrator separately for each angle of incidence of the light rays.

4.3.4 Illuminance detector

A 2-D illuminance detector is placed at the exit aperture of the SEH as illustrated in Figure 4.3; this detector measures the optical flux and energy of the concentrated rays by the SEH on the exit aperture. The results of the 2-D detector are represented in a 2-D map or 3-D map distribution in W/m^2. A similar 2-D detector is placed at the entry aperture of the SEH concentrator to measure the energy of the light rays incident on the SEH concentrator.

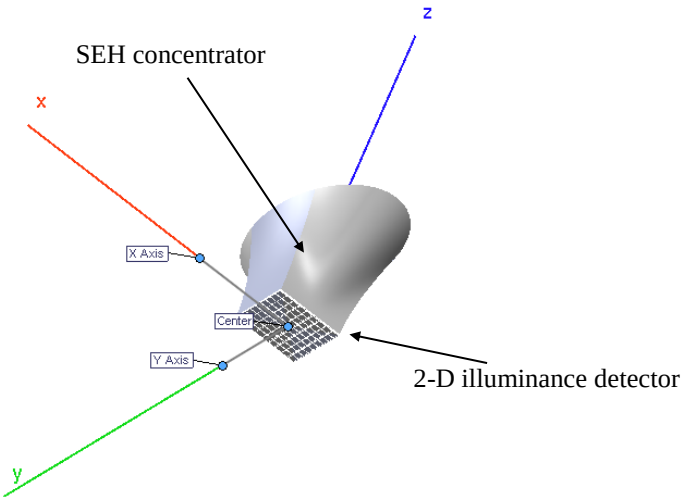

Figure 4.3: Illuminance detector placed at the exit aperture of the SEH

The optical efficiency of the SEH ($Eff_{optical}$) is calculated according to equation (4.1):

$$\text{Eff}_{\text{optical}} = \frac{\varphi_{\text{exit aperture}}}{\varphi_{\text{entry aperture}}} \times 100 \quad (4.1)$$

Where $\varphi_{\text{entry aperture}}$ is the flux in W measured by the detector at the entry aperture and $\varphi_{\text{exit aperture}}$ is the flux in W measured by the detector at the exit aperture.

4.3.5 Boundary conditions

The ray tracing simulation is carried out on a refractive SEH concentrator where the light rays move from one medium to another with different refractive indexes, as discussed in Chapter 2 section 2.8.1. The incident light rays on the SEH concentrator have to move from the air with a refractive index of 1 to the PMMA material that has an average refractive index equal to 1.5. The inside material of the SEH concentrator is set to be PMMA and the external material is set to be air on all of the side surfaces of the

SEH concentrator apart from the square exit aperture where the external material is set to be PMMA. The reason for this is due to a finding that came about after carrying out a visual check on the rays – it was found that many of the rays during the simulation reaching the exit aperture were being reflected back into the SEH (TIR). In order to ensure that the light rays pass through the exit aperture as should and avoid the TIR on that area, an additional part of PMMA material was added at the exit aperture for the purpose of the simulation only. Figure 4.4(a) shows that the light rays pass through the exit aperture with the added part of PMMA, therefore they will be measured by the 2-D detector; on the contrary, in Figure 4.4(b), without the additional part of PMMA, some of the light rays reflect back inside (TIR) the SEH concentrator at the exit aperture and therefore these rays, which would ordinarily pass through the exit aperture, will be not measured with the 2-D detector. On a normal functioning SEH concentrator (i.e. in an experimental setup), all the light rays that reach the square exit aperture will reach the solar cells placed below coupled with the SEH concentrator without the need for the added part of PMMA. This finding highlights the importance of the visual check of the rays using ray trace.

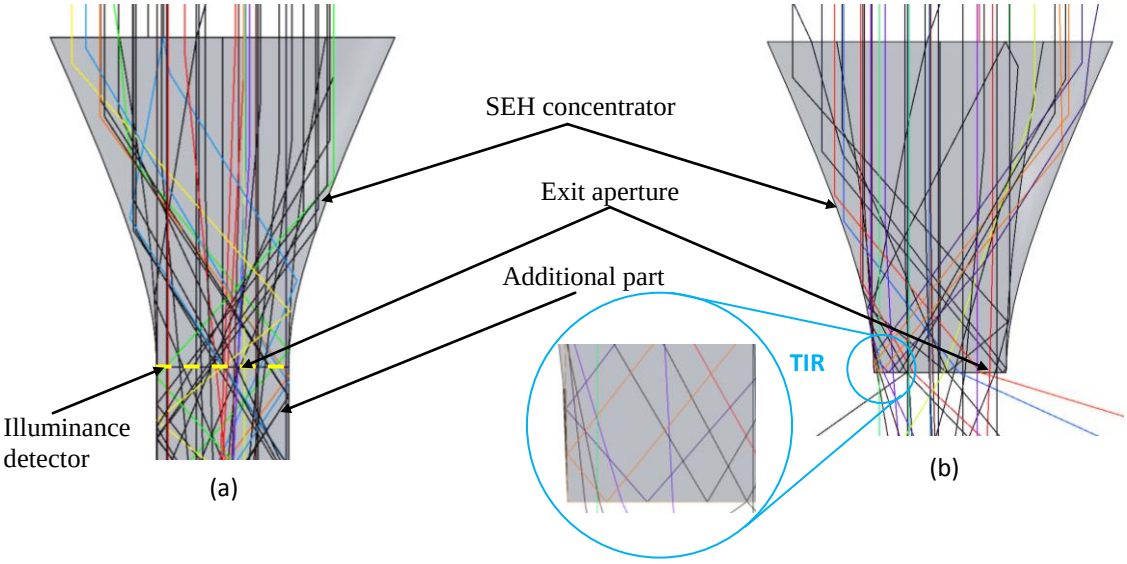

Figure 4.4: Avoiding TIR on the exit aperture. (a) with additional PMMA part, (b) without additional PMMA part

4.3.6 Types of simulations

There are two different types of ray tracing simulation that can be run with OptisWorks. The first is a visual simulation; it enables a visual check on the paths of the concentrated or escaped light rays from the SEH concentrator. All the incident light rays are refracted

into the SEH concentrator; they can face one of three situations as illustrated in Figure 4.5:

- Reflect one time or more on the sides of the SEH concentrator following the law of TIR before escaping from the elliptical entry aperture
- Escape from the sides of the SEH concentrator after one or more reflections
- Reach the exit aperture of the SEH concentrator after refraction and TIR or after refraction only.

The visual simulation of the ray paths is the only way to check that the incident light rays are refracting and reflecting as expected in a SEH concentrator.

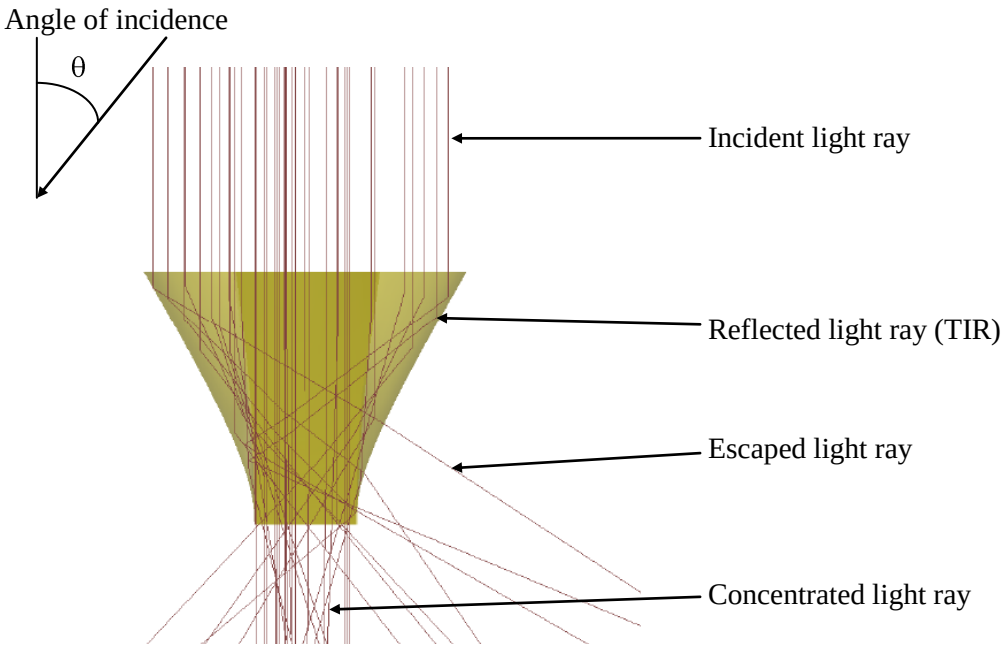

Figure 4.5: Concentrated rays paths. Illustration using SolidWorks & OptisWorks

The second type of simulation is called “direct simulation”. This involves running the actual simulation in OptisWorks; it takes into consideration all of the optical characteristics of the SEH concentrator and the light source in order to obtain both the total energy and the optical flux distribution at the entry and exit aperture of the SEH concentrator. The optical efficiency of the SEH concentrator for the designed conditions is calculated from the results of the direct simulation.

4.3.7 Flow chart of the ray tracing simulation

The ray tracing optical model built using OptisWorks software is followed for all of the SEH concentrator profiles studied in this chapter. It can also be applied to any dielectric

nonimaging concentrator. The optical model is summarised below in the flow chart represented in Figure 4.6.

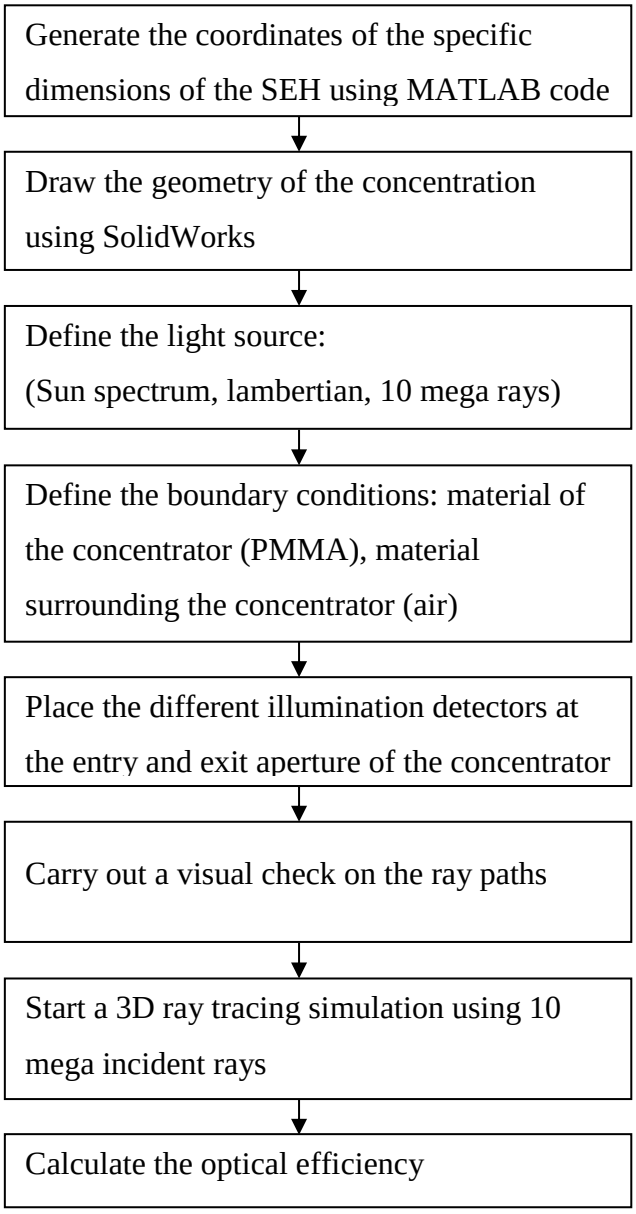

Figure 4.6: Ray tracing simulation process flow chart for the SEH concentrator

4.4 Optimisation of the SEH profile

The ray tracing simulation will be carried out for different SEH concentrators with:

- Various low geometrical concentration ratios: 4 different geometrical concentration ratios are chosen to be studied: 4×, 6×, 8× and 10×.
- Various dimensions and proportions of the geometry.

The aim of this series of ray tracing simulations is to optimise the dimensions of the SEH concentrator based on its optical performance. The optimisation process passes through different stages, starting from finding the optimum profile of the entry aperture of the SEH concentrator to obtaining the optimum height to optimising the geometrical concentration ratio.

4.4.1 Optimisation of the Elliptical Aspect Ratio

The aim of the first set of ray tracing simulations is to optimise the shape of the ellipse at the entry aperture, starting from a circle when $a=b$, moving to a different shape of the same area of an ellipse. The elliptic entry aperture profile is characterised by the Elliptical Aspect Ratio (EAR: b/a ratio), where b is the major axis of the ellipse and a is the minor axis of the ellipse. The maximum b/a ratio possible to build the SEH concentrator is equal to 3.8 for C_g=4, 3.6 for C_g=6 and C_g=8 and 3.25 for C_g=10. Any values higher than these b/a ratios results in the minor axis "a" becoming almost half of the length of the side of the square exit aperture (A/2); this would result in an inability to form the hyperbolic profile on the side of the minor axis "a" of the elliptical entry aperture, and thus the geometry of the SEH concentrator would not be possible.

Different heights of the SEH geometry are also investigated in this initial step of the optical optimisation. The different heights of the SEH concentrators are referred to by the non-dimensional term Height Aspect Ratio (HAR: H/A ratio). For different geometric concentration ratios (different HARs and different EARs) 160 distinctive geometrical profiles of the SEH concentrator are built.

The graphs in Figure 4.7(a-d) illustrate the variation of the optical efficiency of the 160 different SEH concentrators built with different EARs, characterising the elliptical entry aperture and HARs, characterising the height of the concentrator. The optical efficiencies are calculated using equation (4.1) based on the results of 160 ray tracing simulations carried out with a light source at 0º angle of incidence.

Figure 4.7(a) illustrates the optical efficiencies for different SEH concentrators having the same C_g=4. It shows that for HAR=3 and HAR=2.5, the $\text{Eff}_{\text{optical}}$ of the SEH concentrator reaches a maximum value of 68% for the case when EAR=1 (circular entry aperture), it then decreases with the increase of the EAR. When comparing the optical efficiencies of the different SEH concentrators of C_g=4 (Figure 4.7(a)) with the other geometrical concentration ratios studied (Figure 4.7(b-d)), it can be seen that in general the more the elliptic entry aperture is close to a circular shape (EAR close to 1), the higher is the optical efficiency for C_g=4.

Figure 4.7(b) illustrates the optical efficiencies for different SEH concentrators having the same C_g=6. It shows that as the EAR increases the values of the optical efficiencies become more similar for the SEH concentrators with different HAR. It is important to point out that the maximum Eff $_{optical}$ equal to 55% achieved for C_g=6 is less than the maximum Eff $_{optical}$ obtained for C_g=4. As is for C_g=4, the taller SEH concentrators have the higher Eff $_{optical}$ for C_g=6.

Figure 4.7(c) illustrates the optical efficiencies for different SEH concentrators having the same C_g=8. It shows that the maximum Eff $_{optical}$ is equal to 40% and this value corresponds to the tallest SEH concentrator (HAR=3). Figure 4.7 (d) illustrates the optical efficiencies for different SEH concentrators having the same C_g=10. The maximum Eff $_{optical}$ decreases further compared to the cases of C_g=4, 6 and 8; the maximum Eff $_{optical}$ is equal to 32% and again is obtained for the tallest SEH, HAR=3. It can be noticed that the EAR does not have any affects on the optical efficiency of the SEH concentrator with HAR=1 as the Eff $_{optical}$ remains steady with a very low value of 12% for all b/a ratios. For C_g=4, the Eff $_{optical}$ is equal to 40% for the shortest height, HAR=1. This value is higher than and equal to the maximum Eff $_{optical}$ value for the SEH concentrator with C_g=10 and C_g=8 respectively.

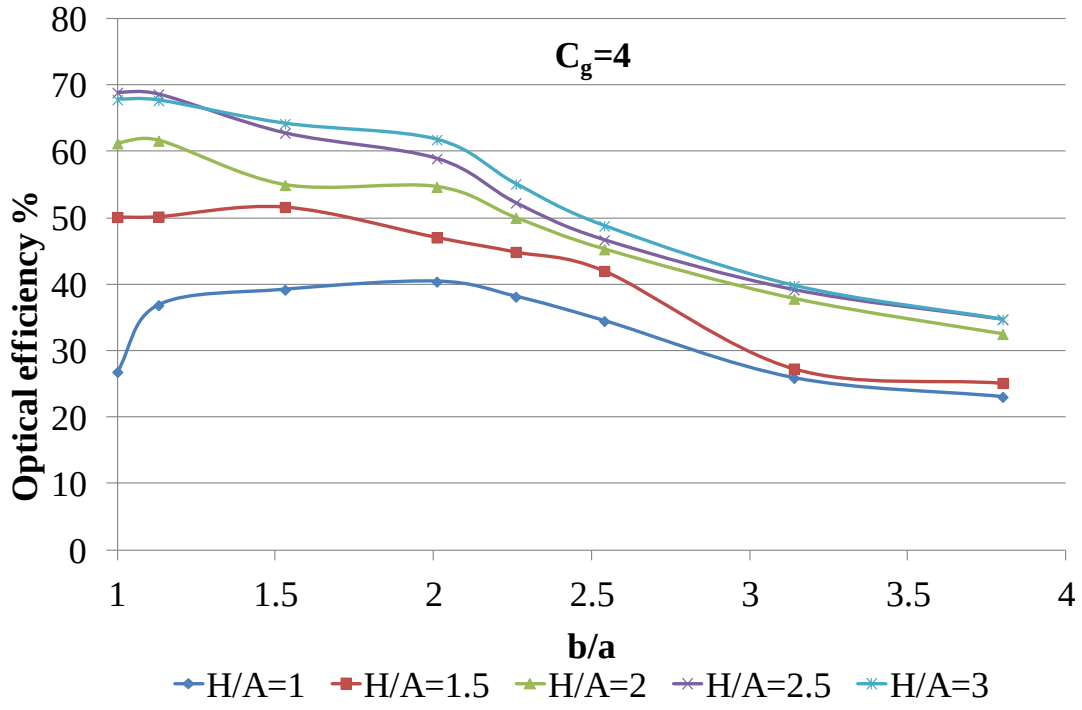

(a)

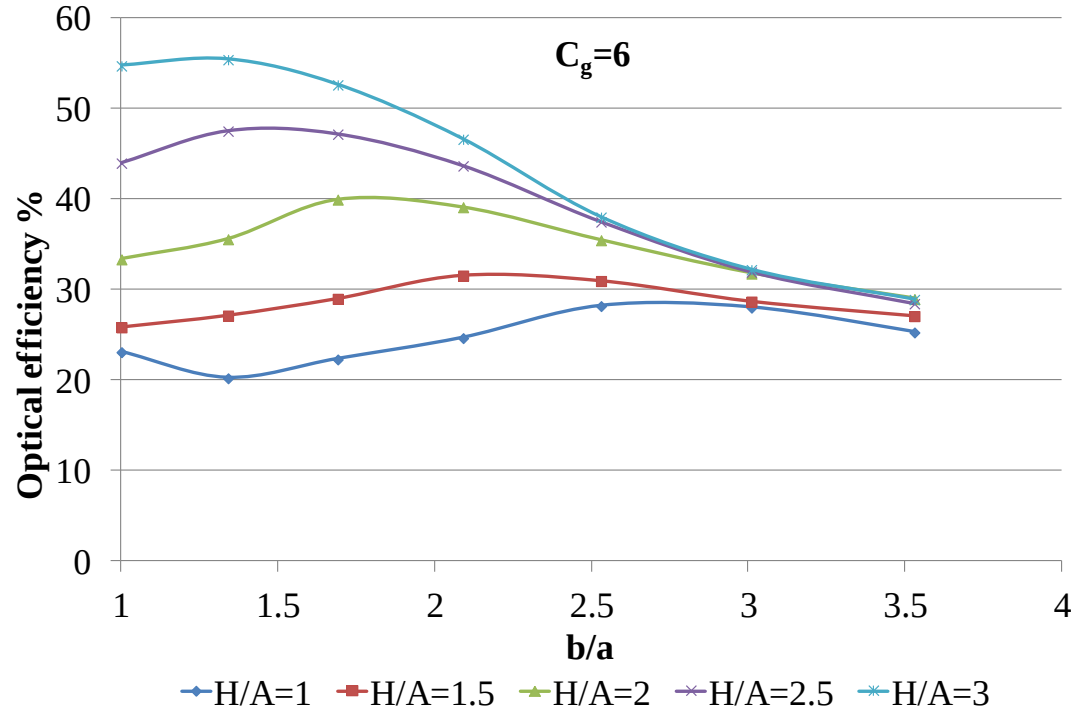
C_g=6
Optical efficiency %
b/a
H/A=1
H/A=1.5
H/A=2
H/A=2.5
H/A=3

(b)

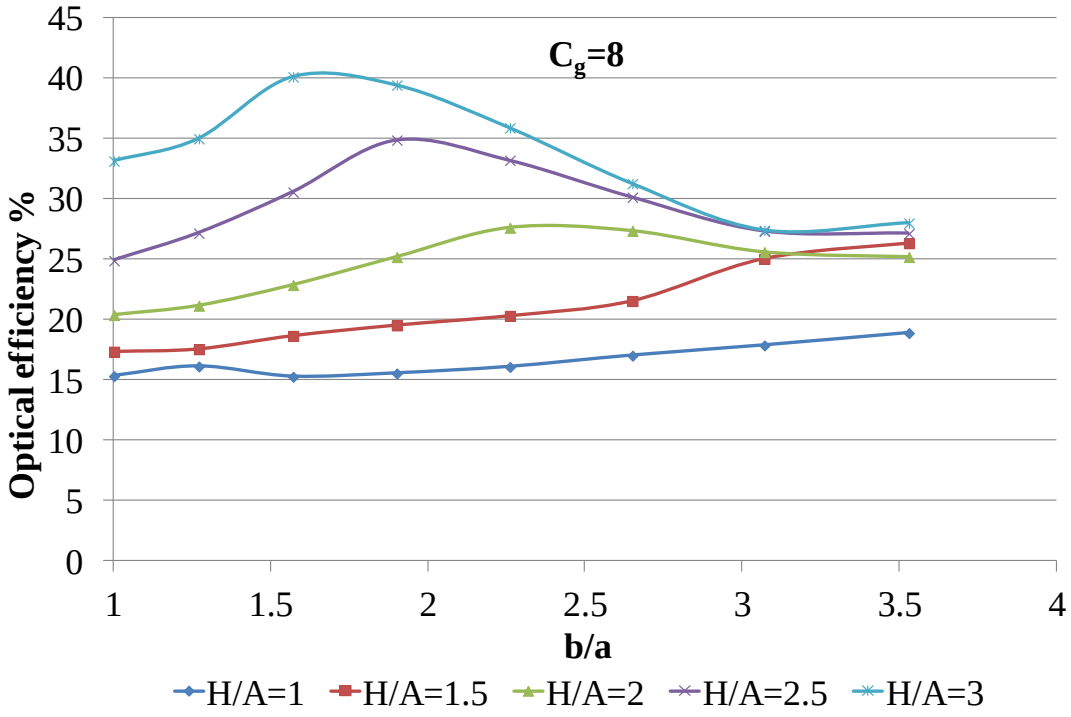
C_g=8
Optical efficiency %
b/a
H/A=1
H/A=1.5
H/A=2
H/A=2.5
H/A=3

(c)

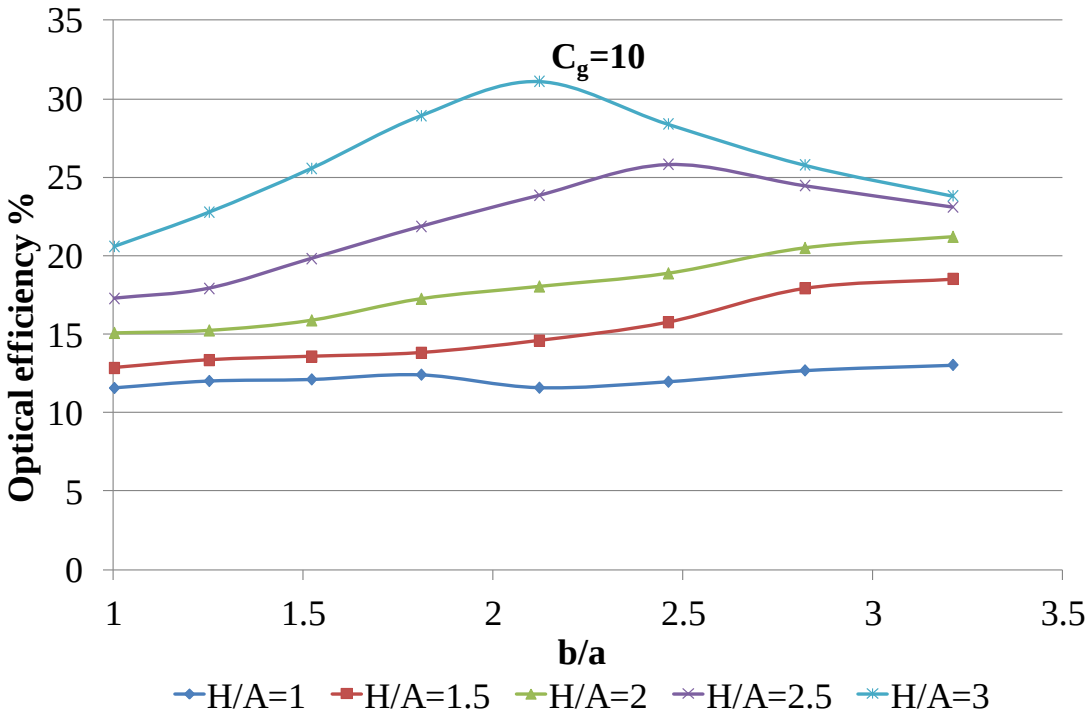

(d)

Figure 4.7: Variation of the optical efficiency versus the b/a ratios for different heights, (a) 4×, (b) 6×, (c) 8× and (d) 10×.

It is important to point out that Eff $_{optical}$ is very low for the short concentrators (HAR=1) with the higher geometric concentration ratios (C_g=8 and C_g=10); this is due to the fact that the hyperbolic profiles on the sides of the SEH concentrator become more sloped to the horizontal which causes more light rays to escape from the sides of the SEH concentrator as can be seen in Figure 4.8. The incident light rays on the hyperbolic sides of the SEH have an angle narrower than the critical angle resulting in the absence of TIR, therefore the rays will refract from the PMMA to air instead of reflecting back inside the concentrator.

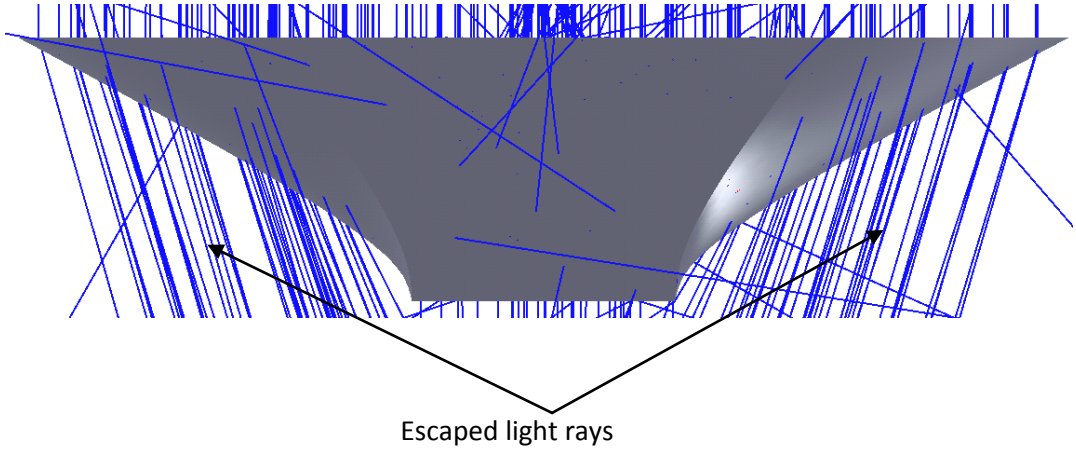

Figure 4.8: Light rays escaping for the SEH: C_g=8, HAR=1 and EAR=1.57

Five optimum SEH concentrators from each geometric concentration ratio and for each height based on their best optical efficiency (giving a total of 20 concentrators out of the original 160) are chosen to be studied further in the next step of the optimisation.

The optimised profiles of the elliptical entry aperture are summarised and illustrated in Figure 4.9. In this optimisation step, 20 SEH concentrators are chosen based on their EAR corresponding to the highest optical efficiency (five values from each C_g). It can be noticed from this figure that the EAR of the optimum SEH concentrators increases with the increase of C_g and the decrease of HAR. For C_g=4, the most efficient SEH concentrator for the highest value of HAR has a circular entry aperture. The best optical performance with the circular entry aperture is only observed for the case of C_g=4; for the other concentrators, C_g= 6, 8 and 10, the best optical efficiency is found to be for an elliptical entry aperture, the shape of the ellipse is more stretched (higher EAR) the higher the C_g. These 20 optimised SEH geometry profiles are subjected to further investigation in the next optimisation step.

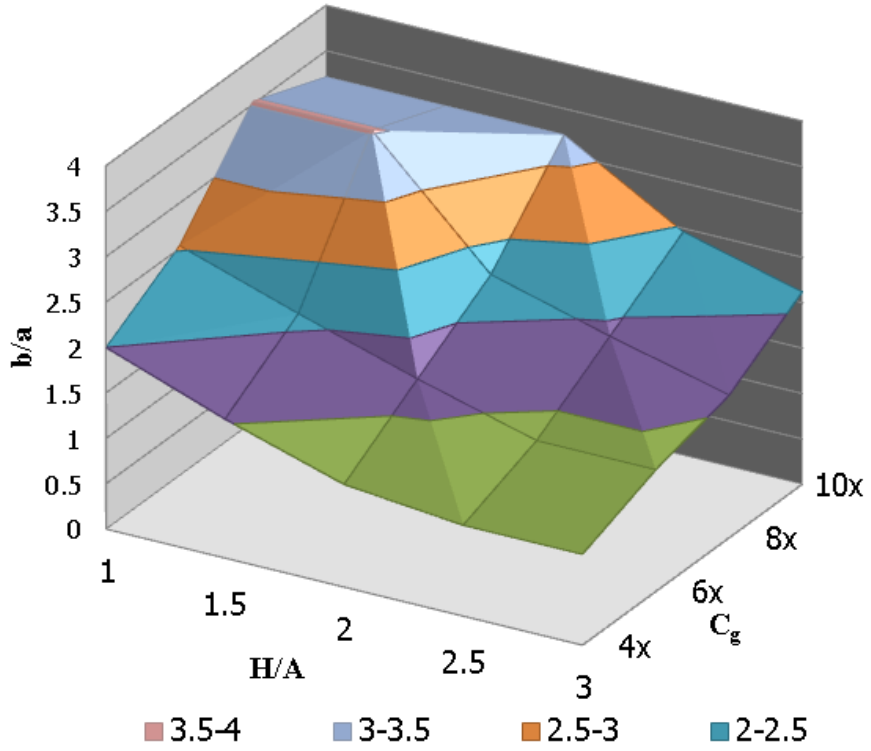

Figure 4.9: Optimised Elliptical Aspect Ratio

4.4.2 Consideration of the acceptance angles

Ray tracing simulations are carried out on the 20 optimised SEH concentrators but this time for various incident angles of the light rays. The incident angles are varied from 0º to 85º with an increment of 5º each time. This results in 18 ray tracing simulations for each optimised SEH concentrator, therefore a total of 360 simulations are carried out for this optimisation step, which consists of comparing the acceptance angles of the different optimised SEH concentrators. It is important to clarify that the angles of incidence of the light rays are varied in the plane perpendicular to the SEH entry aperture and containing the major axis b. Since the SEH is symmetrical along the major axis b, the ray tracing simulations are launched and the corresponding optical efficiencies are calculated only for the positive angles of incidence (0 to 85°); the optical efficiencies for the negative angles of incidence (0 to -85°) are deduced by symmetry.

The graphs in Figure 4.10 show the variation of the optical efficiency at different incident angles for each of the optimised SEH concentrators; they are grouped in different graphs based on their geometric concentration ratio (C_g).

The acceptance angle in this study is defined as when the optical efficiency remains constant (-10% difference from the maximum value) for a larger variation of the incident angle starting from a perpendicular incident angle (at 0º). The graphs neatly illustrate how the choice can be made, based on the acceptance angle, for the optimised SEH concentrator as is necessary for the design of the static solar concentrator; the larger the acceptance angle is, however, the lower is the optical efficiency of the SEH concentrator. This complicates the choice, as the criteria of selection for the optimised SEH are that the geometry has to:

- have the best optical efficiency
- have the highest acceptance angle
- be compact (the lowest *H/A* possible); this is an important factor for BICPV application.

There emerges a dilemma in this step of optimisation; the acceptance angle on its own is not a sufficient criterion to choose the optimised SEH concentrators. It can be observed from the graphs in Figure 4.10 that regardless of the C_g, the SEH concentrators with the largest acceptance angle have the lowest optical efficiency and vice versa. This leads to the next step of optimisation in order to be able to further reduce the selection of the optimised SEH concentrators. The graphs in Figure 4.10 will be discussed in the next section in relation to both the HAR and acceptance angles.

4.4.3 Optimisation of the Height Aspect Ratio

The aim now is to select the SEH concentrators that have the lowest height, as this makes them more compact and easier to be a part of BICPV modules. It soon becomes apparent, however, that this method of selection also involves a major barrier.

Figure 4.10(a) shows the variation of the optical efficiency as a function of the incident angles of the light rays for the optimised SEH concentrators with C_g=4. The lowest height concentrator (*H/A*=1) illustrated in the dark blue line has the largest acceptance angle of 120º (-60º, +60) with an optical efficiency of 40% compared to the tallest SEH concentrator (*H/A*=3) that has the lowest acceptance angle of 40º (-20º, +20º) but the highest optical efficiency of 68%. The choice of the *H/A*=1 SEH concentrator as the optimised SEH concentrator for C_g=4 based on the height and the acceptance angle can be done but with a loss of 28% in optical efficiency compared to the *H/A*=3. Similarly, a dilemma occurs with the choice of the *H/A*=3 SEH concentrator as the optimised SEH concentrator for C_g=4 based on the optical efficiency; this can be adopted but with a loss of 80º in the acceptance angle compared to the *H/A*=1. From the results together, it

transpires that it is not easy to make the choice between a concentrator with a high optical efficiency with a short time of sun ray collection during the day and concentrator with a long time collection of sun rays during the day yet with a lower optical efficiency. Figure 4.10(a) also shows that the taller is the SEH concentrator the lower is the acceptance angle and the higher is the optical efficiency. This characteristic of the SEH concentrator is found to be general for all of the geometric concentration ratios; the same can be observed in Figure 4.10(b) for C_g=6, Figure 4.10(c) for C_g=8 and Figure 4.10(d) for C_g=10. Only a detailed calculation of the yearly solar energy collection for a specific position and location of the SEH concentrator in the world can result in the definitive choice.

Based on the Height Aspect Ratio, therefore, it is not clear which SEH concentrator has the optimised geometry for the best optical performance required for a static concentrator for the BICPV module. Yet another criterion for the selection of the optimum SEH concentrator is required for the next optimisation step.

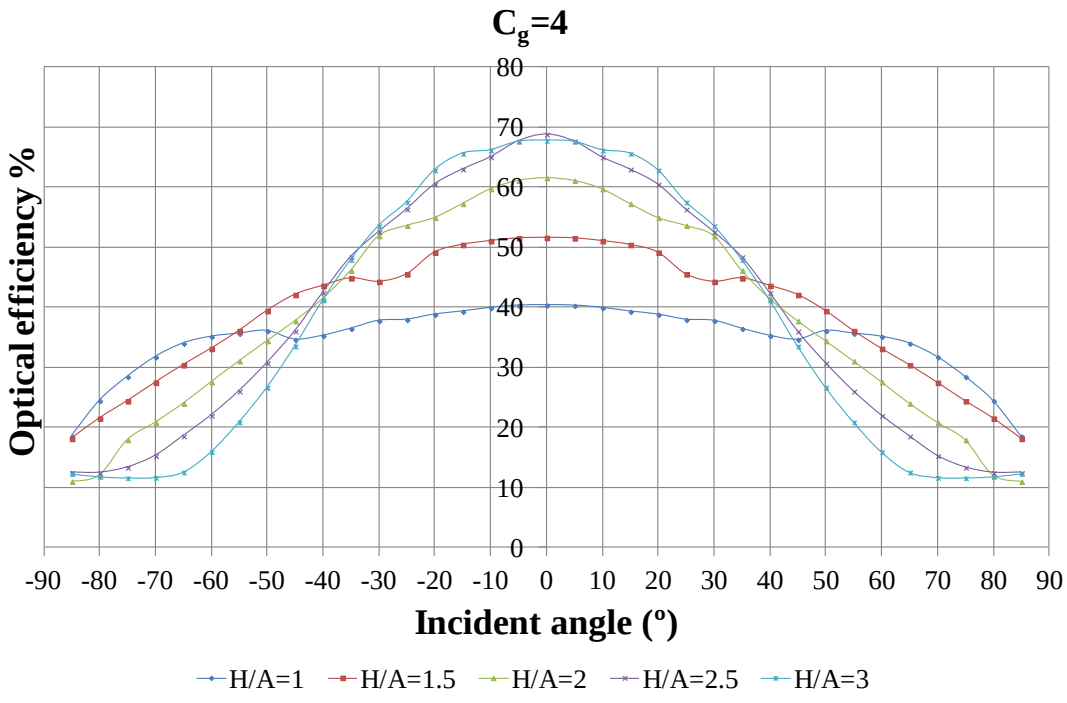

(a)

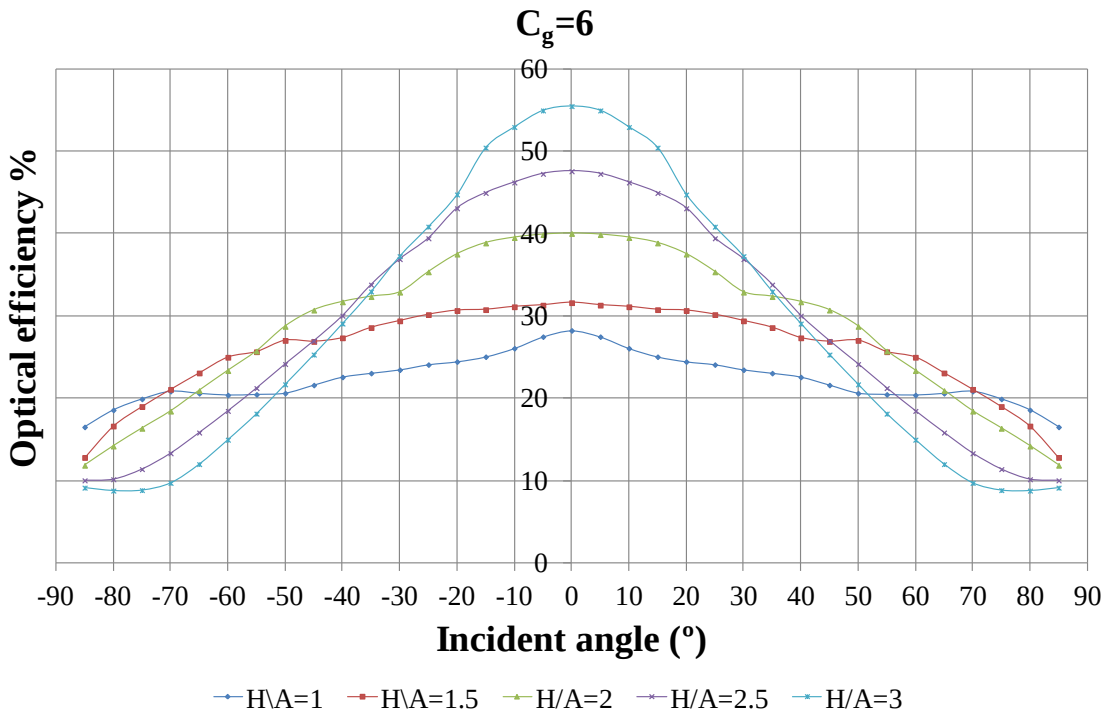
C_g=6
Optical efficiency %
60
50
40
30
20
10
0
-90 -80 -70 -60 -50 -40 -30 -20 -10 0 10 20 30 40 50 60 70 80 90
Incident angle (º)
H\A=1
H\A=1.5
H/A=2
H/A=2.5
H/A=3

(b)

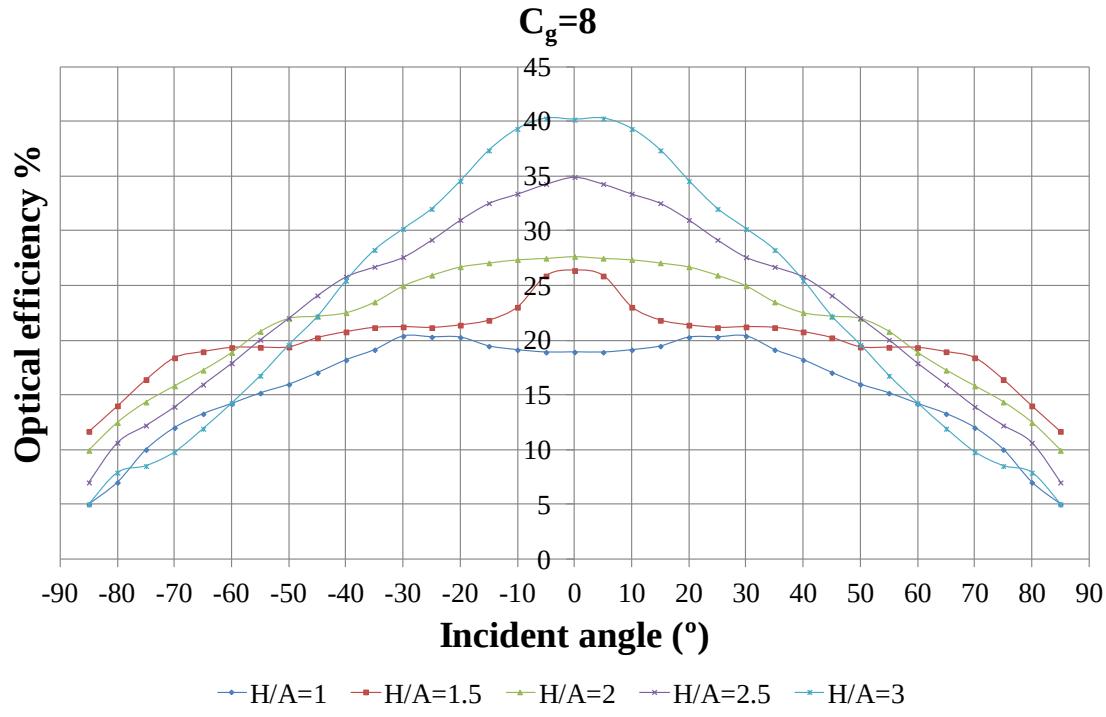
C_g=8
Optical efficiency %
45
40
35
30
25
20
15
10
5
0
-90 -80 -70 -60 -50 -40 -30 -20 -10 0 10 20 30 40 50 60 70 80 90
Incident angle (º)
H/A=1
H/A=1.5
H/A=2
H/A=2.5
H/A=3

(c)

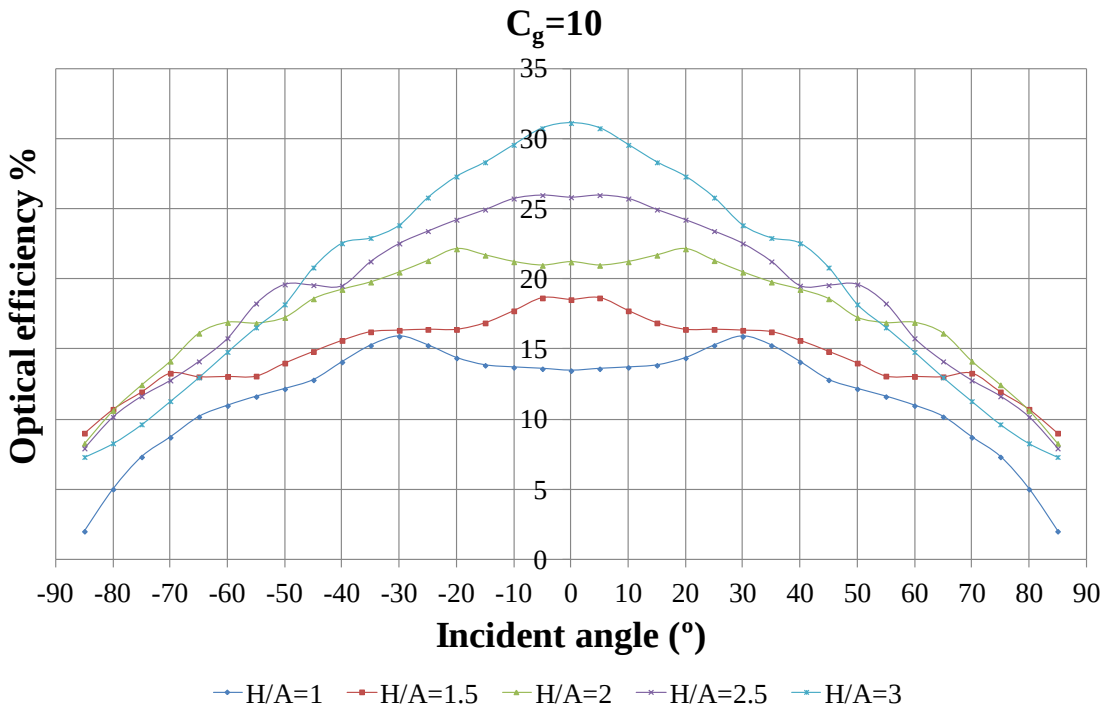

(d)

Figure 4.10: Variation of the optical efficiency versus the incident angles for different Height Aspect Ratios (a) 4×, (b) 6×, (c) 8× and (d) 10×

4.4.4 Optimisation of the geometrical concentration ratio (C_g)

This time the optical efficiency of the twenty SEH solar concentrators is represented in different figures based on their HAR. This will enable us to observe the effect of the geometric concentration ratio on the optical performance of the SEH concentrators and to investigate the possibility of using this criterion for selecting the optimum profile of the SEH concentrator. The higher is the geometric concentration ratio the more material of silicon solar cell will be saved, reducing further the cost of the BICPV module. It can be noticed from the graphs in Figure 4.11 that the SEH concentrators with the same HAR have similar acceptance angles.

The graphs in Figure 4.11 show clearly the effect of the geometrical concentration ratio on the optical efficiency. For all height ratios of the SEH (Figure 4.11 graphs a, b, c, d and e), the optical efficiency increases as the geometrical concentration ratio decreases for all the incident angles.

If the selection is based on the geometric concentration ratio only, the SEH concentrators with C_g=4 have the highest optical efficiency for all HAR. The dilemma

in this case is to select a criterion from the following choice: either a higher optical efficiency with a lower geometric concentration ratio or a lower optical efficiency with a higher geometric concentration ratio.

At this point in the investigation, it was decided that in the next step it would be appropriate to select an optimised SEH concentrator profile for each HAR for two major reasons. By using the HAR as the selection criteria:

- Various optimised SEH concentrator profiles with different heights can be designed allowing architects to have a flexible mode of selection of the BICPV modules required, depending on the transparent façades and different thicknesses of the BICPV modules. If another selection criterion was used, this could ensue in several concentrators with the same height, resulting in less choice for architects to use as potential BICPV modules.
- At least one of the dilemmas of the optimisation process is eliminated as it appears to be impossible to give more importance to any one criterion over the other.

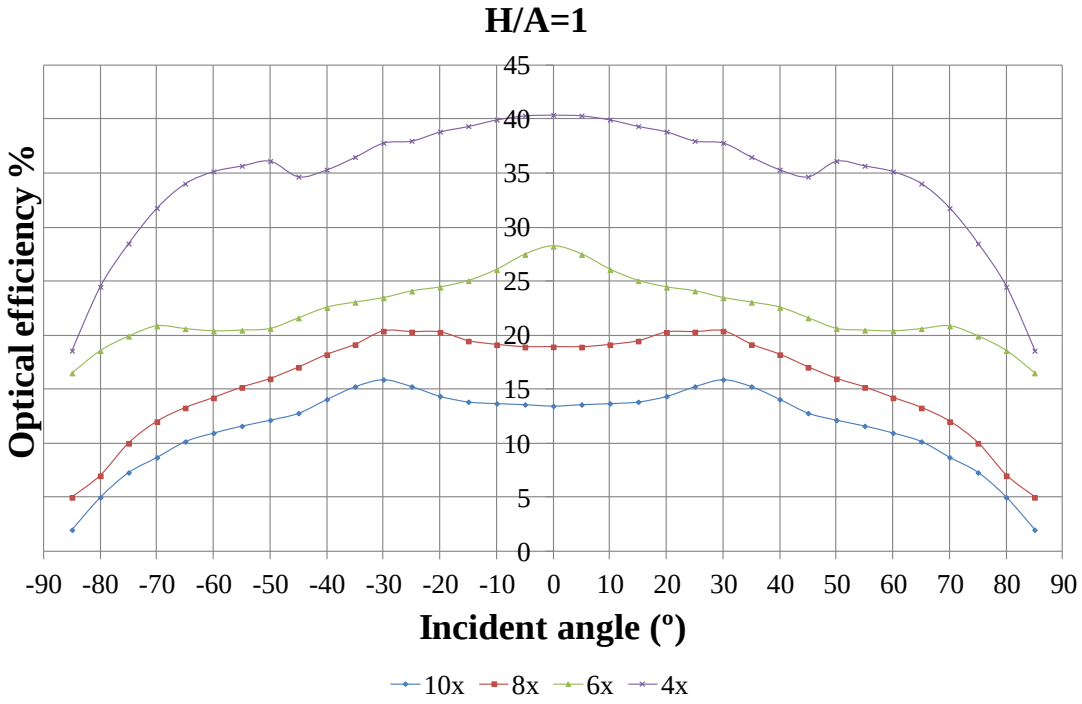

(a)

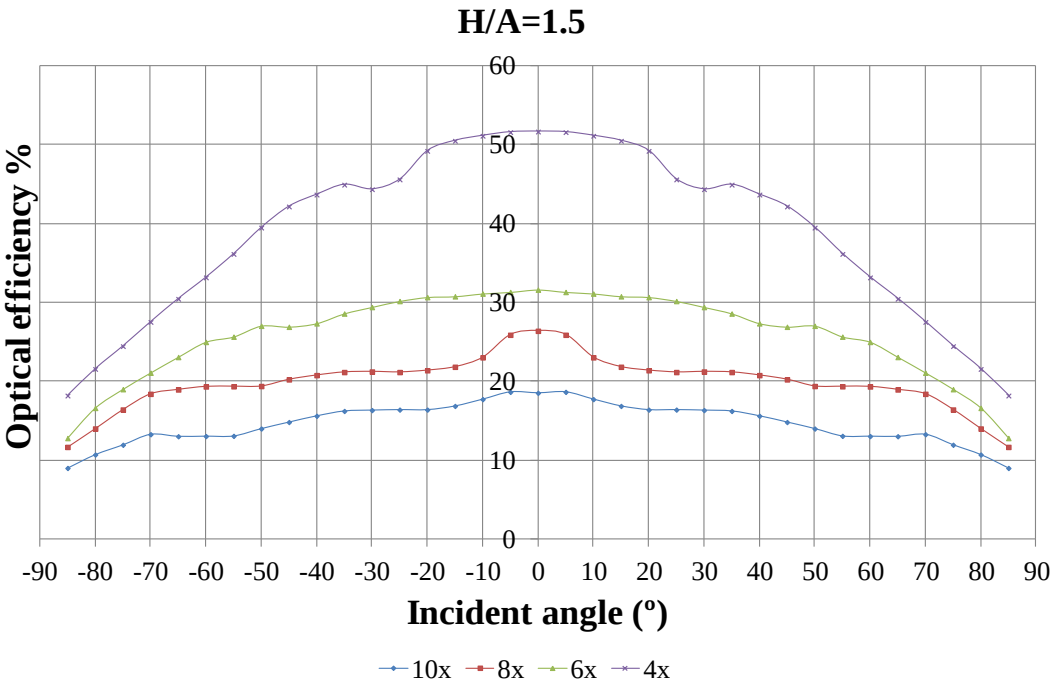
H/A=1.5
Optical efficiency %
60
50
40
30
20
10
0
-90 -80 -70 -60 -50 -40 -30 -20 -10 0 10 20 30 40 50 60 70 80 90
Incident angle (º)
10x 8x 6x 4x

(b)

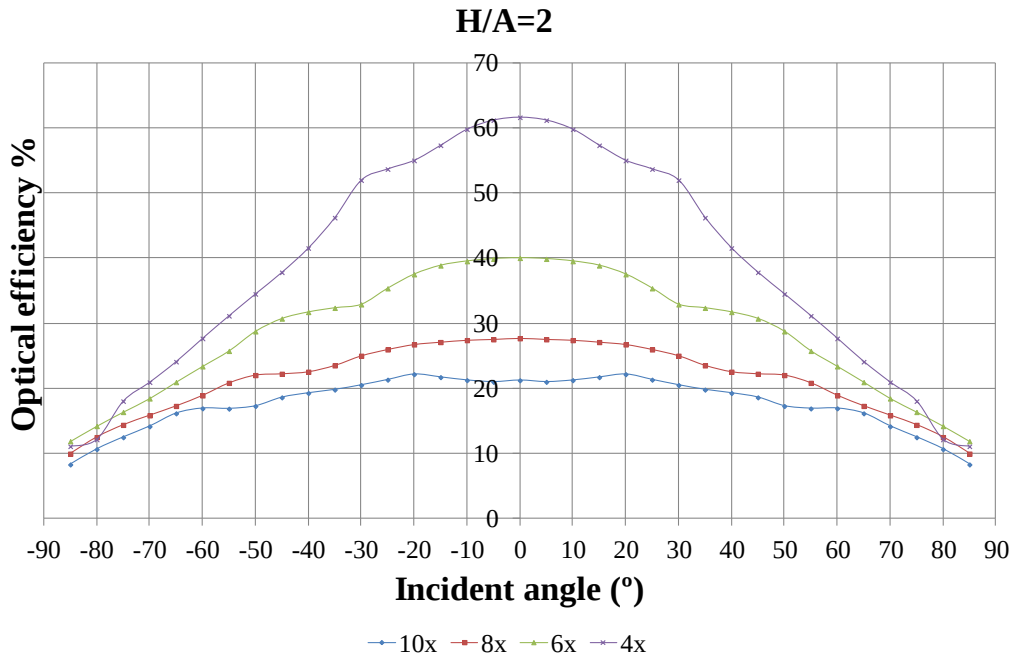
H/A=2
Optical efficiency %
70
60
50
40
30
20
10
0
-90 -80 -70 -60 -50 -40 -30 -20 -10 0 10 20 30 40 50 60 70 80 90
Incident angle (º)
10x 8x 6x 4x

(c)

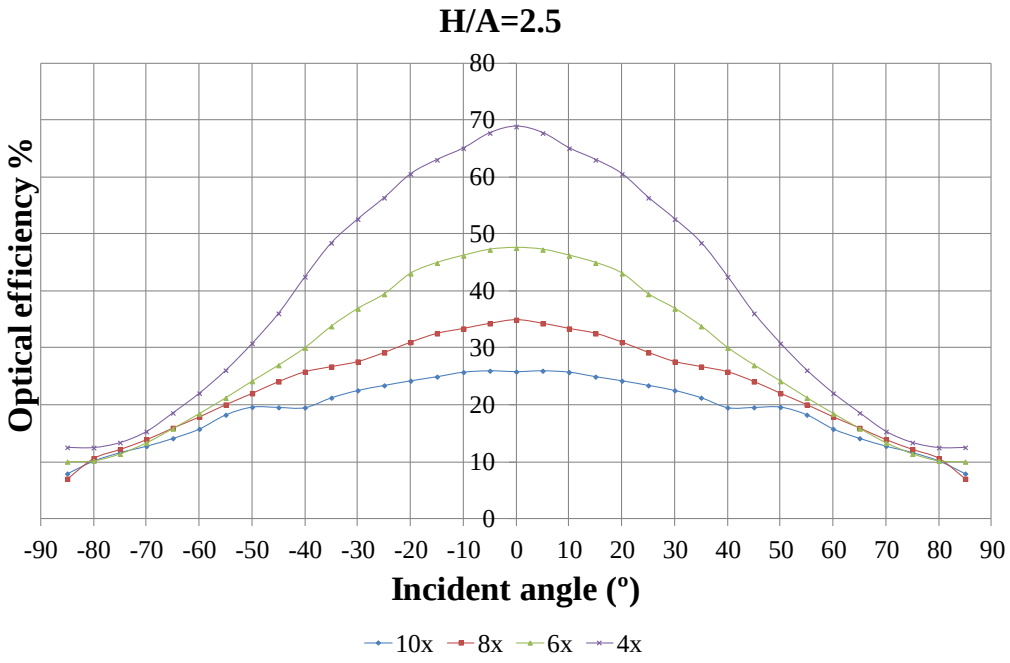

(d)

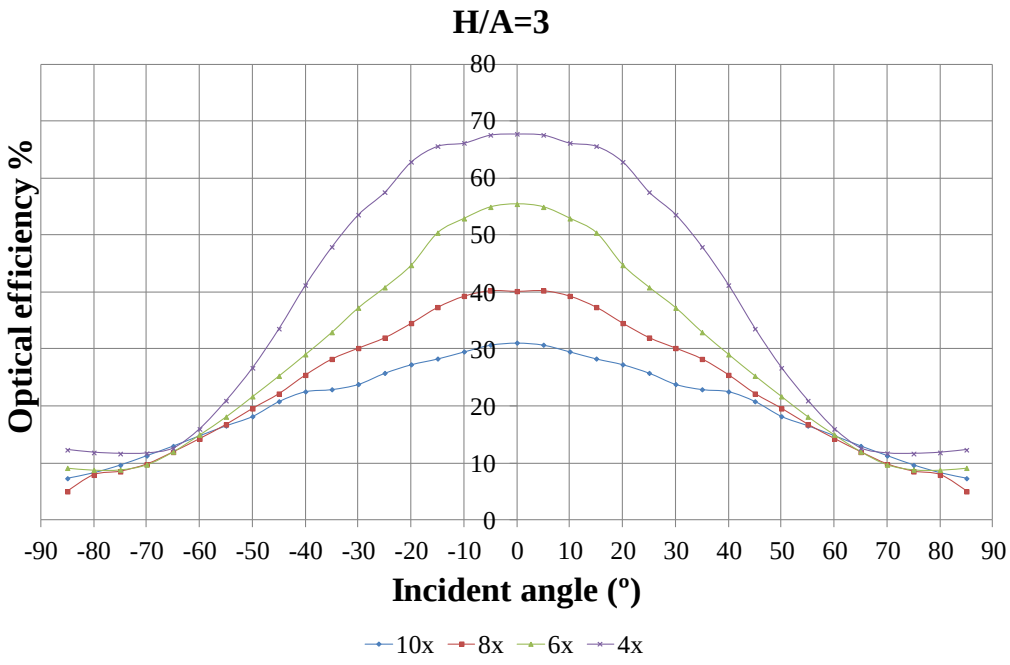

(e)

Figure 4.11: Variation of the optical efficiency for different Geometrical Concentration ratios. (a) *H/A*=1, (b) *H/A*=1.5 (c) *H/A*=2 (d) *H/A*=2.5 (e) *H/A*=3

4.4.5 Consideration of optical concentration ratios (C_{opt})

At the end of each optimisation step above, it transpires that a dilemma remains – one value will be higher with another value being lower. Introducing another factor into the process may further obscure the selection process or indeed provide a solution to narrow the number of potential SEHs. An equally important factor to consider in the design process is how much concentration will reach the exit aperture. This will represent the amount of radiation that will reach the solar cells at the exit aperture after concentration. The optical concentration ratio (equation (4.2)), therefore, defined as the geometrical concentrations multiplied by the optical efficiency, is another factor that needs to be considered as part of the optimisation process of the SEH.

$$\mathrm{C_{opt}} = \mathrm{C_g} \times \mathrm{Eff}_{\,\mathrm{optical}} \tag{4.2}$$

The maximum optical concentration ratio (C_{opt}) is calculated for the twenty different SEH concentrators using equation (4.2). The results are summarised and illustrated in Figure 4.12, the C_{opt} values are grouped with the same HAR as a function of the geometric concentration ratio. The red circles refer to the final optimised SEH concentrators chosen – one for each different HAR based on the maximum optical efficiency.

It can be seen that for the tallest SEH concentrator, *H/A*=3 (light blue line Figure 4.12), the highest C_{opt} corresponds to C_g=6 with a value equal to 3.29×. Interestingly, from the previous results, the SEH concentrator of C_g=6 has a lower $Eff_{Optical}$ equal to 55% compared to the SEH concentrator of C_g=4 which has a $Eff_{Optical}$ equal to 68% for *H/A*=3 (Figure 4.11 (e)). At that point in the study consequently, and using the optical efficiency as the selection criterion, the optimised SEH would be the C_g=4 as it has the higher $Eff_{Optical}$; nevertheless, as discussed above, there remains a dilemma that it has a lower geometric concentration ratio so it is not entirely clear which one is the optimum SEH out of the two. After having carried out the calculations to find the maximum optical concentration ratio (C_{opt}), however, it can be seen that there is now a value that can differentiate between these two SEH concentrators. In this case the choice becomes clearer: the SEH concentrator with C_g=6 is the optimised geometry profile for *H/A*=3 as the difference in $Eff_{Optical}$ is not enough to result in a higher C_{opt} for C_g=4.

In the same way, it was found that for the *H/A*=2.5 (purple line) the best C_{opt} is for C_g=6; for the *H/A*=2 (green line) the best C_{opt} is for C_g=4; for the *H/A*=1.5 (red line) the

best C_{opt} is for C_g=4 and for the H/A=1 (dark blue line) the best C_{opt} is for C_g=4. Looking back to the graphs in Figure 4.11 it can be seen that for every HAR, the SEH with C_g=4 has the highest optical efficiency; this does not mean, however, that it is the optimised SEH – it has the lowest geometric concentration ratio. Only by carrying out this further step in the optimisation process, does it becomes clearer which SEH can be chosen for each HAR. As it transpires, the results show that the five optimised SEH concentrators are the ones with the lowest geometric concentration ratios.

The SEH concentrators with high geometric concentration ratios (C_g=8 and C_g=10) appear to be unsuitable for the static solar concentrator as they have the lowest values of C_{opt} and the lowest values of $Eff_{Optical}$ (<40%) compared to the SEH concentrators with geometric concentration ratios C_g=4 and C_g=6.

Figure 4.12 illustrates that the difference in C_{opt} between C_g=6 and C_g=4 is negligible for these four SEH concentrators (H/A=2.5, 2, 1.5 and 1), however, it is enough to be able to make a selection and reduce the number of SEH concentrators from twenty to five, unlike the previous optimisation steps. Here transpires the importance of selecting the HAR as one of the criterion in order to be able to move forward in the optimisation process. Now, for each HAR, we have an optimised SEH to use for the experimental part of the study.

The five optimised SEH concentrators have different C_{opt} varying from 1.64 to 3.29. The lowest C_{opt} corresponds to the lowest HAR (H/A=1). The C_{opt} increases with the increase of the HAR. The acceptance angle, however, is larger for the lowest HAR (120º for H/A=1) and decreases with the increase of HAR (40º for H/A=3).

There are now two distinct criteria that can be used for choosing the suitable SEH concentrator from the five optimised profiles for the BICPV module. These two criteria are:

- The space available to integrate the SEH concentrators into the transparent glazing façades – if only a small space is available the architect is forced to choose the SEH with the smaller HAR; if no constraint applies for the height of the concentrator, it is necessary to look at the next criterion of selection.
- A yearly prediction of the energy generated by the different optimised SEH concentrators – in this case, the location of the building and the orientation of the transparent glazing façades or roof play a major role in selecting the most efficient SEH concentrators (i.e. producing more electricity).

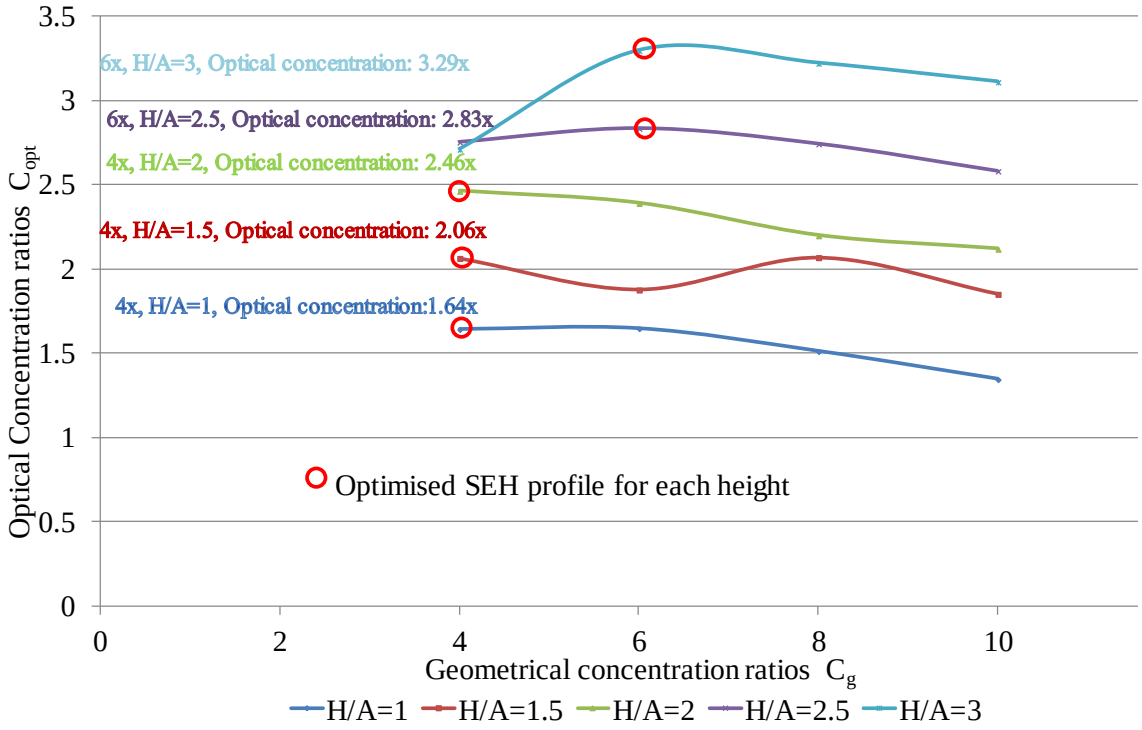

Figure 4.12: Corresponding optical concentration ratios for each geometrical concentration ratio

4.5 Optimised profiles of the SEH concentrator

In this section, the properties of the five optimised SEH concentrators will be summarised. The results of the optical flux distribution will also be presented.

4.5.1 Properties of the optimised SEH concentrators.

The five optimised SEH concentrators illustrated in Figure 4.13 have the geometrical and optical properties summarised in Table 4.1. From this point onwards in the study, the optimised SEH concentrators will be named and referred to accordingly based on their HAR (*H/A*); in other words the optimised SEH concentrator for *H/A*=1 will be called H1 SEH concentrator and the same for the other SEH concentrators as illustrated in Figure 4.13.

Each SEH has three geometric properties represented in Table 4.1:

- b/a which defines the profile of the elliptical entry aperture of the SEH concentrator.
- *H/A* which defines the height proportion of the SEH concentrator based on the square exit aperture.
- C_g which defines the area ratio between the entry aperture and the exit aperture.

In order to finalise the dimensions of the SEH, the area of the solar cell (area of the exit aperture) to be used with the SEH concentrator needs to be confirmed. From this, the area of the entry aperture can then be calculated using C_g. Once the area of the entry aperture is known, the dimensions of the major axis b and the minor axis a can be calculated using b/a. The height of the SEH concentrator is calculated from the *H/A* value, which includes the dimension of the side of the square exit aperture.

Table 4.1: Geometric and optical properties of the optimised SEH concentrators.

Properties	**H1**	**H1.5**	**H2**	**H2.5**	**H3**
b/a	2	1.5	1.13	1.34	1.34
H/A	1	1.5	2	2.5	3
C_g	4	4	4	6	6
C_{opt} (Maximum)	1.64	2.06	2.46	2.83	3.29

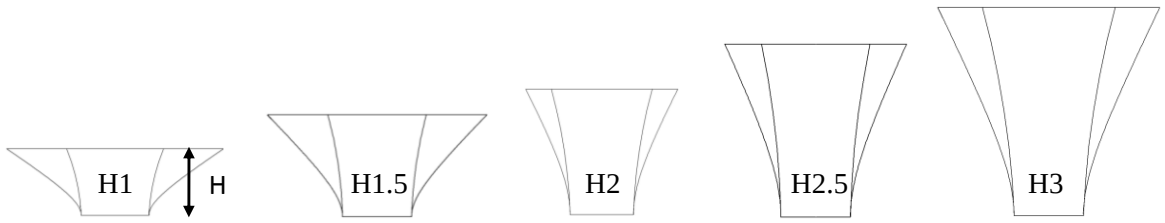

Figure 4.13: Proportional 2-D representation of the five optimised SEH concentrators

4.5.2 Optical flux distribution at the square exit aperture of the SEH concentrator

The optical efficiency of the SEH concentrators is calculated based on the average of the energy of the light rays collected on the exit aperture. The results obtained from the ray tracing simulation, however, carried out via OptisWorks are more detailed as they provide an important result in addition to the average of the energy of light rays: the optical flux distribution on the square exit aperture where the solar cell is to be placed. This data is essential for the study of the effect of the non uniformity of the optical flux distribution on the efficiency of the solar cells. This is a separate study beyond the scope of the current thesis, however, this information can be used in the future to aid and enhance the design of concentrated solar cells to be used with the SEH concentrator.

In this thesis the aim is to design and characterise the new 3-D static solar concentrator for BICPV application; to design solar cells or enhance their performance under concentration is not part of the study. The results of the effect of the different geometric ratios (HAR, EAR and C_g) on the uniformity of the optical flux distribution are presented below; this data is the groundwork for future research aiming to enhance solar cells to be used with the SEH concentrator in BICPV modules.

Figure 4.14(a) shows that the optical flux distribution for the H1 SEH concentrator (shortest) is uniform on the square exit aperture reaching a maximum of 7× (7000W/m^2) on only a few small hot spots. This can be confirmed from the 2-D representation on the *x* and *y* axis of the square exit aperture illustrated in Figure 4.14(b) and Figure 4.14(c) where it can be observed that, apart from the few high peaks, the average variation of the energy of light rays is in the range of 1000W/m^2.

Figure 4.15(a) shows that the optical flux distribution of the H1.5 SEH concentrator is less uniform compared to the H1 SEH concentrator. The concentration of light rays reaches a maximum of 20× in one small area. The concentrated light rays are focused on the centre of the square of the exit aperture; Figure 4.15(c) shows that the concentration is higher on the y axis compared to the concentration on the x axis (Figure 4.15(b)).

Unlike the H1.5 SEH concentrator, the H2 SEH concentrator has the concentration of light rays in four small areas in the centre of the exit aperture as illustrated in Figure 4.16(a). Looking at the figure, it becomes apparent that the four peaks are almost forming an ellipse (one peak can be seen at either end of a major axis and one peak at either end of a minor axis) as though it were a projection of the entry aperture of the SEH onto the exit aperture. The optical flux distribution is non uniform and the concentration of light rays reaches a maximum of 50×.

Figure 4.17(a) and Figure 4.18(a) show that the optical flux distribution is not uniform for the H2.5 and H3 SEH concentrators which have C_g=6. The concentration of the light rays are focused in the central area of the square exit aperture with a difference in value of 40 000 W/m^2 compared to the other areas of the receiver for the H3 SEH concentrator, as can be seen in Figure 4.18(b) and Figure 4.18(c). For the case of the H2.5 SEH concentrator the maximum concentration at the centre is 30× compared to the other areas of non uniformity on the square exit aperture with a value of 15×.

Results show that the shorter the SEH concentrator is, the more uniform is the optical distribution on the square exit aperture. It is important to specify that the shorter the SEH concentrator (HAR) is, however, the lower is the EAR and the lower is the C_g.

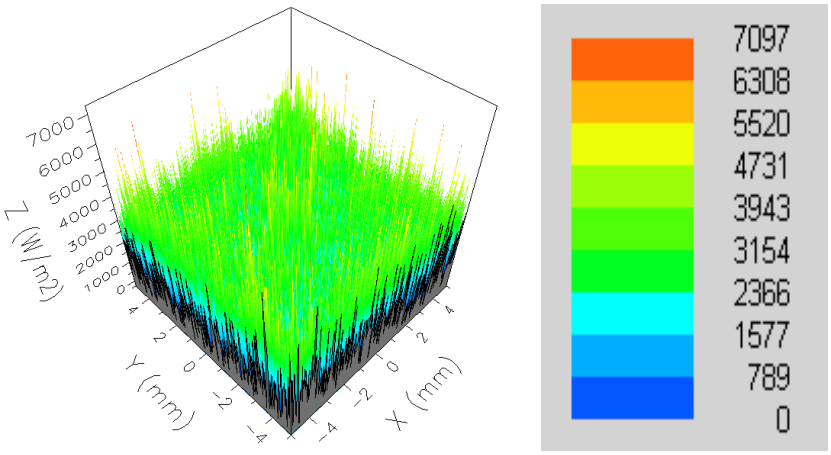

(a) 4x, H/A=1, b/a=2

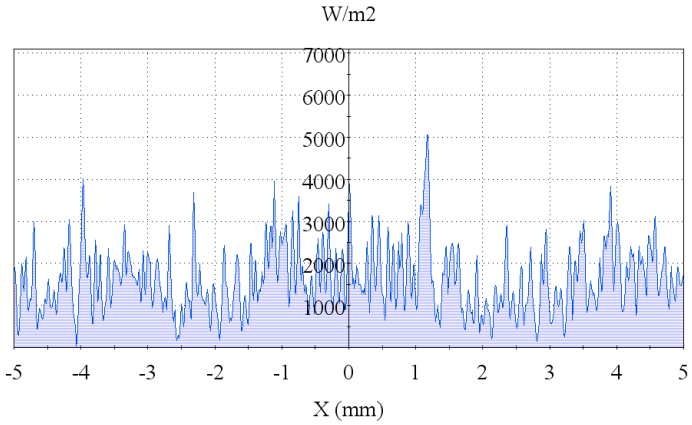

(b) Distribution at y=0

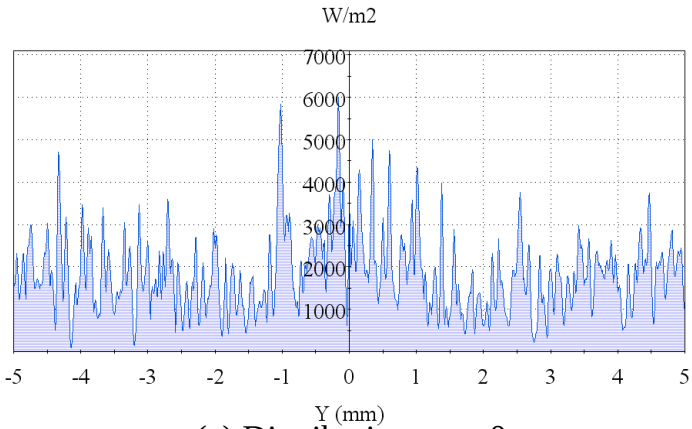

(c) Distribution at x=0

Figure 4.14: Optical distribution of the SEH concentrator at the receiver (C_g=4, HAR=1, EAR=2): (a) 3-D map, (b) 2-D distribution on the x axis, (c) 2-D distribution on the y axis

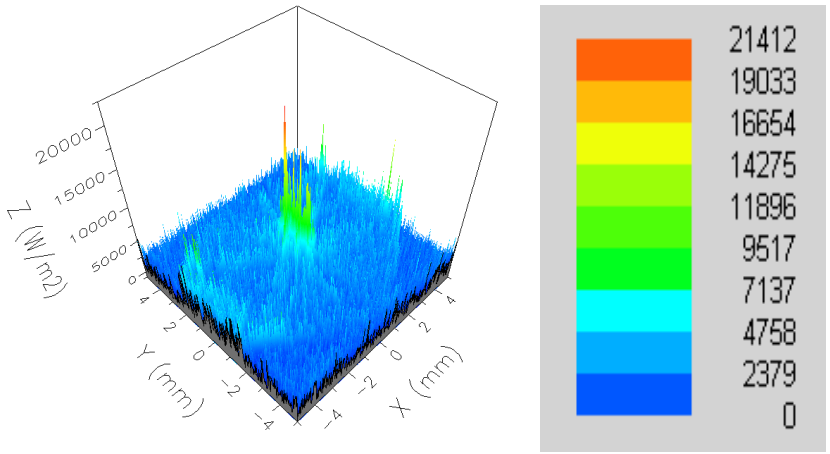

(a) 4x, H/A=1.5, b/a=1.5

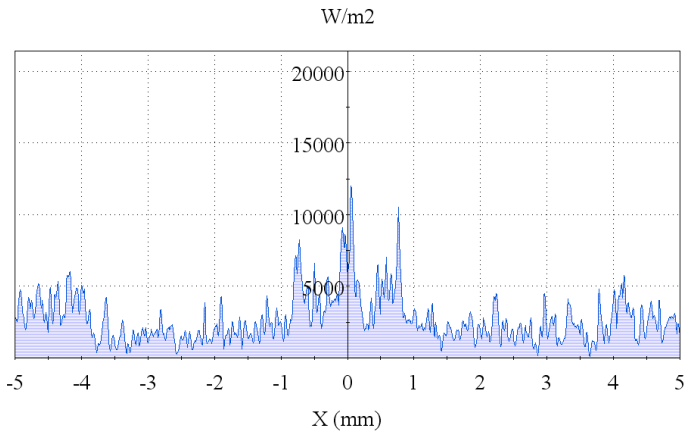

(b) Distribution at y=0

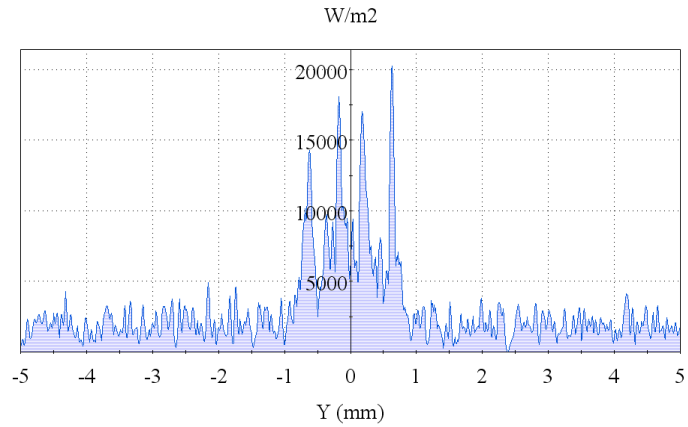

(c) Distribution at x=0

Figure 4.15: Optical distribution of the SEH concentrator at the receiver (C_g=4, HAR=1.5, EAR=1.5): (a) 3-D map, (b) 2-D distribution on the x axis, (c) 2-D distribution on the y axis

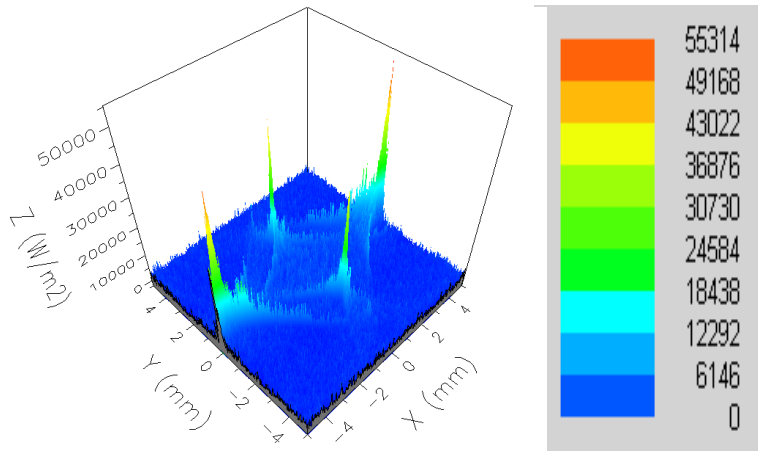

(a) 4x, H/A=2, b/a=1.13

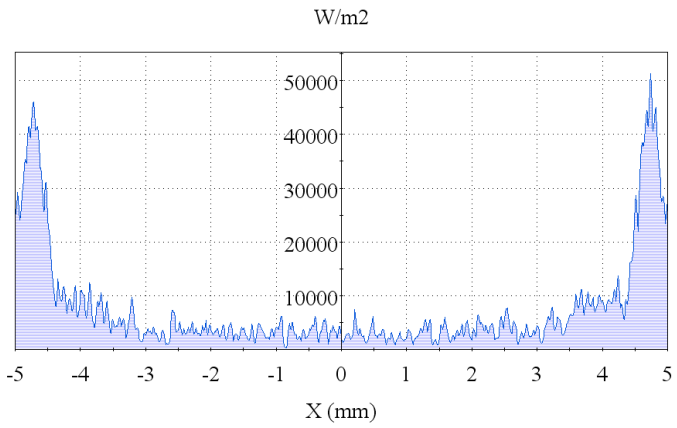

(b) Distribution at y=0

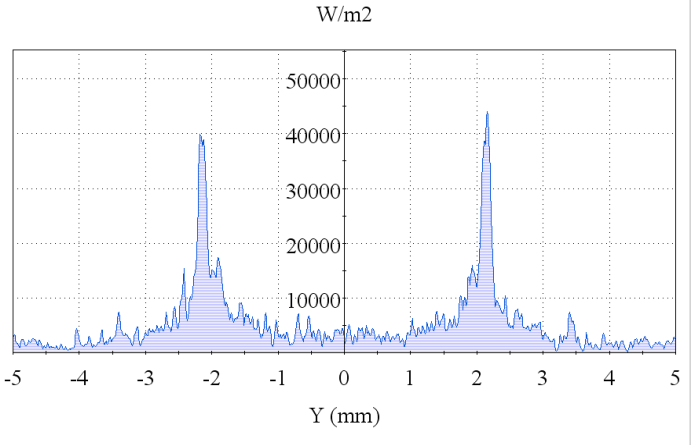

(c) Distribution at x=0

Figure 4.16: Optical distribution of the SEH concentrator at the receiver (C_g=4, HAR=2, EAR=1.13): (a) 3-D map, (b) 2-D distribution on the x axis, (c) 2-D distribution on the y axis

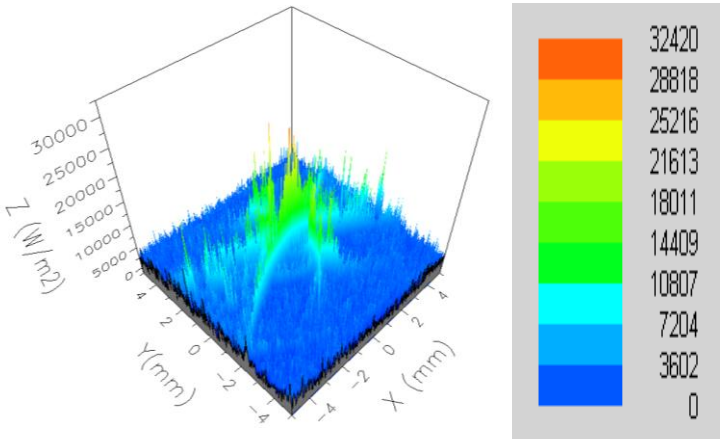

(a) 6x, H/A=2.5, b/a=1.34

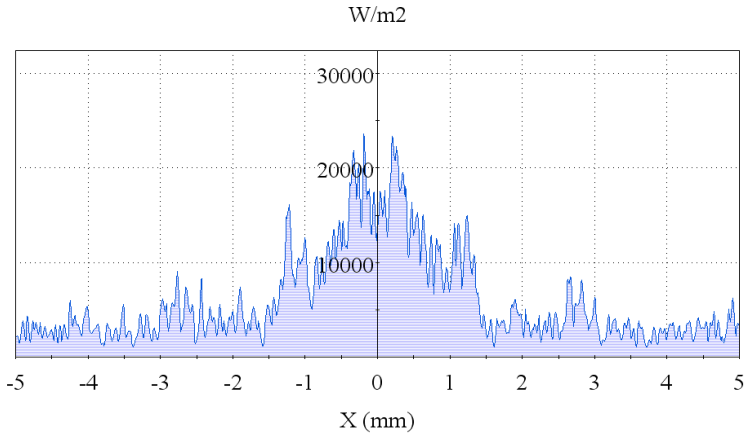

(b) Distribution at y=0

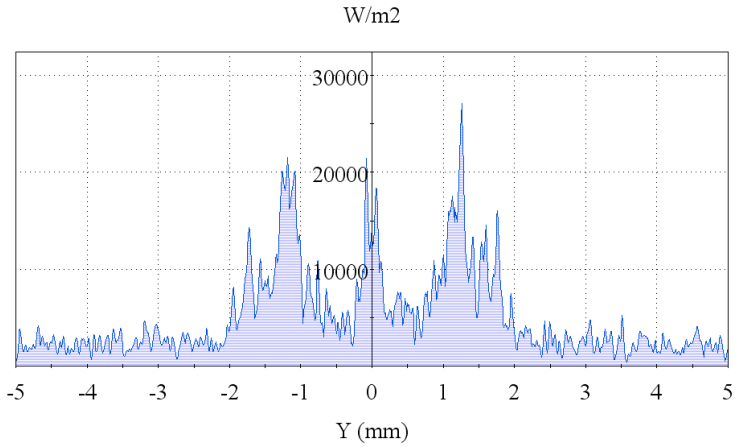

(c) Distribution at x=0

Figure 4.17: Optical distribution of the SEH concentrator at the receiver (C_g=6, HAR=2.5, EAR=1.34): (a) 3-D map, (b) 2-D distribution on the x axis, (c) 2-D distribution on the y axis

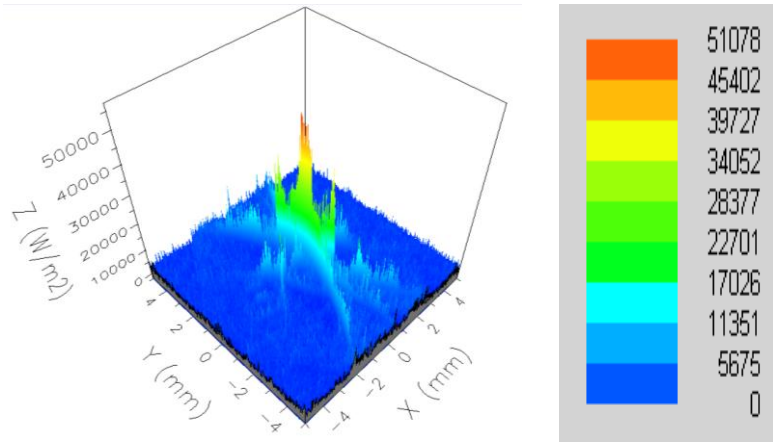

(a) 6x, H/A=3, b/a=1.34

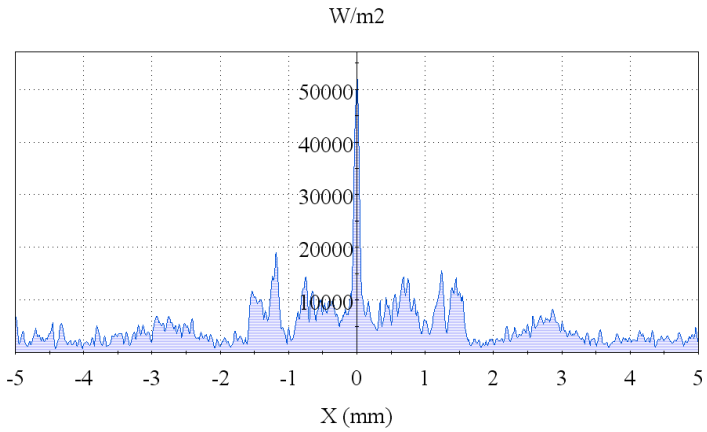

(b) Distribution at y=0

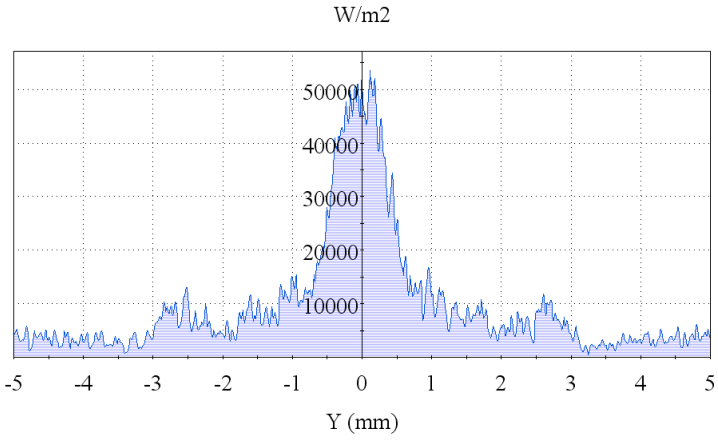

(c) Distribution at x=0

Figure 4.18: Optical distribution of the SEH concentrator at the receiver (C_g=6, HAR=3, EAR=1.34): (a) 3-D map, (b) 2-D distribution on the x axis, (c) 2-D distribution on the y axis

4.6 Conclusion

An optical ray tracing model using OptisWorks has been developed and applied on various geometric profiles of the SEH concentrator. The results have been used to optimise the geometry of the SEH concentrators starting from the profile of the elliptical entry aperture to the height and the geometric concentration ratio. It was decided to select an optimum geometric profile SEH concentrator for each HAR (height ratio of the concentrator) after having encountered barriers for selecting one optimum geometric profile. The optimised SEH concentrators have low geometric concentration ratios (4× and 6×) as they showed better optical performance compared to the higher concentration ratios studied (8× and 10×).

It has been found that the H1 SEH concentrator has a large acceptance angle 120º (-60°+, 60°) with uniform optical flux distribution and the H3 SEH concentrator has a low acceptance angle 40º (-20°, +20°) with a non uniform optical flux distribution. The optical concentration ratio, however, is higher for the H3 SEH (3.29×) compared to the H1 SEH concentrator (1.64×).

The effect of the geometrical characteristics of the SEH concentrator on the uniformity of the optical flux distribution was studied to show that the more uniform the optical flux distribution is, the lower the HAR are, the lower the EAR are and the lower the C_g are.

Now that the five profiles of the SEH concentrator geometry have been selected, an experimental study is required to validate the results obtained by the optical model developed and used in the optimisation process; this is the subject of the next chapter.

Chapter 5: Fabrication and indoor characterisation of the TICPV modules

This chapter provides an overview of the fabrication of the TICPV modules and presents the results of the indoor characterisation of the five different TICPV modules based on the optimisation results obtained in the previous chapter. The casting moulds used to fabricate the SEH concentrators are also presented. The electrical performance of the different IV and power curves of the five different TICPV and TIPV modules manufactured are measured and compared. These results serve to calculate the experimental optical efficiencies which are compared to the simulated optical efficiencies obtained in the previous chapter with the aim of validating the optical model.

5.1 Introduction

The application of the optical model developed using ray tracing techniques on the different SEH concentrator profiles resulted in the selection of five optimised concentrators (H1, H1.5, H2, H2.5 and H3) to be used in the TICPV modules. These five SEH concentrators, with different heights, were obtained after a detailed step-by-step optimisation process. The optical performance of these SEH concentrators has been calculated via ray tracing simulations, however, before the data can be used to predict the electrical performance of the TICPV modules, a validation of the optical model is needed. This will be done by validating the results obtained from the optical simulation with the experimental results. In this chapter, the manufacturing of the TICPV prototypes and results of the test of their performance in indoor conditions is described and presented.

5.2 Material choice and properties

The manufacturing of the prototypes of the optimised SEH concentrators needs to be accomplished in the most economical way possible. There are two possible methods for achieving the task of manufacturing. The first method involves machining transparent dielectric material such as PMMA in to the shapes of the SEH concentrators. The problem with this is that the geometry of the SEH concentrator is a 3-D geometry not

obtained from revolution; it can therefore only be machined using a 5-axis machine[9]. This would be very costly, especially if more than one prototype is to be machined for different experimental setups. Despite the accuracy of the final geometry of the prototype that would be achieved, the machining of PMMA does not give a great surface finish required for refractive optical devices.

The second method of fabrication of the SEH concentrator consists of moulding. This method is generally an expensive method for prototyping as the fabrication of the mould in itself is costly in addition to the machinery needed for this procedure, like injection moulding, for example, which is the most suitable method for the manufacturing of the SEH concentrators. Again, this is not possible within the scope of this research due to the nature of the funding, however, one type of moulding that can be used to manufacture the SEH concentrators within the scale of the research fund, is casting. The process of casting is effectuated by pouring liquid material (either melted material or a mixture of two cold liquid materials) into the mould and then allowing it to solidify. The casting method is the oldest manufacturing process used and the earliest casting was found in Mohenjo-Daro in India of a bronze dancing girl idol [218]. This method is used for making complex shapes such as gold or silver jewellery pieces that would otherwise be difficult or uneconomical to make by other methods [219].

It transpires that the casting method is the most suitable manufacturing process to be used to fabricate the SEH concentrators. The PMMA material used in the ray tracing simulations, however, cannot be used to manufacture the SEH concentrators using the casting method. PMMA has a high shrinkage coefficient compared to other materials which will increase the errors of the casted SEH concentrators compared to the studied geometries in the simulation. Another water clear material is available on the market that has very similar characteristics to PMMA but with a lower shrinkage coefficient. The water clear polyurethane has a shrinkage coefficient of 0.01 % compared to 0.08 % for PMMA; it has the added advantage of having a similar refractive index. The SEH concentrators will be made from polyurethane Crystal Clear 200 Series that can be supplied in small quantities; it is the same material that was used to build the CCPC in

[9] 5-Axis machines are the most advanced CNC milling machines, adding two more axes in addition to the three normal axes (XYZ). 5-Axis milling machines also have a B and C axis, allowing the horizontally mounted workpiece to be rotated, essentially allowing asymmetric and eccentric turning. The fifth axis controls the tilt of the tool itself. When all of these axes are used in conjunction with each other, a competent and experienced machinist can produce extremely complicated geometries with very high precision.

section 2.8.2. In Chapter 2 it was assumed that the polyurethane had similar charteristics to PMMA – this assumption will be verified here.

Despite the optical similarity between the PMMA and the polyurethane, it is necessary to input the exact optical charteristics of the polyurethane into the optical model developed using OptisWorks and re-simulate the optical efficiency of the five optimised SEH concentrators in order to provide a set of results that can be directly comparable and verify the previous assumptions. For this, there are two optical properties of the material that need to be measured experimentally in the lab as they were not supplied by the manufacturer; these are the absorption coefficient and the refractive index variation. These two optical properties are measured using the experimental setup as described below.

5.2.1 Refractive index measurements

Ellipsometry is one of the most precise methods used to measure the refractive index of different materials [211, 220-223]. Ellipsometry is a sensitive optical technique for determining the optical properties of a material with the condition that the thickness of the sample is less than 50 microns [224]. A simple idea to create a thin film of polyurethane was devised:

- Mix the two parts of the polyurethane material (see Chapter 2 section 2.6.1.3)
- Place the mixture of polyurethane between two clean glass plates
- Remove the thin film of polyurethane from between the glass plate after curing time.
- The thin film of polyurethane obtained has a thickness of 4 microns

The sample of polyurethane is then tested using a VASE Ellipsometer (J.A. Woollam Inc.), illustrated in Figure 5.1. Ellipsometric measurements are conducted using light incident at various different angles relative to the normal for different wavelengths on the thin sample of polyurethane. The software provided with the ellipsometer calculates the refractive index variation of the polyurethane as a function of the wavelength. The refractive index of the polyurethane material used to cast the SEH concentrators is illustrated in Figure 5.2 as a function of the wavelength. The graph shows that polyurethane exhibits normal dispersion in the visible and near UV spectral regions down to wavelengths of 400nm. It can be noticed that the refractive index of the polyurethane material is very similar to the refractive index of the PMMA material.

Figure 5.1: J.A. Woollam Inc VASE Ellipsometer

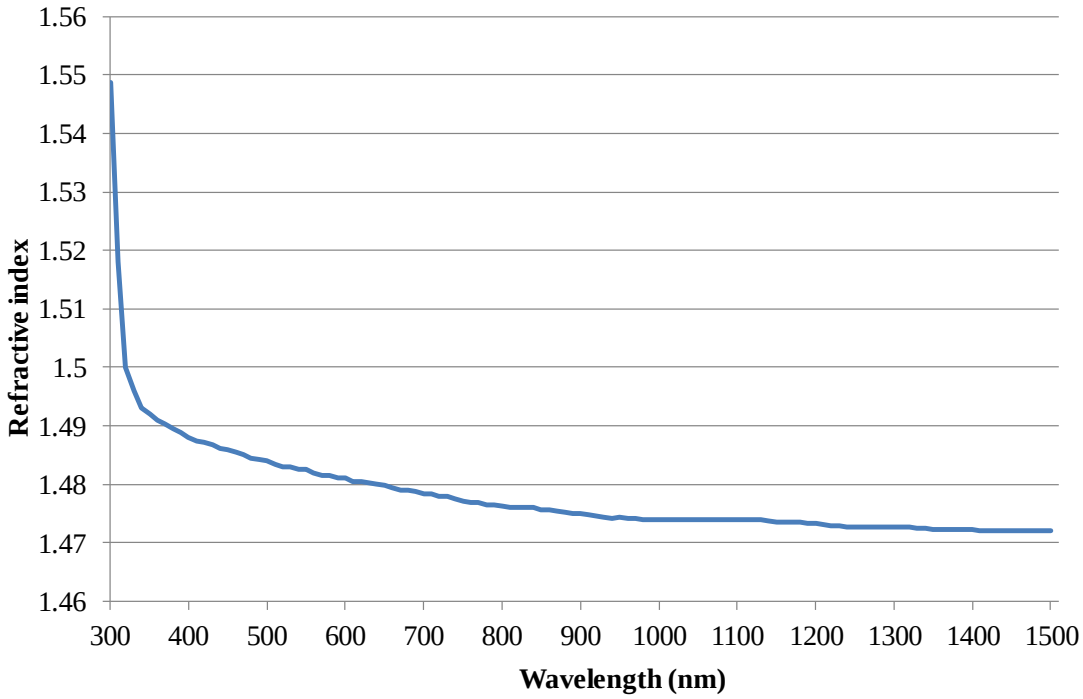

Figure 5.2: Measured refractive index of the thin polyurethane sample

5.2.2 Absorption coefficient measurements

The polyurethane material selected to manufacture the SEH concentrator is water clear material. However, like many other materials the clear polyurethane absorbs part of the incident light in different quantities depending on the wavelength.

The phenomena of absorption of light by the material through which the light is travelling is defined by the Beer–Lambert law [225] that can be written in equation (5.1) as:

$$A = \varepsilon \times c \times l \tag{5.1}$$

Where:

- A = absorbance value (no units)
- ε = extinction coefficient (constant for each substance, units of M^{-1} cm^{-1})
- c = concentration of substance (units of M)
- l = light path length (in cm)

The equation (5.1) can be written as:

$$A = \mu \times l \tag{5.2}$$

Where μ = ε×c is the linear attenuation coefficient also called the absorption coefficient which is the factor of interest. OptisWorks software uses this term to quantify the absorbance of light by the refractive material (polyurethane for the case of the SEH concentrator). The absorbance "A" of the polyurethane is measured using the Lambda 950 Perkin Elmer UV-Vis-NIR spectrometer [226], but it will be specific to the sample tested. The absorption coefficient is then calculated using the thickness of the polyurethane sample and the absorbance "A" measured by the spectrometer. Three parallelepipeds are cast from polyurethane having the same dimensions but with different arbitrary thicknesses (15mm, 23mm and 33 mm); the thickness refers to the side where the light will travel through the sample. The three samples were tested using the spectrometer (Figure 5.3) for each 1nm wavelength interval of light varying from 350nm to 1200nm. The absorbance of the three polyurethane samples as a function of the wavelength is illustrated in Figure 5.4.

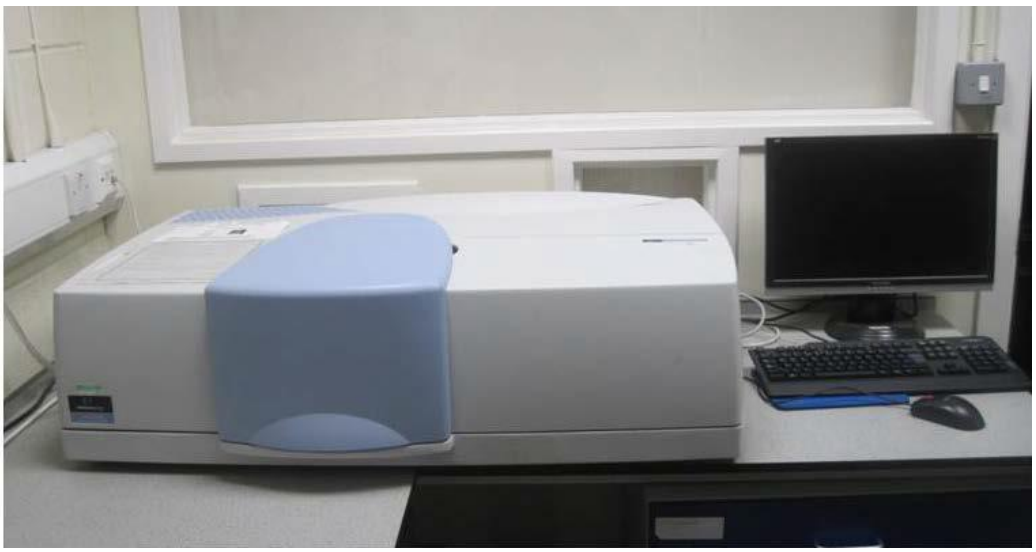

Figure 5.3: The Perkin-Elmer UV-Vis-NIR spectrometer at Heriot-Watt University

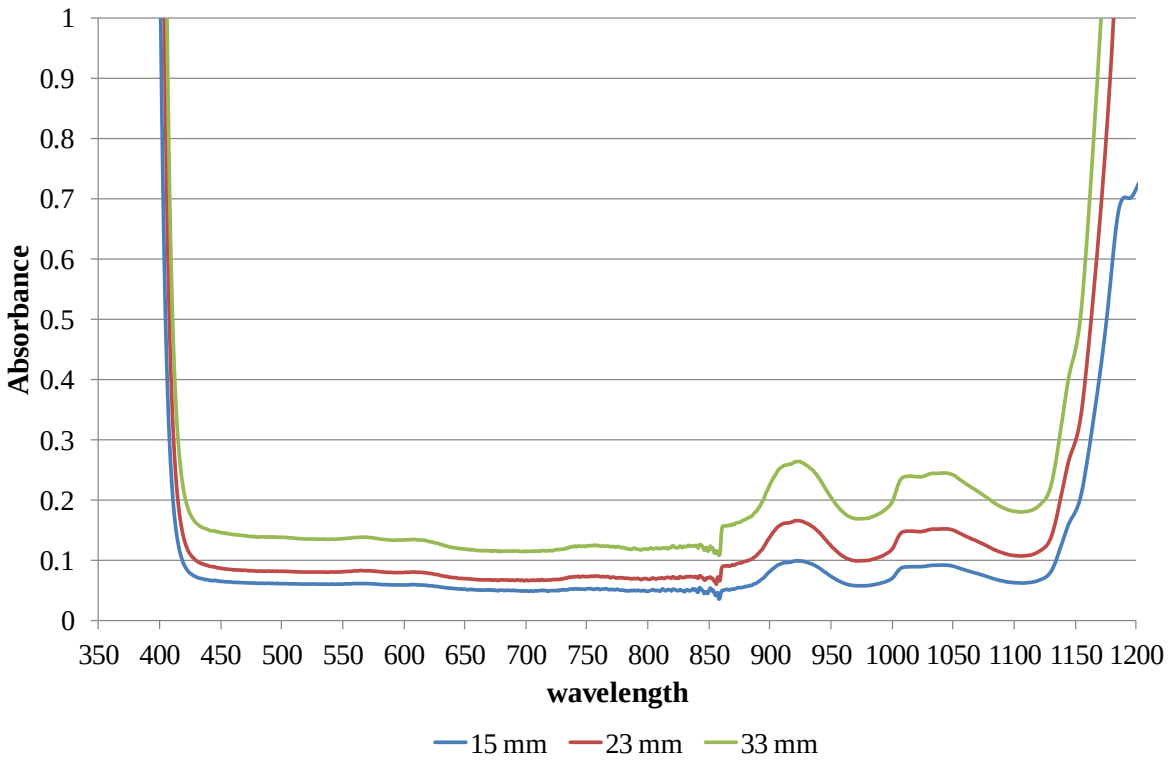

Figure 5.4: Measured absorbance of the polyurethane samples

The values of absorbance for each polyurethane sample in Figure 5.4 are divided by the corresponding thicknesses. The values in the blue line are divided by 15mm, the values in the red line are divided by 23mm and the values in the green line are divided by 33mm. This division is carried out following equation (5.2) in order to calculate the values of the absorption coefficient of the polyurethane to be used to fabricate the SEH

concentrators. The values of the absorption coefficient are illustrated in Figure 5.5 for the three polyurethane samples. As was expected, the values of the absorption coefficient of the three polyurethane samples are the same; the light is absorbed by the polyurethane sample as it is supposed to be. One sample of polyurethane is enough to measure and calculate the absorption coefficient, but it was preferred to use three samples with different thicknesses to ensure the validity of the values measured. The high absorption in this polyurethane material noticed below 400 nm is due to the presence of the UV stabiliser, which is needed for reducing the degradation of the material; therefore all light of wavelengths below 400nm is absorbed. The broad absorption peaks around 930 nm and 1030 nm are due to harmonics of CO and CH bond stretching in the polymer [227].

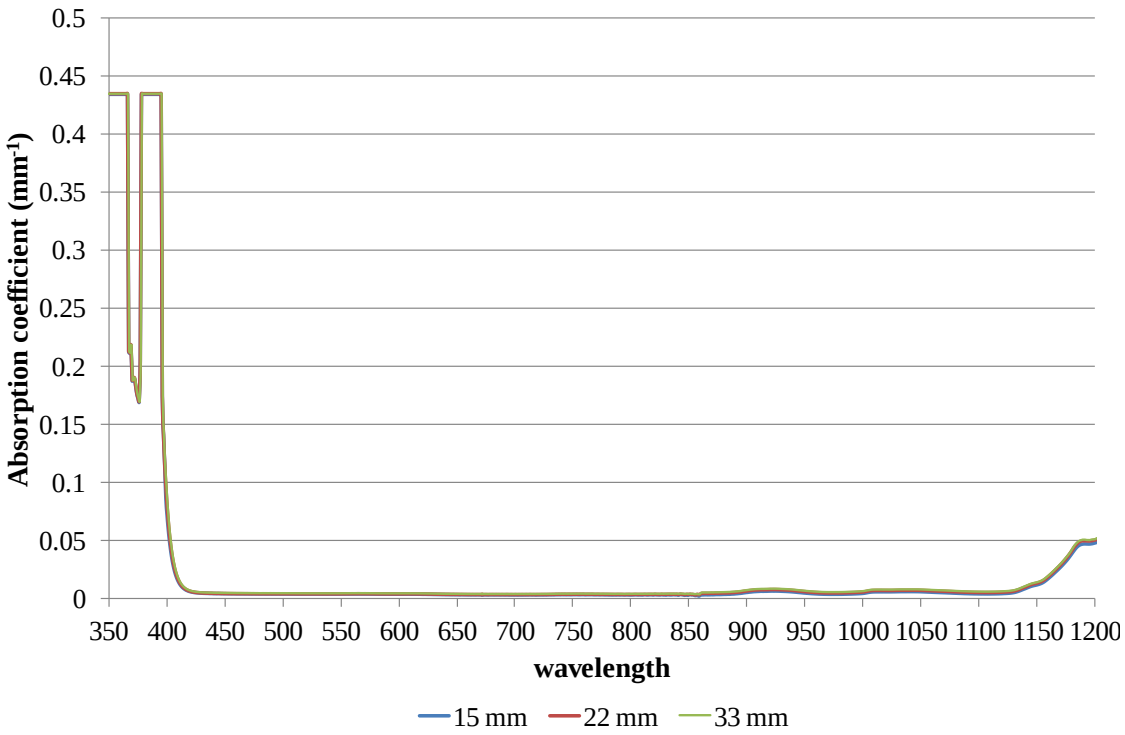

Figure 5.5: Experimental absorption coefficient of the polyurethane material

The values of the absorption coefficient and the refraction index values (from Figure 5.2) are inserted into OptisWorks in the material properties of the SEH concentrator. The characteristics of the PMMA in the optical model developed in section 4.3 (Chapter 4) are now replaced with the polyurethane material characteristics and applied in the optical simulation to the optimised SEH concentrators. It is important to mention that the optical properties measured for the polyurethane material were very similar to the PMMA optical properties measured in the optimisation process; consequently, the

results of the simulated optical efficiency of the five optimised SEH concentrators tested with polyurethane material (illustrated in Figure 5.6) are almost identical to the results of the simulated optical efficiency when tested with PMMA material in the previous chapter.

At this point it is important to specify that the H1.5 SEH concentrator used in the experimental study has an EAR *b/a* equal to 2, instead of *b/a* equal to 1.5 as was calculated for the optimised H1.5 SEH in Chapter 4. This was due to unforeseen circumstances in the manufacturing process – the two concentrators (H1 and H1.5) were ordered prior to completion of the optimisation study in order to begin setting up the experimental part of the study in parallel. This does not affect the overall results, however; the optimised SEH concentrators are elucidated and summarised in Chapter 4; the indoor experimental results are to validate the simulation results and the optical model developed using ray trace via OptisWorks.

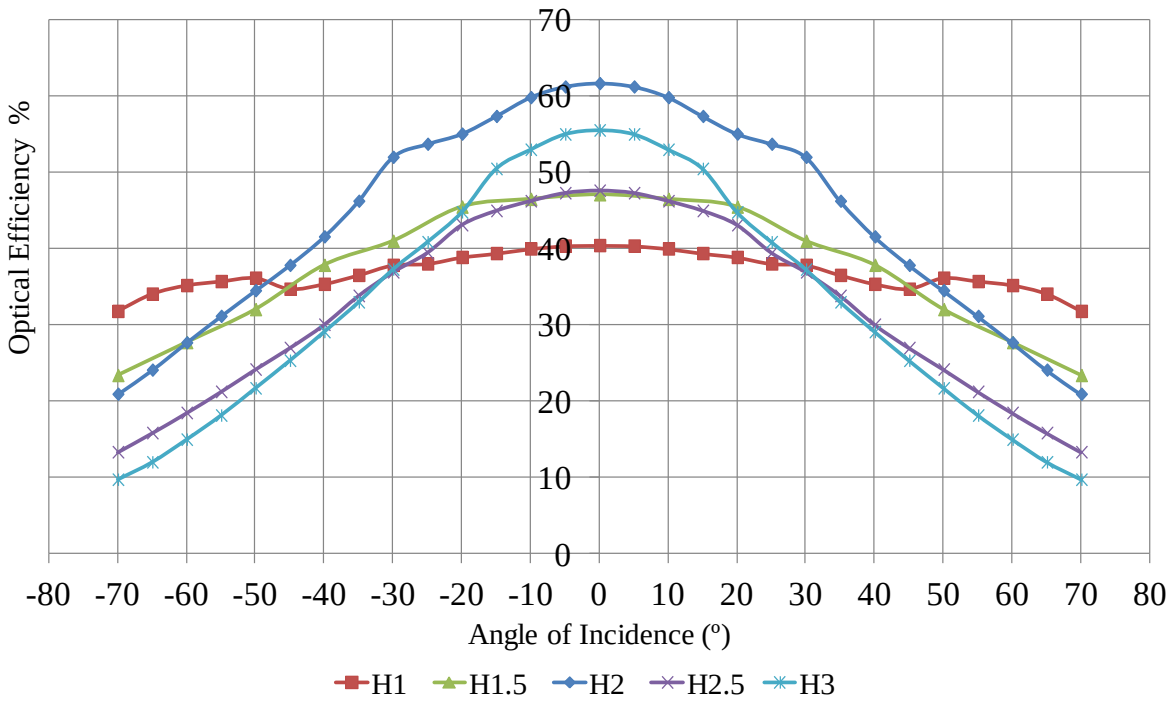

Figure 5.6: Simulated optical efficiency of the optimised SEH concentrator using polyurethane material

5.3 Moulding

5.3.1 Casting moulds

Five casting moulds were designed to fabricate the optimised SEH concentrators (Figure 5.7). This process takes longer than the injection procedure, however, this was

not considered as an obstacle for the current study as only a small number of concentrators were needed for the experimental setup. Furthermore, all of the devices used in this manufacturing process are available in any standard engineering laboratory.

Since the profile of the SEH is not a revolutionary profile, representing a complex geometry, and the finishing of the envelope surface has to be very accurate, the casting moulds were manufactured using Electrical Discharge Machining (EDM) process [228, 229]. EDM is a machining method used for complex shapes; it turns out a smooth surface finish for such a complex and small work piece as the SEH concentrator, which would be very difficult to produce with conventional cutting tools.

The casting moulds are then each coupled with a piece of glass on the underside where the exit aperture of the SEH is formed as shown in Figure 5.8; this is to create the smoothest possible finish to the SEH exit aperture. Glass is the least expensive material with the best smooth finish surface available on the market with a Root Mean Square roughness ~1.2 [230].

The five moulds are designed each with an area covering 100cm^2. Since the optimised SEH concentrators have different geometric dimensions, the number of SEH concentrators that can be cast for each mould is different. An area of 100cm^2 can contain 18 H1 or H1.5 SEH concentrators, 16 H2 SEH concentrators, or 12 H2.5 or H3 SEH concentrators.

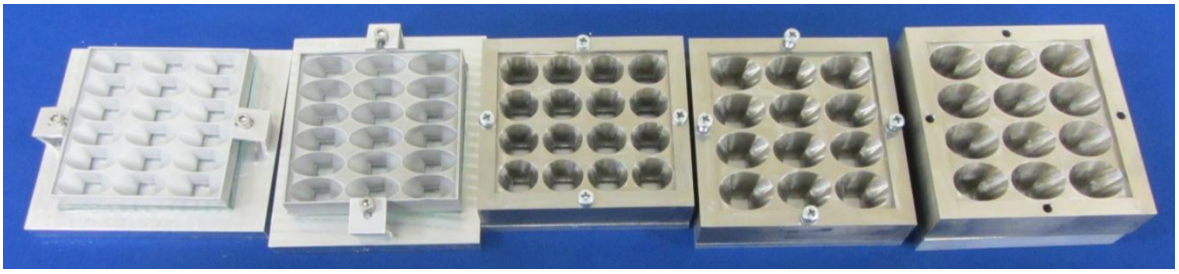

Figure 5.7: The five casting moulds used for the fabrication of the SEH concentrators (H1 to H3 - in order from left to right)

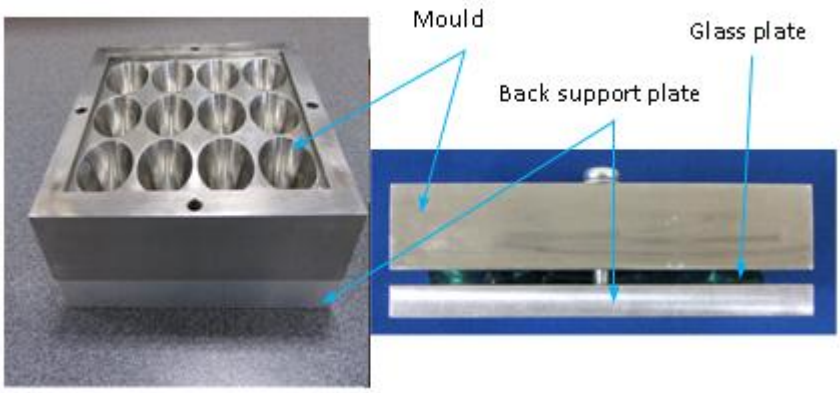

Figure 5.8: Casting mould for the SEH concentrators.

5.3.2 Fabrication of the SEH concentrators

The SEH concentrators are cast using the same procedure described in section 2.8.2 (Chapter 2) to cast the refractive CCPC. The SEH concentrators are made from polyurethane Crystal Clear 200 Series and have a clear transparent look.

Figure 5.9 shows an example of the H3 SEH concentrator cast in the Heriot-Watt University laboratory. The good quality of the cast SEH concentrators obtained confirms the choice of the material, process and method of fabrication for the fabrication of the SEH concentrators. A larger number of SEH concentrators could potentially be manufactured with the same manufacturing process requiring minimal cost and material at this stage of research.

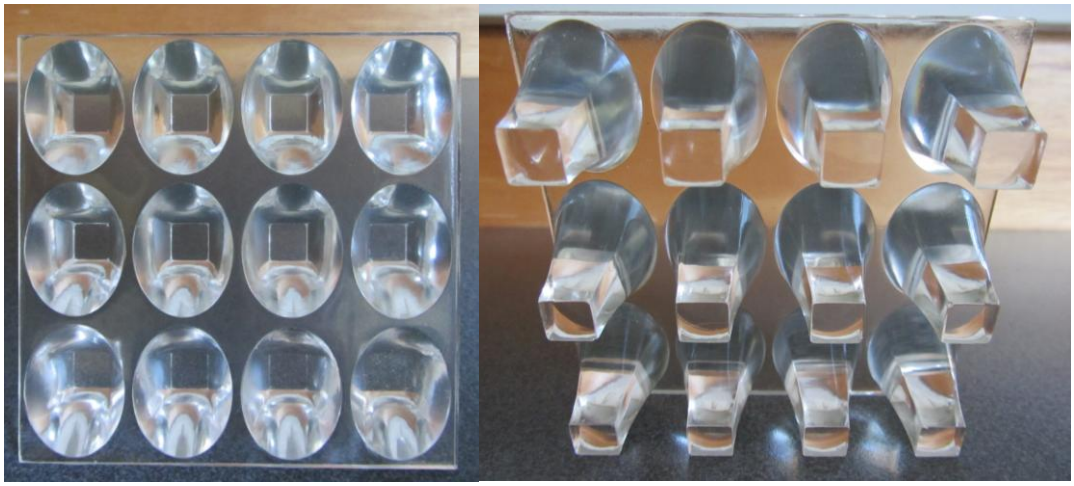

Figure 5.9: Clarity of the cast H3 SEH concentrator using polyurethane material

5.4 TICPV modules assembly

Two PV modules are made with and without being coupled with the SEH concentrators (TICPV) and (TIPV) respectively (Figure 5.10). The TICPV modules are made to be tested in indoor conditions in order to validate the optical efficiency results obtained from the optical simulation. The TIPV modules are necessary to quantify the efficiency of the SEH concentrators.

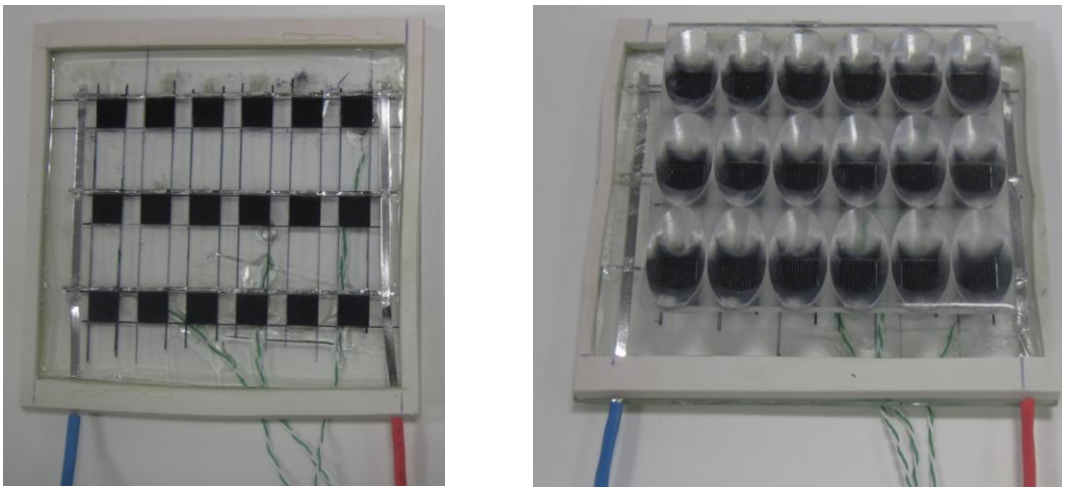

Figure 5.10: Experimental prototype modules (a) without SEH concentrators (TIPV) and (b) with SEH concentrators (TICPV)

The assembly of the TICPV and TIPV modules starts with preparing the back glass plate where the solar cells are placed and connected in the same pattern as the dimensions of the square exit apertures of the SEH concentrators on the mould. The solar cells are soldered using lead free PV ribbon with 0.1mm thickness and 1mm width, the bus bars of the solar cells have a 1mm width. Lead free PV ribbons with 3mm width are used later to connect the TICPV and TIPV modules with the measuring instruments. The solar cells used are $1\,\text{cm} \times 1\,\text{cm}$ laser grooved buried contact silicon concentrating solar cells, described in Chapter 2 section 2.6.1.1. The procedure of soldering the solar cells is outlined in Chapter 2 section 2.6.1.2.

Once this is complete, the soldered solar cells are then covered and protected with the thin layer of encapsulation material Sylgard (as described in Chapter 2 section 2.6.1.3); simultaneously this material is also used to couple the solar cells to the SEH concentrators to complete the TICPV module as illustrated in Figure 5.11. The super

glue used in the initial steps is merely a temporary effect to hold the solar cells in place for the electrical connection part of the fabrication process.

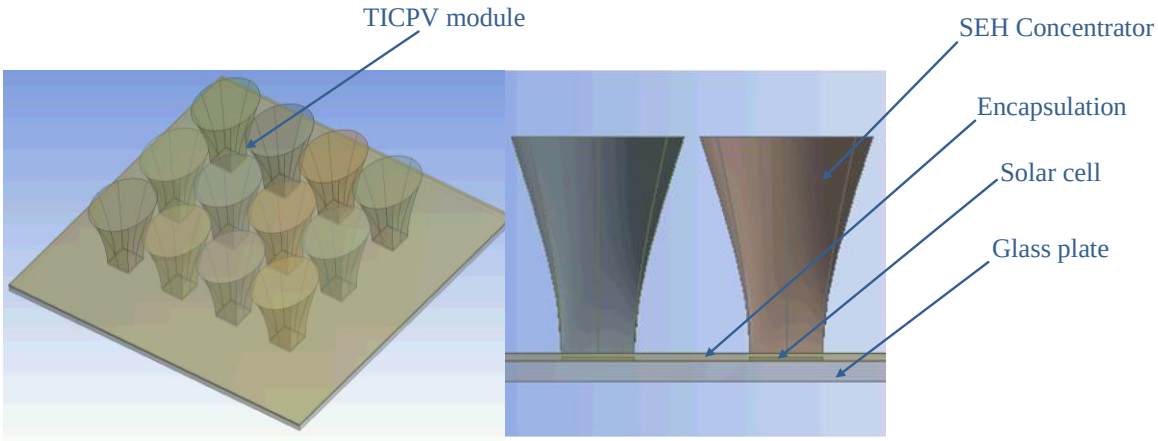

Figure 5.11: Components of the assembled TICPV modules

Five TICPV and TIPV modules were made corresponding to the five optimised SEH concentrators. For the purpose of experimentation, the TICPV and TIPV modules were not covered with the upper glass plate and frame as the objective in this chapter is only to determine the experimental optical efficiency of the SEH concentrators in indoor conditions. The translucent appearance of the TICPV modules made is photographed in Figure 5.12; the hand behind the TICPV module made using 18 SEH concentrators can be seen and is clearly recognisable.

The eight modules (5 TICPV and 3 TIPV) are tested in indoor conditions with the objective of determining the experimental optical efficiency of the SEH concentrators and comparing the results with the simulated results obtained from the optical model developed.

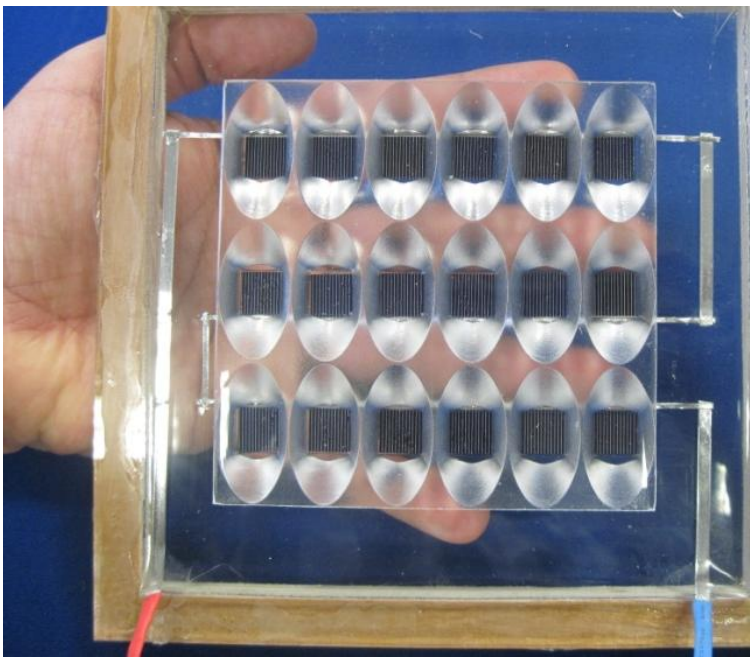

Figure 5.12: Translucent appearance of the TICPV module (made with 18 H1 SEH concentrators)

5.5 Indoor experimental setup

The TICPV modules of each optimised SEH concentrator, and its corresponding TIPV module, are tested exposed to radiated rays from a 1 Sun abet solar simulator. The experimental setup and apparatus are the same as that used for testing the CCPC module described in section 2.6.2 (Chapter 2).

A series of measurements is carried out for different incident angles varying from the normal incident angle to the exit aperture at 0º to an angle of 70º where the power output of the concentrating solar cells is ≈ 0 W. Increments of 5º are considered each time with the measurements taken by the IV tracer at a maintained constant room temperature. Since the incident angle of the irradiation from the solar simulator could not be changed, the different incident angles were achieved by changing the inclination of the CPV module as described in Chapter 2 section 2.6.2.

5.6 IV characteristics of the TICPV and TIPV modules

The electrical performance of the TICPV and the TIPV modules can be characterised by their current-voltage (IV) characteristics. The parameters and description of IV in general curves are described in Chapter 2 section 2.6.2. The different IV and power

curves of the different TICPV and TIPV modules manufactured are presented and compared in this section.

5.6.1 H1 and H1.5 SEH concentrators

The TICPV modules are assembled with 18 solar cells connected in series coupled with either 18 H1 SEH concentrators or 18 H1.5 SEH concentrators. The corresponding TIPV module is composed of 18 solar cells only, connected in series. The IV curve and power curve of the TICPV module made out of the H1 SEH concentrators (H1 TICPV) at 0^o angle of incidence of the light rays are illustrated in Figure 5.13. The maximum short circuit current (I_{sc}) of the TICPV module is found to be 57mA, with a maximum power of 498mW. The fill factor is recorded to be 0.78, which is considered acceptable for modules of crystalline silicon solar cells. The typical fill factor for silicon solar cell >0.7 [231].

Figure 5.14 shows that the TICPV module made out of H1.5 SEH concentrators (H1.5 TICPV) has a higher I_{sc} equal to 64mA coupled with a higher maximum power of 574mW compared to the H1 TICPV modules. The fill factor is recorded to be 0.79.

At the same incident angle 0^o, the IV and power curves of the TIPV module are also illustrated in Figure 5.13 and Figure 5.14. The results show an I_{sc} equal to 34.8mA with a maximum power of 300mW. The fill factor is recorded to be 0.8.

The maximum power produced by the H1 TICPV for $1m^2$ (total module area) is equivalent to 49.8 W/m^2 giving an electrical efficiency ≈ 5%, which is 1.6 times more than the maximum power produced by the TIPV module of 30 W/m^2 giving an electrical efficiency of 3%. The H1.5, which has a higher simulated optical efficiency than the H1 TICPV, produced a maximum power equivalent to 57.4 W/m^2; this power is 1.9 times more that the corresponding TIPV module. The electrical efficiency of the H1.5 TICPV is 5.74%.

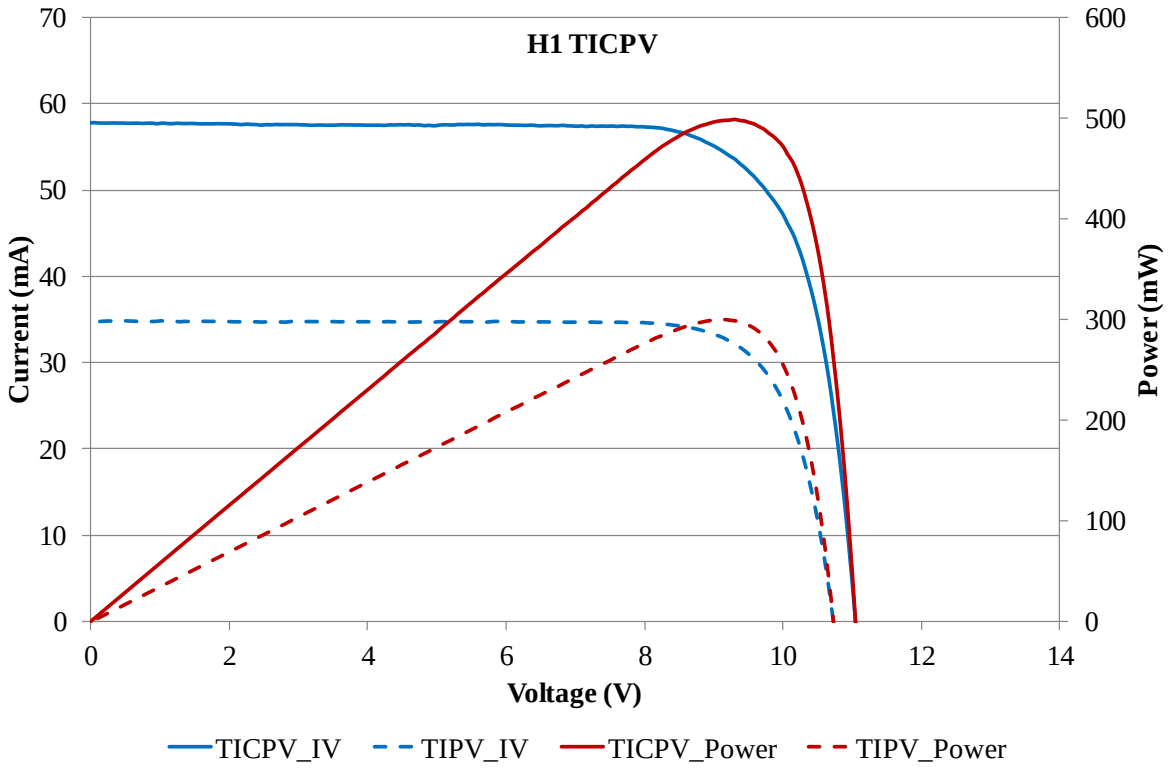

Figure 5.13: IV and power curves of TICPV built with H1 SEH

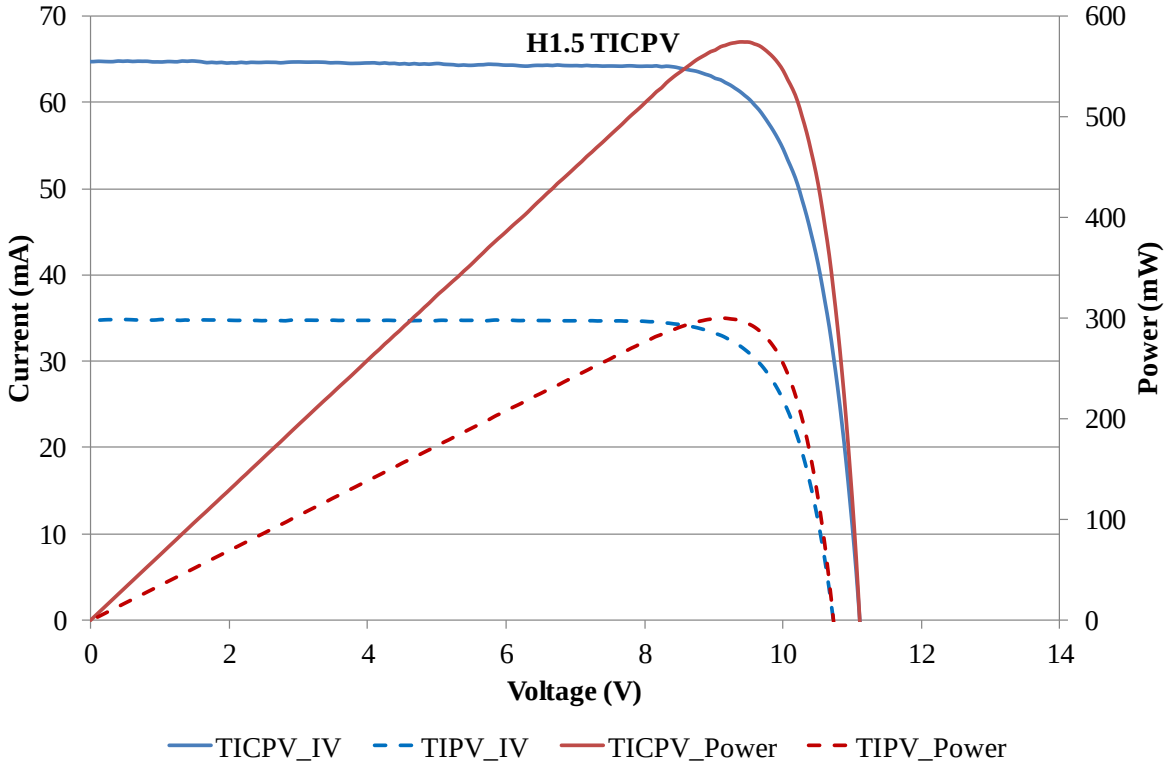

Figure 5.14: IV and power curves of TICPV built with H1.5 SEH

5.6.2 H2 SEH concentrators

This time the TICPV modules are assembled with 16 solar cells connected in series coupled with 16 H2 SEH concentrators. The corresponding TIPV module is composed of 16 solar cells only connected in series. Figure 5.15 shows the IV curve and the power curve of the TICPV module made out of the H2 SEH concentrators (H2 TICPV) at 0^o angle of incidence of the light rays. The maximum short circuit current (I_{sc}) of the H2 TICPV module is found to be 82mA, with a maximum power of 671mW. The fill factor is recorded to be 0.82.

At the same incident angle 0^o, the IV and power curves of the TIPV module are also illustrated in Figure 5.15. The results show an I_{sc} equal to 34.9mA with a maximum power of 264mW. The fill factor is recorded to be 0.8.

The maximum power produced by the H2 TICPV for $1m^2$ (total module area) is equivalent to 67.1 W/m^2 giving an electrical efficiency of 6.7%, which is 2.54 times more than the maximum power produced by the TIPV module of 26.4 W/m^2 giving an electrical efficiency of 2.6%.

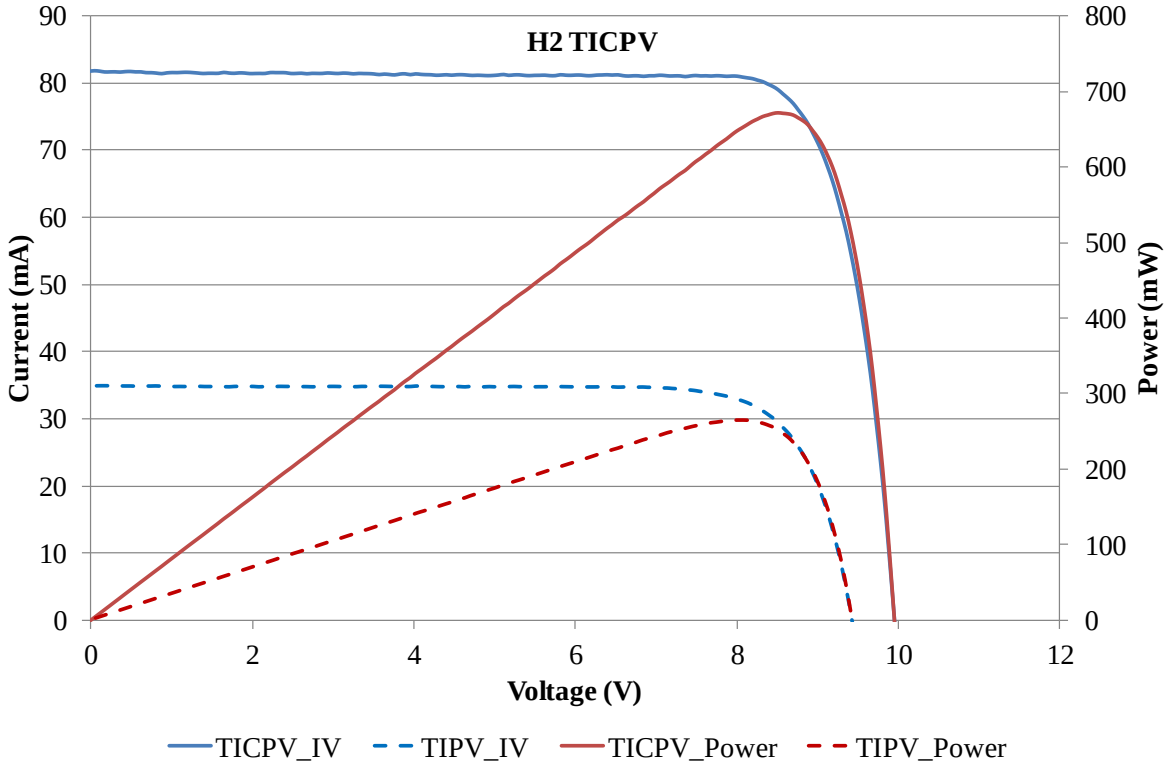

Figure 5.15: IV and power curves of TICPV built with H2 SEH

5.6.3 H2.5 and H3 SEH concentrators

Two TICPV modules are assembled with 12 solar cells connected in series coupled with either 12 H2.5 SEH concentrators or 12 H3 SEH concentrators. The corresponding TIPV module is also composed of 12 solar cells connected in series.

The IV curve and the power curve of the TICPV module made out of the H2.5 SEH concentrators (H2.5 TICPV) at 0^o angle of incidence of the light rays are displayed in Figure 5.16. The maximum short circuit current (I_{sc}) of the TICPV module is found to be 91.8mA, with a maximum power of 566mW. The fill factor is recorded to be 0.82.

Figure 5.17 shows that the TICPV module made out of the H3 SEH concentrators (H3 TICPV) has a higher I_{sc} equal to100mA with a higher maximum power of 623mW compared to the H2.5 SEH. The fill factor is recorded to be 0.83.

At the same incident angle 0^o, the IV and power curves of the TIPV module illustrated in Figure 5.16 and Figure 5.17 show an I_{sc} equal to 34.1mA with a maximum power of 195mW. The fill factor is recorded to be 0.8.

The maximum power produced by the H2.5 TICPV for $1m^2$ (total module area) is equivalent to 56.6 W/m^2 giving an electrical efficiency of 5.6% which is 2.9 times more than the maximum power produced by the TIPV module of 19.5 W/m^2 giving an electrical efficiency of ≈2%. The H3 TICPV which has a higher simulated optical efficiency than the H2.5 TICPV produced a maximum power equivalent to $62.3W/m^2$; this power is 3.2 times more than the corresponding TIPV module. The electrical efficiency of the H3 TICPV is 6.2%.

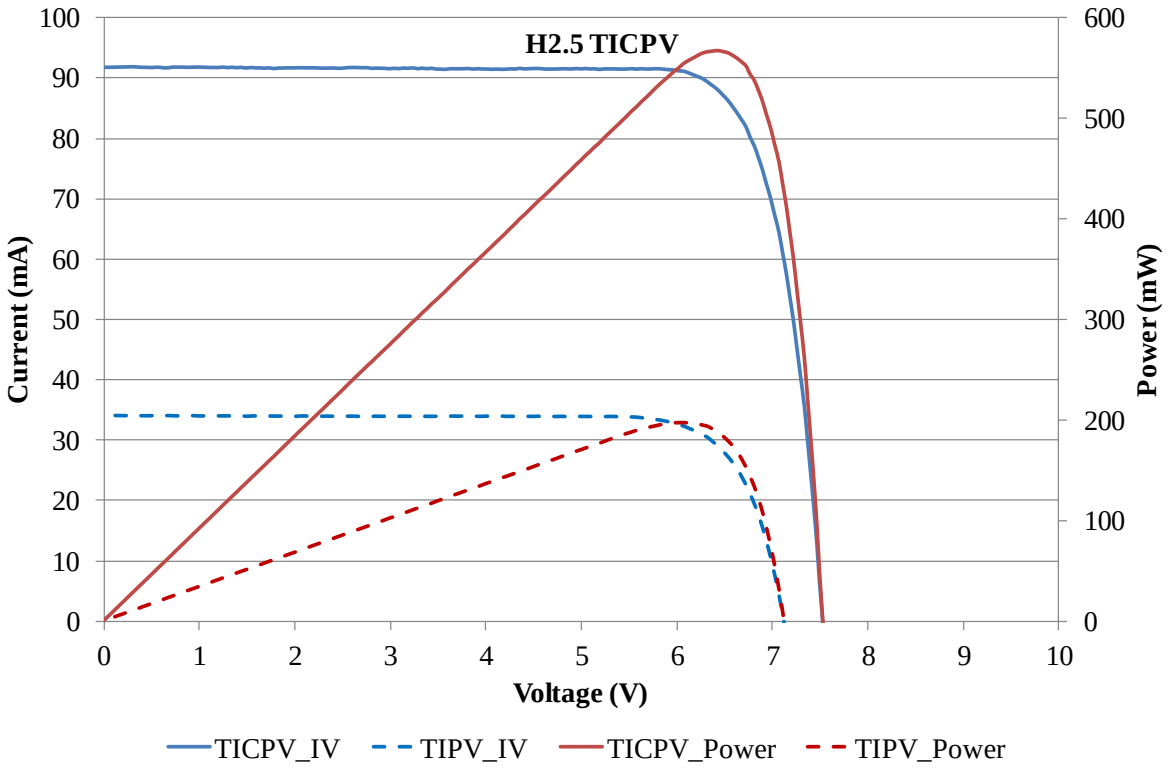

Figure 5.16: IV and power curves of TICPB built with H2.5 SEH

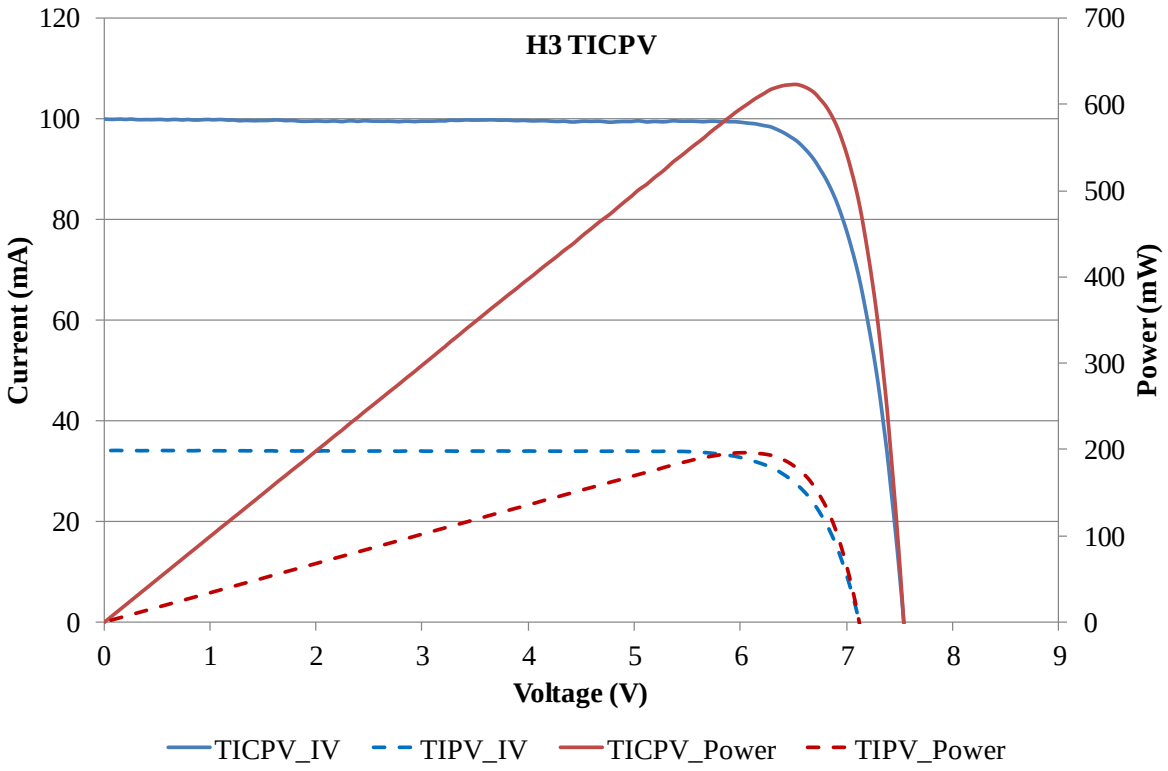

Figure 5.17: IV and power curves of TICPV built with H3 SEH

5.6.4 Comparison between the different TICPV modules

The characteristics of the five TICPV modules fabricated covering an area of 100cm^2 using the different optimised SEH concentrators are summarised in Table 5.1. The H2 TICPV module produces the highest maximum power of 672mW; this is achieved by using 16cm^2 of solar cells. On the other hand, the H3 TICPV module has the highest maximum power produced by one solar cell (1cm^2) equal to 51.91mW compared to 42mW for the H2 TICPV module. When comparing it to the amount of maximum power produced by one solar cell (1cm^2) for the H1 SEH (27.66mW) it can be seen that the H3 SEH produces almost double the amount. The H3 TICPV module uses 12cm^2 of solar cells and uses the C_g=6 SEH concentrator that gives a higher concentration compared to the H2 TICPV module which uses the C_g=4 SEH concentrators and 16cm^2 of solar cells. The values of the gain obtained by the TICPV modules compared to the TIPV module are found to be equal to the optical concentration ratio obtained from the optical simulation in Chapter 4 with a small variation (in the range of 0.02 and 0.18); these values are presented in the last two columns in Table 5.1. These values are considered as the first validation of the simulated results by the experimental results at 0º angle of incidence of the light source. Further validations of the simulated results obtained by OptisWorks are presented in the next section for all the remaining incident angles of the light source.

Table 5.1: Summary of the specification of the five TICPV modules tested

SEH used	TICPV area (cm^2)	C_g	Solar cells area (cm^2)	Maximum power (mW)	Maximum Power/cell (mW)	Gain compared to the TIPV	Simulated C_{opt}
H1	100	4	18	498	27.66	1.66	1.64
H1.5	100	4	18	574	31.88	1.91	2.08
H2	100	4	16	672	42	2.54	2.46
H2.5	100	6	12	566	47.16	2.90	2.83
H3	100	6	12	623	51.91	3.20	3.29

5.7 Validation of the simulated optical efficiency of the SEH

The experimental optical efficiency is calculated from the I_{sc} produced by each TICPV and the corresponding TIPV using equation (2.16) (Chapter 2); it is calculated for the

SEH concentrators at different incident angles of the light source. In order to do this the IV and power curves at each incident angle from 0º to 80º for each of the SEH concentrators is measured.

Figure 5.18 shows an example of the IV and power curves for the H1 TICPV module measured at different angles of incidence of the source light of the solar simulator. It is important to note that the I_{sc} and maximum power produced by the TICPV decrease with the increase of the angles of incidence. The decrease of the I_{sc} goes from 57mA at 0º angle of incidence to less than half (50% decrease) with an I_{sc} value equal to 23mA at 60º angle of incidence. These results of the simulated optical efficiency of the H1 SEH concentrators (H1 TICPV) decreases only 9%, from 40% at 0º angle of incidence to 31% at 60º angle of incidence (red line in Figure 5.6). The percentage decrease of the I_{sc} is larger than the percentage decrease of the $Eff_{Optical}$; this may be due to the fact that when the TICPV is positioned at 60º the radiation received from the solar simulator is less than 1000 W/m^2 as it is received on a sloped surface. This does not, however, affect the method used to calculate the experimental optical efficiency as the two modules (TICPV and TIPV) are exposed to the same conditions; they will both be exposed to the same amount of radiation when they are at the same slope angle, therefore the effects on the I_{sc} will be the same for both modules. In other words, the overall values of maximum power and current for both modules will be lower, due to the effects of the light source at inclinations; however the effects will be comparable for both modules so when calculating the optical efficiencies, the results will not be affected. The only thing that differs between the two modules is the presence of the SEH concentrators on top of the solar cells which will give rise to a higher I_{sc} for the TICPV compared to the TIPV, and from here the optical efficiency can be calculated accordingly. The same issue has been noticed for the other TICPV modules, the H1 TICPV has been used as the example to show the potential effect of the slope on the IV curves.

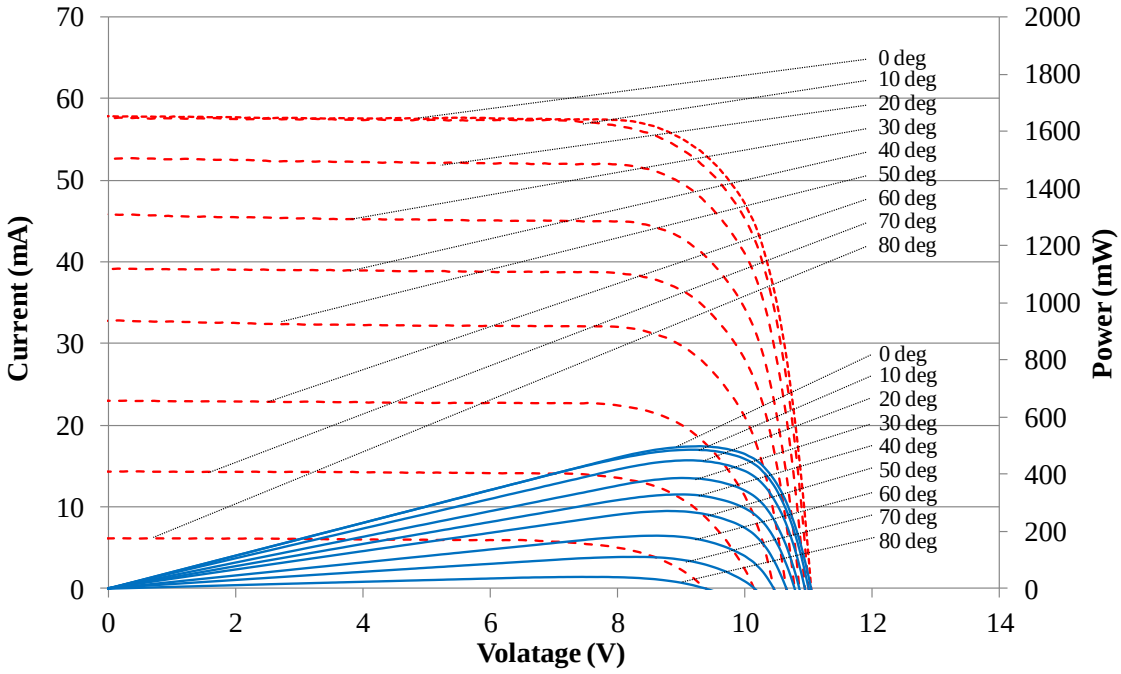

Figure 5.18: IV and power curves of H1 TICPV at different incident angles.

The graphs in Figure 5.19 present the results of the simulated and experimental optical efficiencies of the different optimised SEH concentrators at different incident angles of the light source. Figure 5.19(a) and Figure 5.19(b) show that the experimental optical efficiencies of the H1 SEH and H1.5 SEH concentrators are in good agreement with the simulated optical efficiencies at different incident angles with a negligible variation of 3%. For taller SEH concentrators, the variation between the experimental optical efficiencies and the simulated optical efficiencies is larger but there remains a good agreement between the two trends. Figure 5.19(c, d and e) shows that the variation between the experimental optical efficiencies and the simulated optical efficiencies can reach 8% and that it is larger for higher incident angles of the light source. This variation may be due to the fact that for the H2 SEH, H2.5 SEH and H3 SEH the optical flux distribution is non uniform as discussed in Chapter 4. The I_{sc} of the solar cells increases when they are coupled with the SEH concentrators, however, this value in its self will be affected by the uniformity of the optical flux distribution, therefore creating a variation between the simulation and experimental results. Another general reason for the variation between the experimental and the simulation results of the optical efficiencies can be attributed to slight flaws in the manufacturing process of the SEH concentrators and in the assembly process –there may have been some misalignments of

the solar cells at the exit aperture with the SEH concentrators as this was carried out manually.

The experimental results of the optical efficiencies obtained and illustrated in the graphs in Figure 5.19 can be used to validate the optical model developed using OptisWorks despite the larger variation for taller SEH concentrators between the simulated and experimental results. The graph representing the experimental optical efficiency as a function of the incident angles has a similar trend to the graph representing the simulated optical efficiency as a function of the incident angles.

This validation of the simulated results of the optical efficiency is crucial as they will have a main role in modelling the power output of the TICPV modules in the outdoor conditions which will be discussed in the next chapter.

(a)

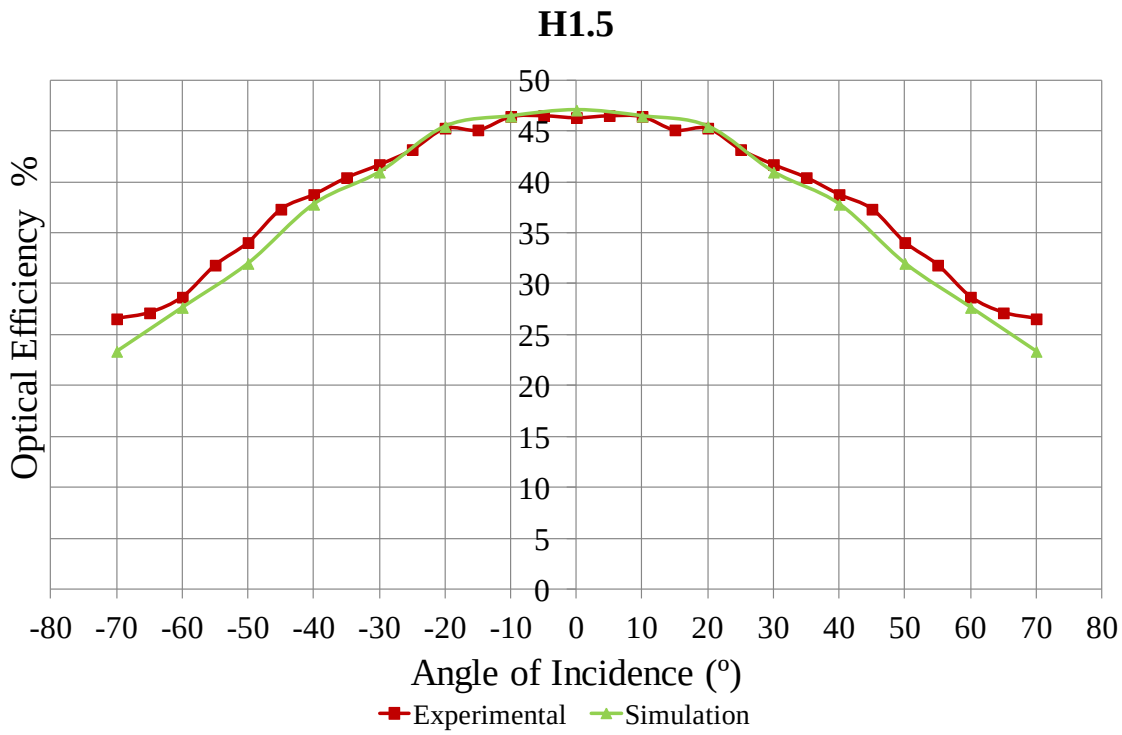
H1.5
Optical Efficiency %
50
45
40
35
30
25
20
15
10
5
0
-80 -70 -60 -50 -40 -30 -20 -10 0 10 20 30 40 50 60 70 80
Angle of Incidence (º)
Experimental
Simulation

(b)

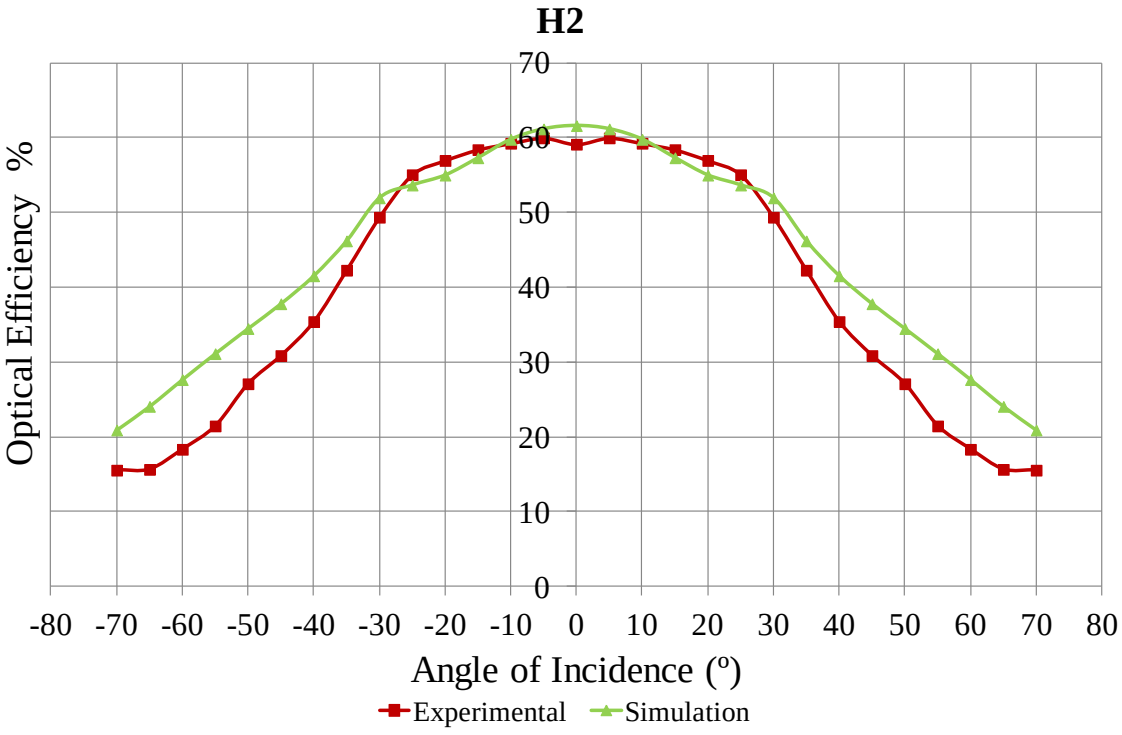
H2
Optical Efficiency %
70
60
50
40
30
20
10
0
-80 -70 -60 -50 -40 -30 -20 -10 0 10 20 30 40 50 60 70 80
Angle of Incidence (º)
Experimental
Simulation

(c)

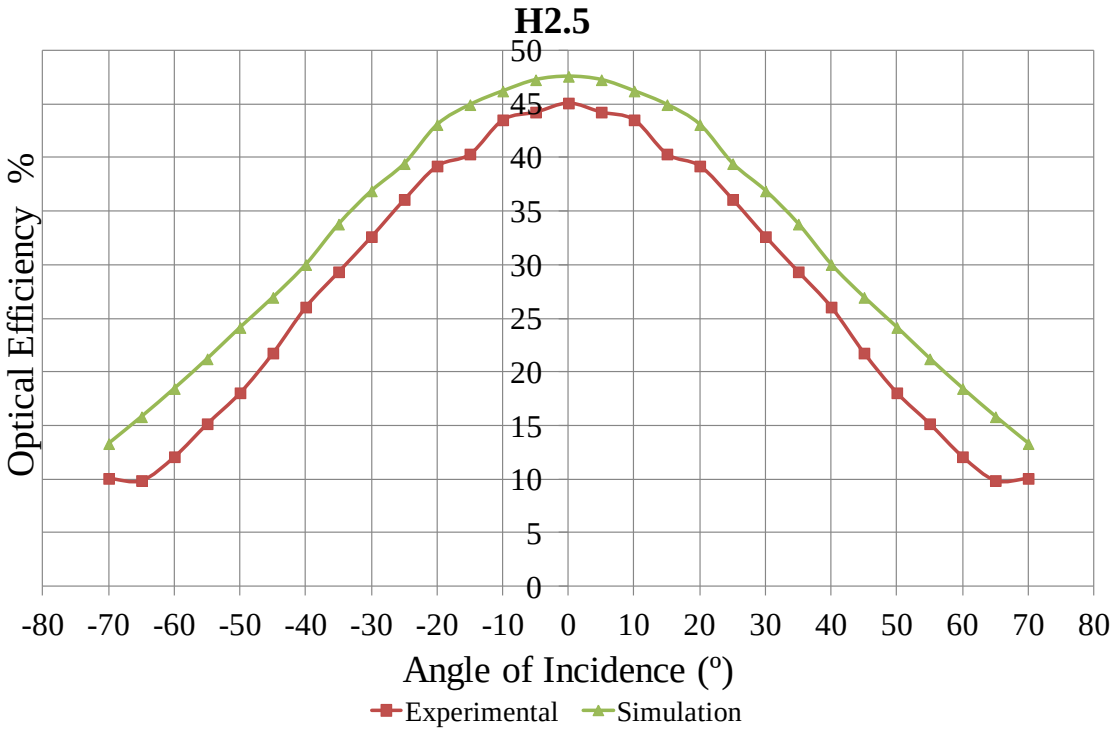

(d)

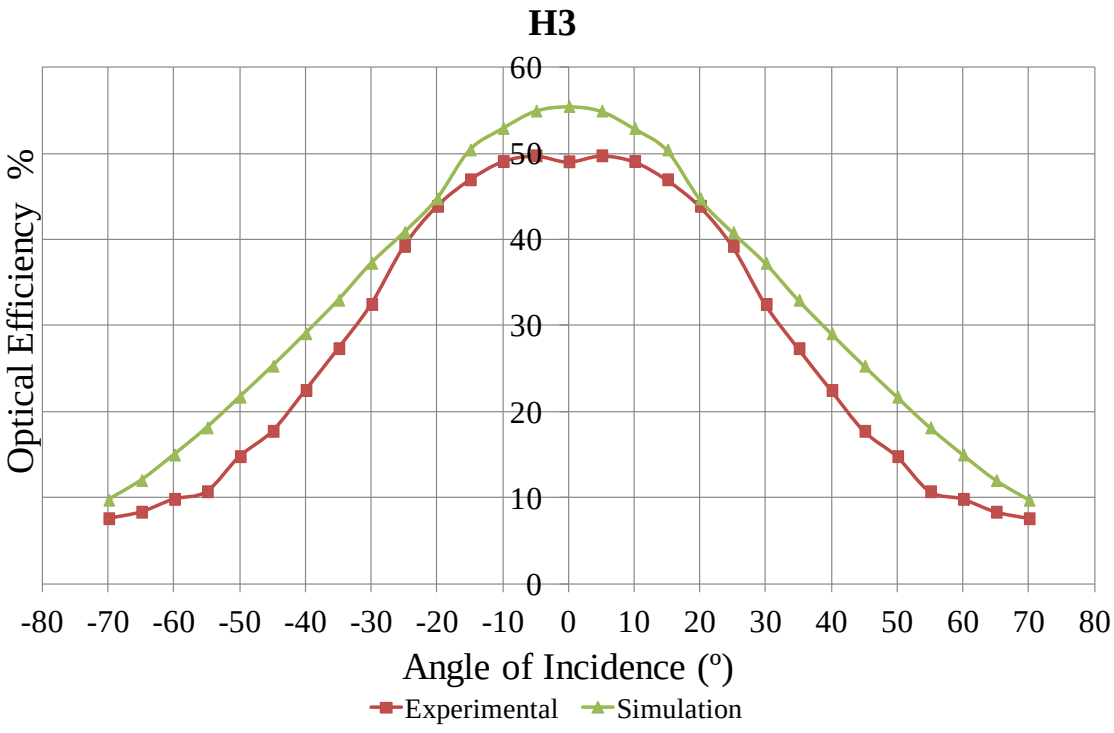

(e)

Figure 5.19: Comparison between experimental and simulation results of optical efficiency: (a) H1TICPV, (b) H1.5 TICPV, (c) H2 TICPV, (d) H2.5 TICPV, (e) H3 TICPV.

5.8 Conclusion

The various steps of the fabrication of the TICPV modules were described in this chapter. The process began with the optical characterisation of the polyurethane material used to cast the SEH concentrators to the electrical connection of the solar cells and involved distinct techniques and high precision devices. The SEH concentrators were cast using smooth surface finish moulds by employing a simple casting method in the Heriot-Watt University laboratory.

The assembled TICPV and corresponding TIPV modules were electrically characterised in indoor conditions using a solar simulator and IV tracer. The results showed that the H2 TICPV module produces 67.2 Watt from $1m^2$ of the module resulting in the highest electrical efficiency of 6.72% using the LGBC solar cells; this value is high when considering that it corresponds to the final product where the power will be produced from a transparent glazing façade or roof of a building in addition to allowing for the light penetration.

The results of the experimental optical efficiencies are in good agreement with the simulated results with a small variation of <3% for the H1 TICPV and H1.5 TICPV and <8% for the TICPV assembled with the taller SEH concentrators. The good agreement between the two results provides validation of the optical model developed permitting and generalising its use for the design of other geometries of optical devices and in particular solar concentrators.

The experimentally validated simulated results of the optical efficiency will be the main input used to model the power output of the TICPV module in outdoor conditions. This is the subject of the next chapter.

Chapter 6: Outdoor experimental characterisation of TICPV modules

This chapter provides details of the outdoor experimental characterisation of the TICPV modules. Five TICPV modules built with the different SEH concentrators are fabricated and assembled to be monitored in outdoor conditions. They are installed in the south east (SE) testing side at Heriot-Watt University in Edinburgh facing the south direction. The outdoor apparatus including the different monitoring and measuring devices are introduced and explained. An integrated model is developed in order to be able to predict the power output by the TICPV modules. As the TICPV module is composed of two main components, (electrical and optical), the modelling of the power output (i.e. the development of the integrated model) requires two types of modelling – electrical and optical. Both models are described and a step by step explanation of the integrated model is outlined. The chapter concludes with the results of the outdoor experimental measurements for the characterisation of the TICPV modules. The results are also used to validate the integrated model (optical and electrical) developed.

6.1 Introduction

Following on from the indoor study, it is important that the performance of the five optimised TICPV modules be studied in real conditions similar to where they would be installed (outdoor conditions). Since the solar concentrators used are static, their performances are directly linked to their positions to the sun rays as this specifies their optical efficiencies and how much energy will be converted to electricity.

The TICPV modules are fabricated for outdoor testing and characterisation. This chapter introduces the TICPV modules that are used in the outdoor setup and presents the methodology used for the outdoor experiment. Furthermore, the development of an integrated model for the prediction and validation of the power generated by the different TICPV modules in outdoor conditions is described; this includes an electrical simulation study in order to determine the parameters of the two-diode equivalent circuit model as well as an optical efficiency simulation study in order to determine the optical efficiency of the SEH concentrators under both direct and diffuse sunlight. Due to the fact that the experiment is carried out outdoors, the characterisation of the TICPV modules needs to incorporate both direct and diffuse solar radiation, unlike the previous experiments (simulation and indoors) which examined only the direct radiation. This

will be used as input for the integrated model to give an idea of what to expect in the outdoor experimental study and provides a set of results with which to compare the experimental values. The chapter concludes with final results of the outdoor experiment.

6.2 Characteristics of the outdoor TICPV modules

Five outdoor TICPV modules are made in different sizes and different frames as if for real applications. The same procedure used to assemble the solar cells and the SEH concentrators to manufacture the indoor TICPV modules was followed (Chapter 5, section 5.3 and 5.4), plus in this case an outer frame and top glass plate is added to the array.

The H1 TICPV is fabricated out of 144 H1 SEH concentrators and the H1.5 TICPV is fabricated out of 54 H1.5 SEH concentrators as shown in Figure 6.1. Both the H1 TICPV and the H1.5 TICPV are integrated into a domestic double glazing window as shown in Figure 6.1(b). It is important to point out that the glass and the frame of the double glazing window are kept the same; the solar cell, the SEH concentrators and the encapsulation material are simply integrated into it without any changes. This was feasible for the H1 and H1.5 SEH concentrators as these are both short in height compared to the other optimised concentrators. By incorporating the concentrators into the double glazing window, it becomes clear as to how easily these TICPV modules can be fabricated and also presents one of the possible installations of the TICPV modules. This effectively shows how the cost of the frame and the front and back glass plate can be saved by using the already existing window components. The positions of the thermocouples placed on the H1 TICPV and H1.5 TICPV to monitor the temperature of the solar cells are represented with the red colour in Figure 6.1(a).

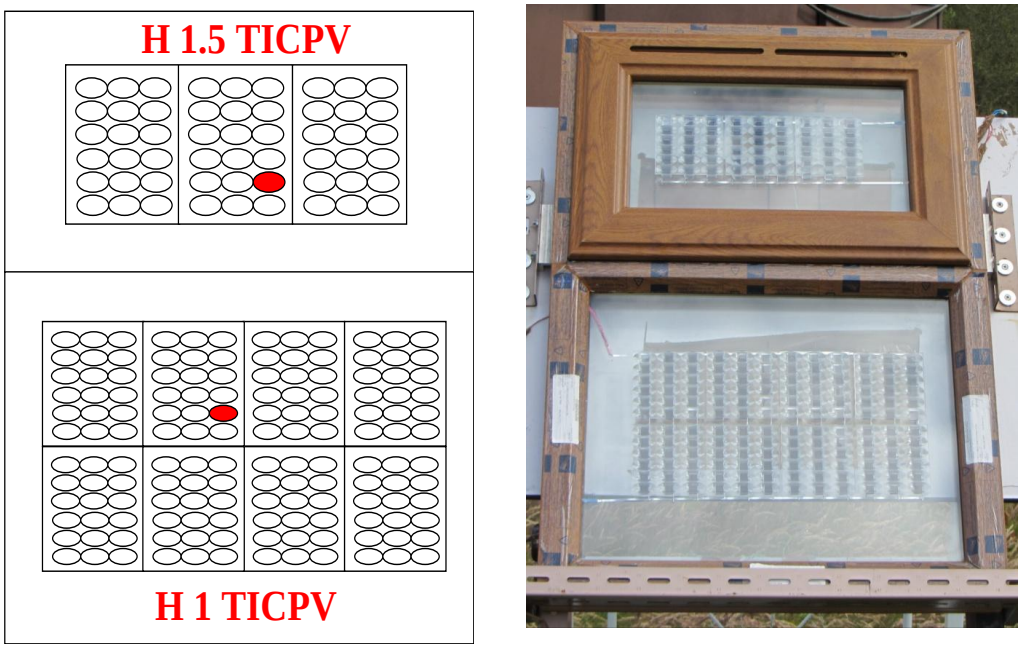

Figure 6.1: H1 TICPV and H1.5 TICPV module formation (a) thermocouple positions, (b) double glazing window with integrated TICPV modules.

The H2 TICPV module is fabricated with 96 H2 SEH concentrators as shown in Figure 6.2(a) and the H2.5 TICPV module is fabricated with 36 H2.5 SEH concentrators as shown in Figure 6.2(b). These two modules are fabricated with an aluminium frame similar to those used for a variety of glazing façades or roofs.

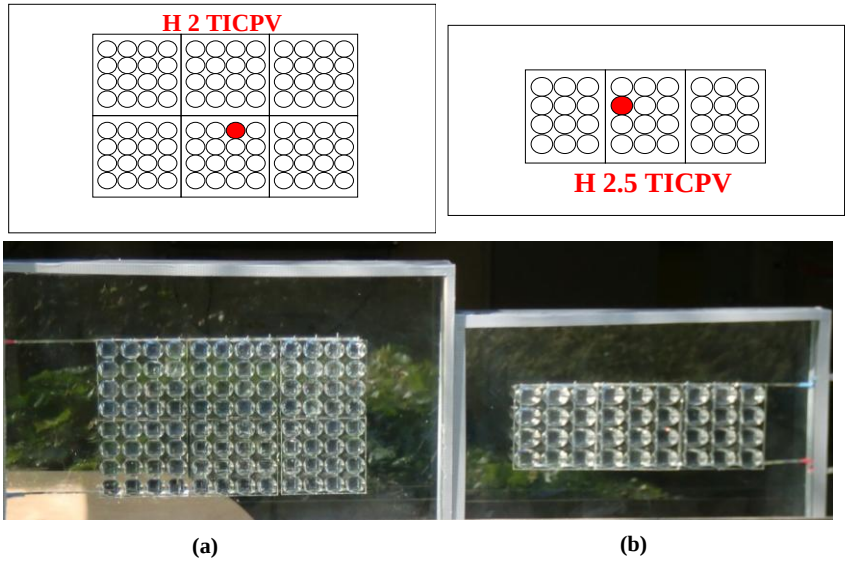

Figure 6.2: Module formation with thermocouple position of (a) H2 TICPV module and (b) H2.5 TICPV module.

The H3 TICPV module is fabricated with 30 H3 SEH concentrators as shown in Figure 6.3. This module is fabricated with a frame made of aluminium profiles used for glazing carton walls supplied by KJN Aluminium as shown in Figure 6.3(b). This aluminium frame is an example of the thick glazing modules available on the market. The thickness between the two glass panes of the glazing module is 3.5cm allowing for the integration of tall SEH concentrators such as the H3 SEH concentrators with the solar cells. The position of the thermocouple is shown in Figure 6.3(a).

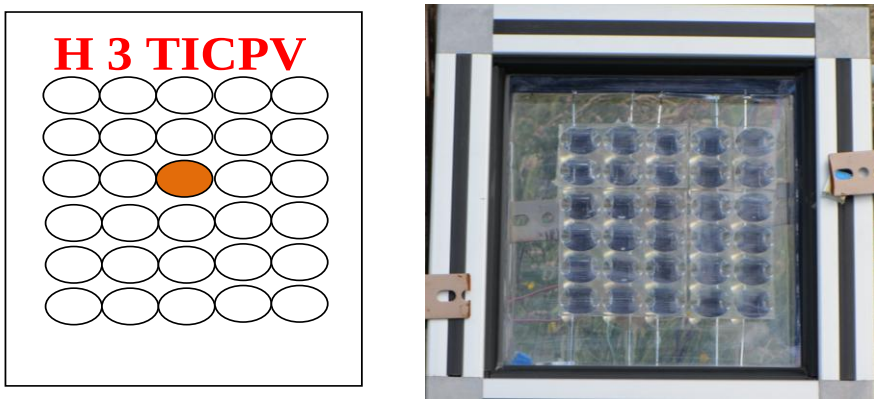

(a) **(b)**

Figure 6.3: H3 TICPV (a) thermocouple position and (b) double glazing window with integrated H3 TICPV

6.3 Experimental location

The five outdoor manufactured TICPV modules described above are installed in Edinburgh (Latitude: 55.9N, Longitude: 3.2W) on a plane tilted 55º to the horizontal facing the south direction.

The choice of Edinburgh as a location is due to the fact that Heriot-Watt University have a solar energy (SE) testing site. It is ideally located in an open field, with no shading from trees or buildings. The location of the SE test site and the photograph of the open field around the test site are shown in Figure 6.4.

(a) **(b)**

Figure 6.4: (a) Location of the SE test-site at Heriot-Watt University Edinburgh campus (b) photograph showing the open field of the test site without obstacles for shading

6.4 Description of outdoor experimental setup and apparatus used

The TICPV modules are mounted on a set-up which can be inclined as required (Figure 6.5 (a)), however the angle 55º was chosen as it corresponds to the slope angle that provides the minimum variation of the angle of incidence of the sun rays at noon in Edinburgh where the outdoor experiments and characterisation of the TICPV modules are carried out. Sellami and Mallick [232] have shown that the variation of the angle of incidence of the sun rays has to be kept the minimum possible for a static solar concentrator; more specifically, it was found that at a slope angle of 55º in Edinburgh they vary only between 0º and 23º. Furthermore, the TICPV modules have to be facing south in order to have this low variation of angle of incidence, hence the chosen orientation and slope of the current experimental setup.

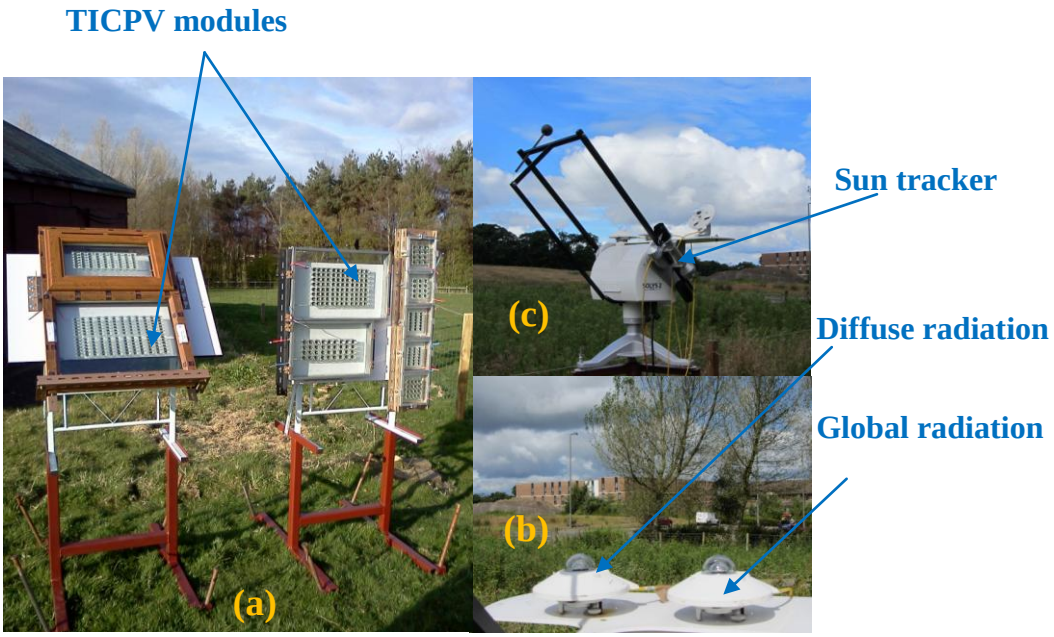

Figure 6.5: Outdoor experimental setup showing (a) TICPV modules mounted at an inclination of 55° (b) two pyranometers, one to measure the global radiation and one to measure the diffuse radiation (c) the sun tracker.

For an accurate measurement of the direct, global and diffuse radiation, a sun-tracker from Kipp & Zonen is used in this study. The characterisation of the five TICPV modules requires the measurement of different solar radiation at different times during the day. This is achieved by using three pyranometers connected to the data logger and IV tracer to measure:

- the solar radiation on the sloped plane of the modules connected to the IV tracer
- the global radiation on the horizontal plane
- the diffuse radiation

In addition, one pyrheliometer is connected to the data logger to measure the direct radiation; this is mounted on the sun tracker. The sun-tracker used is SOLYS 2 where the pyrheliometer is mounted to track the sun and measure the direct radiation as shown in Figure 6.5(c). On the top horizontal plate of the sun-tracker, two pyranometers are installed [233] as shown in Figure 6.5(b), one to measure the global radiation and the other to measure the diffuse radiation with the help of the shading assembly. The shade created on the second pyranometer eliminates the direct radiation and as such only the diffuse radiation can be measured. The shadow is created with precision adjustment of a

ball shape that changes position accordingly to the sun positions. The sun-tracker tracks the sun position using two options depending on the weather condition; it uses:

- A sun sensor when the sky is clear and there are no clouds hiding the direct radiation of the sun (when the solar irradiation is higher than 300 W/m^2). It determines the exact position of the sun. The position accuracy achieved by the sun sensor is about 0.02º.
- An integrated GPS receiver when it is cloudy and no direct sun radiation can be detected. It configures automatically the location, time and the solar position giving accuracy within 0.1º.

All the pyranometers used in this study are CMP-11 from Kipp & Zonen. These pyranometers use temperature compensated detector technology to generate voltage, which can be converted to solar irradiation by the use of a sensitivity factor. The spectral range of the pyranometer is 285nm to 2800nm and it is capable of measuring maximum solar radiation up to 4000 W/m^2 [234].

The pyrheliometer used with the sun tracker is the CHP-1 from Kipp & Zonen [235]. This pyrheliometer has a spectral range of 200nm to 4000nm and it can also measure solar irradiation up to 4000 W/m^2 with a response time of less than five seconds. The direct solar radiation measured from the pyrheliometer is used to confirm the reading from the other pyranometers and to confirm that the solar tracker is working correctly.

To characterise the different TICPV modules a module selector (MI-520) switching device from EKO is connected to the IV tracer. This switching device is compatible with the IV-tracer for continuous characterisation of 12 modules at a time [236]. Each channel of this module selector can be customised for the maximum rated voltage and current of the module under test.

A high speed data acquisition system from National Instruments (NI) is used in this study for the collection of the temperature and solar irradiation data. The NI data logger contains a chassis for the insertion of different NI modules for the measurement of different parameters such as voltage, current and temperature. Different modules from NI are available for different parameters depending on the rating of the device under test. One 24 bit, 16 channel voltage module is used in this study to collect the temperatures of the solar cells and the solar irradiation data. The measured data is collected through a data cable from the chassis. A LabView programme was written to collect the data.

The module selector, IV tracer, data logger and computers mentioned above are kept in a control room located on the SE testing site as shown in the photo in Figure 6.6; they are connected to the TICPV modules and the measuring devices via cables and connectors.

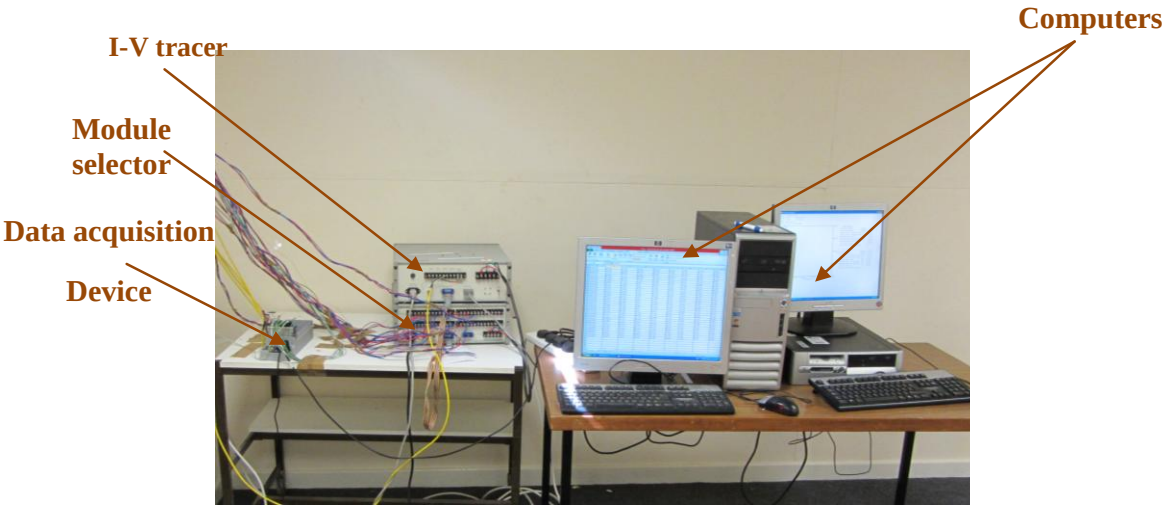

Figure 6.6: Outdoor controlling and measurement instruments located in the control room on the SE testing site

6.5 Measurement of solar cell temperature

The solar radiation from the three pyranometers and the pyrheliometer, the IV curves produced by each TICPV and the temperature of the solar cells of the different TICPV modules are measured and recorded with an interval of one minute from 3 am until 10pm. While the amount of sunlight received is an important factor in a solar cell's power production efficiency, the temperature can reduce efficiency and lower the energy output of the solar cell. For this reason, it is also important that the temperature of the solar cell is measured. This section details the steps taken to measure and validate the temperature of the solar cell.

With regards to measuring the temperature of the solar cells an obstacle was encountered; it was not possible to stick the thermocouples directly on to the surface of the solar cells as is done with flat PV panels due to the presence of the SEH solar concentrators. As a result, the temperature instead needs to be measured on the back of the glass plate directly underneath where the solar cells are located. In this case an assumption had to be made in that the temperature of the glass is equal to the

temperature of the solar cells located at the same position. It is necessary to verify this assumption in order to be sure that the results obtained from the outdoor experiment are valid.

6.5.1 Validation of solar cell temperature

In order to examine the effects of the solar radiation and the concentration of the solar radiation on the temperature of the solar cells in the first instance, a 3-D heat transfer model was employed using ANSYS 12.1, CFX. The model was originally developed and used by Kumar et al. [237] and later by Sarmah [22] to predict the temperatures of similar solar cells in an integrated CPV system. In the 3-D heat transfer model developed, the continuity, momentum and energy equations were solved with convergence criteria of 10^{-4}. The results of the solar cells temperatures obtained were validated by experimental measurements.

In the current study, the same 3-D heat transfer model is applied to the indoor H3 TICPV module composed of 12 solar cells connected in series coupled with 12 SEH concentrators in the $0.01m^2$ modules. The H3 TICPV system is exposed to a uniform radiation of 1000 W/m^2 at the entry aperture of the H3 SEH concentrators. Since it is known that the optical efficiency of the H3 concentrator is equal to $Eff_{Optical} = 0.55$ at 0º angle of incidence, the heat source on the solar cells is equal to $1000 \times Eff_{Optical} \times C_g = 1000 \times 0.55 \times 6$ resulting in a value of $3300W/m^2$. This value corresponds to the amount of energy that will reach the solar cells after concentration; as such, in the heat transfer model a heat source of 3300 W/m^2 is considered on the top surface of each solar cell. The ambient temperature used in the simulation is considered as 19ºC; this is the temperature of the laboratory when a series of measurements is carried out on the TICPV to measure the temperature of the solar cells. The heat transfer coefficient of $7W/m^2$ K is considered between the ambient air and the different components of the TICPV module that are exposed to air. The thermo-physical properties of the components in the H3 TICPV module used in this simulation are shown in Table 6.1.

Table 6.1: Thermo-physical properties of the material used in the H3 TICPV module

Component	Material	Thickness (mm)	Thermal Conductivity ($Wm^{-1}K^{-1}$)	Density ($Kg.m^{-2}$)	Specific Heat Capacity ($J.kg^{-1}.K^{-1}$)
Concentrator	Polyurethane	30	0.1875	1162	1465
Encapsulation	Sylgard	0.5	0.16	1030	1100
Solar cell	Silicon	0.3	148	2330	712
Rear glass plate	Glass	3	1.4	2500	750

The results of the steady state 3-D heat transfer model on the H3 TICPV module are illustrated in Figure 6.7. It shows that the temperature of the solar cells reaches a uniform value of 54ºC (327 K). What is important to notice is that the temperature of the glass below the solar cells is also equal to 54ºC. This result provides verification of the assumption made with regard to the temperature of the solar cell – the results obtained in the outdoor experimental study later in the chapter via the placing of the thermocouple to measure the temperature experimentally directly on the surface of the glass plate as opposed to directly on the solar cell will be valid.

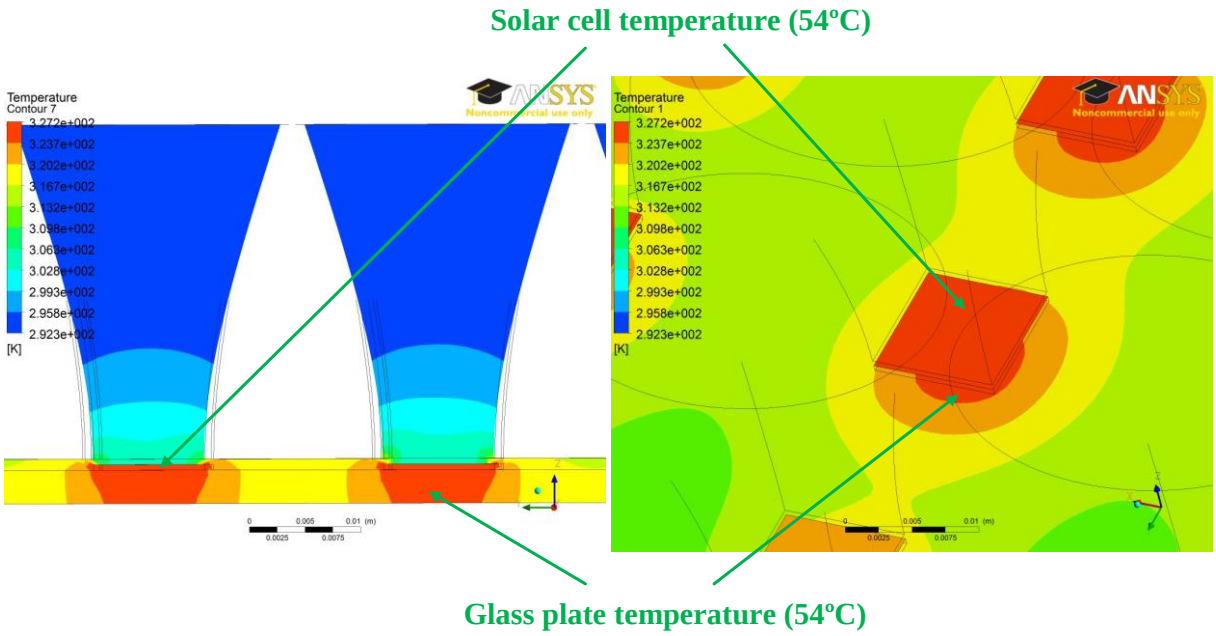

Figure 6.7: Temperature distribution of the H3 TICPV system

6.5.2 Validation of the 3-D heat transfer model

The results of the thermal model above, giving the temperature of the solar cells and of the rear glass plate, validate the assumption of measuring the temperature of the solar cells on the back of the rear glass plate. The 3-D heat transfer model, however, also needs to be validated in order to fully accept this assumption.

The indoor H3 TICPV module is exposed to the radiation of the solar simulator in the same conditions considered in the thermal model presented above. The H3 TICPV is exposed to perpendicular light rays from the solar simulator of 1000 W/m^2 and kept in a room with a temperature of 19ºC, and the temperature of the middle of the rear glass where the solar cells are placed is monitored and recorded. Concurrently, the IV curves and the power generated by the H3 TICPV modules are also recorded. At time 0 minutes, the temperature of the solar cell is equal to 19ºC rising to 46.4°C after 20 minutes. After two hours of testing, it can be seen in Figure 6.8 that the temperature is maintaining a steady value; the temperature measured by the thermocouple at 120 minutes reaches a constant value of 56.25ºC, which coincides with the result of the steady state solved by the 3-D heat transfer model.

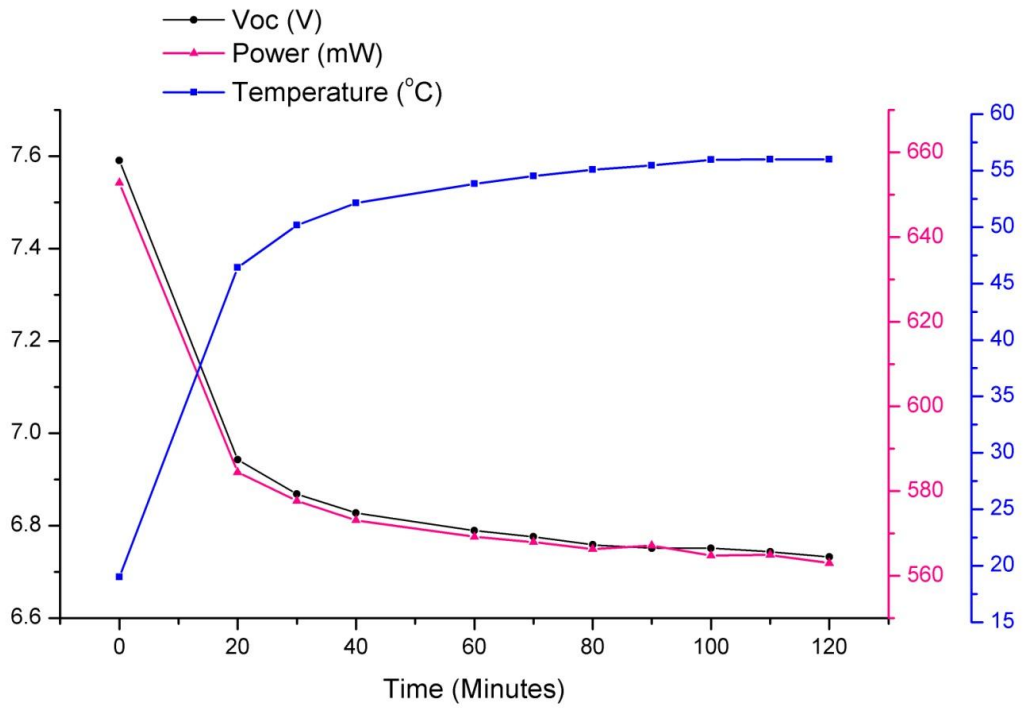

Figure 6.8: Experimental variation of the power, voltage and temperature of the solar cell (H3 TICPV module).

Coincidently, the graph above also shows the experimental power curves of the solar cell (H3 TICPV module) recorded at different temperatures. The increase of the temperature of the solar cell is followed by a decrease of the maximum power due to the decrease of the V_{oc} which is also affected by the increase of temperature. These results show the adverse effects of the temperature on both the power and voltage of the solar cells.

From the results, it can be seen that there is a 2ºC difference between the temperature of the simulation study (54ºC) and the temperature of the experimental study (56.25ºC). This variation is very low (negligible) representing less than a three percent variation between the simulated and experimental results. As such, the experimental results have provided validation of the 3-D thermal model, and therefore the temperature of the solar cells can be assumed to be equal to the recorded temperature of the glass.

6.6 Modelling of the power output of the TICPV modules

As the TICPV module is composed of two main components, the solar cell (electrical component) and the solar concentrator (optical component), the modelling of the power output requires two types of modelling – electrical and optical. The electrical characteristics of a PV module are modelled using the well-known two-diode equivalent circuit model for a single solar cell. This requires, as input, the temperature of the solar cell and the energy radiation on the solar cells which is the output of the SEH concentrator. The acquisition of the energy radiation on the solar cell can only be predicted using the optical modelling which includes the calculation of the angles of incidence and the solar azimuth angles of the sun rays throughout the whole of the day. In other words, knowing the energy of the solar radiation at the entry aperture of the SEH solar concentrators and the solar azimuth and incident angles of the sun rays, the energy (solar radiation) at the exit aperture of the SEH concentrators (on the solar cells) can be calculated using the simulated optical efficiencies. The following sections describe both types of modelling which will then be used to develop an integrated model for the prediction of the power output of the TICPV modules.

6.6.1 Electrical model for the LGBC solar cell

The different parameters of the two-diode model described in section 1.2.4.3 need to be obtained for the LGBC silicon solar cell used in the TICPV modules. The parameters

are needed to complete the electrical model that will be used for the simulation of the power output of the different TICPV modules.

6.6.1.1 Obtainment of parameters for the two-diode model for the LGBC silicon solar cell

The coefficients α and β (short circuit current temperature coefficient and open circuit voltage temperature coefficient respectively) are calculated experimentally. Both the series (R_s) and parallel (R_{sh}) resistance are also calculated to complete the two-diode model. From here, both the I-V and power characteristics for the solar cell for different radiation values can be obtained.

- Ideality factors

The ideality factor n_1 of the diffusion diode is assumed to be equal to 1 in accordance with the diffusion theory of p-n junctions [238] and the ideality factor n_2 is assumed to be equal to 2 in accordance with the theory of recombination via traps [239].

- Calculation of α and β

The silicon solar cell described in Chapter 2 section 2.6.1.1 is used to determine the coefficients α and β experimentally. The solar cell is exposed to 1000W/m^2 radiation of a solar simulator and placed on a temperature controller. The I-V curves generated by the solar cells are recorded for different temperatures using an I-V tracer. The temperature of the solar cell varies from 23.49 ºC to 72.78 ºC; the I-V curves obtained are illustrated in Figure 6.9. It can be seen that the short circuit, I_{sc}, is slightly affected by the increase of temperature. The increase in temperature is characterised by the short circuit current temperature coefficient α that can be written as [240]:

$$\alpha = \frac{1}{I_{sc\ ref}} \times \frac{I_{sc} - I_{sc\ ref}}{T - T_{ref}} \tag{6.1}$$

Unlike the I_{sc}, it can be seen that the open circuit voltage V_{oc}, decreases with an increase in temperature. The effect and the temperature dependence of the V_{oc} is characterised by the open circuit voltage temperature coefficient β that can be written as [240]:

$$\beta = \frac{1}{V_{oc\ ref}} \times \frac{V_{oc} - V_{oc\ ref}}{T - T_{ref}} \tag{6.2}$$

When equation (6.1) and equation (6.2) are applied to the results obtained in Figure 6.9 , it is found that:

- $\alpha \approx 0.0006$ A/ºC
- $\beta \approx -0.0035$ V/ ºC.

In order to verify the results, the decrease of the maximum power generated by the solar cell is also calculated, which can be written as [241]:

$$\varepsilon = \frac{1}{P_M} \times \frac{dP_M}{dT} \tag{6.3}$$

where:

P_M: is the maximum power generated by the silicon solar cell.

Results show that $\varepsilon = -0.4\%/°C$. As it transpires, this is the verified and known figure for the silicon solar cell used [242].

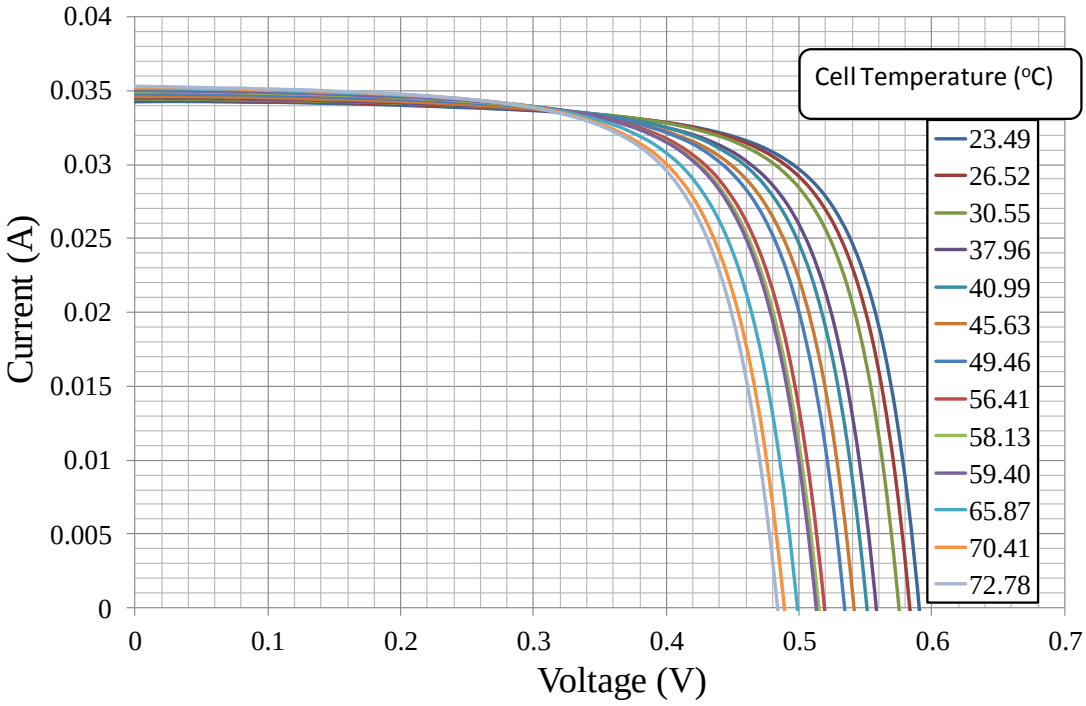

Figure 6.9: I-V curves for one solar cell at different temperatures

- Shunt and series resistance

The only two parameters still missing to complete the two-diode model are the series resistance and the parallel resistance, (R_s) and (R_{sh}) respectively.

In this case a simplified method is used to calculate the R_s and the R_{sh} of one single silicon solar cell from the I-V curve measured experimentally.

The methods consist of solving equation (1.10)**.** by varying the values of R_s and R_{sh} using a MATLAB code which is described in detail in section 6.6.1.2. The simulation is launched, for each iteration; the values of I_m, V_m and the P_m are calculated and compared to the values found experimentally. The run of simulation is ended when the differences between the simulated and experimental values of I_m, V_m and P_m are minimal; the correspondent values of R_s and R_{sh} are recorded and summarised in Table 6.2.

Table 6.2: Experimental and simulation values of maximum current, voltage, and power.

R_s=0.01 Ω **R_{sh}=405 Ω**	**Experimental**	**Simulation**
I_m	0.0302	0.0303
V_m	0.4909	0.4900
P_m	0.014869	0.014869

The simulation is carried out using MATLAB. The code of the electrical model is written and then validated by comparing the obtained I-V and power curves from simulation with the ones obtained experimentally for one solar cell.

Figure 6.10 illustrates two I-V curves of one LGBC silicon solar cell: one measured indoors using an I-V tracer and solar simulator, and the second simulated using the same conditions that are used in the indoor experimental set up (radiation and temperature) and the resistances (R_s and R_{sh}) obtained by iteration. It can be seen that the simulated I-V curve obtained via MATLAB code using the two-diode model coincides with the experimental I-V curve.

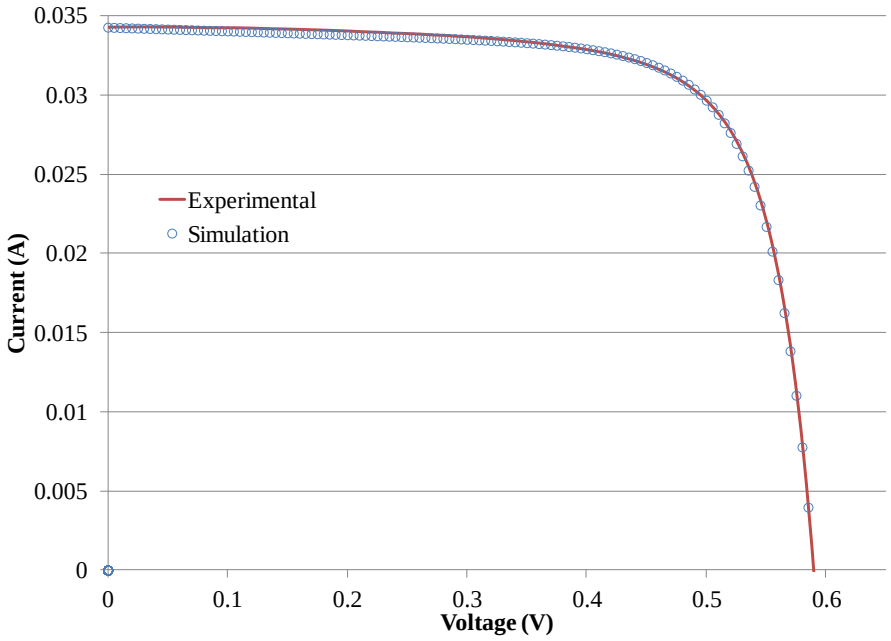

Figure 6.10: I-V curves (simulation and experimental) for one solar cell

Now that the different parameters of the two-diode model have been obtained and validated, they can be used to predict the I-V curves and the maximum power of the different TICPV modules under different weather conditions.

6.6.1.2 MATLAB code of the electrical model

The different parameters of the one single cell obtained and verified are summarised in Table 6.3. These parameters are used to solve equation (1.10) by writing a MATLAB code using the Newton-Raphson Method. The Newton Raphson method is used for solving equations of the form:

$$f\ I\ = -I + I_{Ph} - I_{01}\ \ e^{\frac{q\ V+I\times R_s}{n_1\times K\times T}} - 1\ \ - I_{02}\ \ e^{\frac{q\ V+I\times R_s}{n_2\times K\times T}} - 1\ \ - \frac{V + I \times R_s}{R_{sh}} = 0$$

An initial guess for the root that needs to be found is made, and this initial guess is called I^0.

The sequence I^0, I^1, I^2, I^3, . . . generated in the manner described below will converge to the exact root.

For the implementation of this method analytically, a formula for each approximation in terms of the previous one is needed. It is written as follows:

$$I^{n+1} = I^n - \frac{f\ I_n}{f'\ I_n} \tag{6.4}$$

I^0 is set to an initial value I^0=0.

The iteration is repeated until the difference between I^n and I^{n+1} is the closest to zero.

Table 6.3: Parametric values for a single cell

Conditions	
Radiation	1000 W/m^2 AM 1.5
Temperature	23ºC
Parameters	
I_{sc}	0.0342
V_{oc}	0.5909
I_m	0.0303
V_m	0.4900
P_m	0.0148
n_1	1
n_2	2
q	1.60217646×10^{-19}C
k	1.3806503×10^{-23} J/K
R_s	0.01Ω
R_{sh}	405Ω
β	-0.0035 V/ ºC
α	0.006 A/C

The written code using MATLAB and the parameters of the LGBC solar cells summarised in Table 6.3 represents the electrical model to be used to simulate the power output of the TICPV modules in section 6.7.1.

6.6.1.3 I-V curve simulation results of the electrical model

The simulation of the electrical model is launched to study the effects of the concentration ratios and the temperatures on the V_{oc}, the I_{sc} and the maximum power of the LGBC solar cell. The simulated effects of the temperature on the I-V curves are compared and validated with measured I-V curves at different temperatures.

- Effect of the radiation variation on the solar cell

Figure 6.11 shows clearly that the V_{oc} increases logarithmically with the radiation reaching the solar cell that is used in the TICPV, while the I_{sc} is a linear function of the radiation. The variation of the V_{oc} as a function of the radiation is very low compared to the variation of the I_{sc}.

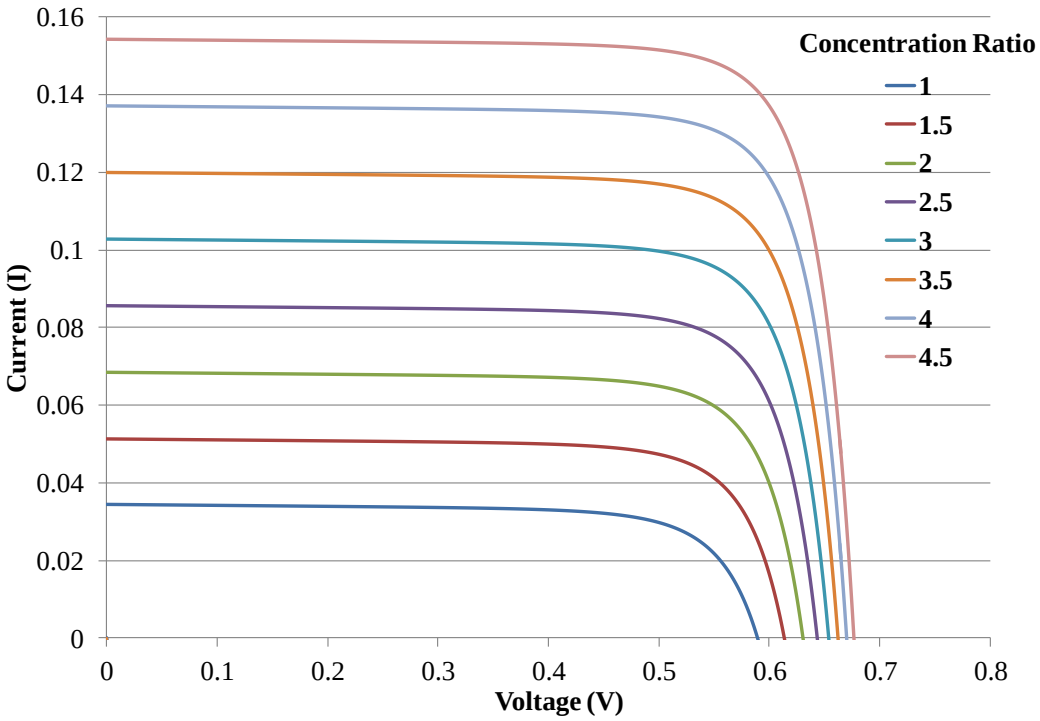

Figure 6.11: Solar cell I-V characteristics for different irradiation values

The power output of the solar cell P_{out} increases with the increase of the radiation fallen on the solar cell as the I_{sc} and the V_{oc} increase. On Figure 6.12, it can be noticed that the P_{out} of the LGBC silicon solar cell increases with the increase of the concentration ratio which represents the increase of radiation on the solar cell. Here, it becomes clear the importance of the use of the concentrators on the solar cells; they increase the radiation falling on the solar cells by keeping the same area of the solar cells and increasing its P_{out}.

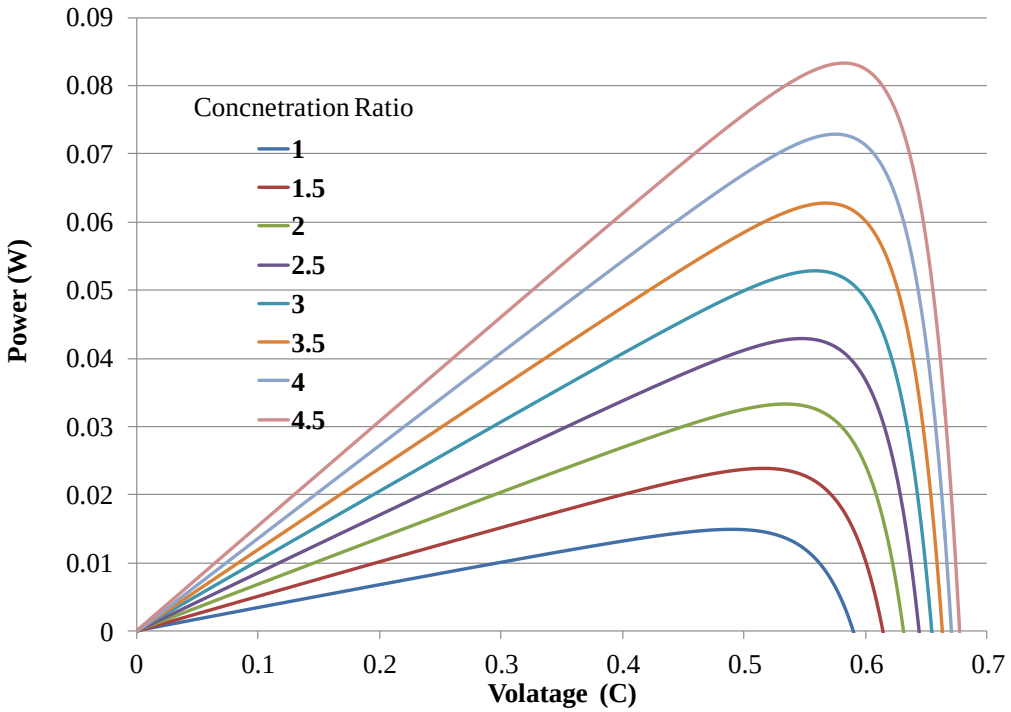

Figure 6.12: Solar cell power characteristics for different irradiation values

- Effect of the temperature variation on the solar cell

The values of β and α were integrated into the two-diode electrical model described in section 6.6.1.2. Different I-V curves at different temperatures have been simulated and are illustrated in Figure 6.13. As mentioned previously, using the same temperature and radiation conditions, the I-V curves of the solar cell are recorded experimentally and are also illustrated in Figure 6.13. There is a clear agreement between the experimental and simulated results of the I-V curves at different temperatures. This is considered as the final validation of the MATLAB code that will be used later in the chapter to predict the power output of the silicon solar cell used to build the TICPV module. The increase of the temperature of the solar cells is followed by a minor increase of the I_{sc} and a more significant decrease of the V_{oc}.

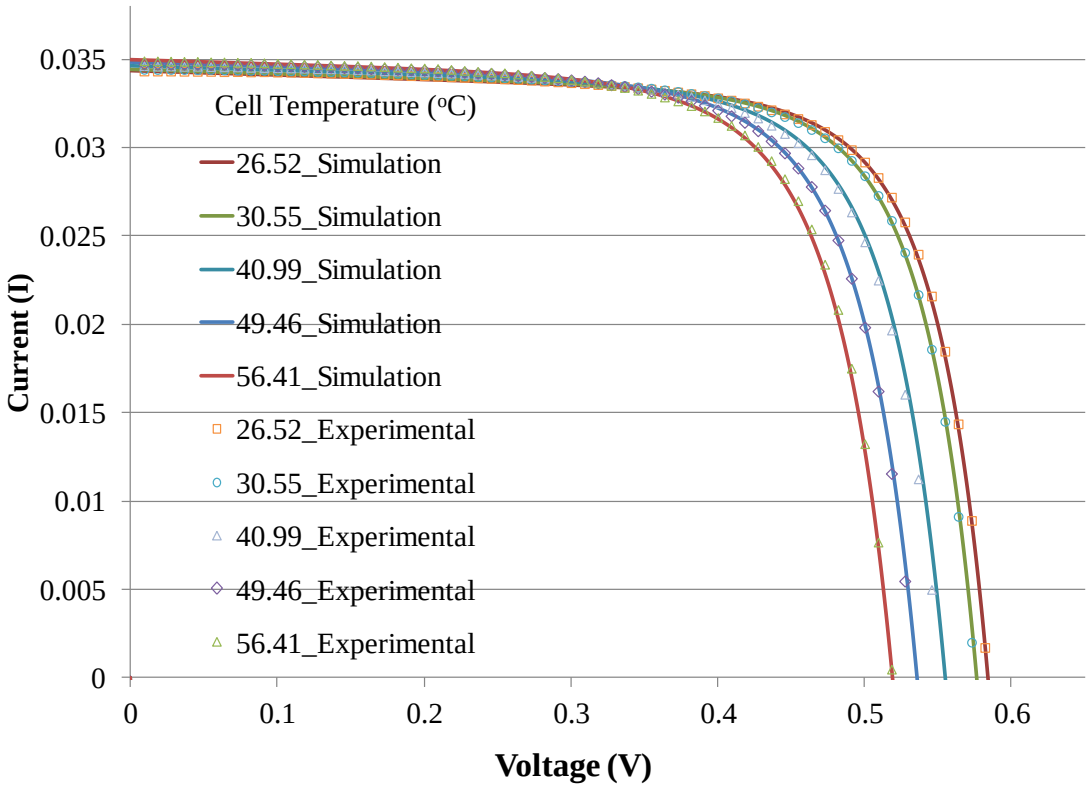

Figure 6.13: Solar cell I-V characteristics dependent on temperature

The I-V curves illustrated in Figure 6.13 above are represented in power variation as a function of the voltage variation in Figure 6.14 below. The increase of the I_{sc} and decrease of V_{oc} due to the increase of the temperature of the solar cells results in a decrease of the maximum power output.

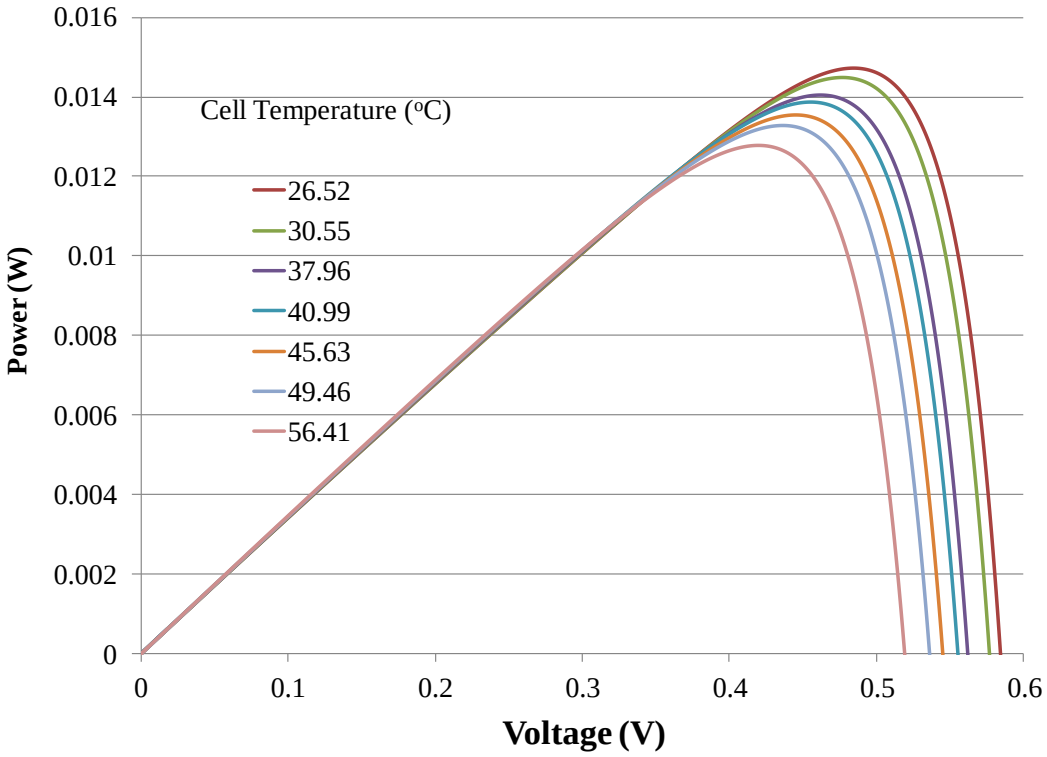

Figure 6.14: Power curves of the solar cell for different temperatures.

The development of this electrical model is vital in order to be able to model the power output of the TICPV modules in outdoor conditions in Edinburgh; its use can also be extended to other locations. In order to use it, the energy radiation on the solar cells of the TICPV modules is required. This can only be achieved by using the different simulated optical efficiencies for outdoor conditions. The following section outlines the second type of modelling required for the power output – the optical model.

6.6.2 Simulated optical efficiency

For the power prediction of the TICPV modules in outdoor conditions, the optical efficiency needs to be simulated for different incident angles in Edinburgh at different solar azimuth angles since the sun moves in different planes throughout the course of the day. The optical efficiency also needs to be calculated for the diffuse radiation as the SEH concentrator when in outdoor conditions will collect both types of solar radiation (direct and diffuse).

6.6.2.1 Calculation of incidence and solar azimuth angles

The calculation of the angles of incidence of the sun rays on the TICPV modules needs an understanding of solar geometry. This describes the relationship between the sun and the earth or more explicitly the relationship between solar radiation, the product of the sun, and any location on the earth.

The relationship between the incoming beam of solar radiation and a plane in any particular orientation is represented by the position of the sun relative to the plane. These positions are illustrated in Figure 6.15 below in terms of different angles.

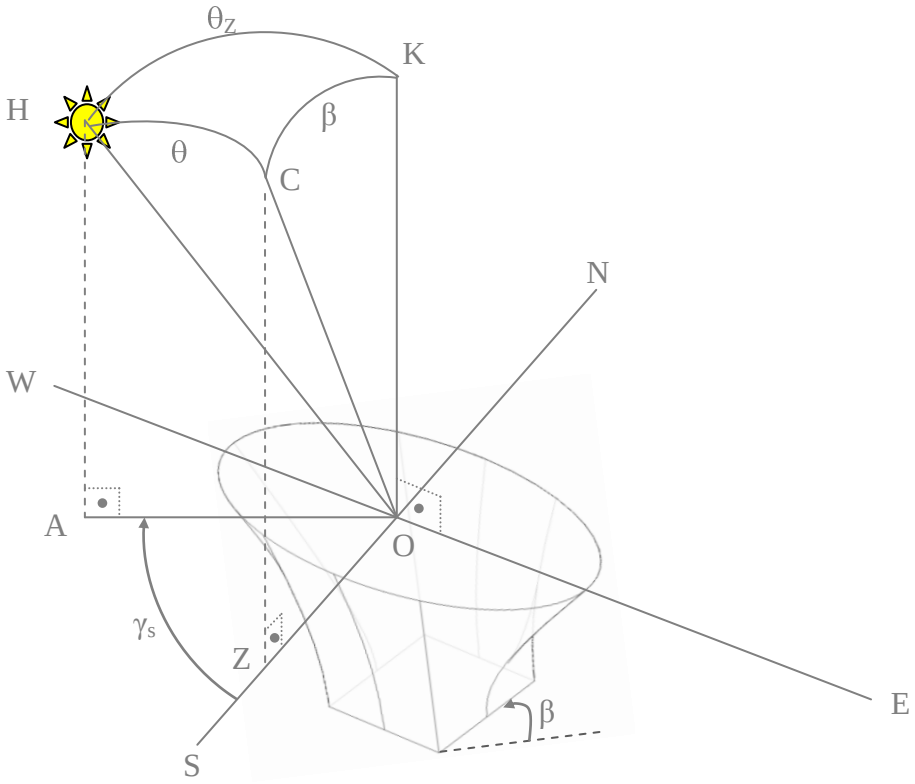

Figure 6.15: Angles characterising the sun and the SEH concentrator position

The description of the angles defining the sun's position in relation to the orientation and position of the entry aperture of the SEH concentrator are detailed below, with the conventional symbols of the angles that are used in the calculations:

- **Latitude** ϕ: The angular location north or south of the equator, $0° \leq \phi \leq 90°$.
- **Declination** δ: The angular position of the sun at solar noon with respect to the plane of the equator, $-23.45° \leq \delta \leq 23.45°$.

- **Surface azimuth angle** γ (SOZ on Figure 6.15): The deviation of the projection on a horizontal plane of the normal to the surface from the local meridian, -180º≤γ≤180°.

- **Slope** β (CÔK on Figure 6.15): The angle between the plane of the surface in question and the horizontal, 0°≤β≤180°.

- **Hour angle** ω: The angular displacement of the sun east or west of the local meridian due to the rotation of the earth on its axis at 15° per hour.

- **Angle of Incidence** θ (HÔC on Figure 6.15): The angle between the beam radiation on a surface and the normal to that surface.

- **Zenith Angle** θ_z (HÔK on Figure 6.15): The angle between the vertical and the line to the sun, i.e. the angle of incidence of beam radiation on a horizontal surface.

- **Solar altitude angle** α_s (HÔA on Figure 6.15): The angle between the horizontal and the incident beam of the sun, i.e. complement of the zenith angle.

- **Solar azimuth angle** γ_s (ZÔA on Figure 6.15): The angular displacement from south of the projection of beam radiation on the horizontal plane.

The angle of incidence θ is calculated using the approximate equation of Cooper [243] as shown in equation (6.5):

$$\cos\theta = \sin\delta \times \sin\phi \times \cos\beta - \sin\delta \times \cos\phi \times \sin\beta \times \cos\gamma + \cos\delta \times \cos\phi \times \cos\beta \times \cos\omega + \cos\delta \times \sin\phi \times \sin\beta \times \cos\gamma \times \cos\omega + \cos\delta \times \sin\beta \times \sin\gamma \times \sin\omega \quad (6.5)$$

In the case of this study, the TICPV modules are facing south, therefore the surface azimuth angle γ=0º. For that reason, equation (6.5) can be written as follows:

$$\cos\theta = \sin\delta \times \sin\phi \times \cos\beta - \sin\delta \times \cos\phi \times \sin\beta + \cos\delta \times \cos\phi \times \cos\beta \times \cos\omega + \cos\delta \times \sin\phi \times \sin\beta \times \cos\omega \quad (6.6)$$

The slope angle β (angle of inclination to the horizontal) of the TICPV module is equal to 55º and ϕ is the latitude of Edinburgh equal to 55º.

The declination δ describes the angle between the sun passing the highest level and the equatorial plane (north positively). The declination angle can be calculated by using another equation of Cooper [243]:

$$\delta = 23.45 \times \sin\ \ 360 \times \frac{284 + nday}{365} \tag{6.7}$$

where nday = number of days in the year.

The hour angle ω is calculated from the solar time, ω = 0º when the sun is at the highest level (12pm solar time) and each hour corresponds to a length of 15º. In the morning, the hour angle is counted negatively and in the afternoon it is counted positively. For example, an hour angle ω = -60º occurs at 8 am or ω = 45º occurs at 3pm.

The local time (LT) differs slightly from the local solar time (LST); the angles of incidence are calculated at the LST but the powers generated by the TICPV modules are measured at the recorded LT. The LT as a function of the LST can be written as given by Duffie and Beckman [244] in the following equation:

$$LT = LST - 4 \times \ \ L_{ST} - L_{LOC}\ \ + E \tag{6.8}$$

where:

- L_{st} is the standard meridian for the local time zone. In the case of this study the local time zone of Edinburgh, L_{st} = 0º.
- L_{loc} is the longitude of Edinburgh, L_{loc} = 3.22º.
- E is the equation of time (in minutes), it can be written as:

$$E = 229.2 \times (0.000075 + 0.001868 \times \cos B - 0.032077 \times \sin B - 0.014615 \times \cos 2B - 0.04089 \times \sin 2B \tag{6.9}$$

  Where B is calculated from the following equation:

$$B = \ \ nday - 1\ \ \times \frac{360}{365} \tag{6.10}$$

Equation (6.5) introduced and detailed above is used to calculate the angles of incidence on the TICPV modules installed at the SE at Heriot-Watt University. For the TICPV modules the lower are the angles of incidence the higher will be the optical efficiency.

It is important to calculate the solar azimuth angle γ_s as this determines the horizontal section plane of the SEH concentrator where the angle of incidence is located.
The solar azimuth angle γ_s can be calculated using the following equation [47]:

$$\gamma_s = \text{sign}\ \omega\ \times \cos^{-1}\ \frac{\cos\theta_z \times \sin\phi - \sin\delta}{\sin\theta_z \times \cos\phi} \tag{6.11}$$

where θ_z can be calculated using the following equation [47]:

$$\sin\theta_z = \sin\delta \times \sin\phi + \cos\omega \times \cos\delta \times \cos\phi \tag{6.12}$$

These equations are imperative steps that contribute to the final calculations for the modelling of the power generated by the outdoor TICPV modules. As mentioned before, the optical efficiencies of the SEH concentrators for all the incident angles in all the vertical section planes also need to be calculated. The next section discusses the methodology used to obtain these optical efficiencies.

6.6.2.2 Simulated optical efficiency for different solar azimuth angles

Both the angles of incidence and the solar azimuth angles are calculated from equation (6.5) and equation (6.12) respectively. When the solar azimuth angle γ_s is equal to 0º the angles of incidence are located in the plane perpendicular to the entry aperture of the SEH concentrator and containing the minor axis of the SEH concentrator. In the previous chapter, the optical efficiencies of the SEH concentrators were simulated for different angles of incidence but only for solar azimuth angle γ_s =90° or γ_s= -90° (on the major axis of the elliptical entry aperture). This sufficed for the simulation study as the indoor study was primarily carried out to validate the optical model, therefore using only γ_s =90° or γ_s= -90° was enough for the optimisation process.
The developed optical model used in the previous chapter is now applied to the five different SEH concentrators. This time, however, a light source with different angles of incidence at different azimuth angles -90°≤γ_s ≤90° is used. Seeing as the TICPV modules will be tested in outdoor conditions, the spectrum of the light emitted by the light source in the simulation is changed to be air mass 1.5 (AM 1.5) as illustrated in Figure 6.16, which is used for standardised testing of terrestrial solar panels as this is the closest to the spectrum of the light emitted by the sun. Riordan and Hulstrom [245]

published an extensive review about AM 1.5 and its use in reporting PV device (cell, module) performance measurements. The air mass gives an indication of the relative path length of the direct solar beam through the atmosphere and it is used to characterise the solar spectrum after the sun rays have travelled through the atmosphere. When the sun is directly overhead (at zenith), the path length is 1.0 (AM 1.0).

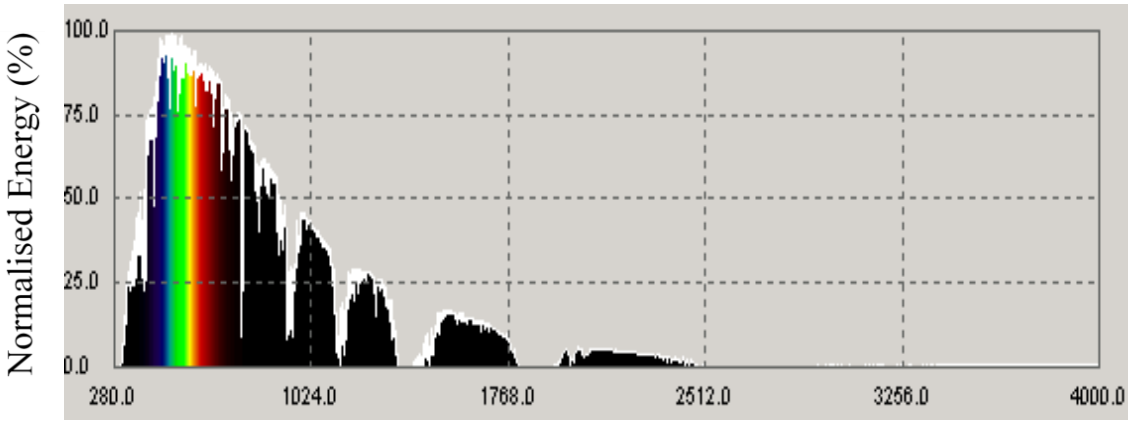

Figure 6.16: Spectrum of the light source

The results of the simulated optical efficiencies for the five optimised SEH concentrators are illustrated in the graphs below in Figure 6.17. For the H1 SEH concentrator the variation between the maximum and minimum value of the optical efficiency for different solar azimuth angles is less than 5% for an incident angle of $-40° \leq \theta \leq 40°$ as shown in Figure 6.17(a). For higher incident angles ($|\theta| > 40°$), the variation in optical efficiency increases to reach a maximum value of 10% difference at the same incident angle. For the H1.5 SEH concentrator the variation between the maximum and minimum value of the optical efficiency for different solar azimuth angles is less than 5% for the incident angles $-30° \leq \theta \leq 30°$ as shown in Figure 6.17(b). For the H2 SEH concentrator the variation is less than 5% for the incident angles $-25° \leq \theta \leq 25°$ as shown in Figure 6.17(c). For both the H2.5 SEH concentrator and H3 SEH concentrator the variation is less than 5% for the incident angles $-10° \leq \theta \leq 10°$ as shown in Figure 6.17(d) and Figure 6.17(e) respectively. In all cases, for $-90° \leq \gamma s \leq 90°$, the variation between the maximum and minimum of the optical efficiency does not go above 10%.

Taking into consideration that this is a static PV system, a variation of 10% and less for all possible incoming ray angles is a sound result. These results highlight the advantage of the 3-D aspect of the concentrator as it can accept radiation from all directions with only a small sacrifice in optical efficiency.

For any SEH concentrator and for any chosen day and time in Edinburgh, the angles of incidence and the solar azimuth angles are calculated; from these two angles calculated from the simulation and the corresponding optical efficiency can be obtained as illustrated in the graphs in Figure 6.17. The values of the different optical efficiencies corresponding to the different incident angles and different solar azimuth angles are saved in excel spreadsheets. These values are the characterising data of each SEH concentrator to be used in the power modelling study.

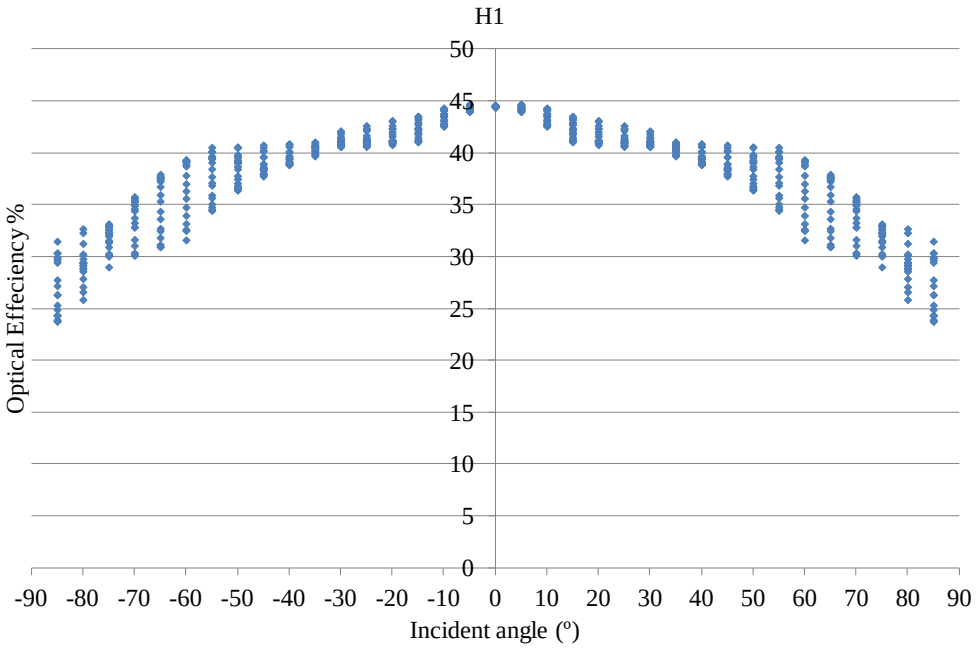

(a)

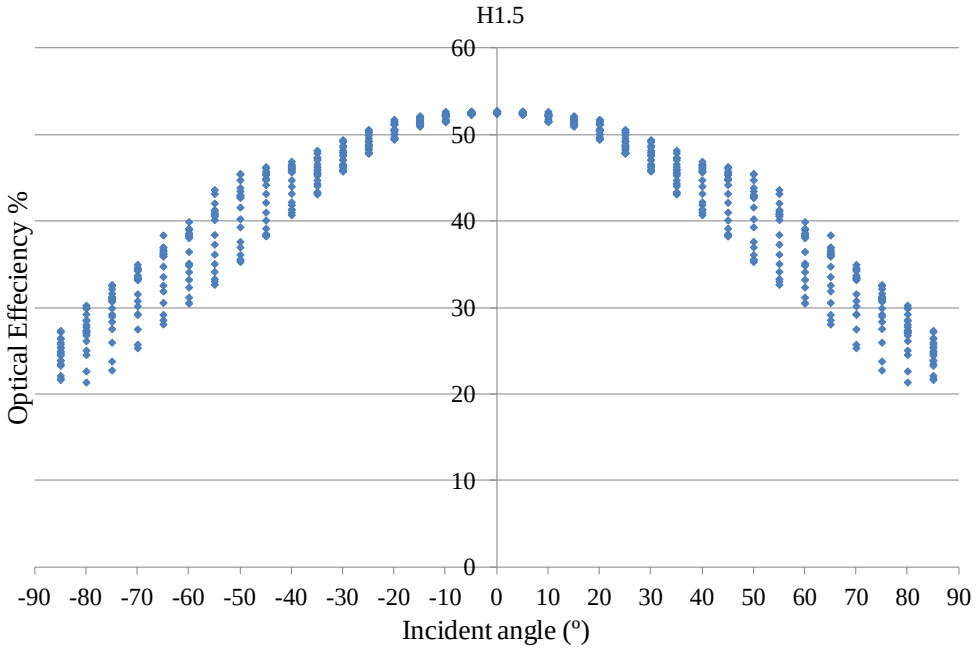
H1.5
Optical Effeciency %
60
50
40
30
20
10
0
-90 -80 -70 -60 -50 -40 -30 -20 -10 0 10 20 30 40 50 60 70 80 90
Incident angle (º)

(b)

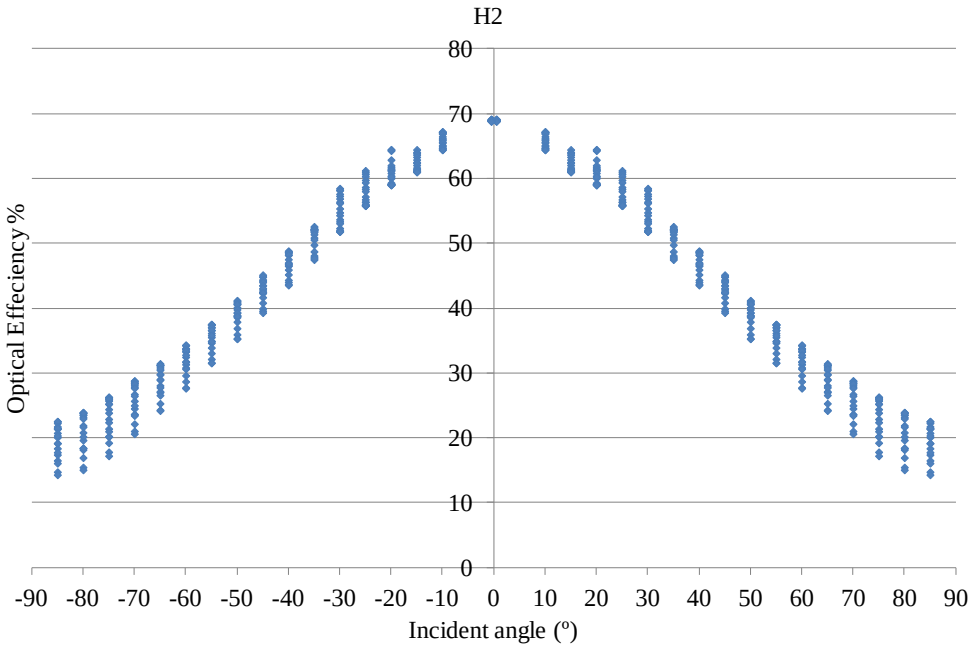
H2
Optical Effeciency %
80
70
60
50
40
30
20
10
0
-90 -80 -70 -60 -50 -40 -30 -20 -10 0 10 20 30 40 50 60 70 80 90
Incident angle (º)

(c)

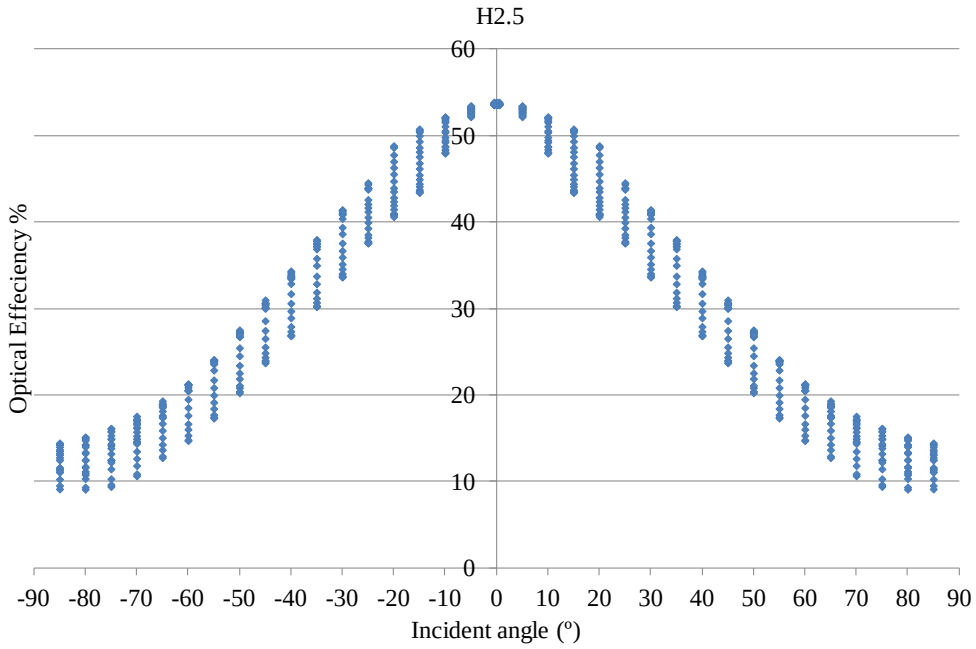

(d)

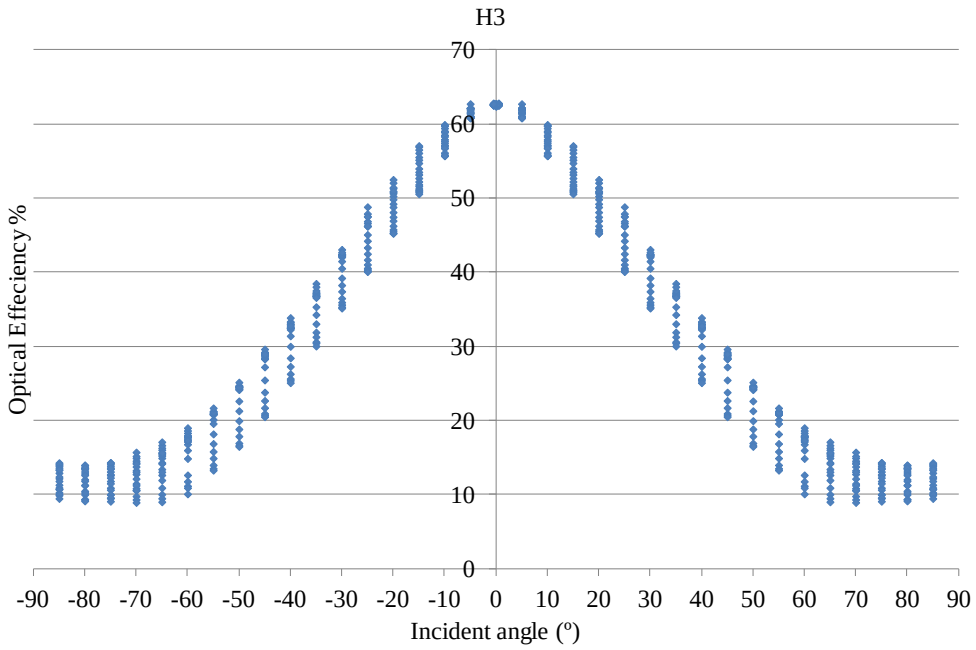

(e)

Figure 6.17: Optical efficiencies of the optimised SEH concentrators for different incident angles and different solar azimuth angles (a) H1 SEH, (b) H1.5 SEH, (c) H2 SEH, (d) H2.5 SEH and (e) (H3) SEH.

Due to the static specification of the TICPV modules, the solar azimuth angle gives an indication of when the TICPV modules start to receive direct solar radiation during the day. It is only when the solar azimuth angle is between - 90º <γ_s <90º, that the sun rays can reach the entry aperture of the SEH concentrators, with different incident angles depending on the day and month of the year. Out with these values, the radiation reaching the entry aperture of the solar concentrator will be from diffuse radiation.

6.6.2.3 Simulated optical efficiency for diffuse radiation

The optical efficiencies simulated and calculated to this point of the thesis are valid only for the direct solar radiation where the sun rays are received by the SEH concentrators at the same incident angles, i.e. all the rays are parallel to each other coming from the same direction. This is due to the fact that for the indoor study, the solar simulator only gives direct (beam) radiation; and as such the calculations for both the simulation and indoor studies only needed to take the direct solar radiation into consideration. The TICPV modules installed outdoors, however, are exposed to the global solar radiation which is the sum of the direct (beam) radiation and the diffuse solar radiation. The direct solar radiation is the radiation received from the sun without taking into consideration the radiation scattered by the atmosphere. The diffuse solar radiation is the radiation received from the sun after being scattered by the atmosphere. For this reason and to quantify the percentage of solar radiation that will reach the solar cells after being concentrated, the optical efficiency of the different SEH concentrators exposed to diffuse radiation are calculated using a modified optical model. The difference to the previous optical model used to calculate the optical efficiency of the SEH concentrators for the direct radiation is the light source; in this case, it is replaced by a semi-sphere which emits light rays with the same energy creating a similar condition as the diffuse radiation as illustrated in Figure 6.18.

The rays emitted by the hemispheric light source come from all directions and will either be concentrated, reflected back out from the entry aperture or escape from the sides of the SEH concentrators. The energy of the entering light rays are measured by the illuminance detector 1 placed at the entry aperture of the SEH concentrator and the energy of the concentrated rays are measured by the illuminance detector 2 placed at the exit aperture of the SEH concentrator.

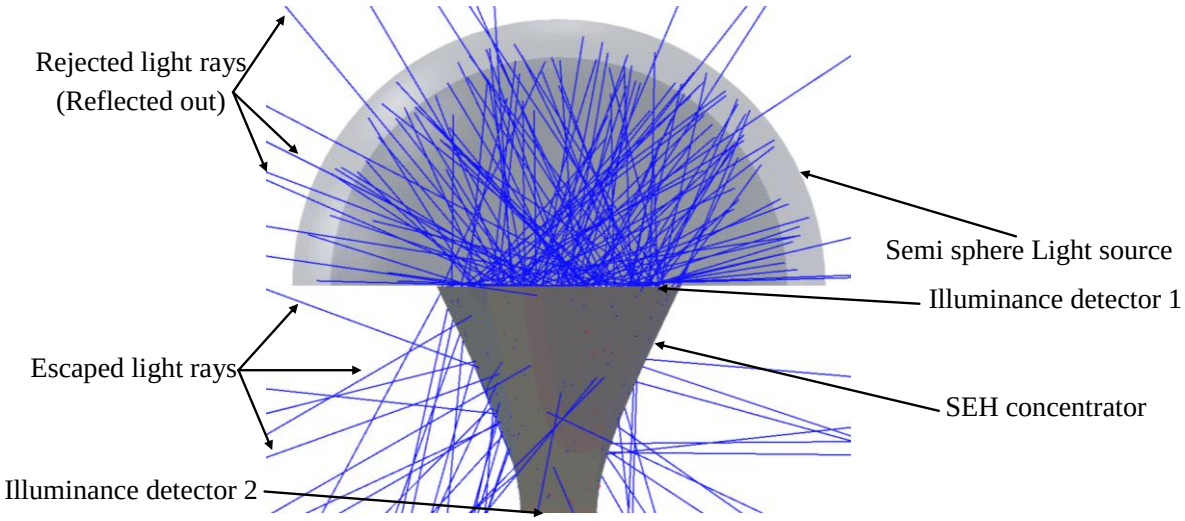

Figure 6.18: Depiction of the diffuse radiation of SEH concentrator by OptisWorks

The optical efficiencies are calculated using equation 4.1 (Chapter 4). The results of the optical efficiencies of the five optimised SEH concentrators exposed to the diffuse radiation are summarised in Table 6.4 below. From the table it can be seen that the H2 SEH solar concentrator has the highest optical efficiency for diffuse radiation (41.3%). Looking back to the results of the optimisation study in Chapter 4, the H1 SEH and the H1.5 SEH solar concentrators have a much lower optical efficiency for direct solar radiation (41% and 47% respectively) compared to the value of 68% for the H2 SEH solar concentrator, however, in this study they have a comparable optical efficiency for the diffuse radiation (37.5% and 40.2% respectively). This can be explained by the fact that both the H1 and H1.5 SEH concentrators have a large acceptance angle which consequently results in a small variation of the optical efficiency for all the incident angles of the direct radiation. For this reason, the values of the optical efficiency for the diffuse radiation do not differ much from the direct radiation values. A possible explanation for why the H2 SEH concentrator has the highest optical efficiency for both types of radiation may be due to the fact that it has the advantage over the H1 and H1.5 SEH concentrators in that it is taller and as the results in Chapter 4 show, the taller is the SEH, the higher is the optical efficiency (for direct radiation).

Despite the fact that the H2.5 SEH and H3 SEH concentrators are taller than the H2 SEH, they both have the lowest optical efficiency for diffuse radiation (25.8% and 26.7% respectively). This can be explained due to the fact that they have low acceptance

angles. The acceptance angle in this case, has more of an influence on the results of the optical efficiency for diffuse radiation than does height, than it did for the direct radiation. It can be said that the optical efficiency for diffuse radiation relies on a combination of the value of the direct radiation and the acceptance angle. From the results in Chapter 4, it can be seen that these two SEH concentrators have a reasonably high optical efficiency (for direct radiation), however, their acceptance angles are very low. Consequently, having a low acceptance angle for these two concentrators is what lowers the value of the optical efficiency for the diffuse radiation as its calculation depends on the acceptance angle. So even although the H2 SEH concentrator is shorter than the H2.5 and H3 SEH concentrators, the fact that it has a larger acceptance angle than these two concentrators combined with the highest optical efficiency for the direct radiation is what makes it have a higher optical efficiency for the diffuse radiation.

Table 6.4: Optical efficiencies of the five optimised SEH concentrators under diffuse radiation

Solar concentrator	H1 SEH	H1.5 SEH	H2 SEH	H2.5 SEH	H3 SEH
Optical efficiency (Diffuse radiation)	37.5%	40.2%	41.3%	25.8%	26.7%

All of the theoretical optical efficiencies characterising the SEH concentrators and the solar cells are now complete and can be used to model the power output of the TICPV modules in outdoor conditions using an integrated model. The development of the integrated model is detailed in the following section.

6.6.3 Integrated model development

An integrated model (electrical and optical) is developed in order to model the power generated by the different TICPV modules. The model is developed using real data input measured on the SE testing site. The real data measured are the diffuse and global solar radiation and the temperature of the solar cells, these are used as input in the integrated model as shown in Figure 6.19. The simulated results of the power output using the integrated model can then be compared with the power measured using the modules selector and the IV tracer in order to validate the model.

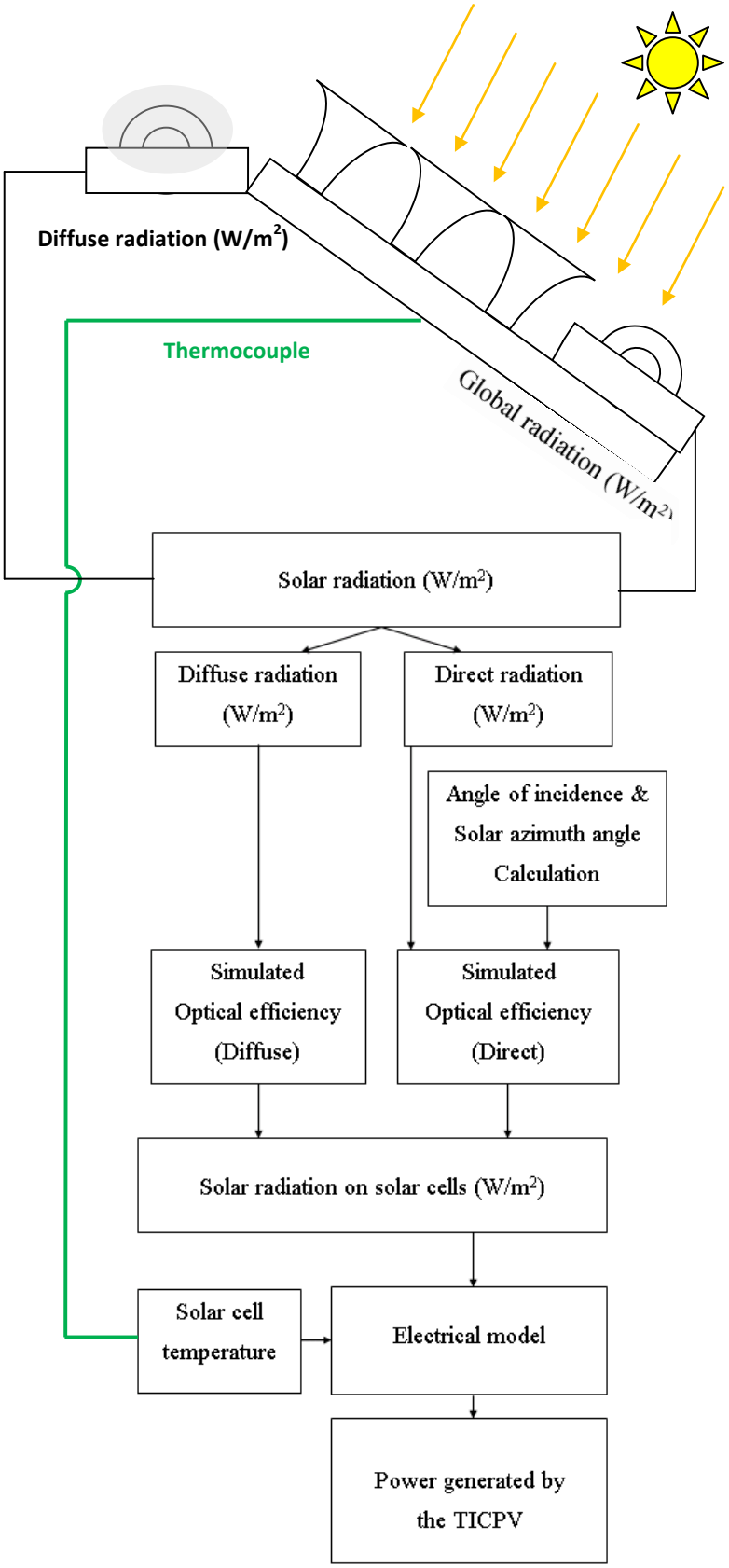

Figure 6.19: Block diagram and flow chart of the outdoor power model

The integrated model simulation is launched via a written code using MATLAB, results of which will be presented in the following section. It is executed following these steps:

- Calculate the radiation that will reach the solar cells from the diffuse radiation by multiplying the optical efficiency (of the diffuse radiation) of the SEH concentrators used in the TIPCV modules by the measured diffuse radiation by the geometrical concentration ratio.
- The angles of incidence and the solar azimuth angles are calculated every minute using equation (6.5) and equation (6.12) respectively corresponding to the same times as to when the solar radiation is measured. These calculations are necessary in order to determine the optical efficiency of the SEH concentrators which will then be used to calculate the direct radiation reaching the solar cells.
- The optical efficiency of the direct radiation of the SEH concentrators used in the TICPV module is determined using the angles of incidence and the solar azimuth angles calculated from the values simulated and illustrated in Figure 6.17.
- The direct radiation on the entry aperture of the SEH concentrator is calculated by the difference of the diffuse radiation from the global radiation (measured on the slope of the TICPV : 55°).
- The radiation that reaches the solar cell from the direct radiation is then calculated by multiplying the optical efficiency (of the direct radiation) of the SEH concentrators by the calculated direct radiation by the geometrical concentration ratio. The total radiation reaching one solar cell is the sum of the two radiations: one from the diffuse and one from the direct.
- The total radiation reaching the solar cells, the measured temperature of the solar cells and the number of solar cells in the TICPV module are used as input for the electrical model developed in section 6.6.1. The results together are used to obtain the power output of the TICPV moules at different times of the day.

6.7 Outdoor experimental results of the TICPV modules

Following a detailed description of the experimental set up in the first part of this chapter, followed by the development of the electrical and optical models, this section presents the results of the outdoor experimental measurements for the characterisation of the TICPV modules. The results will be also be used to validate the integrated model

(optical and electrical) developed. The electrical model was developed using an equivalent two diode circuit – the different parameters of the electrical model were characterised and validated using an indoor experimental study on one LGBC solar cell; the optical model was developed using OptisWorks software and was validated with the indoor experimental study. The integrated model has been developed for the prediction of the power output of the five TICPV modules in outdoor conditions.

The five outdoor TICPV modules (H1 TICPV, H1.5 TICPV, H2 TICPV, H2.5 TICPV and H3 TICPV) designed for building integration are installed, tested and monitored in outdoor conditions collecting both direct and diffuse radiations in the Edinburgh SE testing centre for the period from 24th May 2012 until 28th June 2012 and from 27th July until 30th August 2012. The data measured between 28th June and 27th July are missing following an unfortunate incident at the SE testing centre where it was vandalised and the computer used for the data collection was stolen. Fortunately, the TICPV modules had been installed for a long enough period to monitor their power output (electrical generation) under different weather conditions.

6.7.1 Outdoor power output of the TICPV modules.

The five stationary TICPV modules exposed to solar radiation in the SE test centre at Edinburgh generate different power values during the day and for different days of the year. The amount of solar irradiance on the solar concentrators differs according to the time of the day and the season (day of the year). The experimental data monitored during the period of the summer time in Edinburgh is characterised by a variety of the weather conditions, which is typical of the weather in Scotland. Consequently, the experimental results recorded from testing the TICPV modules in outdoor conditions in Edinburgh will be presented for three possible weather conditions that may occur throughout the year. These situations are a sunny day, a sunny interval day and a cloudy day (which was the case on the 26th May 2012, the 3rd June 2012 and the 29th May 2012 respectively). The nature of the typical weather in Scotland made it possible to monitor the electrical performance of the TICPV modules under these different weather conditions despite the relatively short period of testing from 24th May to 30th August.

The experimental data recorded which will be presented for each TICPV modules at different time of the three chosen days are:

- The experimental power output (W)

- The global irradiance (W/m^2)
- The solar cells temperature (^oC)

The data are illustrated to be compared with:

- The simulated power output (W) obtained from the integrated model
- The optical efficiency of the SEH solar concentrators (%)
- The optical concentration ratio

6.7.1.1 Power output of H1 TICPV module.

Figure 6.20(a) shows the measured power output of the H1 TICPV modules generated for the recorded global solar irradiance on a sunny day (26th May 2012). For a sunny day, the trend of the variation of the measured power output of the H1 TICPV module during the day (black line) follows the trend of the global irradiance (blue line). This shows neatly that the power output is in accordance with the global irradiance – i.e. at maximum global irradiance, the measured power output is also at its maximum value. The red line on the graph in Figure 6.20(a) represents the simulated power output from section 6.6 – it can be seen that the results are similar to the measured power with a maximum difference of 8%.

For a maximum global irradiance of $880W/m^2$ at 13:42, the H1 TICPV module generated 2.7W (corresponding to 33.7W generated by $1m^2$ of H1 TICPV module) with an optical efficiency of 41% and optical concentration ratio of 1.44.

Figure 6.20(b) shows that the optical efficiency of the H1 TICPV module remains constant (around 40%) for 8 hours of the day between 9:30 and 17:30. This is considered as an advantage for a stationary H1 TICPV module as it achieves a constant optical concentration ratio of 1.4 for a period of 8 hours consecutively. An optical concentration ratio of 1.4 represents a 40% increase in the power output for the H1 TICPV module compared to the conventional PV module permitting a saving of 29% of the solar cells material.

Figure 6.20(b) shows the variation of the temperature of the solar cells of the H1 TICPV module on a sunny day. The temperature (green line) shows the same variation compared to the global solar irradiance variation. In other words, the solar cells temperature increase with the increase of the global solar irradiance throughout the day

to reach a maximum of 45ºC and begins to decrease gradually with the decrease of the solar irradiance after 14.00. The solar irradiance for a sunny day without any disruption of cloud or rain shows clearly how the temperature of the solar cells of the H1 TICPV vary with the variation of global solar irradiance. There is a sharp increase and decrease in temperature at the beginning and end of the day which can be attributed to:

- The variation of global solar irradiance at those times of the day
- The increase and decrease of the optical efficiency which magnifies the increase and decrease of the effects of the global solar irradiance on the solar cells.

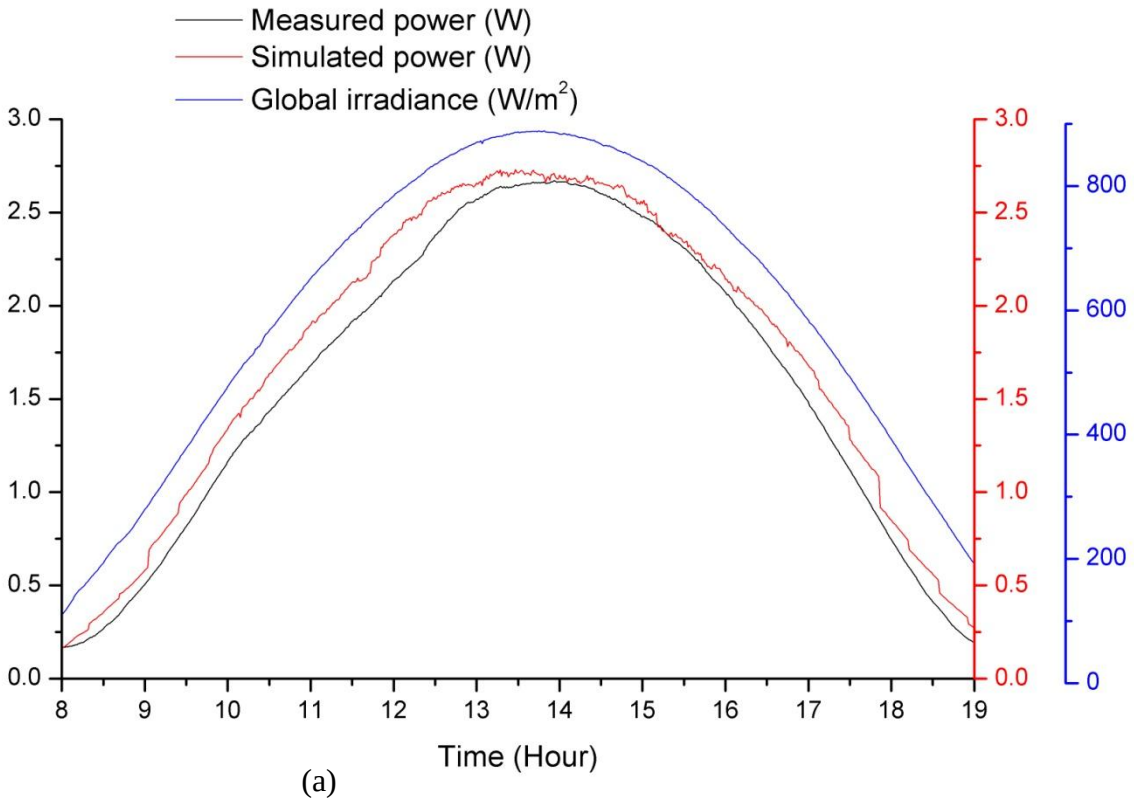

(a)

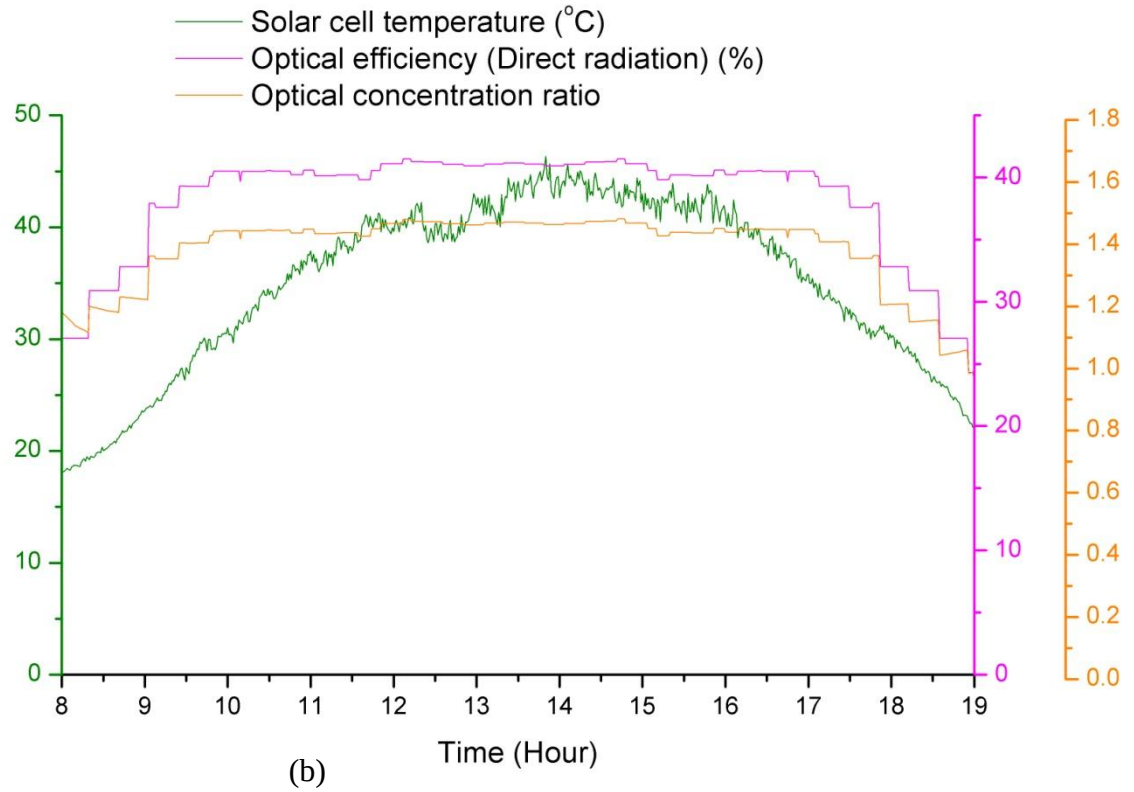

(b)

Figure 6.20: Diurnal variation for H1 TICPV on a sunny day of: (a) power output and irradiance, (b) temperature and optical performance

Figure 6.21(a) shows the measured power output (black line) of the H1 TICPV module generated for the recorded global solar irradiance (blue line) on a sunny interval day (3rd June). The measurements of the solar irradiance are very accurate as they are recorded every minute. The results of the simulated power output using the integrated model are illustrated on the same graph (red line); these results are in line with the expectations as they, with the measured power output, follow the trend of the global solar irradiance. The difference between the simulated power output and the measured power output is very low < 10% for most of the data and reaches 18% only for some cases where the variation of the global solar irradiance is turbulent changing rapidly from high values (>800W/m^2) to low values (<200W/m^2). This variation between the simulated and experimental power output can be attributed not only to flaws in the fabrication of the SEH concentrators but to the errors in precision in the measurement devices. In general, the global solar irradiance measurements are very low, in the order of 200W/m^2, showing from time to time high values of solar irradiance greater than 800W/m^2 before 15:15. This can be explained in terms of the weather condition being mainly cloudy with a quick appearance of direct sunrays from time to time; the variation of the global solar irradiance shows how sudden the appearance of direct sunrays can be. After 15:15, the weather condition remains interval sunny but this time mainly sunny with the appearance of clouds hiding the sun from time to time.

As the weather condition was cloudy for most of the time before 15:15 on 3rd June, the calculation of the optical concentration ratio is obtained based mainly on the optical efficiency of the diffuse radiation; at times of direct sunrays the optical efficiency of both the direct and diffuse radiation are used. The orange line on Figure 6.21(b) representing the variation of the optical concentration ratio of the H1 TICPV module is a horizontal line showing some fluctuations before 15:15. The line is horizontal because the optical efficiency of the diffuse radiation is constant and does not depend on the incidence angle which varies during the day. The fluctuations represent the period of times where the direct sunrays appear; at those points, the optical efficiency of the direct radiation is considered with the optical efficiency of the diffuse radiation in the calculation of the optical concentration ratio.

The green line on Figure 6.21 (b) illustrates the variation of the solar cells temperature of the H1 TICPV module. The temperature reaches a maximum of 35ºC for a maximum

global irradiance of 1360W/m^2 compared to a value of 45ºC for a maximum global irradiance of 880W/m^2 on a sunny day (26th May). The maximum temperature of the solar cells on the 3rd June is lower than the maximum temperature on the 26th May (35ºC <45ºC) despite reaching higher global irradiance (1360W/m^2 >880W/m^2). This highlights that the temperature of the solar cells do not depend only on the amount of the solar irradiance but also on its duration.

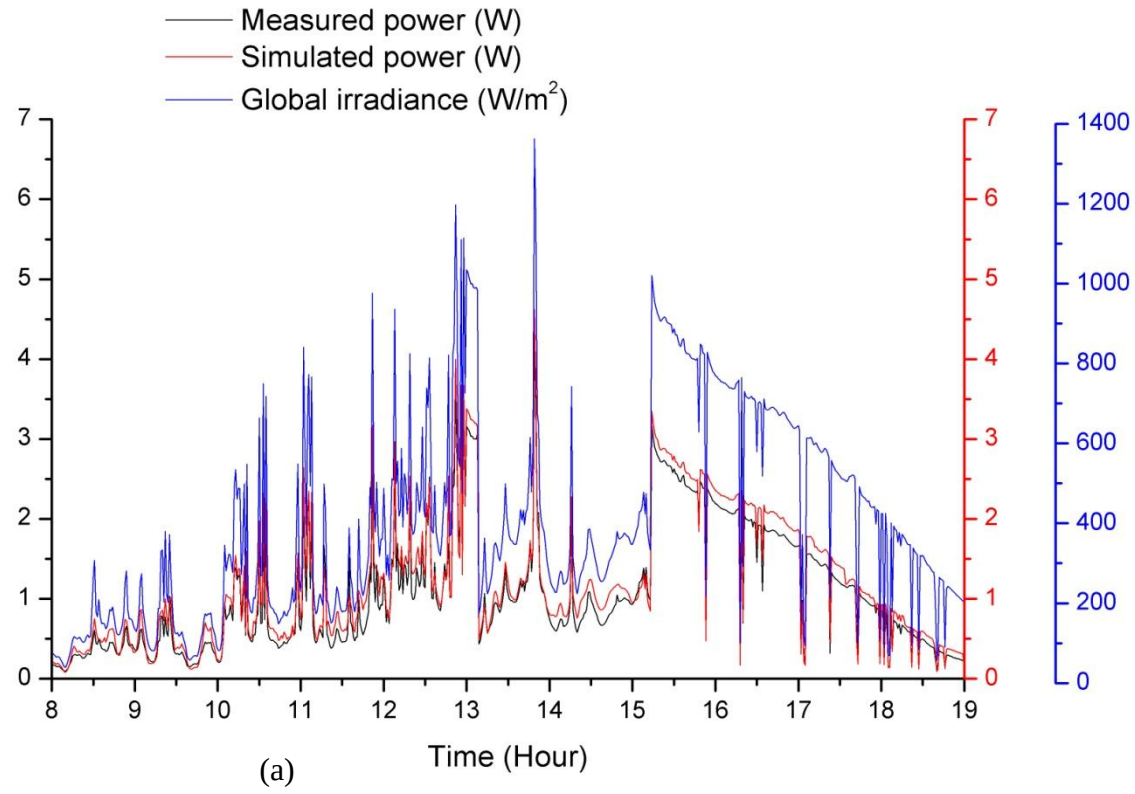

(a)

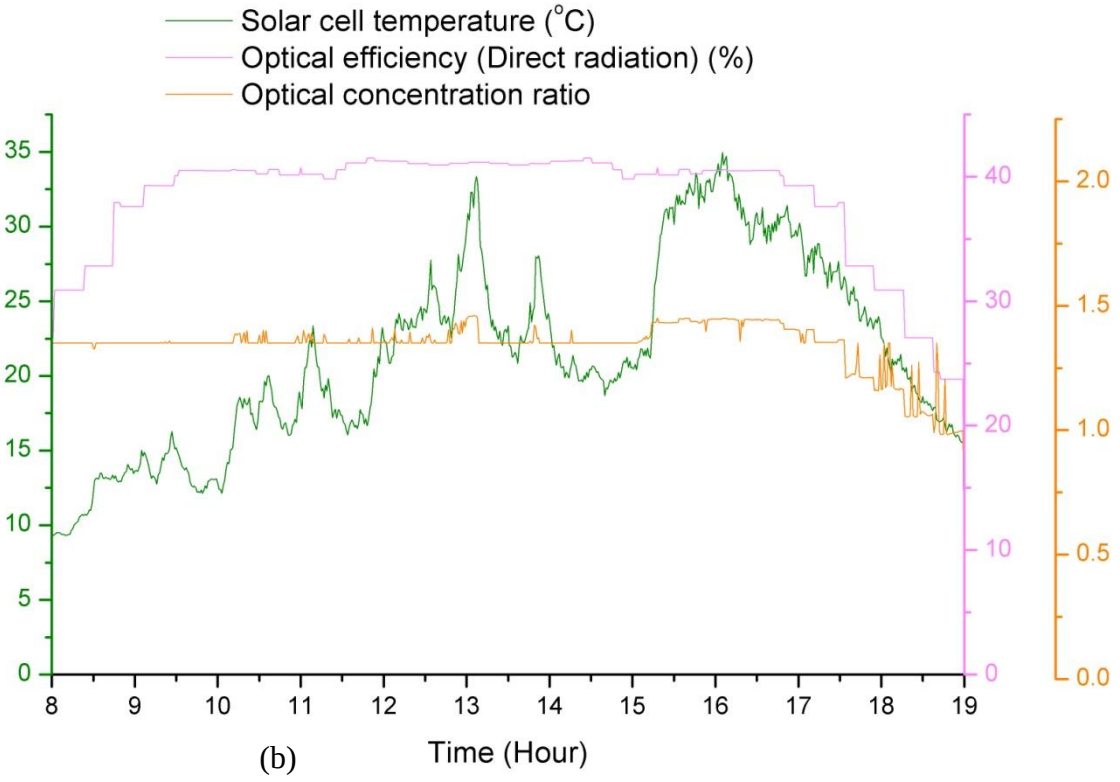

(b)

Figure 6.21: Diurnal variation for H1 TICPV on a sunny interval day of: (a) power output and irradiance, (b) temperature and optical performance

Figure 6.22 (a) shows the measured power output (black line) of the H1 TICPV module generated for the recorded global solar irradiance (blue line) on a cloudy day (29th May). The results of the simulated power output using the integrated model are illustrated on the same graph (red line); these results are in line with expectations as they, with the measured power output, follow exactly the trend of the global irradiance. The difference between the simulated power output and the measured power output is very low <10% for most of the data and reaches 20% for some cases where there are high solar irradiance variations. The global solar irradiance measurements are very low varying from 120W/m^2 to 410W/m^2 during the day. This can be explained in terms of the weather conditions being cloudy and as such the solar irradiance measured is mainly diffuse. For a maximum global irradiance of 410W/m^2 at 15:30, the H1 TICPV module generated 1.19W (corresponding to 38.6W generated by 1m^2 of H1 TICPV module) with an optical efficiency (diffuse radiation) of 33% and an optical concentration ratio of 1.35. The optical efficiency (direct radiation) represented with the pink line in Figure 6.22(b) is not considered in the simulation of the power output as the weather was cloudy and only the optical efficiency (diffuse radiation) is considered. This can be shown on Figure 6.22(b) where the optical concentration ratio is illustrated with a perfect horizontal (straight) orange line; it is constant (1.35) throughout the day from 08:00 to 19:00. This can be attributed to the fact that for the 29th May the solar irradiance was all diffuse.

The green line in Figure 6.22(b) illustrates the variation of the solar cells temperature of the H1 TICPV module on a cloudy day. The temperature reaches a maximum of 26.3ºC for a maximum global irradiance of 410W/m^2. The temperature of the solar cell increases throughout the day until 16:45 when the solar irradiance starts decreasing at the end of the day followed by the decrease in the solar cell temperature.

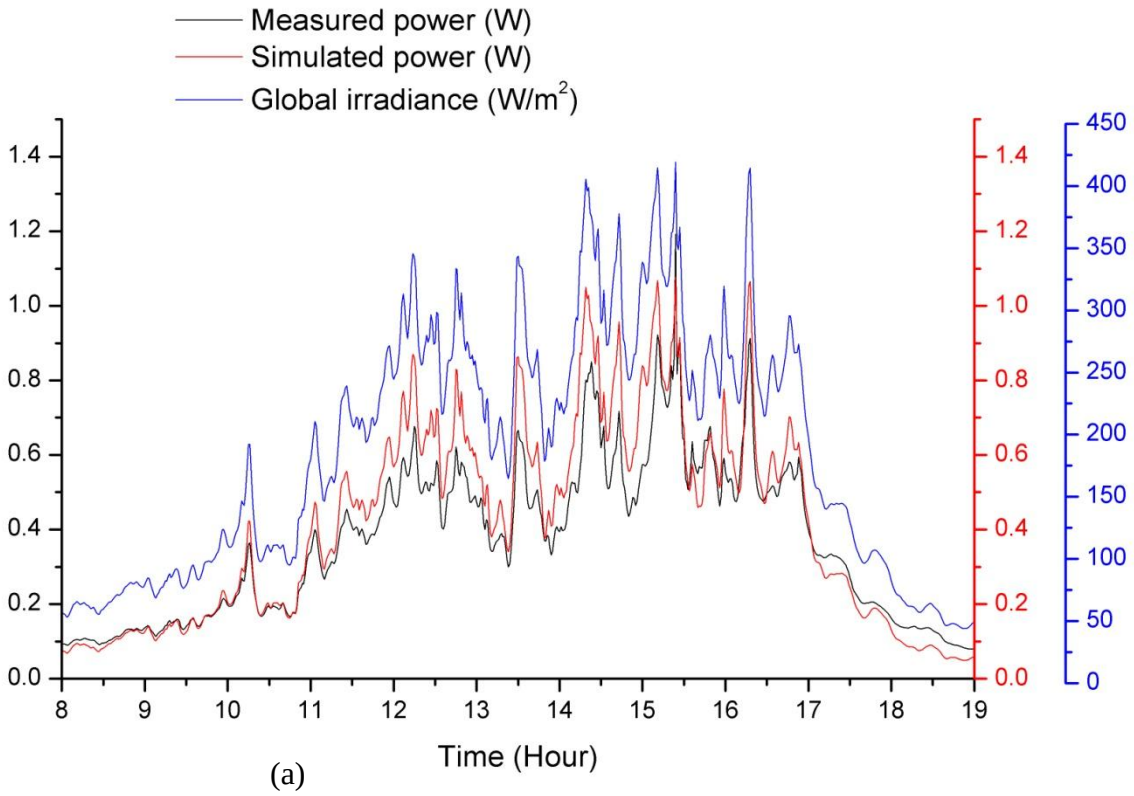

(a)

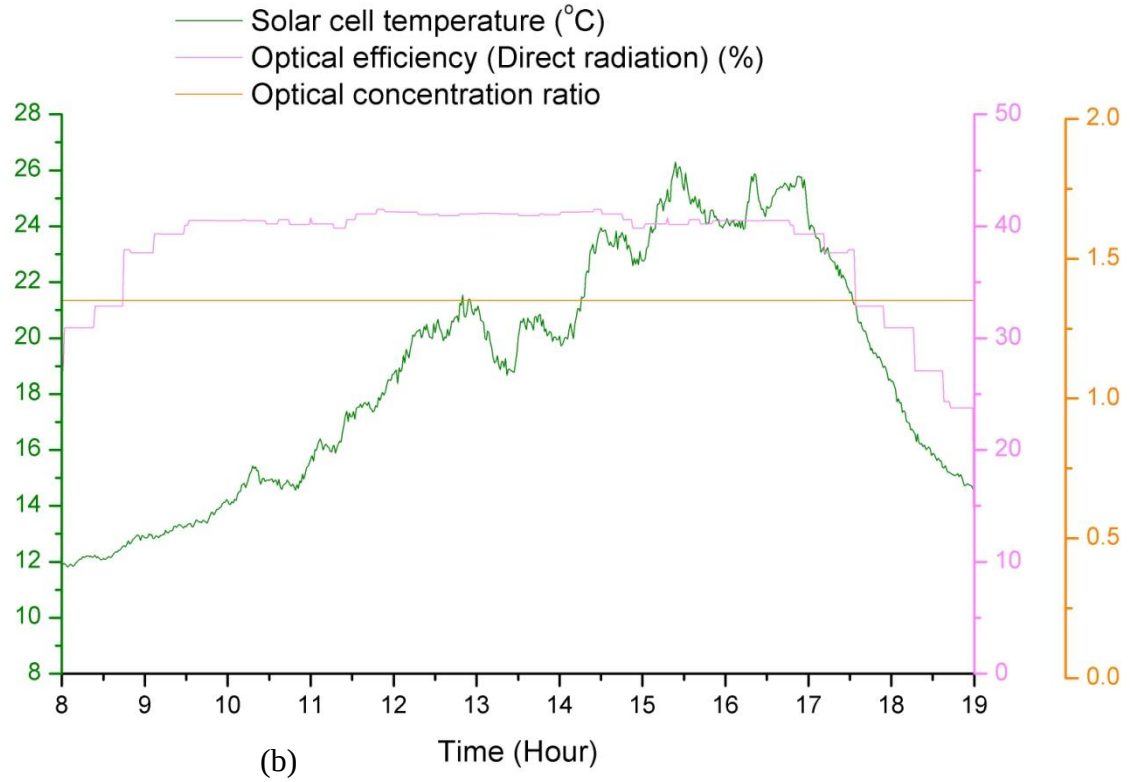

(b)

Figure 6.22: Diurnal variation for H1 TICPV on a cloudy day of: (a) power output and irradiance, (b) temperature and optical performance

6.7.1.2 Power output of H1.5 TICPV module.

Figure 6.23(a) shows the measured power output (black line) of the H1.5 TICPV module generated for the recorded global solar irradiance (blue line) on a sunny day (26th May). For a sunny day, the trend of the variation of the measured power output of the H1.5 TICPV module during the day (black line) follows the trend of the global irradiance (blue line). The red line on the graph in Figure 6.23(a) represents the simulated power output – it can be seen that the results are similar to the measured power with a maximum difference of 10%. For a maximum global irradiance of 880W/m^2 at 13:42, the H1.5 TICPV module generates 1.16W (corresponding to 38.6W generated by 1m^2 of H1.5 TICPV module) with an optical efficiency of 50.6% and an optical concentration ratio of 1.78. Figure 6.23(b) shows that the optical efficiency of the H1.5 TICPV module remains constant (around 50%) for about 5 hours between 11:00 and 16:00. An optical concentration ratio of 1.78 represents a 78% increase in the power output for the H1.5 TICPV module compared to a conventional PV module permitting a saving of 39% of the solar cells material. The H1.5 TICPV is showing sound optical performance because the optical concentration ratio achieved throughout the day is greater than 1 thus achieving concentration as aimed. The temperature of the solar cells of the H1.5 TICPV module on a sunny day reaches a maximum of 47^{o}C (green line Figure 6.24(b)).

With regard to both the sunny interval day (3rd June) and the cloudy day (29th May), the power output of the H1.5 TICPV module also conformed to the values of the simulated power outputs as shown in Figure 6.24(a) and Figure 6.25(a) respectively, with a variation of less than 20%. The maximum power generated on a sunny interval day is 1.8W for a maximum solar irradiance of 1328W/m^2 and the maximum temperature reached is 36^{o}C as shown in Figure 6.24(b). The maximum power output on a cloudy day is 0.146 W for a maximum solar irradiance of 397W/m^2 and the maximum temperature reached is 24^{o}C as shown in Figure 6.25(b). The variation profile of the solar cells temperatures for the three days for the different weather conditions follows the variation profile of the solar irradiance, as expected.

The optical concentration ratio (orange line) of the H1.5 TICPV, illustrated in Figure 6.23(b) increases and decreases with steps rather than in a smooth line for the sunny day. The same profile was obtained for the H1 TICPV on the sunny day. This step profile is due to the fact that the optical efficiency was simulated every five degrees for the incident angles varying from 0^o to 90^o (hence this step pattern is reproduced on the

simulated power output graph – red line Figure 6.23(a). On the sunny interval day (Figure 6.24(b)), the line is horizontal with fluctuations which represent the period of times where the direct sunrays appear. On the cloudy day (Figure 6.25(b)), the optical concentration ratio is constant and equal to 1.44 due to the fact that all of the solar irradiance is diffuse and as such the optical efficiency for the H1.5 TICPV module is constant (40.2%) as it does not depend on the variation of the angles of incidence.

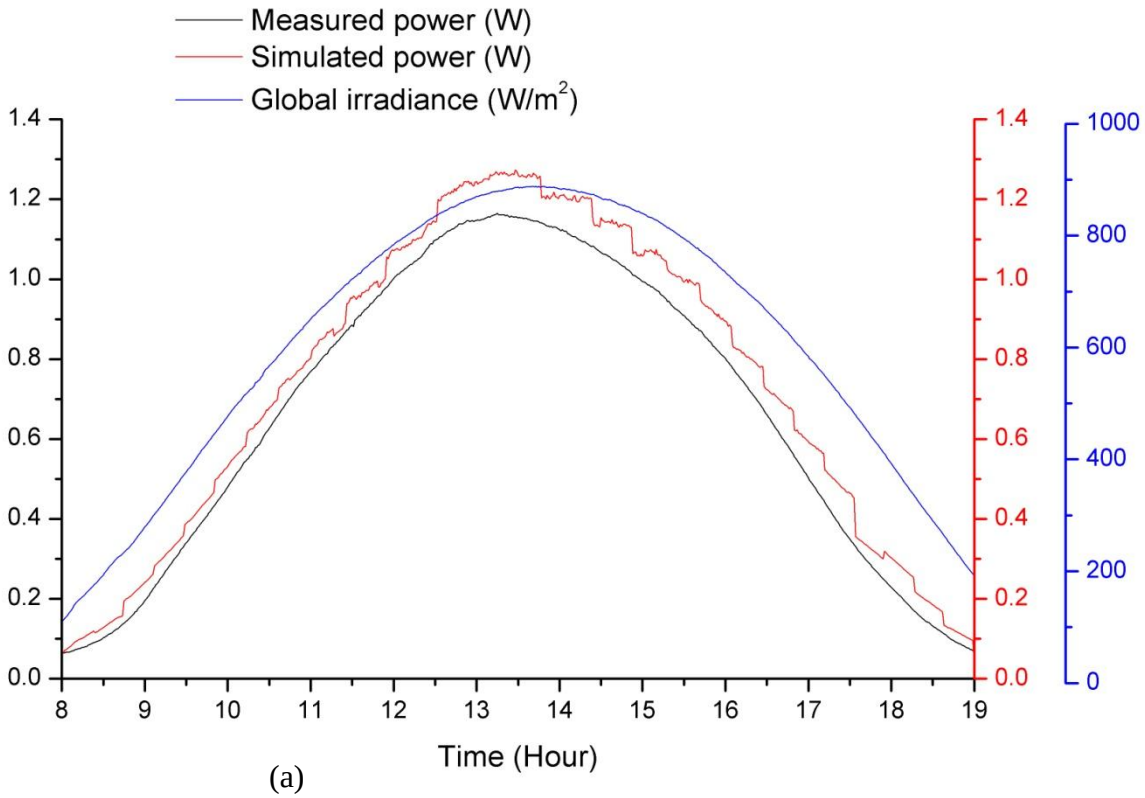

(a)

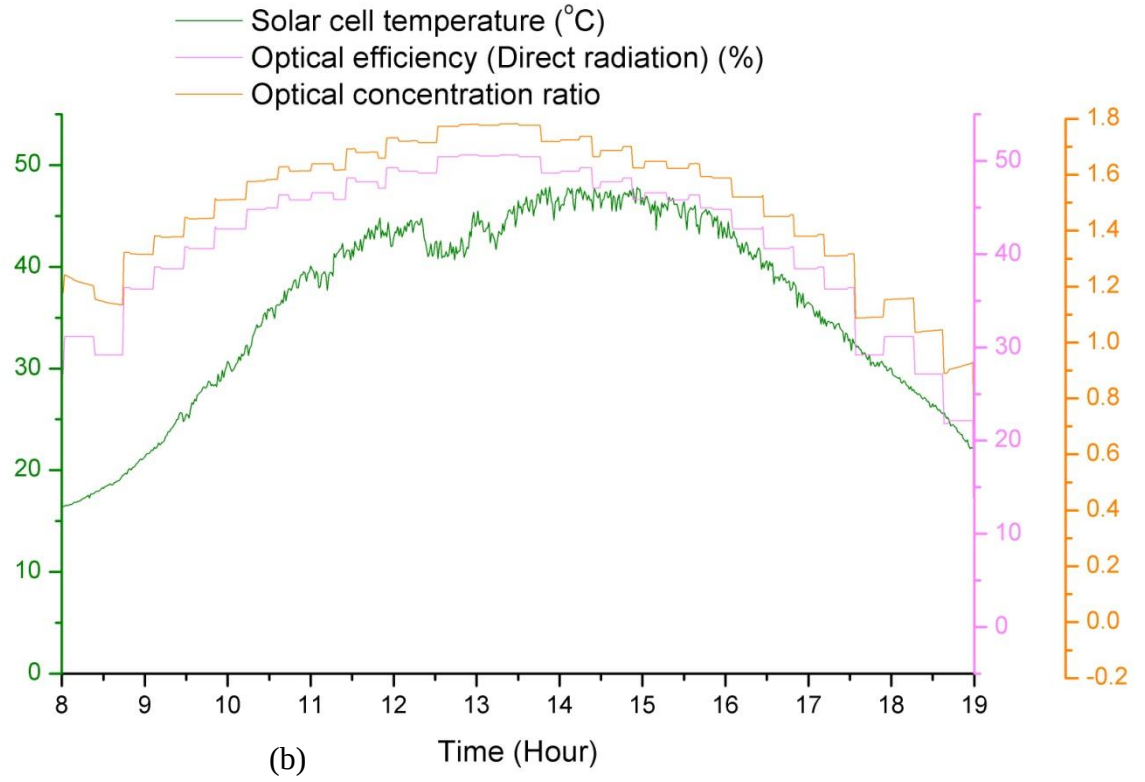

(b)

Figure 6.23: Diurnal variation for H1.5 TICPV on a sunny day of: (a) power output and irradiance, (b) temperature and optical performance

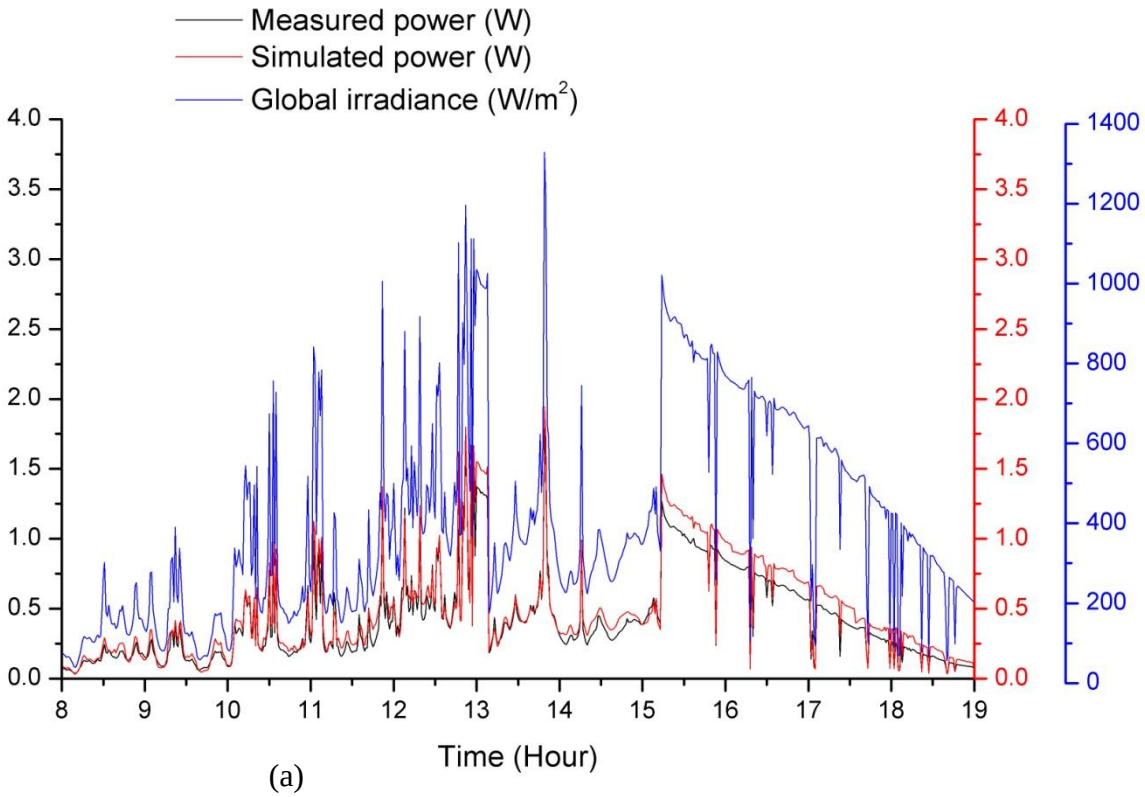

(a)

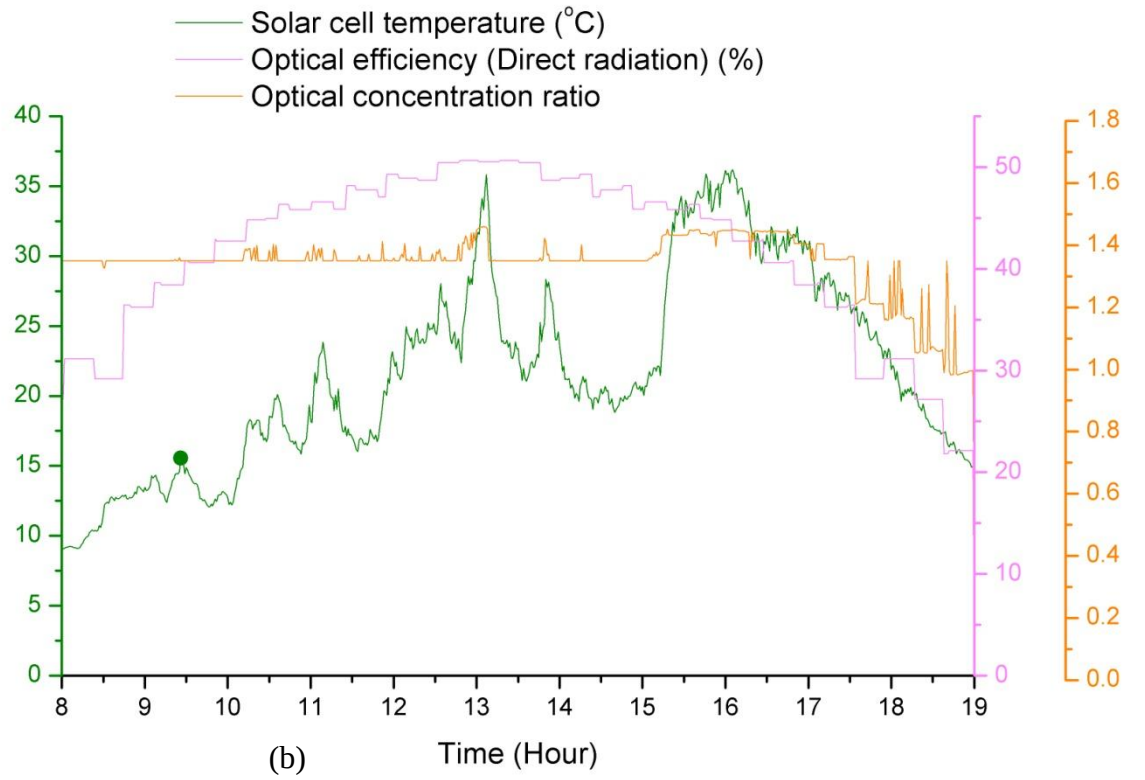

(b)

Figure 6.24: Diurnal variation for H1.5 TICPV on a sunny interval day of: (a) power output and irradiance, (b) temperature and optical performance

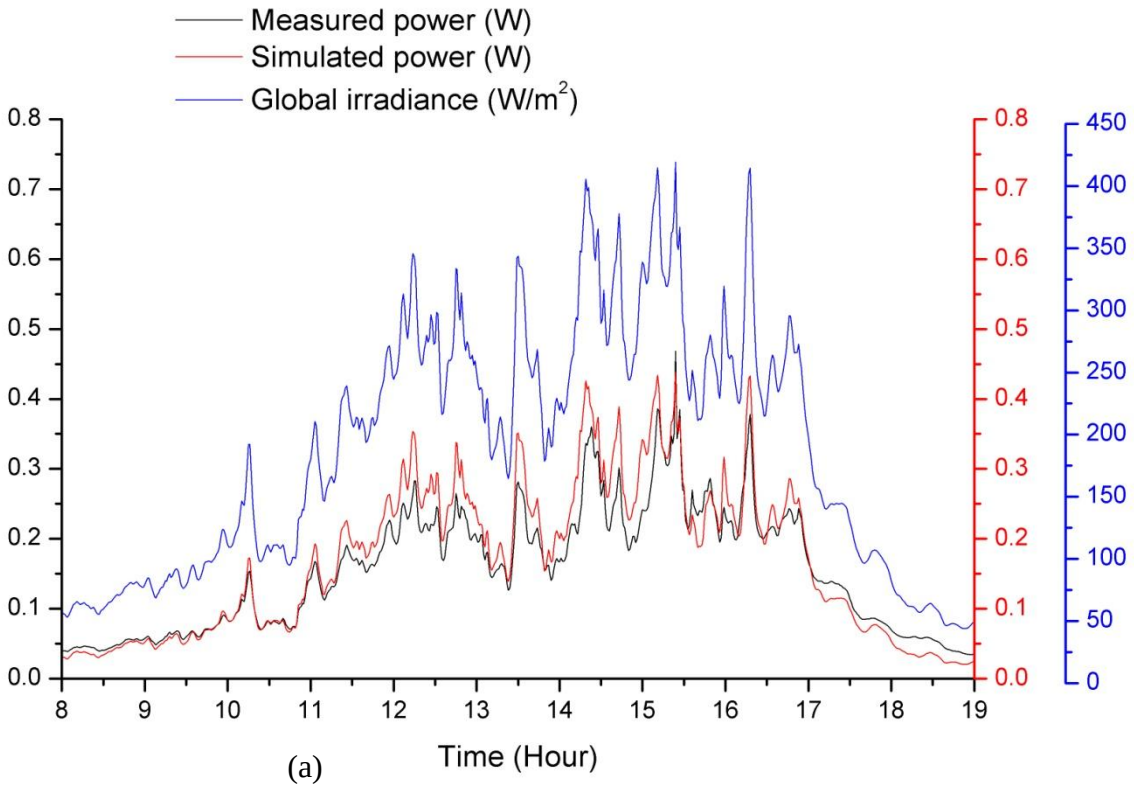

(a)

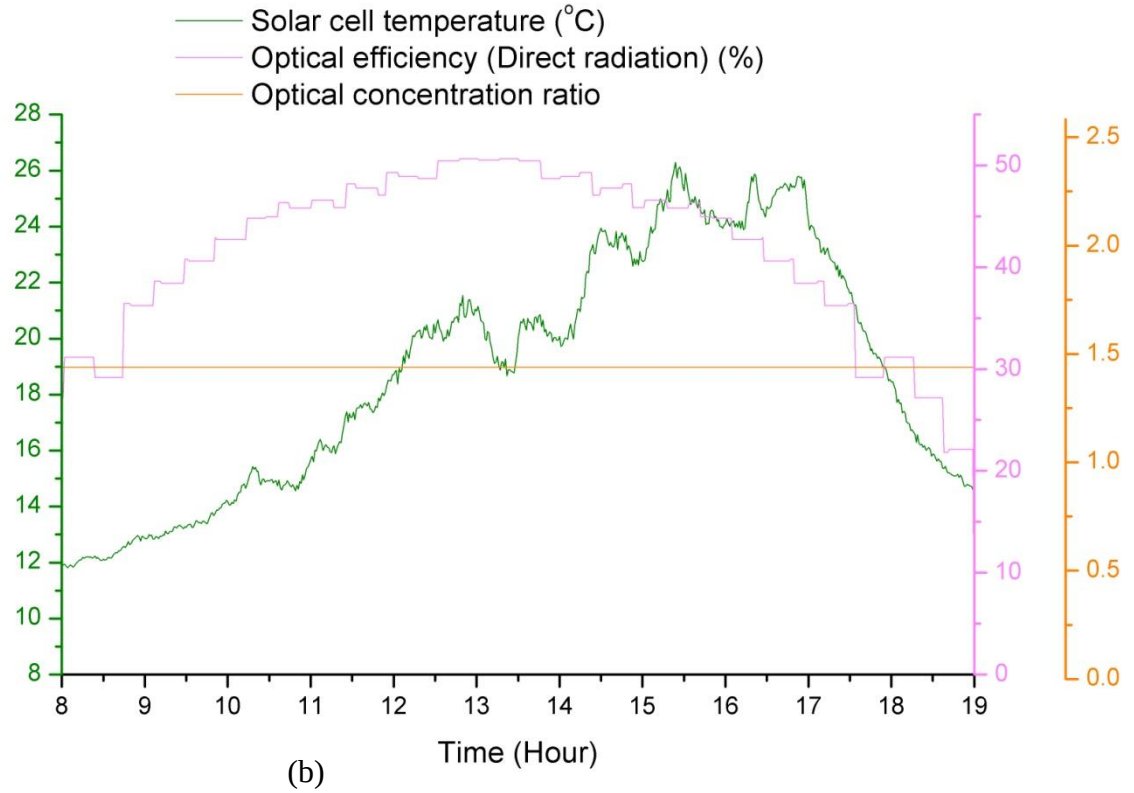

(b)

Figure 6.25 : Diurnal variation for H1.5 TICPV on a cloudy day of: (a) power output and irradiance, (b) temperature and optical performance

6.7.1.3 Power output of the H2 TICPV module

Figure 6.26 (a) shows the measured power output (black line) of the H2 TICPV module generated for the recorded global solar irradiance (blue line) on a sunny day (26th May). For a sunny day, the trend of the variation of the measured power output of the H2 TICPV module during the day (black line) follows the trend of the global irradiance (blue line). The red line on the graph in Figure 6.26(a) represents the simulated power output – it can be seen that the results are similar to the measured power with a maximum difference of 5%. For a maximum global irradiance of 880W/m^2 at 13:42, the H2 TICPV module generates 2.69W (corresponding to 44.83W generated by 1m^2 of H2 TICPV module) with an optical efficiency of 59.1% and an optical concentration ratio of 1.89.Figure 6.26(b) shows that the optical efficiency of the H2 TICPV module remains constant (around 59%) for about 90 minutes between 12:30 and 14:00; this is due to the fact that the H2 SEH has a lower acceptance angle than both the H1.5 and H1 SEH concentrators. An optical concentration ratio of 1.89 represents an 89% increase in the power output for the H2 TICPV module compared to a conventional PV module permitting a saving of 44% of the solar cells material. An optical concentration ratio greater than 1 is achieved by the H2 TICPV for only 6 hours from 10:30 to 16:30 compared to the H1.5 TICPV and H1 TICPV which achieve an optical concentration greater than 1 for the whole day. The temperature of the solar cells of the H2 TICPV module on a sunny day reaches a maximum of 44^{o}C.

The power output of the H2 TICPV module conformed to the simulated power output for both a sunny interval day and a cloudy day as shown in Figure 6.27(a) and Figure 6.28(a) with a variation of less than 20%. The maximum power generated on a sunny interval day is 4.19W for a maximum solar irradiance of 1328W/m^2 and the maximum temperature reached is 34^{o}C as shown in Figure 6.27(b). The maximum power output on a cloudy day is 1.09W for a maximum solar irradiance of 397W/m^2 and the maximum temperature reaches 24^{o}C as shown in Figure 6.28(b). The variation profile of the solar cells temperatures for the three days for the different weather condition follows the variation profile of the solar irradiance, as expected.

As shown and described before for the H1 TICPV and H1.5 TICPV, the optical concentration ratio of the H2 TICPV, illustrated in Figure 6.26(b) (orange line) increases and decreases with steps and not in a smooth line for the sunny day. On the

sunny interval day (Figure 6.27(b)), the line fluctuates corresponding to the fluctuations in global irradiance. On the cloudy day (Figure 6.28(b)), the optical concentration ratio is constant and equal to 1.45 due to the fact that all of the solar irradiance is diffuse and as such the optical efficiency for the H2 TICPV module is constant (41.3%) as it does not depend on the variation of the angles of incidence.

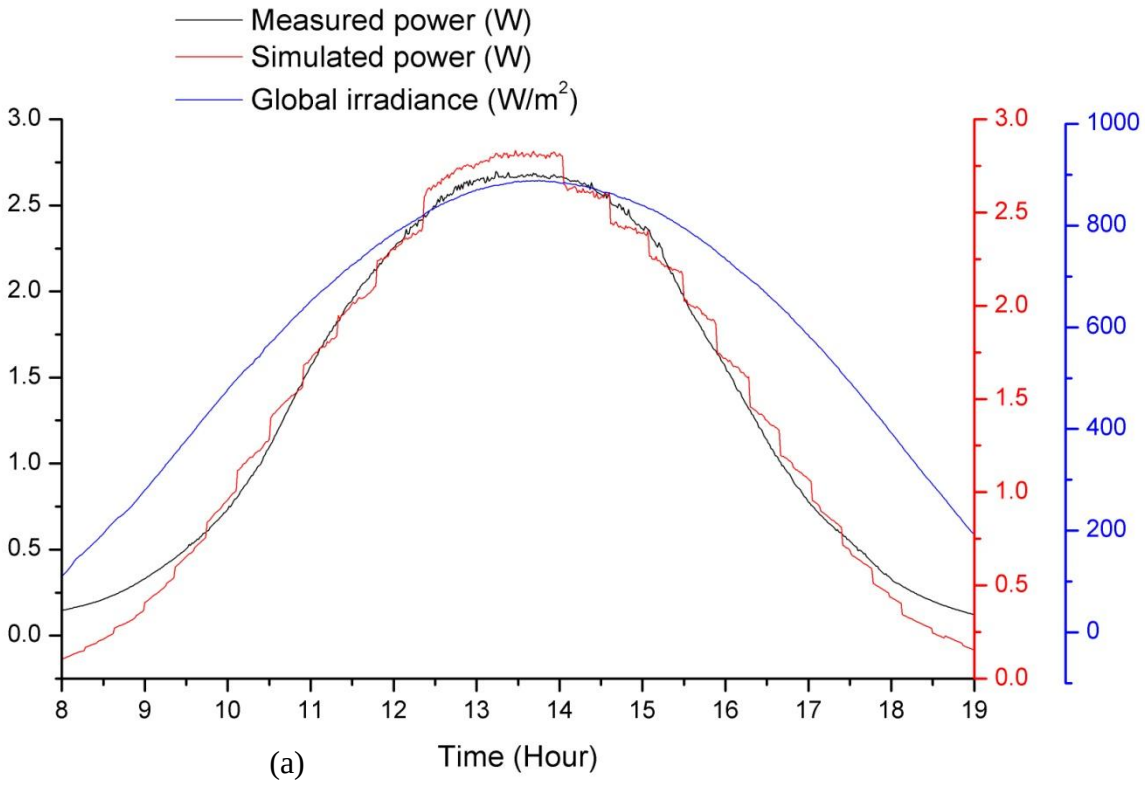

(a)

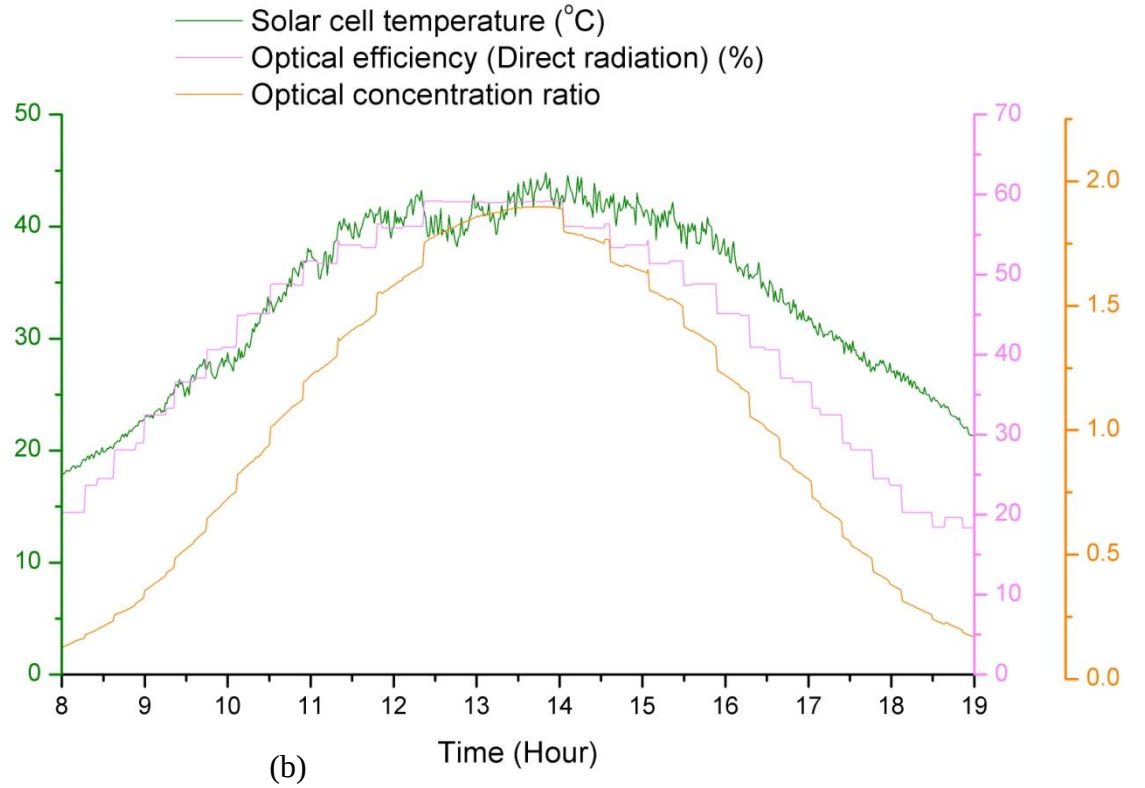

(b)

Figure 6.26 : Diurnal variation for H2 TICPV on a sunny day of: (a) power output and irradiance, (b) temperature and optical performance

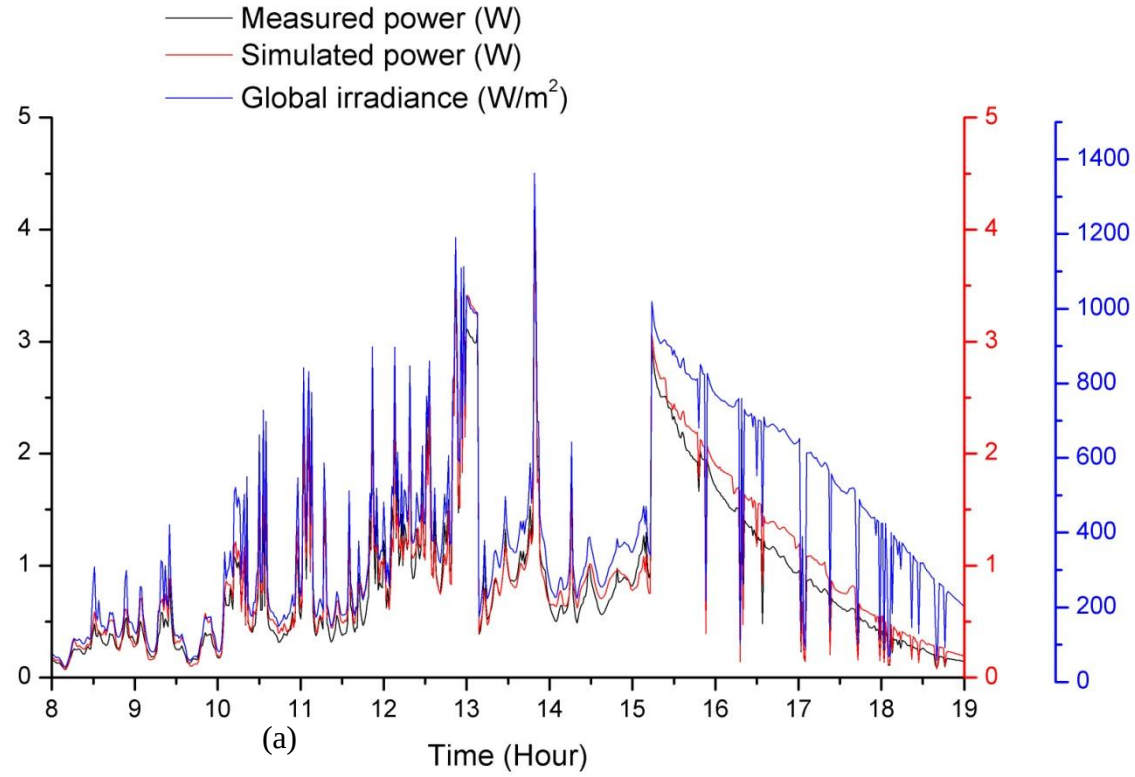

(a)

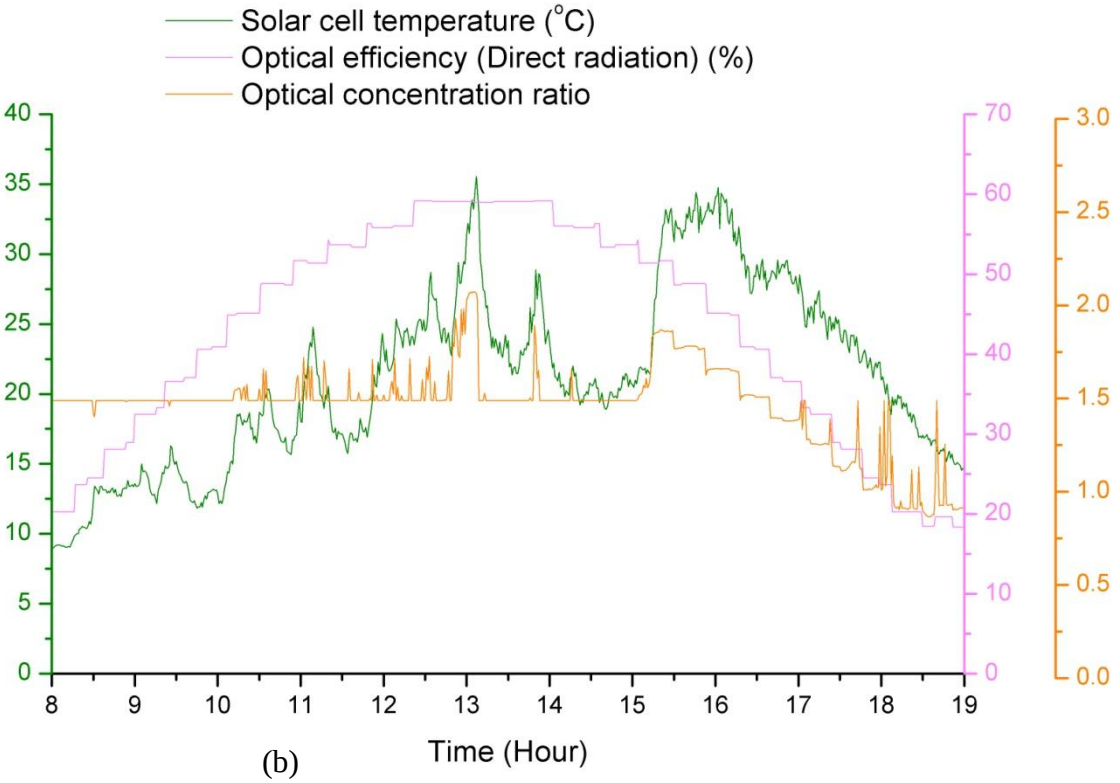

(b)

Figure 6.27 : Diurnal variation for H2 TICPV on a sunny interval day of: (a) power output and irradiance, (b) temperature and optical performance

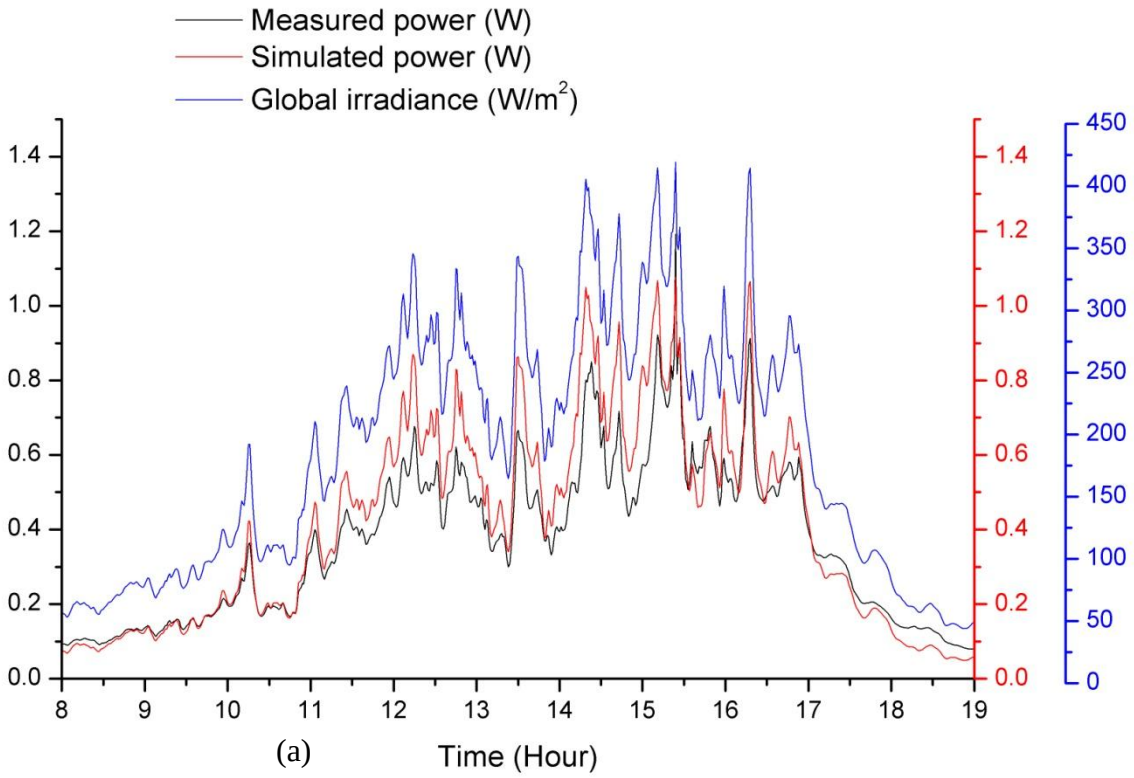

(a)

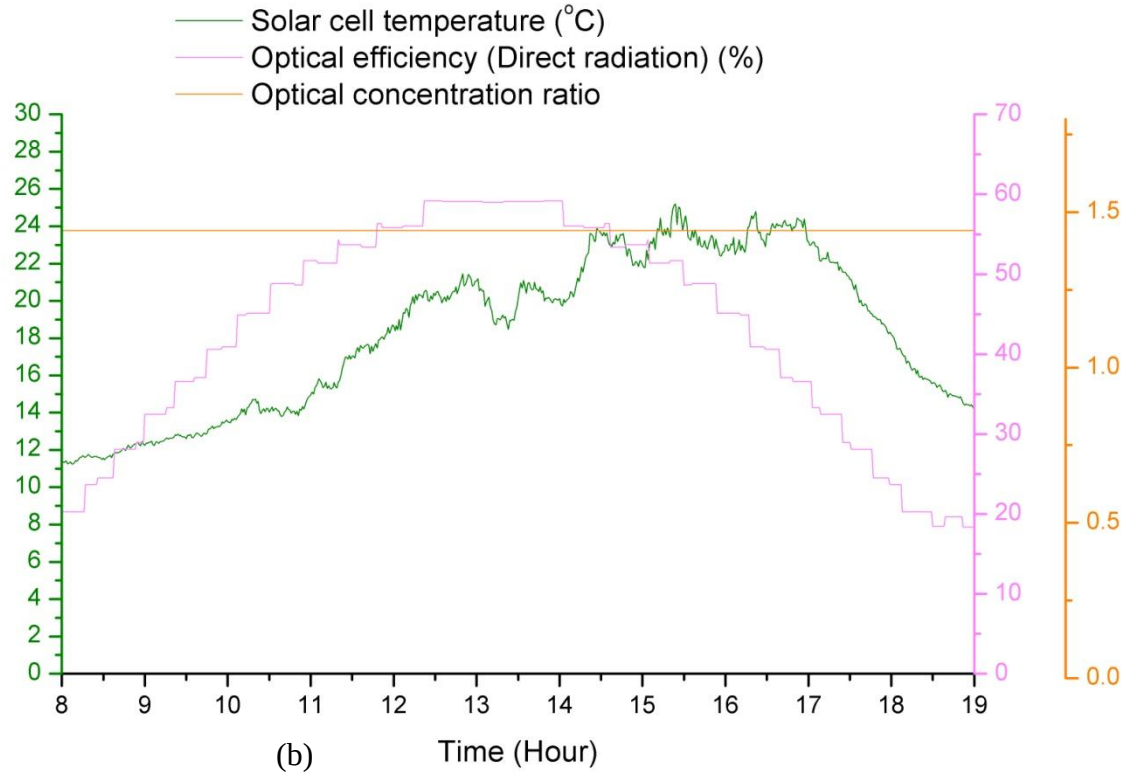

(b)

Figure 6.28 : Diurnal variation for H2 TICPV on a cloudy day of: (a) power output and irradiance, (b) temperature and optical performance

6.7.1.4 Power output of H2.5 TICPV module

Figure 6.29(a) shows the measured power output (black line) of the H2.5 TICPV module generated for the recorded global solar irradiance (blue line) on a sunny day (26^{th} May).

For a sunny day, the trend of the variation of the measured power output of the H2.5 TICPV module during the day (black line) follows the trend of the global irradiance (blue line). The red line on the graph in Figure 6.29(a) represents the simulated power output – it can be seen that the results are similar to the measured power with a maximum difference of 10%. For a maximum global irradiance of 880W/m^2 at 13:42, the H2.5 TICPV module generated 1.08W (corresponding to 36W generated by 1m^2 of H2.5 TICPV module) with an optical efficiency of 40.6% and an optical concentration ratio of 1.97. Figure 6.29(b) shows that the optical efficiency of the H2.5 TICPV module remains constant (around 40%) for about 3 hours between 11:30 and 14:30. An optical concentration ratio of 2 represents a 100% increase in the power output for the H2.5 TICPV module compared to a conventional PV module permitting a saving of 50% of the solar cells material. An optical concentration ratio greater than 1 is achieved by the H2.5 TICPV for only 6 hours from 10:30am to 16:30 similar to the H2 TICPV and less than both the H1.5 TICPV and H1 TICPV which achieve an optical concentration ratio greater than 1 for the whole day. The temperature of the solar cells of the H2.5 TICPV module on a sunny day reaches a maximum of 45^oC.

The power output of the H2.5 TICPV module conforms to the simulated power outputs for a sunny interval day and a cloudy day as shown in Figure 6.30and Figure 6.31(a) with a variation of less than 10%. The maximum power generated on a sunny interval day is 1.66W for a maximum solar irradiance of 1328W/m^2 and the maximum temperature reached is 33^oC as shown in Figure 6.30(b). The maximum power output on a cloudy day is 0.45 W for a maximum solar irradiance of 397W/m^2 and the maximum temperature reached is 24^oC as shown in

Figure 6.31(b). The variation profile of the solar cells temperatures for the three days for the different weather conditions follows the variation profile of the solar irradiance, as expected.

The optical concentration ratio of the H2.5 TICPV on the sunny day, illustrated in Figure 6.29(b) (orange line) increases and decreases with steps not in a smooth line; a similar pattern of results was shown before for the H1 TICPV, H1.5 TICPV and H2

TICPV. For the sunny interval day (Figure 6.30(b)), the line fluctuates corresponding to the fluctuations in global irradiance. On the cloudy day (Figure 6.31(b)), the optical concentration ratio is constant and equal to 1.42 due to the fact that all of the solar irradiance is diffuse and as such the optical efficiency for the H2.5 TICPV module is constant (25.8%) as it does not depend on the variation of the angles of incidence.

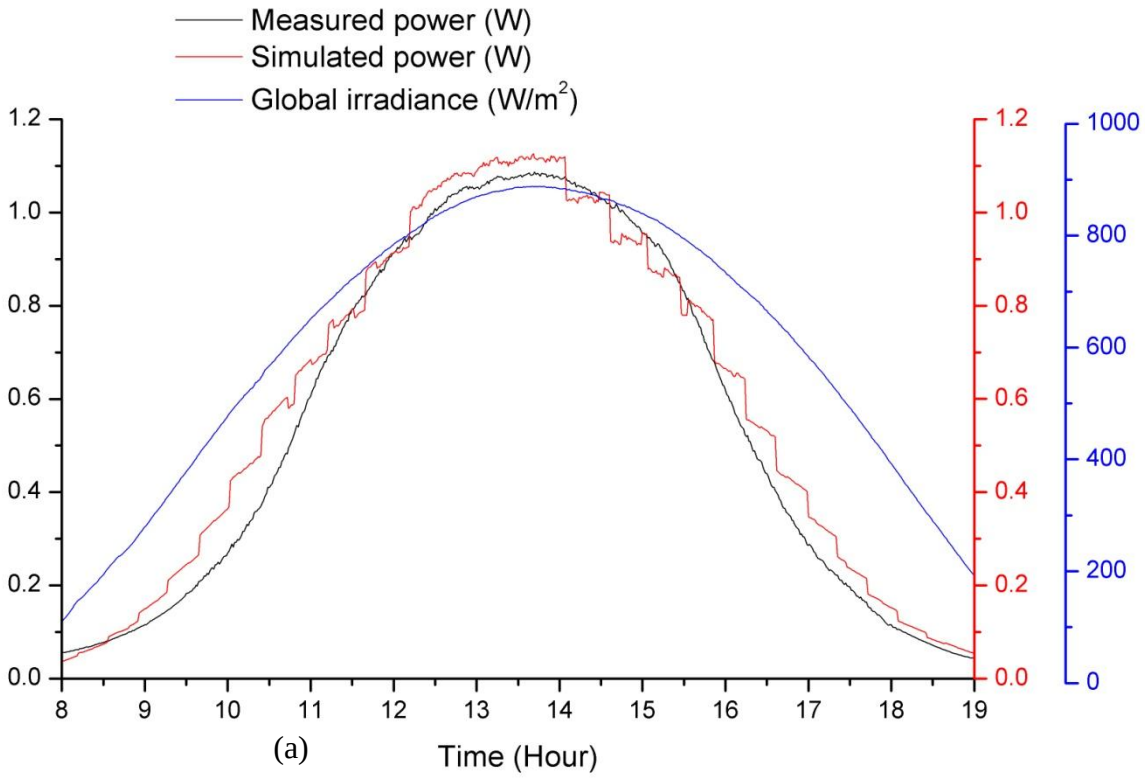

(a)

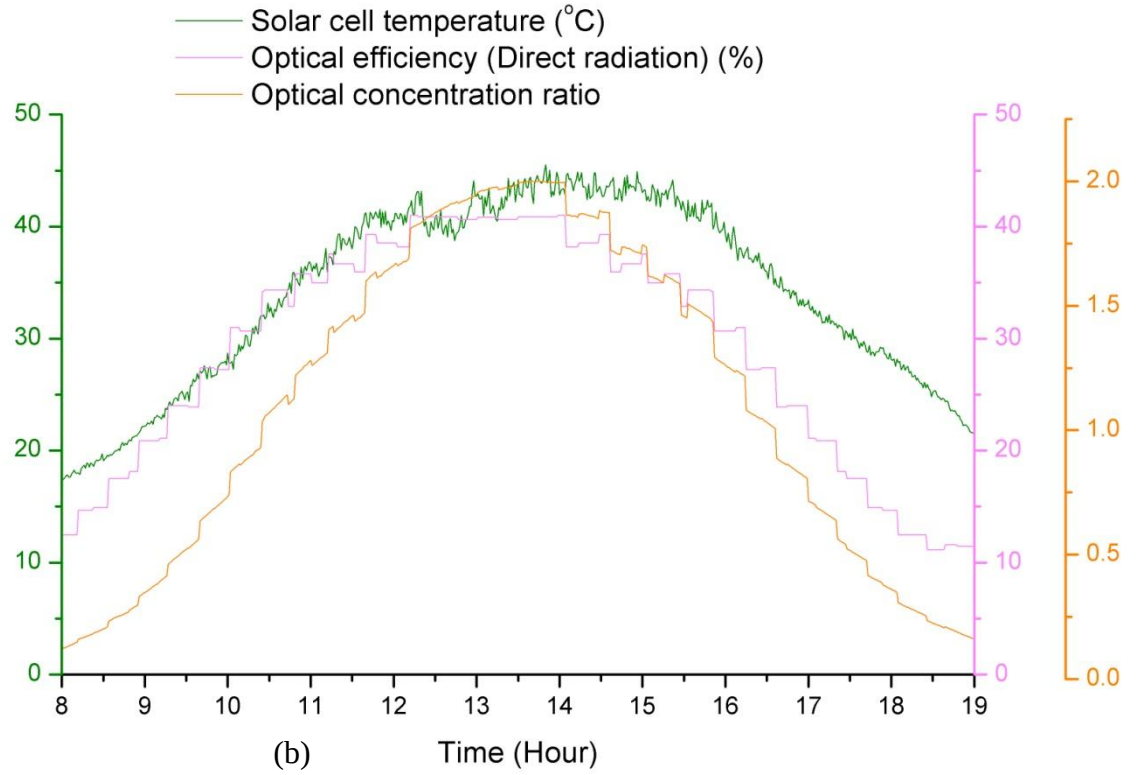

(b)

Figure 6.29 : Diurnal variation for H2.5 TICPV on a sunny day of: (a) power output and irradiance, (b) temperature and optical performance

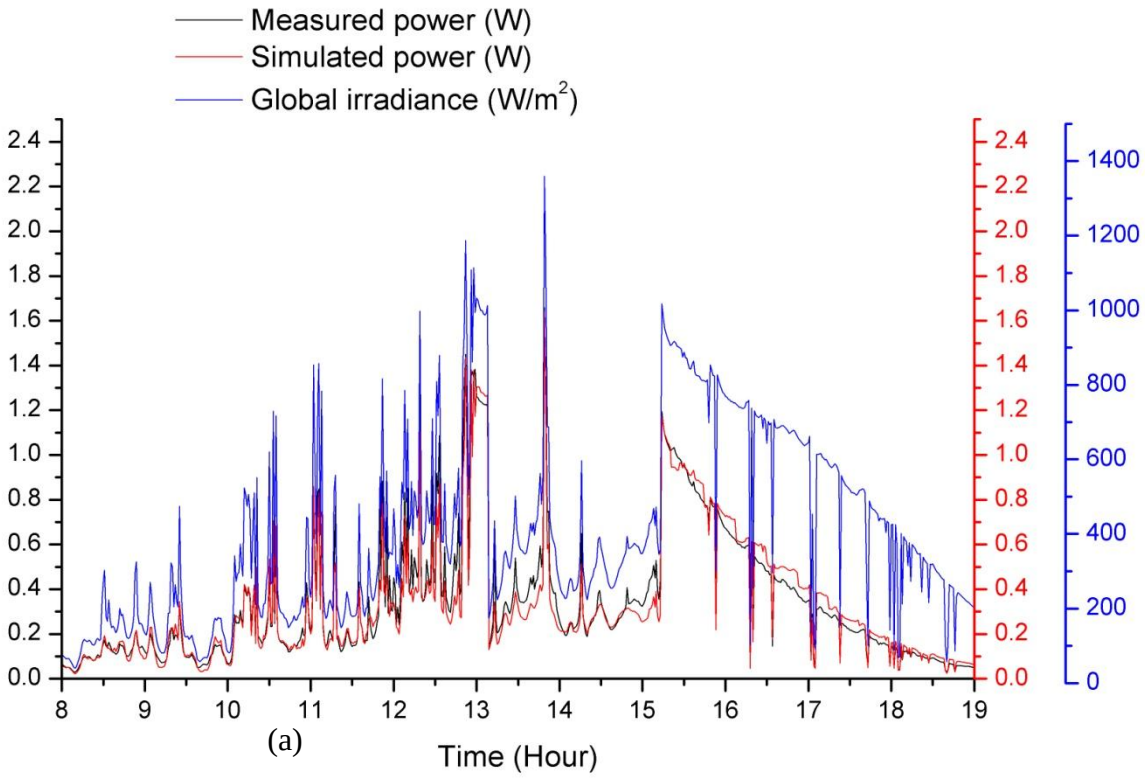

(a)

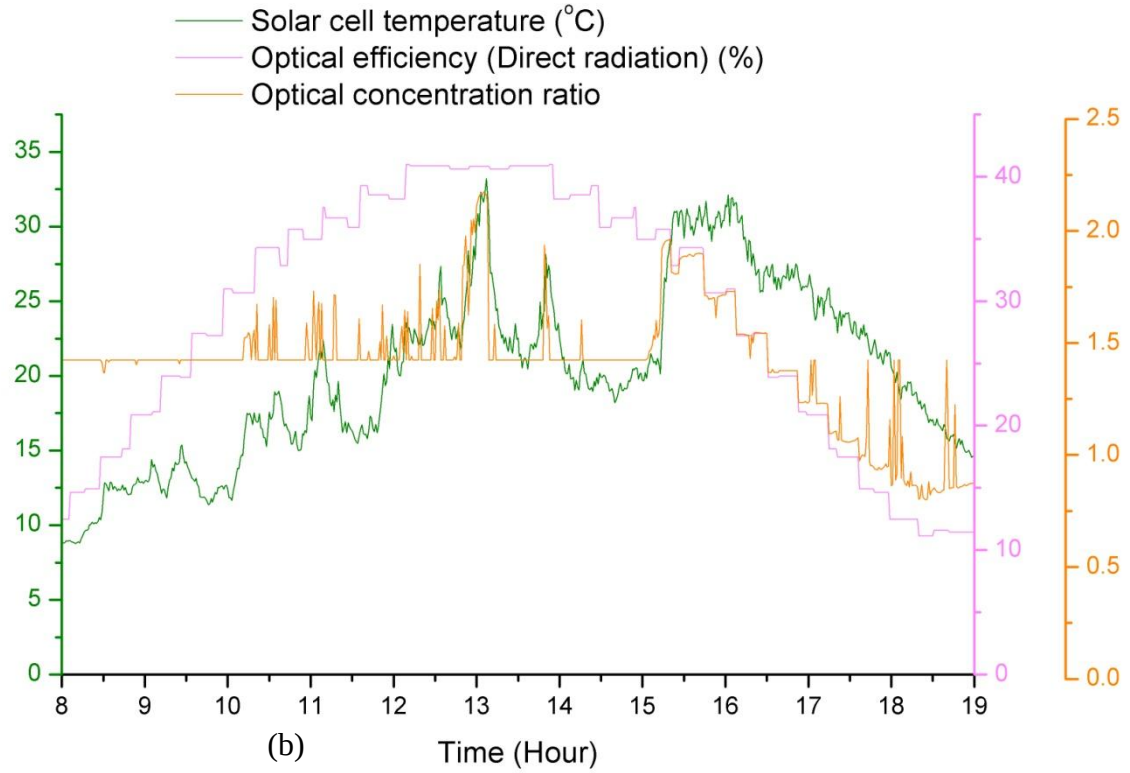

(b)

Figure 6.30: Diurnal variation for H2.5 TICPV on a sunny interval day of: (a) power output and irradiance, (b) temperature and optical performance

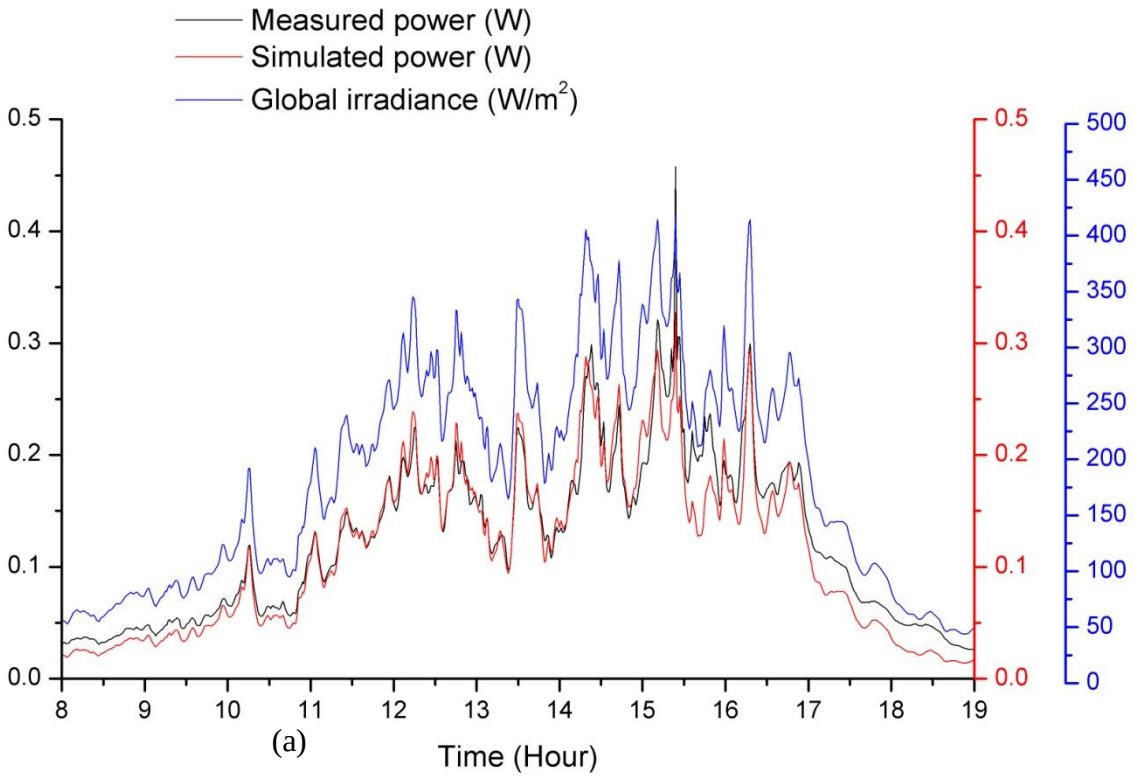

(a)

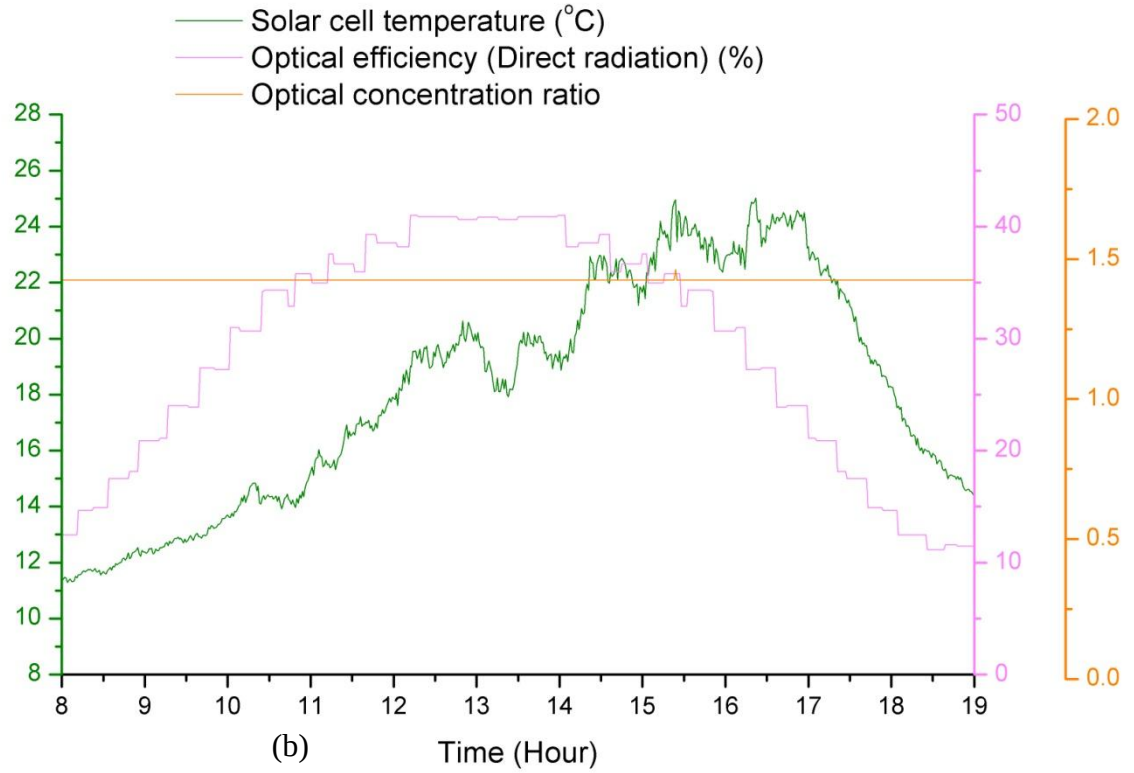

(b)

Figure 6.31: Diurnal variation for H2.5 TICPV on a cloudy day of: (a) power output and irradiance, (b) temperature and optical performance

6.7.1.5 Power output of H3 TICPV module.

Figure 6.32 (a) shows the measured power output (black line) of the H3 TICPV module generated for the recorded global solar irradiance (blue line) on a sunny day (26th May). For a sunny day, the trend of the variation of the measured power output of the H3 TICPV module during the day (black line) follows the trend of the global irradiance (blue line). The red line on the graph in Figure 6.32(a) represents the simulated power output- it can be seen that the results are similar to the measured power with a maximum difference of 10%. For a maximum global irradiance of 880 W/m^2 at 13:42, the H3 TICPV module generates 1W (corresponding to 40W generated by 1m^2 of H3 TICPV module) which correspond to an optical efficiency of 45% and an optical concentration ratio of 2.54 Figure 6.32(b) shows that the optical efficiency of the H3 TICPV module remains constant (around 45%) for about 90 minutes between 12:55 and 14:30. An optical concentration ratio of 2.54 represents a 150% increase in the power output for the H3 TICPV module compared to a conventional PV module permitting a saving of 60% of the solar cells material. An optical concentration greater than 1 is achieved by the H3 TICPV for 8 hours from 09:30 to 17:30, similar to that obtained by the H1.5 TICPV and H1 TICPV which achieved an optical concentration ratio greater than 1 for the whole day. This is due to the combination of the high geometric concentration ratio (6) and the high optical efficiency despite a low acceptance angle for the H3 TICPV. The temperature of the solar cells of the H3 TICPV module on a sunny day reaches a maximum of 43^{o}C.

The power outputs of the H3 TICPV module conformed to simulated power outputs for both a sunny interval day and a cloudy day as shown in Figure 6.33(a) and Figure 6.34(a) with a variation of less than 10%. The maximum power generated on a sunny interval day is 1.5W for a maximum solar irradiance of 1328W/m^2 and the maximum temperature reached is 30^{o}C as shown in Figure 6.33(b). The maximum power output on a cloudy day is 0.4W for a maximum solar irradiance of 397W/m^2 and the maximum temperature reached is 23^{o}C as shown in Figure 6.34(b). The variation profile of the solar cells temperatures for the three days for the different weather conditions follows the variation profile of the solar irradiance showing that the temperature is function of the solar radiation.

The optical concentration ratio of the H3 TICPV, on the sunny day, illustrated in

Figure 6.32(b) (orange line) increases and decreases with steps and not in a smooth line, as shown before for the other TICPV modules. For the sunny interval day (
Figure 6.33(b)), the line fluctuates corresponding to the fluctuations in global irradiance. On the cloudy day (Figure 6.34(b)), the optical concentration ratio is constant and equal to 1.46 due to the fact that all of the solar irradiance is diffuse and as such the optical efficiency for the H3 TICPV module is constant (26.7% Table 6.4) as it does not depend on the variation of the angles of incidence.

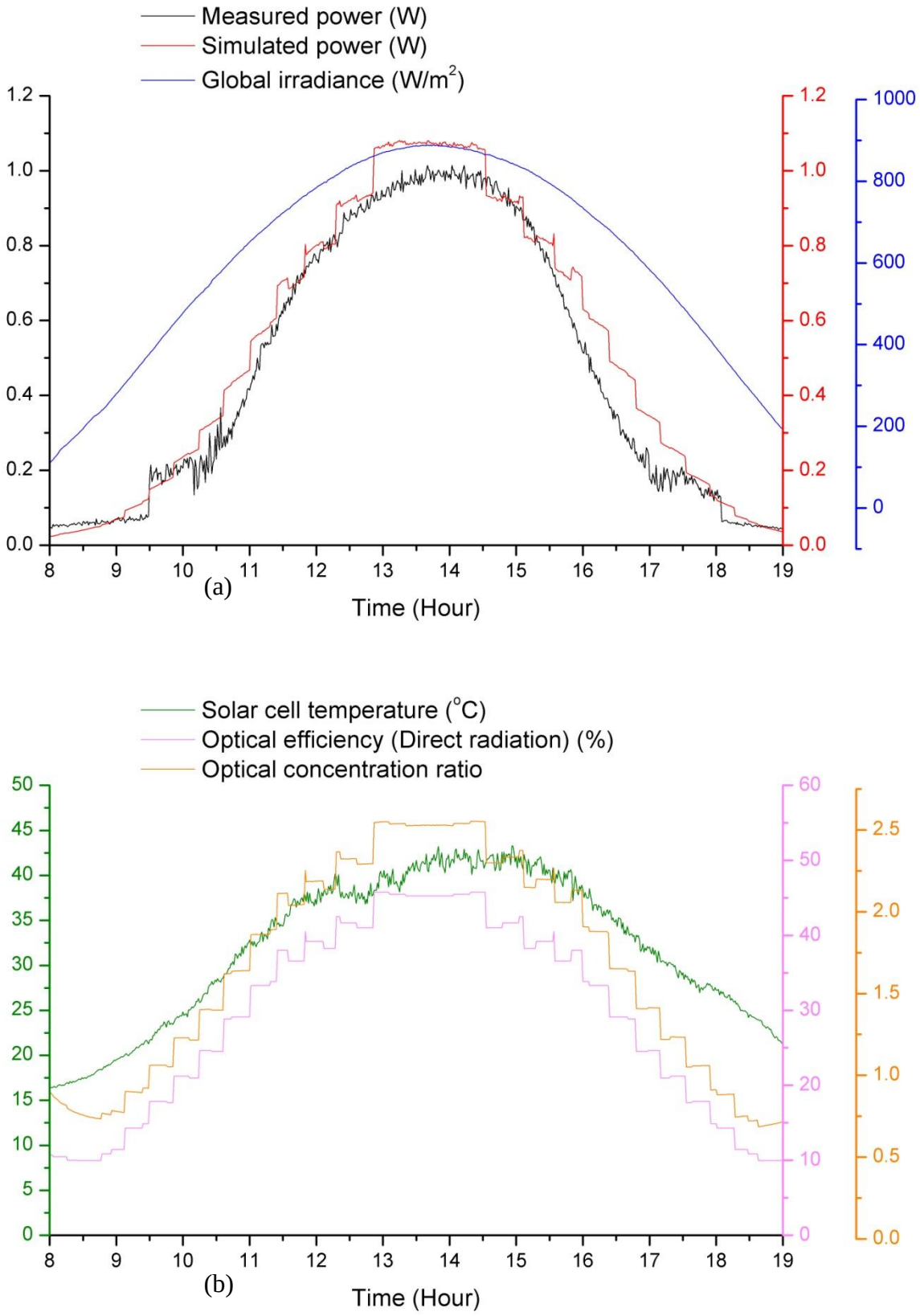

Figure 6.32: Diurnal variation for H3 TICPV on a sunny day of: (a) power output and irradiance, (b) temperature and optical performance

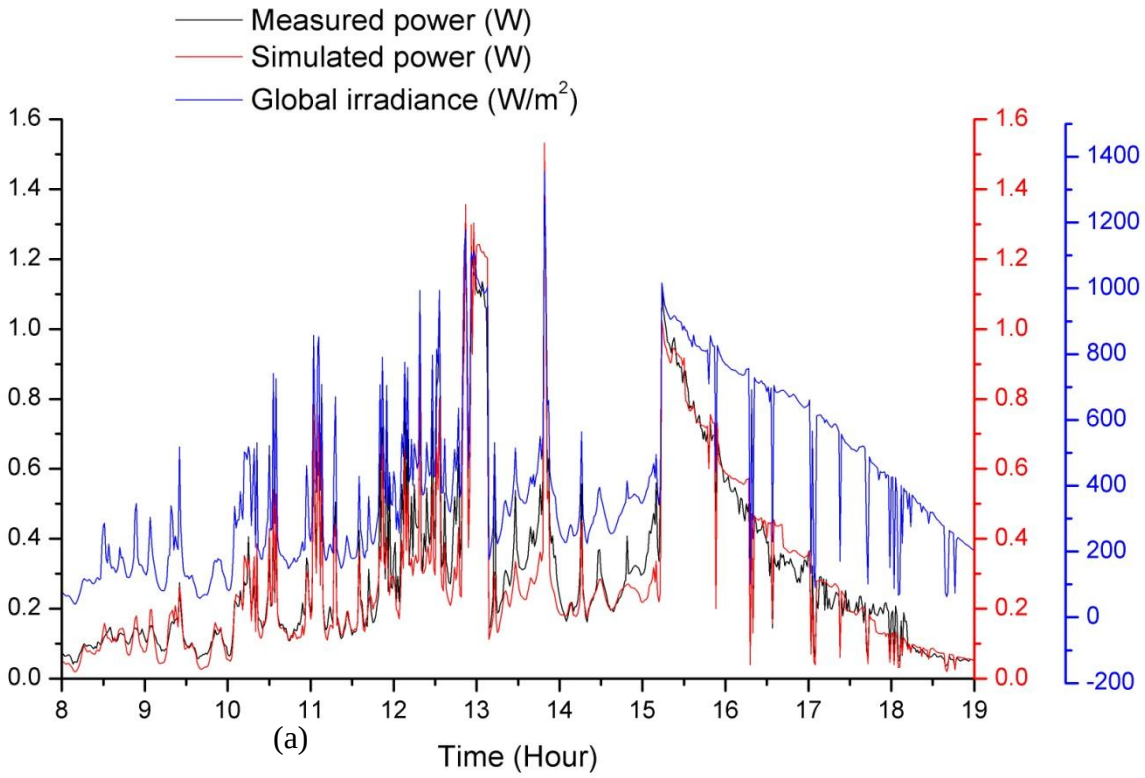

(a)

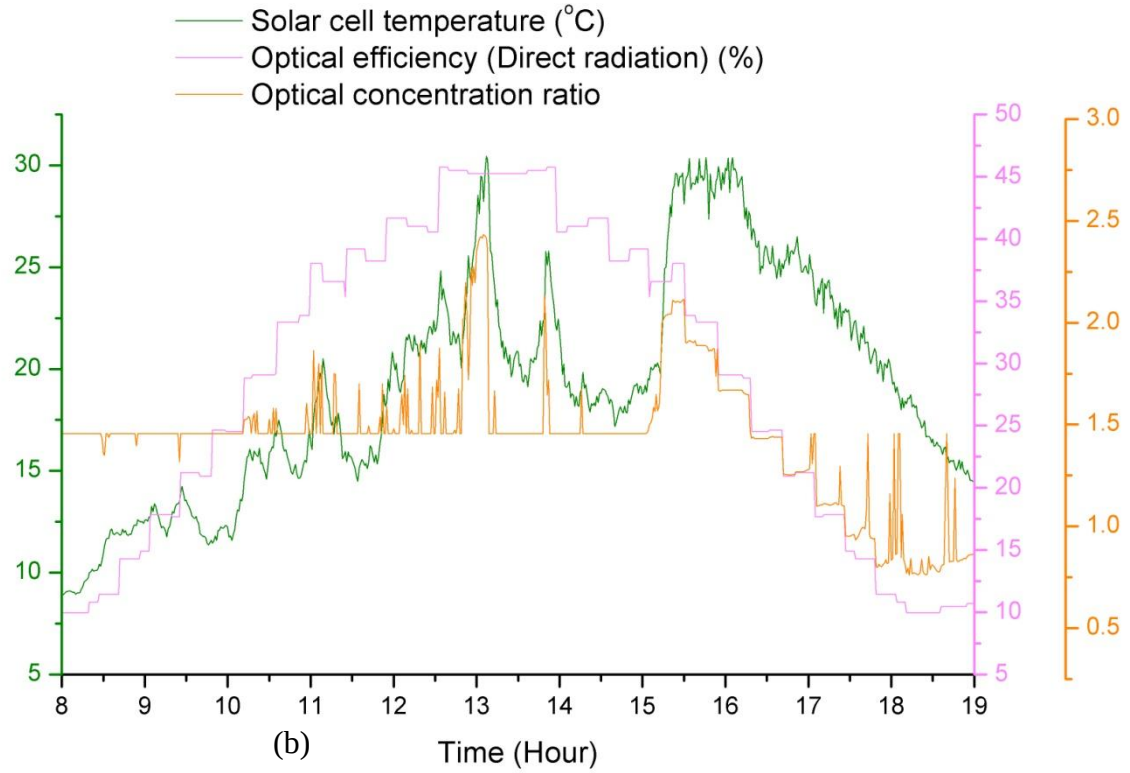

(b)

Figure 6.33: Diurnal variation for H3 TICPV on a sunny interval day of: (a) power output and irradiance, (b) temperature and optical performance

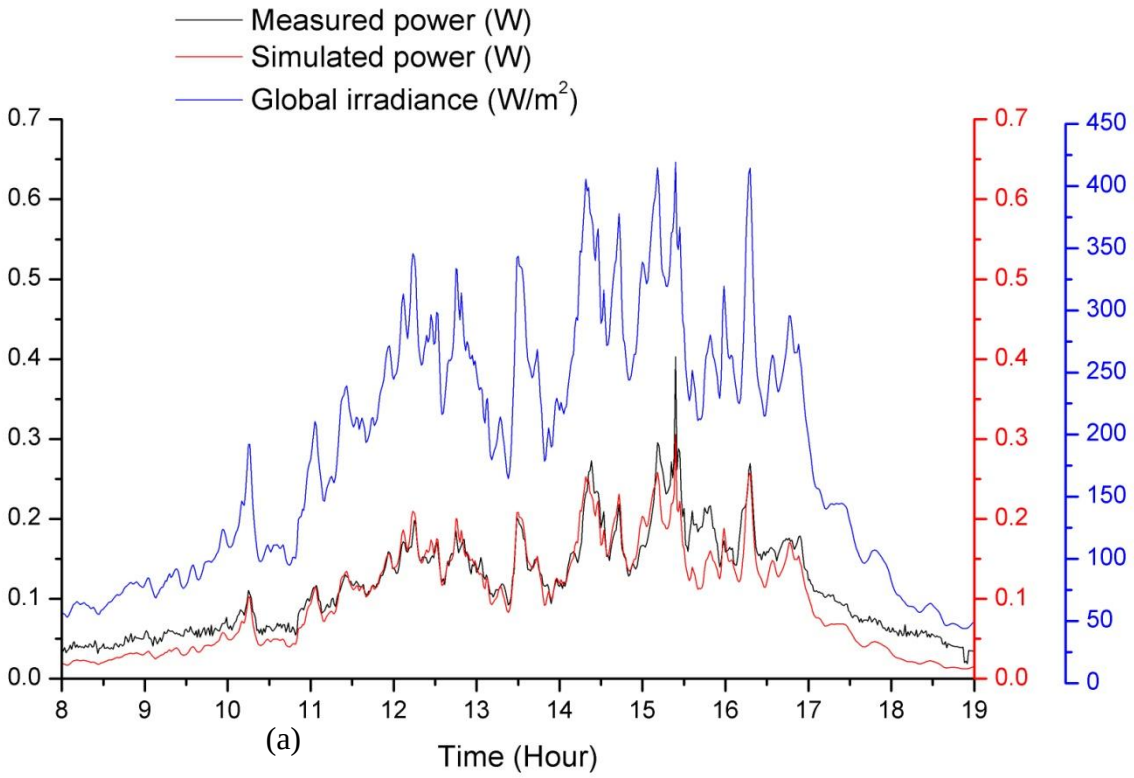

(a)

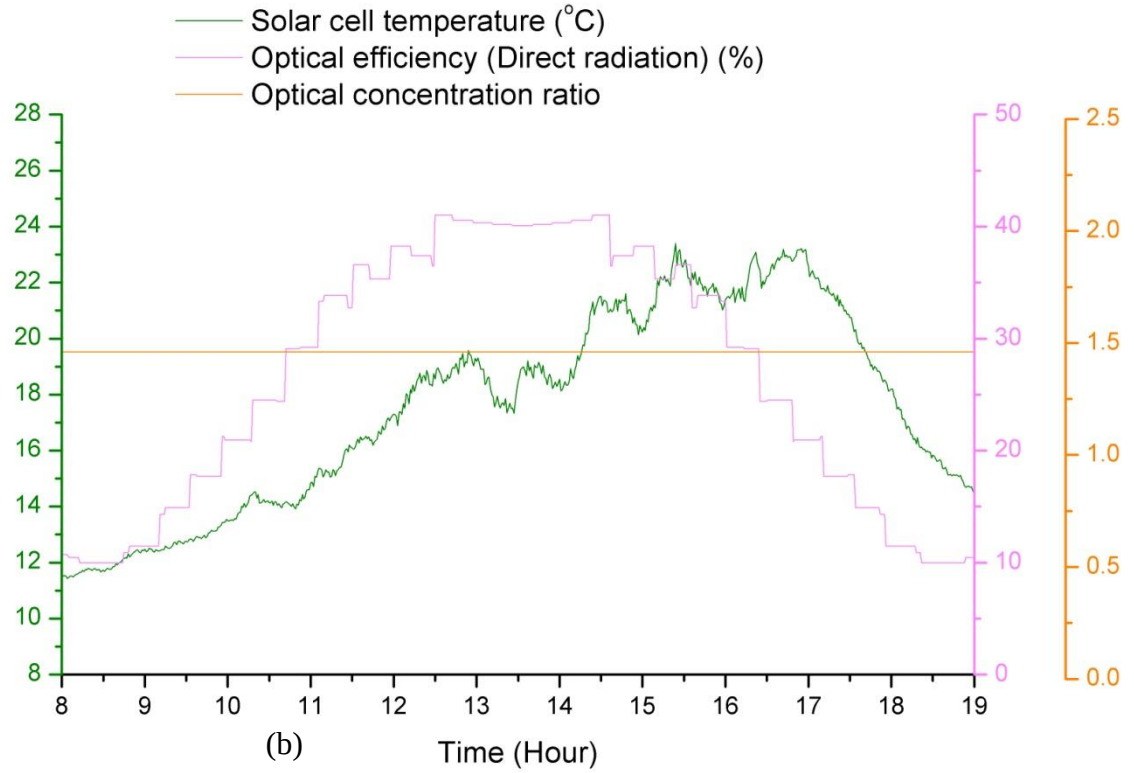

(b)

Figure 6.34: Diurnal variation for H3 TICPV on a cloudy day of: (a) power output and irradiance, (b) temperature and optical performance

Overall all of the comparisons between the simulated and measured power outputs have shown clear validation of the integrated model which will be used in future work to calculate the yearly prediction of the total generated energy of the different TICPV modules in Edinburgh.

6.7.2 Summary of the power output results of the TICPV modules

The outdoor experimental results have shown that the five SEH concentrators when assembled to form a TICPV module give different power outputs and show different performances of optical efficiency and optical concentration over the course of the day. Table 6.5 below shows a summary of the various performance measures obtained for the sunny day (26th May 2012).

Table 6.5: Summary of the performances of the five different TICPV modules on a sunny day in Edinburgh

	Power generated per $1m^2$ of module for a maximum global irradiance of $880W/m^2$	Maximum optical efficiency for no. of hours during day remaining constant	Maximum optical concentration ratio	% Increase in power output compared to conventional PV module	% Saving of solar cells material	Maximum solar cell temperature (ºC)
H1 TICPV	$33.7W/m^2$	~41% for 8 hours of the day	1.44	40	29	45
H1.5 TICPV	$38.6W/m^2$	~50% for 5 hours of the day	1.78	78	39	47
H2 TICPV	$44.83W/m^2$	~59% for ~90 minutes of the day	1.89	89	44	44
H2.5 TICPV	$36W/m^2$	~40% for 3 hours of the day	1.97	100	50	45
H3 TICPV	$40W/m^2$	~45% for ~90 minutes of the day	2.54	150	60	43

From the table, it can be seen that the optical efficiency of the H2 TICPV module is the highest, however, it only remains at this constant value for a period of ~90 minutes during the day compared to the H1 TICPV module which despite having a lower optical efficiency remains constant for the longest amount of time during the day (eight hours). When examining the optical concentration ratios, it can be seen that the H3 TICPV has the highest value; this is related to the fact that it has the highest geometrical concentration ratio (C_g = 6). Consequently, it provides the highest increase in power output (150%) compared to conventional PV modules and therefore, the largest percentage of solar silicon material saving of 60%. Interestingly, when assessing the amount of power generated per $1m^2$ of TICPV module, it can be seen that for the same amount of irradiance ($880W/m^2$) the H2 TICPV produces the highest value ($44.83W/m^2$). This may be related to the highest value of optical efficiency obtained for the H2 TICPV as it has a relatively large acceptance angle.

With regard to the temperature of the solar cells, the maximum temperature recorded for all of the TICPV modules were similar (ranging from 43-47ºC). The small variation is mainly due to the nature of the different frames used (insulation) for each TICPV module and to the amount of solar energy collected on the solar cells.

The results in Table 6.5 show the results for the sunny day. With regard to both the sunny interval day and cloudy day, the optical efficiency results are identical to the sunny day; this is due to the fact that the optical efficiency values are calculated using the direct radiation and are based on the properties of the SEH concentrator so remains the same for all days. For the optical concentration ratio values, however, a different pattern can be observed for the sunny interval and cloudy days. For the sunny interval day, the results of the optical concentration ratio on the whole follow the trend of the global irradiance; this is related to the fact that the optical concentration ratio values are calculated using the optical efficiency for both diffuse and direct radiation together thus the steady line represents parts of the day where the sun is behind a cloud and the peaks represents parts of the day where the sun is present. On the cloudy day, however, the optical concentration ratio is calculated using diffuse solar radiation only and as such the results show a steady line with no variation. With regard to the temperature of the solar cells for both days, it can be seen that the pattern follows the trend of the variation profile of the solar irradiance as expected. These results, together, show the importance

of simulating the optical efficiency for both direct and diffuse radiation for the prediction of the power output of static nonimaging solar concentrators.

Table 6.5 shows that the five TICPV modules tested have different optical efficiencies and use different amount of solar cells achieving different values of optical concentration ratios at different temperatures of the solar cell. However, the factor that is of most importance is the total energy produced during the testing period and will thus be addressed in section 6.8; a comparison of the total power output of the five TICPV modules will give an indication of the most productive module for the specific location and position, Edinburgh, 55º slope south facing.

From the outdoor experimental results, it has been shown that for the five TICPV modules the measured power outputs are as expected – similar to the simulated power outputs with small variations. On the whole, the variation between the simulated and experimental values is in the region of 5-10%, but on some occasions reached a difference of 18%. These variations can be attributed to flaws in the manufacturing process. There may also be slight errors in the positioning of the TICPV modules (i.e. south facing but ±2°, for example) as well as precision errors in the measurement devices (i.e. the precision of the pyranometers is ~ 5%).

In some cases, at the beginning and of the end of the day, when the solar radiation is low and the incident angles are high, it can be observed that the measured power output is higher than the simulated power output. This is due to the fact that the pyranometers have a directional response that begins to give incorrect measurements at 80^o angle of incidence with respect to 1000 W/m^2 irradiance at normal incidence (0^o) [246]. With respect to lower irradiance, which is the case at the beginning and end of the day, this error increases at even lower angles of incidence (<80°) and as such the measured power output values can be higher than the simulated values. On a few occasions during the sunny interval days and cloudy days for the five TICPV modules, the measured power output was higher than the simulated power output at times other than the beginning and middle of the day; this is due to the fact that when the global irradiance rapidly fluctuates, this can cause instability in the measures recorded, causing the higher values of variation obtained at certain points of the day, i.e. there are uncertainties of the

pyranometer with increases in the rapidly varying irradiance or deviation from clear sky atmospheric conditions [247].

6.8 Comparison of the total energy generated by the TICPV modules

As previously stated, the TICPV modules were tested in the SE test centre in Edinburgh from 24/05 to 28/06 and from 27/07 to 30/08 during the summer of 2012. This gives a total of 64 days of monitoring the power output of the TICPV modules. The total energy generated (electricity) is calculated during this period for each TICPV module and converted to the equivalent total energy generated by an area of $1m^2$ of TICPV module, the values are summarised in Table 6.6.

It can be seen that the H2 TICPV generates the highest amount of energy 8810.5Wh using $0.16m^2$ of solar cells. The H1 TICPV and the H1.5 TICPV generates a similar amount of energy 8103Wh and 8299Wh respectively, using the same area of solar cells $0.18m^2$. The H2.5 TICPV generates the lowest amount of energy 6943Wh using $0.12m^2$ and for a similar area of solar cell, the H3 TICPV generates 7718.8Wh.

If the total energy generated by the area of solar cells used is calculated, it can be observed from Table 6.6 that, despite having the least solar cells area, the H3 TICPV generates the highest amount – $64323Wh/m^2$ closely followed by $57858Wh/m^2$ for the H2.5 TICPV, compared to $55062Wh/m^2$ for the H2 TICPV, $46108Wh/m^2$ for the H.5 TICPV and $45016Wh/m^2$ H1 TICPV. This can be attributed to the fact that the H3 and H2.5 TICPV modules have a higher geometrical concentration ratio (6×) compared to the other three TICPV modules (4×).

Table 6.6: Measured generated energy during the period from 24/05 to 28/06 and from 27/07 to 30/08 for the year 2012

TICPV	H1	H1.5	H2	H2.5	H3
Energy (Wh)	8103.7	8299.5	8810.5	6943	7718.8
TICPV area (m^2)	1	1	1	1	1
Solar cells area (m^2)	0.18	0.18	0.16	0.12	0.12
Energy per area of solar cell (Wh/m^2)	45016	46108	55062	57858	64323

These results provide an experimental indication of the productivity of the TICPV modules during the summer period in Edinburgh. Future work aims to show the most productive TICPV module in Edinburgh for the whole year using the simulated results of the integrated model and ultimately use this as a tool to choose the most productive TICPV module for any chosen location and position in the world.

6.9 Conclusion

This chapter brings the study of the SEH concentrators in this thesis to a close: it covered the fabrication of the TICPV modules with different SEH concentrators, detailed the development of the integrated model (electrical and optical), presented the results of the outdoor characterisation of the five TICPV modules and concluded with a comparison of the total energy generated by the modules.

In order to validate part of the fabrication process, a thermal model was used to examine the temperature of the solar cells and the rear glass plate of the TICPV modules. It was found that the temperatures were similar thus validating the use of the measurements of the solar cells temperature on the rear glass plate directly for the ease of the experimental setup. Subsequently, and as part of the development of the electrical model, different parameters of a single LGBC solar cell were characterised and determined experimentally. It was found that the $1cm^2$ LGBC solar cell has an open circuit voltage temperature coefficient β = -0.0035(V/ ºC) and a short circuit current temperature coefficient α=0.0006(A/ºC) characterising the temperature effects on the

solar cell output. The parameters determined were used to develop an electrical model based on a two-diode equivalent circuit of the solar cell, the code was written using MATLAB. The results of the solar cell tested indoors under different temperature conditions validated the results obtained from the written MATLAB code simulation. The electrical model accepts irradiance and temperature as input and consequently will give the outputs of various I-V charteristics of the TICPV to be tested outdoors. The energy radiation on the solar cells is achieved by using the different simulated optical efficiencies for outdoor conditions using the developed optical model. By combining these two models together, an integrated model was elaborated in order to be able to predict the power output by the TICPV modules. The integrated model uses as input the simulated optical efficiencies of the SEH concentrators for both direct and diffuse radiations, solar irradiances and solar cell temperatures. The different steps of the simulation of the integrated modules were detailed.

Following on from here, the measured power output of the five TICPV modules in outdoor conditions in Edinburgh were presented and discussed. The maximum power output and solar cell temperatures were examined for different weather conditions: sunny day, sunny interval day and cloudy day. It was found that the measured power output and the simulated power output were comparable for the five TICPV modules and that this is the case for all three weather conditions; thus the experimental results validated the integrated model. Following an investigation of the measured generated energy over the testing period, it was found that the H2 TICPV generated the highest amount of energy during the 64 days of testing.

On the whole, the results show that the designed TICPV modules have the ability to replace conventional building fenestration by keeping the same function of daylight penetration into the building in addition to generating a considerable amount of free electricity (renewable energy) permitting the buildings to reduce their carbon foot print and increase their energy efficiency. The designed TICPV are the first to use 3-D solar concentrators resulting in the use of minimum solar cells material in BIPV (fenestration). The enhancement of the fabrication procedure for large scale is the next step to follow to take the TICPV toward commercialisation.

Chapter 7: Conclusions and future recommendations

7.1 Summary

The design, optimisation and optical performance of a novel 3-D dielectric static solar concentrator has been detailed and presented in this thesis. The 3-D solar concentrator is coined the Square Elliptical Hyperboloid concentrator (SEH) and designed to be integrated into transparent building façades and roofs in a module making the Translucent Integrated Concentrated Photovoltaic system (TICPV). The TICPV module is primarily designed to replace the fenestration in commercial and domestic buildings providing simultaneously energy efficiency, solar energy generation, and optimised day lighting. The TICPV module is aimed to reduce the cost of the conventional PV module in two ways: (i) reduce the area of silicon solar material used by replacing it with lower cost concentrator material and (ii) save the cost of land, supports and frames that would ordinarily be needed for the installation of conventional flat PV modules, as they use the already existing surfaces and building material. The new design of the TICPV was optimised, then manufactured and tested in different environmental conditions to evaluate its performance. The design and performance of the TICPV module reported in this thesis contribute to the current research as a means of offering an effective solution to increasing the energy efficiency of future buildings by providing users with significant amounts of electricity and reducing the reliance on fossil fuels; it provides a viable solution to the increasing demands of electricity. The main important findings of the project are summarised below.

7.1.1 Optical efficiency of the static solar concentrator

The research carried out in this thesis began with a study on a known 3-D geometry solar concentrator, the Crossed Compound Parabolic Concentrator (CCPC). The study was carried out on both reflective and refractive CCPC's using a written code and commercial software for the optical simulations. In the first instance, the optical performance of the 3-D reflective CCPC was investigated using 3-D ray tracing technique. The theoretical optical performances of the reflective CCPC simulated using a developed MATLAB code were compared and validated with experimental results. The same theoretical results of the optical simulation were further validated using the commercial software OptisWorks. The optical performance of the refractive CCPC was also studied and compared to the performance of the reflective CCPC using OptisWorks

software. Results showed that the CCPC made from refractive material had a larger acceptance angle with only 10% less of the maximum optical efficiency compared to the CCPC made from reflective material. In addition to the optical study of the reflective and refractive CCPC, this part of the thesis presented the main tools needed for the design of the novel solar concentrator for PV applications. This study showed that:

- A 3-D solar concentrator can be obtained in ways different to the conventional methods of extrusion or revolution of the 2-D profile; the CCPC is obtained by the intersection of two 2-D CPC's.
- The reflective CCPC has an advantage compared to the conventional 3-D circular sectional CPC as it has a more convenient entry and exit aperture shape (square) whilst achieving similar optical efficiency.
- The optical simulations show a maximum optical efficiency of the reflective CCPC greater than 90% for a reflectivity of 94% of the side walls.
- The reflective CCPC tested in indoor conditions gave an experimental optical efficiency (>80%) in line with the expectation from the simulated optical efficiencies with a maximum variation of 12%, mainly attributed to flaws during the manufacturing process.
- The purchase and use of OptisWorks for the simulation of the optical efficiency of the reflective CCPC was an important step as it saved time in the simulation process. The simulated optical efficiencies of the reflective CCPC using MATLAB are identical to the optical efficiencies simulated with OptisWorks software confirming the results obtained by the two methods and validating the use of OptisWorks for the remainder of the thesis.
- The results of the optical performance of the refractive CCPC studied using OptisWorks software show a larger acceptance angle but with a lower maximum optical efficiency of 70% compared to the reflective CCPC with a maximum optical efficiency of 80% built with the same dimensions.
- The refractive CCPC showed better overall performance (larger acceptance angle combined with high optical efficiency) and was easier to manufacture compared to the reflective CCPC.
- The indoor conditions and devices used in this part of the study are the same as those to be used for the study of the novel concentrator design, thus facilitating

the indoor experimental study for the remainder of the thesis due to a familiarisation with the equipment and manufacturing techniques required.

7.1.2 TICPV design and optimisation of the SEH concentrator

The integration of a 3-D solar concentrator in the glazing building façades and roofs needed a novel concept and design in order to assure daylight penetration into the building. As such, the design of the TICPV module was based on this need. The main findings and achievements in the design process of the TICPV modules are summarised below:

- The geometry of the SEH concentrator is obtained following a novel method of creating a 3-D geometry. The method will pave the way for the future design of other 3-D geometries for solar concentrators and many other applications. The geometry of the SEH concentrator is very specific as it combines two different types of shapes at the entry and exit aperture: a round shape at the entry aperture (ellipse) and a sharp edge shape at the exit aperture (square).
- The TICPV was designed to be an easily integrated component of conventional building construction.
- The specification of the elliptical entry aperture and the material used (polyurethane) allows for the translucent effect of the TICPV module.
- The specification of the square exit aperture coincides with the shape of the usual square and rectangular solar cells available; it reduces the wastage of solar cells and saves silicon material compared to many other solar concentrator designs.
- The hyperbolic profile, joining the ellipse to the square has the advantage of offering an improved performance in acceptance angle and collecting the incoming rays.
- Following an in-depth investigation into the possible techniques surrounding the development of the SEH, a complex 3-D equation was developed which was a crucial step facilitating the remainder of the research.
- An optical model was then developed using commercial software OptisWorks. In addition to the parametric equation, for the purpose of the simulation, the optical proprieties of the material of the SEH concentrator and the properties of the light source needed to be considered.

- The optical efficiency was investigated for 160 SEH profiles of varying geometric profiles with the aim of choosing an optimised profile.
- This was achieved using ray trace technique via OptisWorks based on different elliptical aspect ratios (EAR), height aspect ratios (HAR), acceptance angles (θ_c) and geometric concentration ratios (C_g) for low concentration ratio (4×, 6×, 8× and 10×) SEH concentrators.
- The optimisation process involved various steps and was more complex than initially envisaged:
    - Results from the simulation investigating the optical efficiencies of the various SEH profiles depending on EAR showed that for SEH concentrators with a high C_g the maximum optical efficiency decreases. The results were not definitive enough to provide an optimised SEH concentrator and as such a second step was investigated for a total of 20 SEH profiles (five from each C_g and for each height based on their optical efficiencies.
    - Upon consideration of the $\theta_{c,}$ results showed that, in general, the larger the acceptance angle, the lower is the optical efficiency of the SEH concentrator. This was the case for all of the 20 SEH concentrators regardless of the $C_{g.}$
    - The 20 SEH concentrators were then categorised according to the HAR, however, this method also proved to be problematic.
    - When examining the effects of C_g on the optical performance of the SEH concentrators based on their HAR, it was found that for all height ratios of the SEH, the optical efficiency increases as the C_g decreases. Furthermore, the SEH concentrator with the lowest C_g (4×) has the highest optical efficiency for all HAR.
- From each set of optimisation results (EAR, HAR, θ_c and C_g) it transpired that the selection of an optimum SEH concentrator with optimum height, higher optical efficiency and larger acceptance angle was far from simple.
- In order to move forward in the optimisation process, it was decided to investigate the optical concentration ratio (C_{opt}) as this factor provides essential information on the amount of concentration that will reach the solar cells at the exit aperture.

  - The results were grouped together according to the HAR as a function of the $C_{g.}$ Here, it was clear that the concentrators with the high C_g (8× and 10×) have the lowest values of optical concentration ratio and the lowest optical efficiencies. The concentrators with C_g 8× and 10× were therefore discarded from the remainder of the optimisation process.
  - Based on the maximum optical efficiency, five optimised SEH concentrators were chosen from the 20 investigated, one for each HAR, in order to allow a selection of heights for the TICPV modules depending on the needs. This offers for a range of SEH concentrators with different heights providing the flexibility in use according to the different gaps/space available in the building fenestrations.

- An investigation of the optical flux distribution at the square exit aperture of the SEH concentrator found that the shorter the SEH concentrator is, the more uniform the optical flux distribution is. From the optimisation steps above, however, the shorter is the SEH (lower HAR), the lower the EAR and the lower the C_g are.
- The dimensions and geometric properties of the five optimised SEH concentrators were ascertained and summarised in this part of the study and it was from these five SEH concentrators that the remainder of the research was formed.

7.1.3 Validation of the optical model

The five optimised SEH concentrators were manufactured and tested in indoor conditions. The theoretical optical efficiencies were compared to the experimental optical efficiencies; the theoretical optical performances of the five SEH concentrators, H1 SEH, H1.5 SEH, H2 SEH, H2.5 SEH and H3 SEH were the results of the simulation using the optical model. The main results found are summarised below:

- A simple method of casting the refractive SEH concentrators using minimum laboratory equipment and budget was introduced and detailed.
- The optical properties of the polyurethane material used to cast the SEH concentrators were determined experimentally and used in the optical simulations. The polyurethane was found to have similar optical characteristics as the PMMA material used in the optimisation process.

- The I_{sc} of the solar cells coupled with the SEH concentrators (TICPV) were compared to the I_{sc} generated without being coupled with the concentrators (TIPV) in order to determine the experimental optical efficiencies.
- The experimental optical efficiencies of the SEH concentrators were in good agreement with the simulated optical efficiencies at different incident angles.
- Furthermore, the values of the gain obtained by the TICPV modules compared to the TIPV modules were found to be equal to the optical concentration ratios obtained from the optical simulation with only a small variation.
- The experimental results obtained for the different incident angles confirmed the results obtained from the optical simulation thus validating the optical model developed.
- By validating the optical model used, a trusted tool for the study and the investigation of any refractive optical device (solar concentrator) has been established for use in future work.

7.1.4 Performance of the TICPV modules in outdoor environment

An integrated model (optical and electrical) was developed involving the calculation of the sun position. The integrated model was developed in order to be able to predict the energy generation of the TICPV modules in different locations and for different weather conditions. Outdoor testing in real conditions (outdoor environment exposed to solar radiation) was necessary for the validation of the integrated model and the monitoring of the power output of the TICPV modules in different weather conditions. The main results of the outdoor testing are summarised below:

- The electrical model, which is part of the integrated model, was developed using a two-diode equivalent circuit; the different parameters of the electrical model were determined experimentally using the same solar cells used in the TICPV module (LGBC solar cells). The electrical model was validated twice; in the first instance using the experimental results of one of the LGBC solar cells tested indoors and in the second instance using the overall results of the power output of the TICPV modules tested outdoors.
- With regard to the optical model, more optical simulations were carried out in order to take into account the diffuse radiation and the variation of the solar azimuth angle during the day. It was found that there is a maximum of 10%

difference between the same incident angles measured at different solar azimuth angles.

- The power output of the TICPV modules followed the same pattern of variation as the variation of the solar irradiance during the day.
- The H1 TICPV module is able to collect sunrays for eight hours during the day due to its large acceptance angle of 120^{o}.
- The taller the SEH concentrator used in the TICPV module is, the lower the acceptance angle is and the fewer sunrays are collected during the day.
- The simulated power output calculated using the integrated model confirmed the measured power output of the TICPV module for all possible weather conditions. The matching of the simulated and experimental results of the power output with small variations validated the integrated model.
- The optical concentration ratios of the TICPV modules vary during the day when there is direct solar radiation, but remain constant during a cloudy day when only diffuse radiation is available, as in the latter case, it does not depend on the variation of the angles of incidence.
- The total energy generated by the H2 TICPV module was the highest for the period of outdoor testing (64 days) during the summer time in Edinburgh (8810Wh). This is due to a combination of having the highest optical efficiency and a relatively large acceptance angle. This result gives an indication that a higher optical efficiency may indeed have more weight during the optimisation process than does acceptance angle in relation to this location, Edinburgh south facing.

7.2 Preliminary work carried out using the integrated model to predict the yearly energy production

After having compared the experimental power output and the simulated power output predicted using the integrated model in the previous chapter, this section presents preliminary work on the yearly prediction of the energy generated by the different TICPV modules which is calculated using the integrated model and predicted weather data in Edinburgh; the integrated model uses predicted values of the solar radiation over the course of one year as well as the predicted solar cells temperature. The results can be taken as an example of the type of calculations that would be needed in order to

choose the most productive TICPV module out of the five optimised SEH concentrators studied for any chosen location.

As mentioned, in order to predict the energy production of the TICPV modules, it is necessary to calculate the temperature of the PV cells which is usually a function of ambient temperature, wind speed, wind direction, total irradiance, and relative humidity. The temperature of the PV cells also depend on the module encapsulating material, its thermal dissipation and absorption properties and the working point of the module. The temperature of the solar cells were measured, as presented in Chapter 6 section 6.5, however, these values are not available for the whole year which is a necessary factor in order to be able to predict the yearly energy production.

One widely used linear expression to predict the temperature of the flat PV panels can be written as follows [248]:

$$T_m = T_{amb} + \left(NOCT - 20\right) \times \frac{E}{800} \tag{7.1}$$

where:

T_m: solar cells temperature

T_{amb}: ambient temperature

NOCT: Nominal Operation Cell Temperature

E: solar radiation (W/m^2)

Consequently, in order to carry out a yearly prediction of the energy generation of the TICPV modules in the current study, equation (7.1) is used to predict the temperature of the solar cells despite the fact that it is for flat PV panels and does not take into consideration the wind speed, the wind direction, the relative humidity and the thermal dissipation and absorption properties of the TICPV modules. The accurate temperature of the solar cells in the TICPV modules can only be predicted using numerical transient thermal modelling taking into consideration the daily weather variations. This is a difficult task to achieve as it is time consuming, in addition to the memory load on the equipment at the simulation station, to run the simulation for one year. By using equation (7.1), the integrated model can be generalised to all locations in the world for any of the five TICPV modules.

The NOCT of the different TICPV modules are extracted from the outdoor experimental measurements of the temperature of the solar cells when the solar radiation is equal to 800W/m^2 on the solar cells and the ambient temperature is equal 20ºC [249]. The NOCT of the different TICPV modules are presented in Table 7.1 below.

Table 7.1: NOCT of the different TICPV modules

	H1 TICPV	H1.5 TICPV	H2 TICPV	H2.5 TICPV	H3 TICPV
NOCT (ºC)	35.2	36	39	41	38

The calculation of the yearly energy prediction of the different TICPV modules is computed using the developed integrated model. The ambient temperature and solar radiation (global and diffuse) for Edinburgh are used from the database of the Institute for Energy and Transport (IET) that belongs to the European commission [250]. The temperatures of the solar cells are predicted using equation (7.1).

7.2.1 Results of the yearly energy production modelling

The integrated model is applied to the five TICPV modules using the predicted solar radiation data and the predicted solar cells temperatures as explained in the previous chapter, section 6.6.3. The monthly predicted energy generation of 1m^2 of the five TICPV modules is illustrated in Figure 7.1. From the graph, it can be seen that:

- The H1.5 TICPV and H2 TICPV modules have the highest amount of energy generated for the twelve months of the year.
- The five TICPV modules generate the highest amount of energy in the month of April and the lowest amount of energy in the month of December.
- The H2.5 TICPV module generates the lowest energy in the twelve months of the year apart from the month of September.

It is important to remember that these results are based on predicted solar radiation values and predicted ambient temperature.

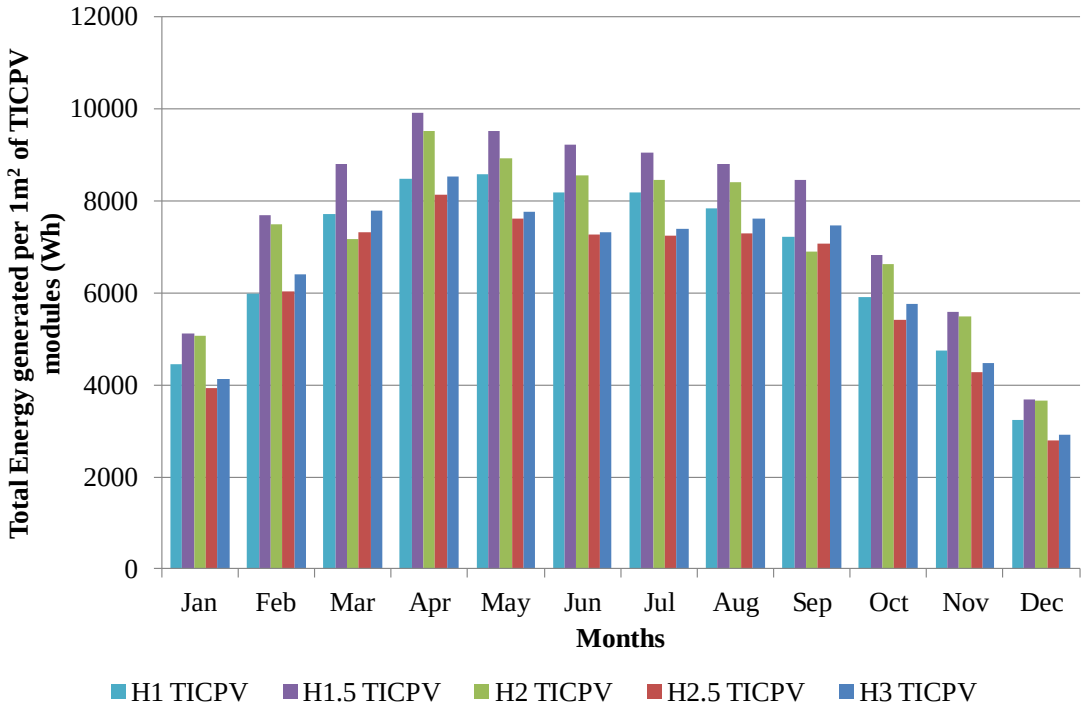

Figure 7.1: Monthly predicted values of the energy generated by $1m^2$ of TICPV modules

The total yearly predicted generated energy of $1m^2$ of the five different TICPV modules are summarised in Table 7.2. From the results, it appears that for the TICPV modules to be installed in Edinburgh facing south at a slope angle of 55^o, the H1.5 TICPV is expected to produce the highest amount of energy 92.68 kWh over the course of an entire year – this is enough energy to use a 100W bulb for two hours and half daily for the whole year. The H2.5 TICPV module is expected to generate the lowest amount of energy, 75.72 kWh per year.

Table 7.2: Predicted yearly generated energy by TICPV module (Edinburgh south direction, 55^o slope)

TICPV	H1	H1.5	H2	H2.5	H3
Energy (kWh)	80.15	92.68	86.21	75.72	77.54
TICPV area (m^2)	1	1	1	1	1
Solar cells area (m^2)	0.18	0.18	0.16	0.12	0.12

The implementation of the integrated model showed that the H1.5 TICPV module is predicted to generate the highest amount of energy (92.68kWh); the H2 TICPV module, however, is predicted to produce a comparable amount of energy (86.21 kWh) using less solar cell material. The H1.5 TICPV module achieves an average total efficiency of 8% for a total global irradiation per square meter received 1140kWh/m^2. This is considered as sound performance compared to conventional flat PV panels which have an efficiency between 12.6% and 13.2% [251].

It is important to bear in mind that these results are specific to the installation in Edinburgh south facing at a slope angle 55^o; the predicted energy generated, however, can be calculated for any location and position due to the nature of the developed code and as such it may transpire that a different TICPV module generates the highest amount of energy at a different location and position. More accurate values regarding the prediction of the energy generated using the integrated model is the aim for the future when a new method of prediction of the solar cells temperatures of TICPV module can be developed.

A detailed cost analysis based on the predicted yearly energy generated for the period of the life time of the TICPV modules would be beneficial in order to know which TICPV module is the most cost effective; this is because the TICPV modules use different areas of solar cells and as such each module will not only be affected in a different way but will also have different associated costs.

7.3 Limitations

The major limitations of the studies carried out in this thesis are related to the manufacturing process and procedure. The manufacturing of the different solar concentrators designed and studied in this thesis (reflective CCPC, refractive CCPC and SEH concentrator) and the assembly of the different components of the TICPV modules were carried out manually using minimum laboratory equipment. The procedures, in general, were very time consuming and involved a lot of human errors that may have been avoided by following an industrial manufacturing process. The different limitations observed in the manufacturing process are described below.

- Covering the reflective CCPC with the reflective film was carried out manually which was very difficult as the side walls of the CCPC concentrators are very

small and difficult to manipulate. Consequently, the side walls of the CCPC were not covered 100% as the corners were difficult to access and cover manually. A potential solution to this obstacle is the use of aluminium vacuum deposition. This procedure, however, is very costly and would only be cost effective for large scale production.

- Casting the refractive CCPC and the SEH concentrator was carried out using ambient pressure and polyurethane mixed manually. This procedure is ideal for making a few prototypes of the solar concentrators for testing purposes; however it would be too time consuming for large scale manufacturing. The preparation and curing process of one set of refractive concentrators took 6 hours. Preferably, the moulding injection manufacturing procedure is the solution to make a large number of solar concentrators in just a few minutes. The price of the injection mould, however, is beyond the budget of the current research project.
- Soldering hundreds of $1cm^2$ solar cells manually was a time consuming task. In addition, the cells are very sensitive and are susceptible to breaking, hence, the positioning and soldering of the solar cells together manually caused the damage of many cells and created the misalignment of the solar cells with the refractive solar concentrators. This problem could be avoided when making TICPV modules for a large scale when following industrial assembly and soldering procedures.
- In addition to the limitations observed during the manufacturing process, it transpires that the prediction of the solar cell temperature for the yearly prediction poses a real problem. No accurate method or equation is available to predict the temperature of the solar cells of a static solar concentrator. As such the results presented relating to the yearly prediction cannot be used definitively as a means of choosing an optimum SEH concentrator in this study for all locations; they can only be used tentatively to give a vague idea of the annual energy production for each of the five optimised SEH concentrators, in Edinburgh south facing, as an initial progression to the research carried out in the current thesis.

7.4 Recommendations for future work

The work carried out in this thesis is scientifically diverse. It presents the design of a novel concept, including the geometrical design and parametric equation development, numerical modelling using written code and commercial software, in addition to the manufacturing of the TICPV modules, testing in different environments (indoor and outdoor) and the development of an integrated model for the yearly prediction of energy for the TICPV modules. In achieving these tasks, a wide range of knowledge and skills were gained regarding the design and characterisation of solar concentrators, developing at the same time new ideas about different aspects that can be investigated in the future for the enhancement of the study of solar concentrators in general. The recommendations for future work are detailed and presented below:

- A study covering the procedure of the large scale production of the TICPV modules would be beneficial for the development of the SEH concentrator. This would take the TICPV module from the academic research stage to the level of commercialisation. Many companies have shown an interest in the concept of the TICPV after having filed the patent. The study would optimise a procedure for manufacturing the SEH concentrators and how best to assemble them with the solar cells to comprise the final TICPV module.
- A longitudinal study investigating the durability of the TICPV modules is recommended for the final stage of commercialisation. The study would be carried out by applying an accelerated weathering test on the TICPV modules.
- As the TICPV modules replace conventional building fenestration, a study is recommended to determine the U-value of the TICPV module as it is expected to be lower than the conventional glazing system. The integration of the SEH concentrators into the TICPV module is expected to reduce the heat losses through the TICPV module and reduce the cooling load on the building. The study would be carried out to quantify the energy performance of the building fitted with the TICPV modules: electric energy generated, reduction of cooling load (sun ray entering the building reduced) and reduction of heating energy needed (lower U-value).
- Part of the results obtained from the optical study pertained to the optical flux distribution on the solar cells. No method exists at the moment allowing quantifying the effect of the non uniformity of the optical flux distribution on the efficiency of the solar cells. It is recommended to develop an experimental

setup and a numerical model or equation (function of the optical flux distribution pattern) for determining the effects of the non uniformity of the optical flux distribution on the solar cell efficiency. Once the model is developed and the effects of the non uniformity of the optical flux distribution become fully known, another study is recommended to be conducted. The study would examine optimising the distance between the fingers of the solar cells and their thicknesses based on the effects of the non uniformity of the optical flux distribution.

- The prediction of the solar cells temperature of a static CPV system has not been studied before despite its importance for the yearly energy prediction. A study aiming to develop an equation for the temperature of the solar cells is recommended. The equation would be developed to be function of the weather conditions and the previous temperature of the solar cells. The equation can be developed after extensive transient simulations of the temperature of the solar cell for different weather condition variations.
- The comparison of the yearly energy generation of the different TICPV modules in different locations around the world and in different orientations and inclinations is recommended. This study would enable a definitive choice to be made with regard to the right TICPV module with the optimum SEH concentrator for each chosen installation location. This would also allow the calculation of the payback time of the TICPV modules installed in the chosen location.

The above mentioned recommendations are intended mainly to take the TICPV modules to the next level of commercialisation but also to provide new solutions that will aid the design process of solar concentrators in general in the future. These recommendations can be the subject of new research projects as well as business projects aiming for the commercialisation of the TICPV modules in the near future.

7.5 Conclusions

In summary this thesis has demonstrated the optical performance of a novel static 3-D nonimaging concentrator: the SEH. Beginning with the investigation of a known 3-D geometry, the CCPC, to the development and fabrication of the SEH TICPV module, a variety of different techniques were used facilitating an in depth study of the SEH

concentrator. The research carried out in this thesis has not only expanded our knowledge of the CCPC but has introduced a new geometry that shows significant potential for use in buildings of the future. By basing the design of the SEH concentrator on the needs, a novel geometry was obtained with a square exit aperture in accordance with the shape of solar cells available on the market, an elliptical entry aperture to allow penetration of the daylight and a hyperbolic profile on the sides of the concentrator in accordance to results obtained from the trumpet concentrator showing an elevated optical performance compared to other profiles. It is the first design of its kind and is the only scientific study of the use of a translucent 3-D solar concentrator in BICPV.

This thesis has broadened the knowledge surrounding static solar concentrators with a particular focus on Translucent Integrated Concentrating Photovoltaics (TICPV) and has presented a viable solution to replacing the fenestration in buildings with minimal interference to daylight penetration. The importance of the development of an integrated model for the annual prediction of energy output to assess the viability of the TICPV modules at any location and orientation has been highlighted. The inability to predict the temperature of the solar cells of a static CPV system, in order to predict the annual energy output more accurately, was highlighted and the need for a study to develop an equation of the temperature as a function of the weather conditions and the previous temperature of the solar cells has been identified. Further research should be aimed at investigating the effects of the optical flux distributions on the efficiency of the SEH concentrators and should aim to develop a numerical model or equation (as a function of the optical flux distribution pattern) in order to present a more complete picture of the optical efficiencies of the SEH concentrators. With the patent filed for the SEH concentrators, it is anticipated that further work on the TICPV modules will lead to a fully commercialised cost-effective product that will enable clean, energy efficient self powered buildings and as such aid the UK and other countries achieve their renewable energy targets. The aim is to contribute to the research that will ensure a secure supply of energy for the future, with the ultimate aim of reducing the greenhouse gas emissions to slow down the effects of climate change.

References

[1] Anon, World electricity generation by source of energy OECD 2012.

[2] R.K. Pachauri, A. Reisinger, Contribution of Working Groups I, II and III to the Fourth Assessment in: IPCC (Ed.) Climate Change 2007: Synthesis Report, IPCC, Geneva, Switzerland, 2007 pp. 104.

[3] V.A. Dergachev, O.M. Raspopov, Reconstruction of the Earth's surface temperature based on data of deep boreholes, global warming in the last millennium, and long-term solar cyclicity. Part 1. Experimental data, Geomagn. Aeron., 50 (2010) 383-392.

[4] C. Ngo, J. Natowitz, Our Energy Future: Resources, Alternatives and the Environment Wiley-Blackwell, New Jersy, 2009.

[5] A. Goodrich, M. Woodhouse, D. Hsu, Si Solar Manufacturing Cost Models, National Renewable Energy Laboratory (NREL). (2011).

[6] Z. Dobrotkova, A. Goodrich, M. Mackay, C. Philibert, G. Simbolotti, X. Wenhua, Cost Analysis of Solar Photovoltaics, IRENA woRkINg pA g p pER, Power Sector (2012).

[7] A. Luque, Static concentrators: a venture to meet the low cost target in photovoltaics, Solar cells 12 (1984) 141-145.

[8] R. Bentley, B. Anstey, J. Callear, Sylvain Chonavel, I. Clark, I. Collins, Alfonso Ramallo, H. Scanlon, C. Weatherby., Concentrating Photovoltaic Systems, in: Smart Grids & Cleanpower Conference, Cambridge, 2010.

[9] M. Gutschner, S. Nowak, D. Ruoss, P. Toggweiler, T. Schoen, Potential for Building Integrated Photovoltaics, in, Iternational Energy Agency, Potential for Building Integrated Photovoltaics, 2002, pp. 11.

[10] M. Oliver, T. Jackson, Energy and economic evaluation of building-integrated photovoltaics, Energy, 26 (2001) 431-439.

[11] D. Chemisana, Building Integrated Concentrating Photovoltaics: A review, Renew. Sust. Energ. Rev., 15 (2011) 603-611.

[12] B. Norton, P.C. Eames, T.K. Mallick, M.J. Huang, S.J. McCormack, J.D. Mondol, Y.G. Yohanis, Enhancing the performance of building integrated photovoltaics, Solar Energy, 85 (2011) 1629-1664.

[13] G.R. Whitfield, R.W. Bentley, C.K. Weatherby, A.C. Hunt, H.D. Mohring, F.H. Klotz, P. Keuber, J.C. Minano, E. Alarte-Garvi, The development and testing of small concentrating PV systems, Solar Energy, 67 (1999) 23-34.

[14] A.J. Rivera, B. Garcia-Domingo, M.J. del Jesus, J. Aguilera, A Performance Study of Concentrating Photovoltaic Modules Using Neural Networks: An Application with (CORBFN)-R-2, in: V. Snasel, A. Abraham, E.S. Corchado (Eds.) Soft Computing Models in Industrial and Environmental Applications, Springer-Verlag Berlin, Berlin, 2013, pp. 439-448.

[15] H. Rezk, A.H.M. El-Sayed, Sizing of a stand alone concentrated photovoltaic system in Egyptian site, Int. J. Electr. Power Energy Syst., 45 (2013) 325-330.

[16] Y.S. Tsou, Y.H. Lin, A.C. Wei, Concentrating Photovoltaic System Using a Liquid Crystal Lens, IEEE Photonics Technol. Lett., 24 (2012) 2239-2242.

[17] B. Du, E. Hu, M. Kolhe, Performance analysis of water cooled concentrated photovoltaic (CPV) system, Renew. Sust. Energ. Rev., 16 (2012) 6732-6736.

[18] G. Grasso, A. Righetti, M.C. Ubaldi, F. Morichetti, S.M. Pietralunga, Competitiveness of stationary planar low concentration photovoltaic modules using silicon cells: A focus on concentrating optics, Solar Energy, 86 (2012) 1725-1732.

[19] A. Al-Alili, Y. Hwang, R. Radermacher, I. Kubo, A high efficiency solar air conditioner using concentrating photovoltaic/thermal collectors, Applied Energy, 93 (2012) 138-147.

[20] R. Kumar, M.A. Rosen, A critical review of photovoltaic-thermal solar collectors for air heating, Applied Energy, 88 (2011) 3603-3614.

[21] D.M. Chapin, C.S. Fuller, G.L. Pearson, A New Silicon p-n Junction Photocell for Converting Solar Radiation into Electrical Power, Journal of Applied Physics, 25 (1954) 676-677.

[22] N. Sarmah, Design and Performance Evaluation of a Low Concentrating Line-axis Dielectric Photovoltaic System, in: Institute of Mechanical, Process and Energy Engineering, Heriot-Watt University, Edinburgh, 2012, pp. 306.

[23] R. Williams, Becquerel Photovoltaic Effect in Binary Compounds, The Journal of Chemical Physics, 32 (1960) 1505-1514.

[24] R.R. King, D.C. Law, K.M. Edmondson, C.M. Fetzer, G.S. Kinsey, H. Yoon, R.A. Sherif, N.H. Karam, 40% efficient metamorphic GaInP/GaInAs/Ge multijunction solar cells, Applied Physics Letters, 90 (2007).

[25] D. Markham, New World Record Set for Solar Cells: 44% Efficiency in: Treehugger, Canada, 2012.

[26] M.A. Green, K. Emery, Y. Hishikawa, W. Warta, E.D. Dunlop, Solar cell efficiency tables (version 39), Progress in Photovoltaics: Research and Applications, 20 (2012) 12-20.

[27] J. Martin, Monocrystalline vs Polycrystalline Solar Panels: Busting Myths, in: Solar Panels/Modules,Solar System Products, Solar choice, 2012.

[28] Empa, Empa takes thin film solar cells to a new level, A new world record for solar cell efficiency, in, Swiss Federal Laboratories for Materials Testing and Research 2013.

[29] E. Meza, TSMC records 15.7% champion module, in: PV magazine, 2013.

[30] A.G. Aberle, Thin-film solar cells, Thin Solid Films, 517 (2009) 4706-4710.

[31] N. Strevel, L. Trippel, M. Gloeckler, Performance characterization and superior energy yield of First Solar PV power plants in high-temperature conditions, in: Photovoltaic international, Perrysburg, Ohio, USA, 2012.

[32] R.W. Miles, K.M. Hynes, I. Forbes, Photovoltaic solar cells: An overview of state-of-the-art cell development and environmental issues, Progress in Crystal Growth and Characterization of Materials, 51 (2005) 1-42.

[33] A.D. Vos, Detailed balance limit of the efficiency of tandem solar cells, Journal of Physics D: Applied Physics, 13 (1980) 839.

[34] J. Hyvarinen, J. Karila, New analysis method for crystalline silicon cells, 2003.

[35] Z. Salam, K. Ishaque, H. Taheri, An improved two-diode photovoltaic (PV) model for PV system, in: Power Electronics, Drives and Energy Systems (PEDES) & 2010 Power India, 2010 Joint International Conference on, 2010, pp. 1-5.

[36] D. Rekioua, E. Matagne, Optimization of Photovoltaic Power Systems, in: Optimization of Photovoltaic Power Systems, Springer, London, 2012, pp. 31-87.

[37] D. Sera, R. Teodorescu, P. Rodriguez, Ieee, PV panel model based on datasheet values, 2007.

[38] E.D. Mammo, N. Sellami, T.K. Mallick, Performance analysis of a reflective 3D crossed compound parabolic concentrating photovoltaic system for building façade integration, Progress in Photovoltaics: Research and Applications, (2012) n/a-n/a.

[39] J.A. Gow, C.D. Manning, Development of a photovoltaic array model for use in power-electronics simulation studies, Electric Power Applications, IEE Proceedings -, 146 (1999) 193-200.

[40] G.D.J. HARPER, Solar collectors, in: Solar Energy Projects for the Evil Genius TAB electronics, 2007, pp. 61-64.

[41] J. Perlin, From Space to Earth: The Story of Solar Electricity, aatec publications, 1999.

[42] A.B. Maish, Progress in the Concentrator Initiative Program, in: Photovoltaic Specialists Conference, 1993., Conference Record of the Twenty Third IEEE, 1993, pp. 1203-1208.

[43] G. Sala, J.C. Arboiro, A. Luque, J.C. Zamorano, J.C. Minano, C. Dramsch, T. Bruton, D. Cunningham, The EUCLIDES prototype: An efficient parabolic trough for PV concentration, in: Photovoltaic Specialists Conference, 1996., Conference Record of the Twenty Fifth IEEE, 1996, pp. 1207-1210.

[44] H.D. Mohring, H. Gabler, Solar electric concentrators with small concentration ratios: field experience and new developments, in: Photovoltaic Specialists Conference, 2002. Conference Record of the Twenty-Ninth IEEE, 2002, pp. 1608-1611.

[45] Anne-Marie, L. Humphrey, World-leading mega scale solar power station for Victoria, in, Solar systems, Victoria, 2006, pp. 2.

[46] A. Rabl, Comparison of solar concentrators, Solar Energy, 18 (1976) 93-111.

[47] J.A. Duffie, W.A. Beckman, Solar Engineering of Thermal Processes, 3rd Edition ed., John Wiely & Sons, New Jersey, 2006.

[48] T.K. Mallick, P.C. Eames, T.J. Hyde, B. Norton, The design and experimental characterisation of an asymmetric compound parabolic photovoltaic concentrator for building façade integration in the UK, Solar Energy, 77 (2004) 319-327.

[49] M. Li, X. Ji, G.L. Li, S.X. Wei, Y.F. Li, F. Shi, Performance study of solar cell arrays based on a Trough Concentrating Photovoltaic/Thermal system, Applied Energy, 88 (2011) 3218-3227.

[50] G. Sala, J.C. Arboiro, A. Luque, J.C. Zamorano, J.C. Minano, C. Dramsch, T. Bruton, D. Cunningham, Ieee, The EUCLIDES prototype: An efficient parabolic trough for PV concentration, 1996.

[51] M.F. Piszczor, M.J. Oneill, L.M. Fraas, Ieee, A novel space photovoltaic module using a linear fresnel lens and a line-focus tandem cell receiver, in: Ieee Phot Spec Conf, 1993, pp. 1386-1391.

[52] R. Leutz, A. Suzuki, A. Akisawa, T. Kashiwagi, Design of a nonimaging Fresnel lens for solar concentrators, Solar Energy, 65 (1999) 379-387.

[53] A. Luque, S. Hegedus, Photovoltaic Concentrators, in: Handbook of Photovoltaic Science and Engineering Wiley, 2002, pp. 481.

[54] P.J. Verlinden, A. Lewandowski, H. Kendall, S. Carter, K. Cheah, I. Varfolomeev, D. Watts, M. Volk, I. Thomas, P. Wakeman, A. Neumann, P. Gizinski, D. Modra, D. Turner, J.B. Lasich, Ieee, Update on two-year performance of 120 KWp concentrator PV systems using multi-junction lll-V solar cells and parabolic dish reflective optics, in: Pvsc: 2008 33rd Ieee Photovoltaic Specialists Conference, Vols 1-4, 2008, pp. 1552-1557.

[55] R. Winston, J.C. Minano, P.G. Benitez, Nonimaging Optics, Elsevier, California, 2005.

[56] H. Hinterberger, R. Winston, Efficient Light Coupler for Threshold Cerenkov Counters, Review of Scientific Instruments, 37 (1966) 1094-1095.

[57] R. Winston, Principles of solar concentrators of a novel design, Solar Energy, 16 (1974) 89-95.

[58] R. Winston, H. Hinterberger, Principles of cylindrical concentrators for solar-energy, Solar Energy, 17 (1975) 255-258.

[59] A. Rabl, R. Winston, Ideal concentrators for finite sources and restricted exit angles, Appl. Opt., 15 (1976) 2880-2883.

[60] J. Chaves, Introduction to Nonimaging Optics Taylor & Francis Group, 2008.

[61] J. Chaves, Fundamental Concepts, in: Introduction to Nonimaging Optics Taylor & Francis Group, 2008, pp. 13.

[62] Y. Tripanagnostopoulos, P. Yianoulis, S. Papaefthimiou, S. Zafeiratos, CPC solar collectors with flat bifacial absorbers, Solar Energy, 69 (2000) 191-203.

[63] A.J. Pavlak, Fin-Type compound parabolic concentrator, in: Patentdocs, Thales research, inc, 2009.

[64] Y. Tripanagnostopoulos, M. Souliotis, ICS solar systems with horizontal cylindrical storage tank and reflector of CPC or involute geometry, Renewable Energy, 29 (2004) 13-38.

[65] H.P. Baum, J.M. Gordon, Geometric characteristics of ideal nonimaging (CPC) solar collectors with cylindrical absorber, Solar Energy, 33 (1984) 455-458.

[66] T.K. Mallick, Optics and Heat Transfer for Asymmetric Compound Parabolic Photovoltaic Concentrators for Building Integrated Photovoltaics, in: Faculty of Engineering, University of Ulster, 2003, pp. 306.

[67] I.R. Edmonds, I.R. Cowling, H.M. Chan, The design and performance of liquid filled stationary concentrators for use with photovoltaic cells, Solar Energy, 39 (1987) 113-122.

[68] W. Welford, R. Winston, The Optics of Nonimaging Concentrators: Light and Solar Energy Academic Press Incorporated, New York, 1978.

[69] S. Bowden, S.R. Wenham, P. Coffey, M. Dickinson, M.A. Green, High efficiency photovoltaic roof tile with static concentrator, in: Photovoltaic Specialists Conference, 1993., Conference Record of the Twenty Third IEEE, 1993, pp. 1068-1072.

[70] S. Bowden, S.R. Wenham, P. Coffey, M. Dickinson, M.A. Green, High-Efficiency Photovoltaic Roof Tile with Static Concentrator, Ieee Phot Spec Conf, (1993) 1068-1072.

[71] K. Yoshioka, K. Endoh, M. Kobayashi, A. Suzuki, T. Saitoh, Design and properties of a refractive static concentrator module, Sol Energ Mat Sol C, 34 (1994) 125-131.

[72] K. Yoshioka, M. Kobayashi, A. Suzuki, K. Endoh, N. Ohe, T. Saitoh, Ieee, An optimum design and properties of a static concentrator with a non-imaging lens, in: Ieee Phot Spec Conf, 1994, pp. 1119-1122.

[73] K. Yoshioka, K. Endoh, A. Suzuki, N. Ohe, Performance simulation of a three-dimensional lens for a photovoltaic static concentrator, in: 13th European Photovoltaic Solar Energy Conference, Nice, France, 1995.

[74] K. Yoshioka, S. Goma, K. Kurokawa, T. Saitoh, Improved design of a three-dimensional, static concentrator lens using meteorological data, Prog Photovoltaics, 7 (1999) 61-69.

[75] K. Yoshioka, S. Goma, S. Hayakawa, T. Saitoh, Preparation and properties of an experimental static concentrator with a new three-dimensional lens, Prog Photovoltaics, 5 (1997) 139-145.

[76] T. Uematsu, Y. Yazawa, T. Joge, S. Kokunai, Fabrication and characterization of a flat-plate static-concentrator photovoltaic module, Sol Energ Mat Sol C, 67 (2001) 425-434.

[77] J. Parada, J.C. Miñano, J.L. Silva, Construction and Measurement of a Prototype of P.V. Module with Static Concentration, in: A. Luque, G. Sala, W. Palz, G. Santos, P. Helm (Eds.) Tenth E.C. Photovoltaic Solar Energy Conference, Springer Netherlands, 1991, pp. 975-978.

[78] I. Zanesco, E. Lorenzo, Optimisation of an asymmetric static concentrator: the PEC-44D, Progress in Photovoltaics: Research and Applications, 10 (2002) 361-376.

[79] J. Alonso, V. Diaz, M. Hernandez, F. Bercero, C. Canizo, I. Pou, R. Mohedano, P. Benitez, J.C. Minano, A. Luque, S. Steckemetz, A. Metz, R. Hezel, J.C. Jimeno, R. Gutierrez, F. Recart, G. Bueno, V. Rodriguez, F. Hernando, V.M. Sukhostavets, S. Beringov, K. Sassoli, C. Iachetti, G. Carotid, A new static concentrator PV module with bifacial cells for integration on facades: the PV VENETIAN store, in: Photovoltaic Specialists Conference, 2002. Conference Record of the Twenty-Ninth IEEE, 2002, pp. 1584-1587.

[80] M. Morimoto, T. Maruyama, Static solar concentrator with vertical flat plate photovoltaic cells and switchable white/transparent bottom plate, Sol Energ Mat Sol C, 87 (2005) 299-309.

[81] M. Morimoto, T. Maruyama, Static solar concentrator with vertical flat plate photovoltaic cells and switchable white/transparent bottom plate, Sol Energ Mat Sol C, 87 (2005) 299-309.

[82] S. Hatwaambo, H. Hakansson, J. Nilsson, B. Karlsson, Angular characterization of low concentrating PV–CPC using low-cost reflectors, Sol Energ Mat Sol C, 92 (2008) 1347-1351.

[83] J. Nilsson, R. Leutz, B. Karlsson, Micro-structured reflector surfaces for a stationary asymmetric parabolic solar concentrator, Sol Energ Mat Sol C, 91 (2007) 525-533.

[84] Y. Su, G. Pei, S.B. Riffat, H. Huang, Radiance/Pmap simulation of a novel lens-walled compound parabolic concentrator (lens-walled CPC), Energy Procedia, 14 (2012) 572-577.

[85] Y.H. Su, G. Pei, S.B. Riffat, H.L. Huang, A Novel Lens-Walled Compound Parabolic Concentrator for Photovoltaic Applications, J. Sol. Energy Eng. Trans.-ASME, 134 (2012).

[86] T.K. Mallick, P.C. Eames, Design and fabrication of low concentrating second generation PRIDE concentrator, Sol Energ Mat Sol C, 91 (2007) 597-608.

[87] T.K. Mallick, P.C. Eames, Electrical performance evaluation of low-concentrating non-imaging photovoltaic concentrator, Prog Photovoltaics, 16 (2008) 389-398.

[88] T.K. Mallick, P.C. Eames, B. Norton, Power losses in an asymmetric compound parabolic photovoltaic concentrator, Sol Energ Mat Sol C, 91 (2007) 1137-1146.

[89] N. Sarmah, B.S. Richards, T.K. Mallick, Evaluation and optimization of the optical performance of low-concentrating dielectric compound parabolic concentrator using ray-tracing methods, Applied Optics, 50 (2011) 3303-3310.

[90] Globaldata, Building Integrated Photovoltaic (BIPV) - Global Market Size, Technology Road-Map, Regulations, Competitive Landscape and Pricing Analysis to 2015, in, Globaldata, 2011.

[91] J.G. Ingersoll, C.A. Perkins, The 2.1 kW photovoltaic electric vehicle charging station in the city of Santa Monica, California, in: Photovoltaic Specialists Conference, 1996., Conference Record of the Twenty Fifth IEEE, 1996, pp. 1509-1512.

[92] N. Ishikawa, M. Kanai, I. Hide, T. Nagai, T. Ito, T. Yoshida, T. Nii, K. Tazawa, T. Harada, PV glass curtain walls using color solar cells: the examination of structures and integration on buildings, in: Photovoltaic Specialists Conference, 1996., Conference Record of the Twenty Fifth IEEE, 1996, pp. 1243-1246.

[93] S. Roberts, N. Guariento, Shading systems, in: Birkhäuse (Ed.) Building Integrated Photovoltaics: A Handbook 2009, pp. 178.

[94] M. Mandalaki, K. Zervas, T. Tsoutsos, A. Vazakas, Assessment of fixed shading devices with integrated PV for efficient energy use, Solar Energy, 86 (2012) 2561-2575.

[95] S. Roberts, N. Guariento, Rainscreen systems, in: Birkhäuse (Ed.) Building Integrated Photovoltaics: A Handbook 2009, pp. 178.

[96] N.M. Pearsall, A.R. Wilshaw, Performance analysis of the Northumberland building photovoltaic facade, in: Photovoltaic Specialists Conference, 1996., Conference Record of the Twenty Fifth IEEE, 1996, pp. 1247-1250.

[97] S. Roberts, N. Guariento, Design of the building envelope, in: Birkhäuse (Ed.) Building Integrated Photovoltaics: A Handbook 2009, pp. 178.

[98] G.E. Lau, G.H. Yeoh, V. Timchenko, R.K.K. Yuen, Natural Convection in a PV-Integrated Double-Skin Facade using Large-Eddy Simulation, in: L.H. Fai (Ed.) Proceedings of the Twelfth East Asia-Pacific Conference on Structural Engineering and Construction, 2011.

[99] D.H.W. Li, T.N.T. Lam, K.L. Cheung, Energy and cost studies of semi-transparent photovoltaic skylight, Energy Conversion and Management, 50 (2009) 1981-1990.

[100] R. Gangemi, J.E. Hart, Sun Energy Tile, in, Grass Valley, 2009.

[101] K. Murata, T. Yagiura, K. Takeda, M. Tanaka, S. Kiyama, New type of photovoltaic module integrated with roofing material (highly fire-resistant PV tile), Sol Energ Mat Sol C, 75 (2003) 647-653.

[102] N. Okuda, T. Yagiura, M. Morizane, N. Nakamura, M. Ohnishi, S. Nakano, T. Ito, S. Omoto, Y. Yamashita, H. Ito, T. Fujiwara, Ieee, A new type of photovoltaic shingle, in: Ieee Phot Spec Conf, 1994, pp. 1008-1011.

[103] T. Yagiura, M. Morizane, K. Murata, K. Uchihashi, S. Tsuda, S. Nakano, T. Ito, S. Omoto, Y. Yamashita, H. Yamakawa, T. Fujiwara, Exchangeable PV shingle, Sol Energ Mat Sol C, 47 (1997) 227-233.

[104] T. James, A. Goodrich, M. Woodhouse, R. Margolis, S. Ong, Building-Integrated Photovoltaics (BIPV) in the Residential Sector: An Analysis of Installed Rooftop System Prices, in: NREL (Ed.), NREL, 2011.

[105] G. Research, Building-Integrated Photovoltaics: An Emerging Market, in: Solar market research 2010

[106] Polysolar, Guide to BIPV, in, Cambridge", 2012.

[107] I.E. Service, Acceptance Criteria for Building-Integrated Photovoltaic (BIPV) Roof Covering Systems, in: The International Cod Council (Ed.) AC365, 2011.

[108] F.S.R. Service, European Building Integrated Photovoltaics Market, in, 2008.

[109] M. Pagliaro, R. Ciriminna, G. Palmisano, BIPV: merging the photovoltaic with the construction industry, Progress in Photovoltaics: Research and Applications, 18 (2010) 61-72.

[110] R.M. Swanson, The promise of concentrators, Progress in Photovoltaics: Research and Applications, 8 (2000) 93-111.

[111] D. Chemisana, J.I. Rosell, Design and optical performance of a nonimaging Fresnel transmissive concentrator for building integration applications, Energy Conversion and Management, 52 (2011) 3241-3248.

[112] J.I. Rosell, X. Vallverdu, M.A. Lechon, M. Ibanez, Design and simulation of a low concentrating photovoltaic/thermal system, Energy Conversion and Management, 46 (2005) 3034-3046.

[113] T.T. Chow, K.F. Fong, W. He, Z. Lin, A.L.S. Chan, Performance evaluation of a PV ventilated window applying to office building of Hong Kong, Energy and Buildings, 39 (2007) 643-650.

[114] C. Downey, W. Talarico, Giving back to the environment (The Mont-Cenis-Academy complex, Sodingen, in the Ruhrgebiet, Jourda-&-Perraudin-Architects in collaboration with Hegger-Hegger-Schleiff), Archit. Rec., 187 (1999) 199.

[115] J.E. Hoffner, M.M. Palani, M.C. Russell, I. Ieee, A PV window awning system on the University of Texas Houston Health Science Center using ac-modules, in: Conference Record of the Twenty-Eighth Ieee Photovoltaic Specialists Conference - 2000, 2000, pp. 1545-1547.

[116] P.W. Wong, Y. Shimoda, M. Nonaka, M. Inoue, M. Mizuno, Semi-transparent PV: Thermal performance, power generation, daylight modelling and energy saving potential in a residential application, Renewable Energy, 33 (2008) 1024-1036.

[117] L. Lu, K.M. Law, Overall energy performance of semi-transparent single-glazed photovoltaic (PV) window for a typical office in Hong Kong, Renewable Energy, 49 (2013) 250-254.

[118] K. Vats, G.N. Tiwari, Energy and exergy analysis of a building integrated semitransparent photovoltaic thermal (BISPVT) system, Applied Energy, 96 (2012) 409-416.

[119] G. Quesada, D. Rousse, Y. Dutil, M. Badache, S. Hallé, A comprehensive review of solar facades. Transparent and translucent solar facades, Renewable and Sustainable Energy Reviews, 16 (2012) 2643-2651.

[120] P.P.C. Verbunt, S. Tsoi, M.G. Debije, D.J. Broer, C.W.M. Bastiaansen, C.-W. Lin, D.K.G. de Boer, Increased efficiency of luminescent solar concentrators after application of organic wavelength selective mirrors, Opt. Express, 20 (2012) A655-A668.

[121] N.C. Giebink, Luminescent solar concentrator gets more efficient with addition of CPC, Laser Focus World, 48 (2012) 10-10.

[122] L. Desmet, A.J.M. Ras, D.K.G. de Boer, M.G. Debije, Monocrystalline silicon photovoltaic luminescent solar concentrator with 4.2% power conversion efficiency, Opt. Lett., 37 (2012) 3087-3089.

[123] J.W.E. Wiegman, E. van der Kolk, Building integrated thin film luminescent solar concentrators: Detailed efficiency characterization and light transport modelling, Sol Energ Mat Sol C, 103 (2012) 41-47.

[124] M. Buffa, S. Carturan, M.G. Debije, A. Quaranta, G. Maggioni, Dye-doped polysiloxane rubbers for luminescent solar concentrator systems, Sol Energ Mat Sol C, 103 (2012) 114-118.

[125] D.K.G. de Boer, D.J. Broer, M.G. Debije, W. Keur, A. Meijerink, C.R. Ronda, P.P.C. Verbunt, Progress in phosphors and filters for luminescent solar concentrators, Optics Express, 20 (2012) A395-A405.

[126] J. Gutmann, M. Peters, B. Blaesi, M. Hermle, A. Gombert, H. Zappe, J.C. Goldschmidt, Electromagnetic simulations of a photonic luminescent solar concentrator, Optics Express, 20 (2012) A157-A167.

[127] A. Sanguineti, A. Monguzzi, G. Vaccaro, F. Meinardi, E. Ronchi, M. Moret, U. Cosentino, G. Moro, R. Simonutti, M. Mauri, R. Tubino, L. Beverina, NIR emitting ytterbium chelates for colourless luminescent solar concentrators, Physical Chemistry Chemical Physics, 14 (2012) 6452-6455.

[128] M.G. Debije, P.P.C. Verbunt, Thirty Years of Luminescent Solar Concentrator Research: Solar Energy for the Built Environment, Advanced Energy Materials, 2 (2012) 12-35.

[129] Y.R. Do, Cylindrical luminescent solar concentrators are more efficient if they're hollow, Laser Focus World, 47 (2011) 10-+.

[130] D.J. Farrell, M. Yoshida, Operating regimes for second generation luminescent solar concentrators, Prog Photovoltaics, 20 (2012) 93-99.

[131] J.-J. Geng, J. Zhang, Y. Zhang, J.-J. Ding, S. Sun, Z.-L. Luo, J. Bao, C. Gao, Simulation and optimization of the cascaded luminescent solar concentrator photovoltaic system, Acta Physica Sinica, 61 (2012).

[132] H. Hernandez-Noyola, D.H. Potterveld, R.J. Holt, S.B. Darling, Optimizing luminescent solar concentrator design, Energy & Environmental Science, 5 (2012) 5798-5802.

[133] F. Purcell-Milton, Y.K. Gun'ko, Quantum dots for Luminescent Solar Concentrators, Journal of Materials Chemistry, 22 (2012) 16687-16697.

[134] P.P.C. Verbunt, M.G. Debije, D.J. Broer, C.W.M. Bastiaansen, D.K.G. de Boer, Organic wavelength selective mirrors for luminescent solar concentrators, in: R. Wehrspohn, A. Gombert (Eds.) Photonics for Solar Energy Systems Iv, 2012.

[135] M.G. Debije, P.P.C. Verbunt, B.C. Rowan, B.S. Richards, T.L. Hoeks, Measured surface loss from luminescent solar concentrator waveguides, Appl. Opt., 47 (2008) 6763-6768.

[136] S. Chandra, J. Doran, S.J. McCormack, M. Kennedy, A.J. Chatten, Enhanced quantum dot emission for luminescent solar concentrators using plasmonic interaction, Sol Energ Mat Sol C, 98 (2012) 385-390.

[137] J.L. Horner, J.E. Ludman, Single holographic element wavelength demultiplexer, Appl. Opt., 20 (1981) 1845-1847.

[138] J.R. Magarinos, D.J. Coleman, Stationary, self-tracking holographic solar conentrator, Journal of the Optical Society of America, 71 (1981) 1614-1614.

[139] J.E. Ludman, Holographic solar concentrator, Appl. Opt., 21 (1982) 3057-3058.

[140] W.H. Bloss, M. Griesinger, E.R. Reinhardt, Dispersive concentrating systems based on transmission phase holograms for solar applications, Appl. Opt., 21 (1982) 3739-3742.

[141] J.E. Ludman, Approximate bandwidth and diffraction effeciency in thick holograms, American Journal of Physics, 50 (1982) 244-246.

[142] J. Hull, J. Lauer, D. Broadbent, Holographic solar concentrators, Energy, 12 (1987) 209-215.

[143] J.E. Ludman, Approximate bandwidthe and diffraction efficiency in thick holograms, American Journal of Physics, 50 (1982) 244-246.

[144] B.N. Gupta, H.L. Yadav, A.K. Chatterjee, S.N. Sinha, Chapter 427 - Optimization of Processing Parameters of Holographic Solar Concentrator for Large Acceptance Angle with Appreciable Diffraction Efficiency for its Use in Sola, in: A.A.M. Sayigh (Ed.) World Renewable Energy Congress VI, Pergamon, Oxford, 2000, pp. 2009-2012.

[145] F. Muhammad-Sukki, R. Ramirez-Iniguez, S.G. McMeekin, B.G. Stewart, B. Clive, Optimised Dielectric Totally Internally Reflecting Concentrator for the Solar Photonic Optoelectronic Transformer System: Maximum Concentration Method, in: R. Setchi, I. Jordanov, R.J. Howlett, L.C. Jain (Eds.) Knowledge-Based and Intelligent Information and Engineering Systems, Pt Iv, Springer-Verlag Berlin, Berlin, 2010, pp. 633-641.

[146] X. Ning, R. Winston, J. O?Gallagher, Dielectric totally internally reflecting concentrators, Appl. Opt., 26 (1987) 300-305.

[147] N. Yamada, K. Kanno, K. Hayashi, T. Tokimitsu, Performance of see-through prism CPV module for window integrated photovoltaics, Optics Express, 19 (2011) A649-A656.

[148] O. Aharon, A. Sasi, BeeHive PV in, Nesher, 2007.

[149] G. Fink, I. Baruchi, Pythagoras Solar, in, Petach Tikva 2010.

[150] N. Sellami, T.K. Mallick, Optical efficiency study of PV Crossed Compound Parabolic Concentrator, Applied Energy, (2012).

[151] N. Sellami, T.K. Mallick, D.A. McNeil, Optical characterisation of 3-D static solar concentrator, Energy Conversion and Management, 64 (2012) 579-586.

[152] N. Sellami, T.K. Mallick, Optical efficiency study of PV Crossed Compound Parabolic Concentrator, Applied Energy, 102 (2013) 868-876.

[153] S. Goma, K. Yoshioka, T. Saitoh, Effect of concentration distribution on cell performance for low-concentrators with a three-dimensional lens, Solar Energy Materials and Solar Cells, 47 (1997) 339-344.

[154] A. Rabl, Optical and thermal properties of compound parabolic concentrators, Solar Energy, 18 (1976) 497-511.

[155] W. Lipinski, A. Steinfeld, Annular compound parabolic concentrator, Journal of Solar Energy Engineering-Transactions of the Asme, 128 (2006) 121-124.

[156] W.T. Welford, R. Winston, High collection nonimaging optics Academic Press, San Diego, 1989.

[157] N. Yehezkel, J. Appelbaum, A. Yogev, M. Oron, Losses in a three-dimensional compound parabolic concentrator as a second stage of a solar concentrator, Solar Energy, 51 (1993) 45-51.

[158] A.A. Radu, J. Mattox, Ray tracing simulations for a modified compound parabolic concentrator to be considered for the VERITAS project, Astroparticle Physics, 11 (1999) 275-276.

[159] A.G. Molledo, A. Luque, Analysis of static and quasi-static cross compound parabolic concentrators, Appl. Opt., 23 (1984) 2007-2016.

[160] J. O'Callagher, Nonimaging Optics in Solar Energy, 2008.

[161] M.J. Carvalho, M. Collarespereira, J.M. Gordon, A. Rabl, TRUNCATION OF CPC SOLAR COLLECTORS AND ITS EFFECT ON ENERGY COLLECTION, Solar Energy, 35 (1985) 393-399.

[162] H. Hinterberger, R. Winston, Efficient Light Coupler for Threshold Čerenkov Counters, Review of Scientific Instruments, 37 (1966) 1094-1095.

[163] M. Brunotte, A. Goetzberger, U. Blieske, Two-stage concentrator permitting concentration factors up to 300X with one-axis tracking, Solar Energy, 56 (1996) 285-300.

[164] V. Andreev, V. Grilikhes, V. Rumyantsev, N. Timoshina, M. Shvarts, Effect of nonuniform light intensity distribution on temperature coefficients of concentrator solar cells, 2003.

[165] Z.H. Lu, Q. Song, S.Q. Li, Q. Yao, A. Othman, The effect of non-uniform illumination on the performance of conventional polycrystalline silicon solar cell, 2007.

[166] E. Franklin, J.S. Coventry, Effects of highly non-uniform illumination distribution on electrical performance of solar cells, in: ANZSES solar conference, Newcastle, Australia, 2002.

[167] A.L. López, V.M. Andreev, Concentrator Photovoltaics, Springer, 2007.

[168] P. Morvillo, E. Bobeico, F. Formisano, F. Roca, Influence of metal grid patterns on the performance of silicon solar cells at different illumination levels, Materials Science and Engineering B-Advanced Functional Solid-State Materials, 159-60 (2009) 318-321.

[169] A. Cole, I. Baistow, L. Brown, T. Bruton, S.D. Iuliis, S. Devenport, K. Drew, K. Heasman, M. Izzi, D. Morrison, L. Pirozzi, E. Salza, L. Serenelli, M. Tucci, Silicon Based Photovoltaic Cells for Concentration – Research and Development Progress in Laser Grooved Buried Contact Cell Technology, in: 7 international conference on Concentrating Photovoltaic System. , Las Vegas USA, 2010.

[170] E.D. Mammo, N. Sellami, T.K. Mallick, Performance analysis of a reflective 3D crossed compound parabolic concentrating photovoltaic system for building façade integration, Progress in Photovoltaics: Research and Applications, (2012).

[171] Optis, OptisWorks, in, 2011, pp. World-leading light and human vision simulation solutions directly in SolidWorks®

[172] C.C. Tsui, H.C. Wei, W.F. Chang, G.D.J. Su, Design and fabrication of a mid-wavelength infrared Fresnel lens via liquid poly(methyl methacrylate), J. Micromech. Microeng., 22 (2012).

[173] T. Hornung, M. Steiner, P. Nitz, Estimation of the influence of Fresnel lens temperature on energy generation of a concentrator photovoltaic system, Sol. Energy Mater. Sol. Cells, 99 (2012) 333-338.

[174] D.C. Miller, S.R. Kurtz, Durability of Fresnel lenses: A review specific to the concentrating photovoltaic application, Sol. Energy Mater. Sol. Cells, 95 (2011) 2037-2068.

[175] A. Rabl, Edge-ray method for analysis of radiation transfer among specular reflectors, Applied Optics, 33 (1994) 1248-1259.

[176] H. Ries, A. Rabl, Edge-ray principle of nonimaging optics, Journal of the Optical Society of America a-Optics Image Science and Vision, 11 (1994) 2627-2632.

[177] M. Adsten, A. Helgesson, B. Karlsson, Evaluation of CPC-collector designs for stand-alone, roof- or wall installation, Solar Energy, 79 (2005) 638-647.

[178] M.E. Blanco, E. Gomezleal, J.M. Gordon, Asymmetric CPC solar collectors with tubular receiver - Geometric characteristics and optimal configurations, Solar Energy, 37 (1986) 49-54.

[179] J. Chaves, Design of two-Dimensional Concentrators, in: Introduction to Nonimaging Optics Taylor & Francis Group, 2008, pp. 531.

[180] J.M. Gordon, H. Ries, Tailored edge-ray concentrators as ideal second stages for Fresnel reflectors, Appl. Opt., 32 (1993) 2243-2251.

[181] D. Jenkins, R. Winston, Tailored reflectors for illumination, Appl. Opt., 35 (1996) 1669-1672.

[182] P.T. Ong, J.M. Gordon, A. Rabl, Tailored edge-ray designs for illumination with tubular sources, Appl. Opt., 35 (1996) 4361-4371.

[183] R. Winston, H. Ries, Nonimaging reflectors as functionals of the desired irradiance, J. Opt. Soc. Am. A, 10 (1993) 1902-1908.

[184] J.M. Gordon, H. Ries, Tailored edge-ray concentrators as ideal 2nd stages for fresnel reflectors, Applied Optics, 32 (1993) 2243-2251.

[185] J.M. Gordon, Simple string construction method for tailored edge-ray concentrators in maximum-flux solar energy collectors, Solar Energy, 56 (1996) 279-284.

[186] R. Winston, W.T. Welford, Geometrical vector flux and some new nonimaging concentrators, J. Opt. Soc. Am., 69 (1979) 532-536.

[187] C.-F. Chen, C.-H. Lin, H.-T. Jan, Y.-L. Yang, Design of a solar concentrator combining paraboloidal and hyperbolic mirrors using ray tracing method, Optics Communications, 282 (2009) 360-366.

[188] J. O'Gallagher, R. Winston, Test of a "trumpet" secondary concentrator with a paraboloidal dish primary, Solar Energy, 36 (1986) 37-44.

[189] E.M. Gray, Possible cost advantage of a primary paraboloid/secondary hyperboloid tandem solar concentrator, Solar Energy, 37 (1986) 397-404.

[190] H. Stephen, C. Gary, G. Jeffrey, F. David, M. Pat, S. Eric, Z. Thomas, A Solid 500 Sun Compound Concentrator PV Design, in: Photovoltaic Energy Conversion, Conference Record of the 2006 IEEE 4th World Conference on, 2006, pp. 694-697.

[191] I.M. Bassett, W.T. Welford, R. Winston, Nonimaging optics for flux concentration, Progress in Optics, 27 (1989) 163-226.

[192] A. Garcia-Botella, A. Alvarez Fernandez-Balbuena, D. Vazquez, E. Bernabeu, Ideal 3D asymmetric concentrator, Solar Energy, 83 (2009) 113-117.

[193] T. Mallick, N. Sellami, Solar Concentrator Design for Double Glazing Window Units, in: H.-W. University (Ed.) Senior Inventor, UK, 2011.

[194] J. Ogallagher, R. Winston, W.T. Welford, Axially-Symmetrical Nonimaging Flux Concentrators with the Maximum Theoretical Concentration Ratio, Journal of the Optical Society of America a-Optics Image Science and Vision, 4 (1987) 66-68.

[195] A. Garcia-Botella, A.A. Fernandez-Balbuena, D. Vazquez, E. Bernabeu, A. Gonzalez-Cano, Hyperparabolic concentrators, Applied Optics, 48 (2009) 712-715.

[196] A. Garcia-Botella, A.A. Fernandez-Balbuena, D. Vazquez, Field method for Dielectric Concentrator Design, in: T.E. Kidger, S. David (Eds.) Illumination Optics Ii, 2011.

[197] R. Winston, W. Zhang, Pushing concentration of stationary solar concentrators to the limit, Optics Express, 18 (2010) A64-A72.

[198] T. Uematsu, T. Warabisako, Y. Yazawa, S. Muramatsu, Static Micro-Concentrator Photovoltaic Module with an Acorn Shape Reflector, in: 2nd World Conference on Photovoltaic Solar Energy Conversion Vienna, Austria 1998, pp. 1570-1573.

[199] Dassult, SolidWorks, in, Vélizy-Villacoublay, 2012, pp. 3D mechanical CAD (computer-aided design) program that runs on Microsoft Windows.

[200] X. Ye, H. Liu, L. Chen, Z. Chen, X. Pan, S. Zhang, Reverse innovative design — an integrated product design methodology, Computer-Aided Design, 40 (2008) 812-827.

[201] G.H. Spencer, M.V.R.K. Murty, General Ray-Tracing Procedure, J. Opt. Soc. Am., 52 (1962) 672-676.

[202] H. Zheng, T. Tao, J. Dai, H. Kang, Light tracing analysis of a new kind of trough solar concentrator, Energy Conversion and Management, 52 (2011) 2373-2377.

[203] J.A. Colina-Marquez, A.F. Lopez-Vasquez, F. Machuca-Martinez, Modeling of direct solar radiation in a compound parabolic collector (CPC) with ray tracing technique, Dyna-Colombia, 77 (2010) 132-140.

[204] D. Groulx, B. Sponagle, Ray-tracing analysis of a two-stage solar concentrator, Transactions of the Canadian Society for Mechanical Engineering, 34 (2010) 263-275.

[205] G. Pei, G.Q. Li, Y.H. Su, J. Ji, S. Riffat, H.F. Zheng, Preliminary Ray Tracing and Experimental Study on the Effect of Mirror Coating on the Optical Efficiency of a Solid Dielectric Compound Parabolic Concentrator, Energies, 5 (2012) 3627-3639.

[206] Synopsys, LightTools, in, Pasadena, 2012, pp. LightTools is a 3D optical engineering and design software product that supports virtual prototyping, simulation, optimization, and photorealistic renderings of illumination applications.

[207] C.W. Chen, G.W. Hopkins, Ray tracing through funnel concentrator optics, Appl. Opt., 17 (1978) 1466-1467.

[208] X. Wei, Z. Lu, W. Yu, W. Xu, Ray tracing and simulation for the beam-down solar concentrator, Renewable Energy, 50 (2013) 161-167.

[209] D.B. Leviton, J.W. Leitch, Experimental and ray trace results for throat-to-throat compound parabolic concentrators, Journal of the Optical Society of America a-Optics Image Science and Vision, 2 (1985) P65-P66.

[210] Y. Ota, K. Nishioka, Total simulator for concentrator photovoltaic modules using ray-trace and circuit simulators, in: Photovoltaic Specialists Conference (PVSC), 2009 34th IEEE, 2009, pp. 002416-002418.

[211] A. Dobroiu, C. Otani, Measurement of the complex refractive index of liquids in the terahertz range using ellipsometry, in: Infrared Millimeter and Terahertz Waves (IRMMW-THz), 2010 35th International Conference on, 2010, pp. 1-1.

[212] B.S. Negi, N.C. Bhowmik, S.S. Mathur, T.C. Kandpal, Ray trace evaluation of solar concentrators including limb darkening effects, Solar Energy, 36 (1986) 293-296.

[213] J.C. Daly, Solar concentrator flux distributions using backward ray tracing, Applied Optics, 18 (1979) 2696-2699.

[214] E.A. Karabassi, G. Papaioannou, C. Fretzagias, T. Theoharis, Exploiting multiresolution models to accelerate ray tracing, Computers & Graphics, 27 (2003) 91-98.

[215] D.P. Luebke, A developer's survey of polygonal simplification algorithms, IEEE Comput. Graph. Appl., 21 (2001) 24-35.

[216] Anon, Solar simulation, in: Newport (Ed.) Oriel xenon arc lamp solar simulator, Stratford, 2012.

[217] A.E.F. Taylor, Basic Radiometric and Photometric Measurement, in: R.P. Institute (Ed.) Illumination Fundamentals, California, 2000.

[218] B. Ravi, Metal Casting- Overview, in: E.E. Edition (Ed.) Metal Casting: Computer-Aided Design And Analysis, New Delhi, 2005, pp. 4.

[219] E.P. Degarmo, J.T. Black, R. Kohser, Materials and Processes in Manufacturing Wiley, 2003.

[220] J.H. Ho, C.L. Lee, T.F. Lei, Refractive index profile measurement of compound thin films by ellipsometry, Electronics Letters, 25 (1989) 1084-1086.

[221] V.R. Fernandes, C.M.S. Vicente, E. Pecoraro, N. Wada, P.S. Andre, R.A.S. Ferreira, Refractive index characterization of waveguide channels using spectroscopic ellipsometry, in: EUROCON - International Conference on Computer as a Tool (EUROCON), 2011 IEEE, 2011, pp. 1-4.

[222] L. Goddard, W. Kai Yeen, A. Garg, E. Behymer, G. Cole, T. Bond, Measurements of the complex refractive index of Pd and Pt films in air and upon adsorption of H2 gas, in: IEEE Lasers and Electro-Optics Society, 2008. LEOS 2008. 21st Annual Meeting of the, 2008, pp. 569-570.

[223] M. Amiotti, G. Landgren, Ellipsometric determination of thickness and refractive index at 1.3, 1.55, and 1.7 μm for In(1−x)GaxAsyP(1−y) films on InP, Journal of Applied Physics, 73 (1993) 2965-2971.

[224] J.A. Woollam, VASE ellipsometer in, Lincoln, 2012.

[225] S. Svanberg, Atomic and Molecular Spectroscopy: Basic Aspects and Practical Applications, Springer, 2004.

[226] Anon, Datasheet: Perkin Elmer Lambda 900 UV-Vis spectrometer, in: P. Elmer (Ed.), Massachusetts, USA, 2010.

[227] J. Ballato, S.H. Foulger, J.D.W. Smith, Optical properties of perfluorocyclobutyl polymers. II. Theoretical and experimental attenuation, J. Opt. Soc. Am. B, 21 (2004) 958-967.

[228] S. Kumar, R. Singh, T.P. Singh, B.L. Sethi, Surface modification by electrical discharge machining: A review, Journal of Materials Processing Technology, 209 (2009) 3675-3687.

[229] N. Pellicer, J. Ciurana, J. Delgado, Tool electrode geometry and process parameters influence on different feature geometry and surface quality in electrical

discharge machining of AISI H13 steel, Journal of Intelligent Manufacturing, 22 (2011) 575-584.

[230] N.P. Mellott, S.L. Brantley, J.P. Hamilton, C.G. Pantano, Evaluation of surface preparation methods for glass, Surface and Interface Analysis, 31 (2001) 362-368.

[231] Anon, Photovoltaic Cell I-V Characterization Theory and LabVIEW Analysis Code, in: N. Instruments (Ed.) NI Developer Zone, 2012.

[232] N. Sellami, Design and optimisation of Crossed Compound Parabolic Concentrator for Photovoltaic Application, in: Mechanical engineering Heriot-Watt University, Edinburgh 2009, pp. 84.

[233] Anon, Datasheet: SOLYS 2, in: D. Kipp & Zonen (Ed.), The Netherlands, 2010.

[234] Anon, Datasheet: CMP-11 pyranometer, in: D. Kipp & Zonen (Ed.), Delft, The Netherlands, 2010.

[235] Anon, Datasheet: CHP1 pyrhaliometer, in: D. Kipp & Zonen (Ed.), Delft, The Netherlands, 2010.

[236] Anon, Datasheet: EKO MI-520 Module selector, in: E.I.C. (Ed.) (Ed.), Tokyo, Japan, 2010.

[237] N. Sendhil Kumar, K. Matty, E. Rita, W. Simon, A.l. Ortrun, C. Alex, W. Roland, G. Tim, M. Tapas Kumar, Experimental validation of a heat transfer model for concentrating photovoltaic system, Applied Thermal Engineering, 33–34 (2012) 175-182.

[238] H. Müllejans, J. Hyvärinen, J. Karila, E.D. Dunlop, Reliability of routine 2-diode model fitting of PV modules, in: 19th European Solar Energy Conference and Exhibition, Paris, France,, 2004.

[239] B.G. Streetman, S. Banerjee, Solid State Electronic Devices, in: Solid state electronic devices, Prentice-Hall, 2000, pp. 214.

[240] D.L. King, J.A. Kratochvil, W.E. Boyson, Temperature coefficients for PV modules and arrays: measurement methods, difficulties, and results, in: Photovoltaic

Specialists Conference, 1997., Conference Record of the Twenty-Sixth IEEE, 1997, pp. 1183-1186.

[241] C.R. Osterwald, T. Glatfelter, J. Burdick, Comparison of the temperature coefficients of the basic I-V parameters for various types of solar cells, in: IEEE (Ed.) IEEE PV Specialists Conference, 1987, pp. 188-193.

[242] R. Platz, D. Fischer, M.A. Zufferey, J.A.A. Selvan, A. Haller, A. Shah, Hybrid collectors using thin-film technology, in: Photovoltaic Specialists Conference, 1997., Conference Record of the Twenty-Sixth IEEE, 1997, pp. 1293-1296.

[243] P.I. Cooper, The absorption of radiation in solar stills, Solar Energy, 12 (1969) 333-346.

[244] J. Duffie, W. Beckman, Solar Radiation, in: WILEY (Ed.) Solar engineering of thermal processes, New Jersey, 2006, pp. 908.

[245] C. Riordan, R. Hulstron, What is an air mass 1.5 spectrum? [solar cell performance calculations], in: Photovoltaic Specialists Conference, 1990., Conference Record of the Twenty First IEEE, 1990, pp. 1085-1088 vol.1082.

[246] Anon, Instruction Manual, in: K. Zonen (Ed.) CMP series Pyranometer, The Netherlands, 2006.

[247] J. Meydbray, E. Riley, L. Dunn, K. Emery, S. Kurtz, Pyranometers and Reference Cells: Part 2: What Makes the Most Sense for PV Power Plants?, NREL, JA-5200-56718 (2012).

[248] A.Q. Malik, S.J.B.H. Damit, Outdoor testing of single crystal silicon solar cells, Renewable Energy, 28 (2003) 1433-1445.

[249] D. Faiman, Assessing the outdoor operating temperature of photovoltaic modules, Progress in Photovoltaics: Research and Applications, 16 (2008) 307-315.

[250] Anon, Geographical Assessment of Solar Resource and Performance of Photovoltaic Technology in: I.f.E.a.T. (IET) (Ed.), 2012.

[251] J.M. Kuitche, V. Sharma, O. Jaewon, R. Pan, G. TamizhMani, Statistical analysis of commercial c-Si PV module photovoltaic efficiency distribution over 10-years

period, in: Photovoltaic Specialists Conference (PVSC), 2012 38th IEEE, 2012, pp. 002421-002425.